



NAVAL FACILITIES ENGINEERING SERVICE CENTER
Port Hueneme, California 93043-4370

Technical Report TR-2065-SHR

DEVELOPMENT AND ANALYSIS OF THE NAVAL FACILITIES ENGINEERING SERVICE CENTER AVIATION ENGINE SIMULATION FACILITY

by

Eugene E. Cooper

October 1996

Sponsored by
Office of Naval Research

DTIC QUALITY INSPECTED 2

19970131 007

Approved for public release; distribution unlimited.

REPORT DOCUMENTATION PAGE			Form Approved OMB No. 0704-018	
Public reporting burden for this collection of information is estimated to average 1 hour per response, including the time for reviewing instructions, searching existing data sources, gathering and maintaining the data needed, and completing and reviewing the collection of information. Send comments regarding this burden estimate or any other aspect of this collection information, including suggestions for reducing this burden, to Washington Headquarters Services, Directorate for Information and Reports, 1215 Jefferson Davis Highway, Suite 1204, Arlington, VA 22202-4302, and to the Office of Management and Budget, Paperwork Reduction Project (0704-0188), Washington, DC 20503.				
1. AGENCY USE ONLY (Leave blank)		2. REPORT DATE October 1996		3. REPORT TYPE AND DATES COVERED Final; Oct 1990 through Sep 1996
4. TITLE AND SUBTITLE DEVELOPMENT AND ANALYSIS OF THE NAVAL FACILITIES ENGINEERING SERVICE CENTER AVIATION ENGINE SIMULATION FACILITY			5. FUNDING NUMBERS RS34S54, Task E-7	
6. AUTHOR(S) Eugene E. Cooper				
7. PERFORMING ORGANIZATION NAME(S) AND ADDRESSE(S) Naval Facilities Engineering Service Center 1100 23rd Avenue Port Hueneme, CA 93043-4370			8. PERFORMING ORGANIZATION REPORT NUMBER TR-2065-SHR	
9. SPONSORING/MONITORING AGENCY NAME(S) AND ADDRESSES Office of Naval Research 800 North Quincy Street Arlington, VA 22217-5000			10. SPONSORING/MONITORING AGENCY REPORT NUMBER	
11. SUPPLEMENTARY NOTES				
12a. DISTRIBUTION/AVAILABILITY STATEMENT Approved for public release; distribution unlimited.			12b. DISTRIBUTION CODE	
13. ABSTRACT (Maximum 200 words) This report documents the development of the Naval Facilities Engineering Service Center (NFESC) Aviation Engine Simulation Facility (AESF). The objective of this effort was to develop a facility which can repetitively expose candidate pavement specimens to convective heat transfer rates equal to those which pavements at operational airfields experience due to jet exhaust impingement. Damage of concrete pavements has become a chronic problem at Navy, Marine Corps and Air Force bases. The damage is due to impingement of vertically directed jet exhaust flow from auxiliary power unit (APU) engines of the F/A-18 and B-1 aircraft, and from the main propulsion engines of the AV-8B aircraft during vertical takeoff and landing. The main component of the AESF is a burner and nozzle assembly in which there is combustion of natural gas. By controlling the combustion chamber pressure and temperature, along with the nozzle diameter and distance from the specimen, the AESF can impose convective heating rates on the specimen that equal the heating rates imposed on operational airfields by full scale engines. The experimental data validated the applicability of the exhaust simulation. Specimens can be repetitively exposed to the simulated exhaust flow to evaluate their performance under the simulated exhaust conditions.				
14. SUBJECT TERMS Jet engine exhaust, pavement damage, thermal fatigue, F/A-18, AV-8B, aircraft, simulation			15. NUMBER OF PAGES 189	
			16. PRICE CODE	
17. SECURITY CLASSIFICATION OF REPORT Unclassified	18. SECURITY CLASSIFICATION OF THIS PAGE Unclassified	19. SECURITY CLASSIFICATION OF ABSTRACT Unclassified	UL	

EXECUTIVE SUMMARY

This report describes the design of the Naval Facilities Engineering Service Center (NFESC) Aviation Engine Simulation Facility (AESF), and presents data that demonstrate capabilities of the facility and that verify the design objectives were met.

In designing the NFESC AESF, the objective was to develop a facility which can repetitively expose specimens of pavement to convective heat transfer rates equal to those which pavements at operational airfields experience due to jet exhaust impingement. Spalling of concrete pavements has become a chronic problem at Navy and Air Force bases where F/A-18, B-1, and AV-8 aircraft operate. The spalling is due to impingement of vertically directed jet exhaust flow from auxiliary power unit (APU) engines of the F/A-18 and B-1 aircraft, and from the main propulsion engine of the AV-8B aircraft during vertical takeoff and landing. Proposed future aircraft and engines may be even more damaging to airfield pavements. The NFESC was tasked to develop concrete mixtures with greater resistance to spalling. The AESF was designed to test specimens of the candidate mixtures under the same conditions that the mixtures will experience in operational settings.

The main component of the AESF is a burner and nozzle assembly in which there is combustion of natural gas. The combustion products flow out the nozzle and form an exhaust plume. By controlling the combustion chamber pressure and temperature, along with the nozzle diameter and distance from the nozzle to the test specimen, the AESF can impose convective heating rates on the specimen that equal the heating rates imposed on operational airfields by full scale engines. Specimens can be repetitively exposed to the simulated exhaust flow until spalling occurs, or until the mix design proves to be resistant to spalling under the imposed conditions.

Design criteria originally established for the AESF were:

1. Flow Parameters

Temperature at nozzle exhaust:	Variable, up to 2,000°F
Velocity at nozzle exhaust:	Variable, up to 500 mph
Duration of continuous flow:	Up to 8 hours
Nozzle geometry:	2-inch diameter, subsonic, variable height and angle

2. Operational Parameters

- Manual startup
- Manual control of flow parameters
- Unattended control panel after setting flow parameters
- Automated safeties
- Initial temperatures of test specimens: 0 to 150°F
- Repeated exposure of specimens until failure occurs
- Concurrent testing of several different test specimens

3. Characteristics of Test Specimens

Size: 24-inch diameter by 6-inch thickness

Makeup of test specimens: various cementing agents, various aggregates

Contaminants: lubricating oil (MIL-L-23699)

Data in this report show that the design criteria were met or exceeded. This report includes detailed descriptions of the analysis procedures used to design the AESF. There are analyses of the combustion processes in the combustion chamber, the nozzle flow, the plume flow, the boundary layer formation in the zone of impingement of the exhaust flow on a specimen, the convective heat transfer rates from the boundary layer to the specimen, and the temperature distribution as a function of time in the specimen. The analyses were used to design the AESF, and later to determine operating settings to simulate the F/A-18 APU engine and the rear nozzle of the AV-8B engine. The AESF was then operated at the predicted settings and data were taken for comparison with, and validation of, the analytical procedures. The experimental data and the calculations are presented in this report, and are compared where possible. The experimental data validate that the analytical procedures can predict the performance of the AESF with acceptable accuracy.

This report concludes with recommendations to lengthen the combustion chamber for better mixing of the combustion products and cooling airflow in the combustion chamber, and to fabricate a new smaller nozzle for better simulation of the AV-8B exhaust flow.

CONTENTS

	Page
OBJECTIVES	1
BACKGROUND	1
DESCRIPTION OF THE NFESC AVIATION ENGINE SIMULATION FACILITY	4
Design Criteria and Considerations	4
Components of the Facility	5
Natural Gas Supply Subsystem	5
Air Supply Subsystem	6
Burner and Test Enclosure Subsystem	6
Monitoring and Control Subsystem	8
Data Acquisition Subsystem	10
Specimen Handling and Preconditioning Subsystem	12
CONSIDERATIONS IN THE DESIGN OF THE NFESC AVIATION ENGINE SIMULATION FACILITY	13
Design Philosophy	13
Design Approach	13
Scaling Factor	14
PERFORMANCE DATA AND DESIGN VERIFICATION DATA FOR THE NFESC AVIATION ENGINE SIMULATION FACILITY	19
Summary of Design of the Burner and Nozzle	19
Results from Attempted Simulations of the F/A-18 Engine and the AV-8B Rear Nozzle	20
Characteristics of the Plume of the Simulated F/A-18 APU Engine	20
Characteristics of the Plume of the Simulated AV-8B Engine Rear Nozzle	24
Impingement of the Exhaust Flow on the Specimens: Pressure Data and Analysis of the Boundary Layer	26
Pressure Distributions on Specimens Due to Impingement of the Exhaust Flow	26
Calculated Characteristics of the Boundary Layers Formed in the Impingement Zone	26
Transient Temperatures of the Specimens During Impingement of the Exhaust Flow: Experimental Data and Predicted Values	28
Transient Temperatures Induced by Impingement of the F/A-18 APU Engine Exhaust	30

	Page
Transient Temperatures Induced by Impingement of the AV-8B Engine Rear Nozzle Exhaust	33
CONCLUSIONS	37
RECOMMENDATIONS	40
REFERENCES	42
APPENDIX - Theory and Analysis Procedures for Design of the NFESC Aviation Engine Simulation Facility	A-1

LIST OF TABLES

<u>Table Number</u>	<u>Title</u>	<u>Page</u>
1	Nozzle and combustion chamber conditions to simulate the F/A-18 APU and the AV-8B rear nozzle	45

Appendix Tables

A-1	Enthalpies and heats of formation for compounds of the combustion of methane and propane	A-44
-----	---	------

LIST OF FIGURES

<u>Figure Number</u>	<u>Title</u>	<u>Page</u>
1	NFESC compound, showing location of Building 566 and the AESF within the compound	48
2	Layout of the Aviation Engine Simulation Facility at Building 566	49
3	Schematic diagram of the natural gas supply subsystem	50
4	Schematic diagram of the air supply subsystem	51

<u>Figure Number</u>	<u>Title</u>	<u>Page</u>
5	Section view of the AESF burner, showing the general flow pattern within the burner	52
6	Burner and test enclosure of the NFESC Aviation Engine Simulation Facility	53
7	Design of the natural gas injector in the burner of the AESF	54
8	Design of the igniter of the burner of the NFESC Aviation Engine Simulation Facility	55
9	Control panel of the NFESC Aviation Engine Simulation Facility	56
10	Circuit diagram for the control panel of the NFESC Aviation Engine Simulation Facility	57
11	Rig to measure temperatures and pressures in the plumes of the NFESC Aviation Engine Simulation Facility	58
12	Design of plate to measure surface pressure distribution on specimens due to plume impingement on the specimens	59
13	Design of instrumented concrete specimens to measure temperature distributions resulting from impingement of the jet flow on the concrete	60
14	The impact echo fault detector used to determine when subsurface cracks have formed parallel to the heated surface of a specimen	61
15	Profile of total pressure in attempted simulation of F/A-18 APU exhaust plume, $Z=0.5''$	62
16	Profile of total pressure in attempted simulation of F/A-18 APU exhaust plume, $Z=6''$	63
17	Profile of total pressure in attempted simulation of F/A-18 APU exhaust plume, $Z=12''$	64

<u>Figure Number</u>	<u>Title</u>	<u>Page</u>
18	Profile of total pressure in attempted simulation of F/A-18 APU exhaust plume, Z=18"	65
19	Profile of total temperature in attempted simulation of F/A-18 APU exhaust plume, Z=0.5"	66
20	Profile of total temperature in attempted simulation of F/A-18 APU exhaust plume, Z=6"	67
21	Profile of total temperature in attempted simulation of F/A-18 APU exhaust plume, Z=12"	68
22	Profile of total temperature in attempted simulation of F/A-18 APU exhaust plume, Z=18"	69
23	Profile of velocity in attempted simulation of F/A-18 APU exhaust plume, Z=0.5"	70
24	Profile of velocity in attempted simulation of F/A-18 APU exhaust plume, Z=6"	71
25	Profile of velocity in attempted simulation of F/A-18 APU exhaust plume, Z=12"	72
26	Profile of velocity in attempted simulation of F/A-18 APU exhaust plume, Z=18"	73
27	Profile of total pressure in attempted simulation of AV-8B exhaust plume, Z=0.5"	74
28	Profile of total pressure in attempted simulation of AV-8B exhaust plume, Z=6"	75
29	Profile of total pressure in attempted simulation of AV-8B exhaust plume, Z=9"	76
30	Profile of total pressure in attempted simulation of AV-8B exhaust plume, Z=12"	77
31	Profile of total pressure in attempted simulation of AV-8B exhaust plume, Z=15"	78

<u>Figure Number</u>	<u>Title</u>	<u>Page</u>
32	Profile of total temperature in attempted simulation of AV-8B exhaust plume, Z=0.5"	79
33	Profile of total temperature in attempted simulation of AV-8B exhaust plume, Z=6"	80
34	Profile of total temperature in attempted simulation of AV-8B exhaust plume, Z=9"	81
35	Profile of total temperature in attempted simulation of AV-8B exhaust plume, Z=12"	82
36	Profile of total temperature in attempted simulation of AV-8B exhaust plume, Z=15"	83
37	Profile of velocity in attempted simulation of AV-8B exhaust plume, Z=0.5"	84
38	Profile of velocity in attempted simulation of AV-8B exhaust plume, Z=6"	85
39	Profile of velocity in attempted simulation of AV-8B exhaust plume, Z=9"	86
40	Profile of velocity in attempted simulation of AV-8B exhaust plume, Z=12"	87
41	Profile of velocity in attempted simulation of AV-8B exhaust plume, Z=15"	88
42	Static pressure as a function of distance from stagnation point on concrete specimens exposed to the simulated F/A-18 APU plume, Z=6"	89
43	Static pressure as a function of distance from stagnation point on concrete specimens exposed to the simulated F/A-18 APU plume, Z=9"	90
44	Static pressure as a function of distance from stagnation point on concrete specimens exposed to the simulated F/A-18 APU plume, Z=12"	91

<u>Figure Number</u>	<u>Title</u>	<u>Page</u>
45	Static pressure as a function of distance from stagnation point on concrete specimens exposed to the simulated F/A-18 APU plume, Z=15"	92
46	Static pressure as a function of distance from stagnation point on concrete specimens exposed to the simulated F/A-18 APU plume, Z=18"	93
47	Static pressure as a function of distance from stagnation point on concrete specimens exposed to the simulated AV-8B plume, Z=6"	94
48	Static pressure as a function of distance from stagnation point on concrete specimens exposed to the simulated AV-8B plume, Z=9"	95
49	Static pressure as a function of distance from stagnation point on concrete specimens exposed to the simulated AV-8B plume, Z=12"	96
50	Static pressure as a function of distance from stagnation point on concrete specimens exposed to the simulated AV-8B plume, Z=15"	97
51	Static pressure as a function of distance from stagnation point on concrete specimens exposed to the simulated AV-8B plume, Z=18"	98
52	Flow velocity at the edge of the boundary layer on concrete specimens exposed to the simulated F/A-18 APU plume, z=18"	99
53	Radial distribution of boundary layer parameter (λ) on concrete specimens exposed to the simulated F/A-18 APU plume, Z=18"	100
54	Radial distribution of boundary layer thickness on concrete specimens exposed to the simulated F/A-18 APU plume, Z=18"	101

<u>Figure Number</u>	<u>Title</u>	<u>Page</u>
55	Radial distribution of convective heat transfer coefficients on concrete specimens exposed to the simulated F/A-18 APU plume, $Z=18"$	102
56	Flow velocity at the edge of the boundary layer on concrete specimens exposed to the simulated AV-8B plume, $z=6"$	103
57	Radial distribution of boundary layer parameter (λ) on concrete specimens exposed to the simulated AV-8B plume, $Z=6"$	104
58	Radial distribution of boundary layer thickness on concrete specimens exposed to the simulated AV-8B plume, $Z=6"$	105
59	Radial distribution of convective heat transfer coefficients on concrete specimens exposed to the simulated AV-8B plume, $Z=6"$	106
60	Comparison of measured and predicted temperatures of a concrete specimen exposed to the simulated F/A-18 APU exhaust, $Z=18"$ (surface, $r=0"$)	107
61	Comparison of measured and predicted temperatures of a concrete specimen exposed to the simulated F/A-18 APU exhaust, $Z=18"$ (surface, $r=1"$)	108
62	Comparison of measured and predicted temperatures of a concrete specimen exposed to the simulated F/A-18 APU exhaust, $Z=18"$ (surface, $r=2"$)	109
63	Comparison of measured and predicted temperatures of a concrete specimen exposed to the simulated F/A-18 APU exhaust, $Z=18"$ (surface, $r=4"$)	110
64	Comparison of measured and predicted temperatures of a concrete specimen exposed to the simulated F/A-18 APU exhaust, $Z=18"$ (0.25" below surface, $r=0"$)	111

<u>Figure Number</u>	<u>Title</u>	<u>Page</u>
65	Comparison of measured and predicted temperatures of a concrete specimen exposed to the simulated F/A-18 APU exhaust, Z=18" (0.5" below surface, r=0")	112
66	Comparison of measured and predicted temperatures of a concrete specimen exposed to the simulated F/A-18 APU exhaust, Z=18" (1" below surface, r=0")	113
67	Comparison of measured and predicted temperatures of a concrete specimen exposed to the simulated F/A-18 APU exhaust, Z=18" (2" below surface, r=0")	114
68	Comparison of measured and predicted temperatures of a concrete specimen exposed to the simulated AV-8B rear nozzle exhaust, Z=6" (surface, r=0")	115
69	Comparison of measured and predicted temperatures of a concrete specimen exposed to the simulated AV-8B rear nozzle exhaust, Z=6" (surface, r=1")	116
70	Comparison of measured and predicted temperatures of a concrete specimen exposed to the simulated AV-8B rear nozzle exhaust, Z=6" (surface, r=2")	117
71	Comparison of measured and predicted temperatures of a concrete specimen exposed to the simulated AV-8B rear nozzle exhaust, Z=6" (surface, r=4")	118
72	Comparison of measured and predicted temperatures of a concrete specimen exposed to the simulated AV-8B rear nozzle exhaust, Z=6" (0.25" below surface, r=0")	119
73	Comparison of measured and predicted temperatures of a concrete specimen exposed to the simulated AV-8B rear nozzle exhaust, Z=6" (0.5" below surface, r=0")	120
74	Comparison of measured and predicted temperatures of a concrete specimen exposed to the simulated AV-8B rear nozzle exhaust, Z=6" (1" below surface, r=0")	121

<u>Figure Number</u>	<u>Title</u>	<u>Page</u>
75	Comparison of measured and predicted temperatures of a concrete specimen exposed to the simulated AV-8B rear nozzle exhaust, Z=6" (4" below surface, r=0")	122

Appendix Figures

A-1	Combustion temperatures as a function of excess air for methane and propane	A-45
A-2	Illustrations of subsonic, sonic, and supersonic nozzle configurations and required combustion chamber pressures	A-46
A-3	Features of a turbulent jet flowing into still air, and impinging on a concrete specimen	A-47
A-4	Total pressure as a function of mass flow rate for streamlines of the F/A-18 APU engine plume, Z=12"	A-48
A-5	Total temperature as a function of mass flow rate for streamlines of the F/A-18 APU engine plume, Z=12"	A-49
A-6	Static pressure as a function of distance from stagnation point on concrete specimens exposed to the simulated F/A-18 APU plume, Z=12"	A-50
A-7	Comparative illustrations of classical boundary layer and boundary layer formed by jet impingement	A-51

OBJECTIVES

The objectives of this report are: (1) to describe the design and the design analyses of the Naval Facilities Engineering Service Center (NFESC)¹ Aviation Engine Simulation Facility (AESF); and (2) to present data that demonstrate the performance capabilities of the AESF and that verify the design analyses.

BACKGROUND

Design and construction of the NFESC Aviation Engine Simulation Facility was funded by the High Temperature Pavements Project, sponsored by the Office of Naval Research and managed by the Naval Facilities Engineering Command. The project was initiated with the objective of developing one or more mix designs for concrete which can be used at airfields where impingement of jet exhausts can cause spalling of Portland cement concrete. The AESF enables testing of specimens of the various mix designs at conditions which simulate those at an operational airfield. This Background discussion summarizes work leading up to design and construction of the NFESC AESF that influenced the design parameters.

Several new types of aircraft in the military inventory cause spalling of concrete at airfields:

1. The Navy and Marine Corps F/A-18 aircraft cause concrete to spall at their parking slots on airfield parking aprons. Spalling occurs in the area where the exhaust of the auxiliary power unit (APU) impinges during preflight preparations of the aircraft.
2. The Marine Corps AV-8 aircraft cause concrete to spall from the surfaces of the landing pads used for vertical takeoffs and landings. The spalling occurs where the exhaust flow from the main propulsion engine, which is directed almost straight downward during vertical takeoff and landing, impinges repeatedly on the landing pad.
3. Each Air Force B-1 bomber has an APU which is responsible for the spalling on the parking aprons at Air Force bases. The spalling at the Air Force bases appears to be like the spalling at the parking slots for the Navy F/A-18s.
4. Although the Marine Corps V-22 aircraft are not yet in production, the vertically directed exhaust flows from the turboprop engines are expected to cause spalling of the concrete at the airfields where V-22s will operate.

¹ Formerly the Naval Civil Engineering Laboratory (NCEL). Work and reporting done prior to formation of NFESC is attributed to NCEL.

There have been various attempts in the past to prevent spalling and/or to repair the airfield concrete in the areas of spalling. Based on References 1 and 2, the Naval Civil Engineering Laboratory (NCEL) formulated a specification for construction of V/STOL landing pads using Fondue Fire[®] refractory concrete impregnated with small stainless steel fibers. The specification calls for refractory concrete material which is more expensive than ordinary Portland cement concrete, for special installation equipment to mix the concrete and stainless steel fibers, and for personnel trained to operate the equipment. The specification was only used for the construction of one AV-8 landing pad, which is at the Marine Corps Air Station (MCAS), Cherry Point, North Carolina. Use elsewhere was deferred until the durability of the pad at MCAS Cherry Point could be evaluated. Objections to widespread use were raised over the cost of materials, the requirement for special equipment and specially trained operators, and the possibility that some stainless steel fibers might become detached and present a hazard of foreign object damage (FOD) to the aircraft engines. After about 3 years of operation, the landing pad was closed by the Operations Officer at the MCAS due to exposure and incipient detachment of some of the stainless steel fibers, and due to the cosmetic appearance of the pad.

For the F/A-18 parking aprons, the Naval Facilities Engineering Command (NAVFAC) developed a specification for a concrete mixture called the "NAVFAC High Temperature Pavement" (Ref 3). The NAVFAC High Temperature Pavement is made of Portland cement concrete with a high temperature basalt aggregate. The specification was used to construct three AV-8 landing pads, also at MCAS Cherry Point. No periodic inspections have been made of the pads at MCAS Cherry Point. After about 3 years of service, the three landing pads at Cherry Point are still in use, but their condition is not quantified.

The problems caused by the APUs of the F/A-18 and B-1 aircraft typically begin to appear from 1 to 3 years after F/A-18 or B-1 operations begin at a base (Ref 4). The shorter periods before spalling of the parking aprons occur in the colder climates, and the longer periods before spalling occur in the warmer climates. The Naval Air Test Center (NATC) and the Naval Aviation Engineering Center (NAEC) have measured temperatures at the surface and slightly beneath the surface of concrete in the area of impingement of an F/A-18 APU engine (Refs 5 and 6). A maximum surface temperature of 321°F was measured. NCEL calculated stress levels in the concrete pads using the measured temperatures as input data. Properties of the cementing agent and of the aggregate were varied parametrically as part of the analyses. It was determined that thermally induced tensile stresses in the top 1/4 inch of the concrete would slightly exceed the tensile strength of concrete, especially when the initial temperature of the concrete was low (Ref 7). Samples of spalled concrete from various bases indicate that, indeed, failure is by delamination (tensile failure) at approximately 1/4 inch below the surface (Ref 4). An investigation of the effects of free moisture in the concrete revealed that the free moisture will increase the tensile stresses when heated (Ref 8). Examination of the spalled concrete, the temperature measurements, and the stress analysis results led NCEL to postulate that the spalling of the concrete heated by jet exhausts is caused by repeatedly inducing tensile stresses which are near the tensile strength of the concrete. Failure is not immediate, but occurs after numerous cycles. In other words, the NCEL postulate was that failure is a thermally induced fatigue failure of the concrete within the upper 1/4 inch of the material.

Reference 9 reports a similar conclusion based on analytical studies of V/STOL exhaust flow impinging on various airfield surfaces. Reference 9 shows concrete surfaces reaching temperatures that normally cause concrete to fail structurally.

Reference 10 reports a different conclusion as to the cause of spalling. In Reference 10, the U.S. Air Force Engineering and Services Center, Tyndall Air Force Base (AFB), Florida, reports investigations of weakening of the concrete due to reactions between calcium hydroxide in the concrete and esters in hydraulic fluid which leaks from aircraft. The postulate is that the reaction weakens the concrete to the point that the downwardly directed jet exhaust flows can dislodge particles of concrete from the surface. References 11 through 16 report results of tests at the South Dakota School of Mines and Technology in which concrete samples were soaked with water, jet fuel, or hydraulic fluids, then a simulated jet exhaust was directed onto the samples, and the effects on spalling were measured. The data of References 11 through 16 do not conclusively support the postulate of Reference 10.

The NFESC AESF is designed to give a laboratory simulation of the conditions to which the airfield concrete is exposed in the areas of spalling. Basically, the intent is to obtain the same convective heat input rate in the laboratory as occurs at the airfields, and to repeatedly expose samples of concrete to the same convective heat input until failure occurs, or the ability is demonstrated to resist failure. With the same convective heat input rate, the temperature distribution and the tensile stress distribution will be the same in the laboratory samples as in the airfield concrete. If desired, the samples can be soaked with hydraulic fluid or other contaminants to study the effects of such spillage.

As mentioned above, prior laboratory tests in which concrete samples were heated by simulated jet exhausts have been conducted at the South Dakota School of Mines and Technology (References 11 through 16). The British Aerospace Corporation has also conducted tests in which specimens of various candidate airfield pavement mixtures were heated by the exhaust flow of a scale model engine (Ref 17). During Reference 18, the Air Force Engineering and Service Center demonstrated equipment and discussed plans for tests of instrumented concrete specimens exposed to a simulated jet exhaust developed by a propane burner. Due to the informal nature of References 17 and 18, it is not known just how the convective heat transfer rates in the laboratories compared to those at operational sites. Theoretical bases for design of the experiments were not presented. However, the extremely high temperatures and/or velocities of the simulated engine flows caused rapid and severe damage to the specimens, and it was apparent that the laboratory conditions did not match operational conditions. In the tests at the South Dakota School of Mines and Technology, the simulated engine exhaust conditions were not so severe, but spalling of the specimens was intentionally accelerated by making the heating rates higher than those at operational airfields.

This report describes the design of the NFESC test facility and its data acquisition system, and presents the theory and mathematical expressions for determining the convective heat transfer rates and the other parameters of the test facility.

DESCRIPTION OF THE NFESC AVIATION ENGINE SIMULATION FACILITY

Design Criteria and Considerations

The following design criteria were established for the NFESC Aviation Engine Simulation Facility:

1. Flow Parameters

Temperature at nozzle exhaust:	Variable, up to 2,000°F.
Velocity at nozzle exhaust:	Variable, up to 500 mph
Duration of continuous flow:	Up to 8 hours
Nozzle geometry:	2-inch diameter, subsonic, variable height and angle

2. Operational Parameters

- Manual startup
- Manual control of flow parameters
- Unattended control panel after setting flow parameters
- Automated safeties
- Initial temperatures of test specimens: 0 to 150°F
- Repeated exposure of specimens until failure occurs
- Concurrent testing of several different test specimens

3. Characteristics of Test Specimens

- Size: 24-inch diameter by 6-inch thickness
- Makeup of test specimens: various cementing agents, various aggregates
- Contaminants: lubricating oil (MIL-L-23699)

Except for the criterion of manual startup, the design criteria were established during the conceptual design phase. Originally, an automated startup procedure was planned. At that time, it was also planned that four burners would be built and operated with frequent startups and shutdowns. It was later decided that only one burner would be built initially, and that it would typically run for several hours before shutdown.

After consideration of several locations within the NFESC compound, the decision was made to put the AESF at Building 566. Figure 1 shows the location of Building 566 within the compound. Factors leading to the choice of Building 566 included:

1. The natural gas line for the NFESC compound passes adjacent to Building 566. Adequate electrical power was also available within the building.

2. There was space available for the AESF components, both for the components which needed to be inside a building and those which had to be outside. In fact, the ell

attached to Building 566, which was previously used for storage space, was one of the few available interior spaces on the NFESC compound.

3. Building 566 contains the office of the technician who would coordinate fabrication of the AESF, and who would later coordinate the operation and maintenance activities.

4. Building 566 also contains the NFESC environmental chambers which can be used to precondition the concrete test specimens prior to exposure to simulated jet exhaust flows.

One disadvantage of locating the AESF at Building 566 is the proximity to the photographic studios in Building 567, and the offices in Buildings 566, 564, and 559. Noise from the compressors and simulated jet exhausts may be a nuisance to the personnel in these nearby buildings.

Components of the Facility

The layout of the AESF, with some of the major components identified, is shown in Figure 2. Figure 2 shows that the natural gas compressor and natural gas storage tank, as well as the air blower and air storage tank, are on a skid beside Building 566. The control room with its control panel and the burner and the test enclosure, where samples are placed for exposure to the simulated jet exhaust, are located in the ell attached to Building 566. The cold chamber, where test samples are preconditioned between exposures to the simulated jet exhaust, is in Building 566.

The AESF can be considered as a combination of six subsystems. They are: (1) the natural gas supply subsystem; (2) the air supply subsystem; (3) the burner and test enclosure subsystem; (4) the monitoring and control subsystem; (5) the data acquisition subsystem; and (6) the specimen handling and preconditioning subsystem. These are described and discussed below.

Natural Gas Supply Subsystem. This subsystem is comprised of the components which take gas from the Southern California Gas Company (SCGC) distribution line and deliver the gas to the burner. Figure 3 is a schematic of the natural gas supply subsystem.

The SCGC line brings gas at 5 psig to a meter located beside the natural gas compressor outside Building 566. The gas then flows sequentially through the following components shown in Figure 3: the totalizing gas meter; the pressure regulator which drops the pressure to 8 inches H₂O; the natural gas compressor which raises the gauge pressure to nominally 35 lb_f/in.²; the 1-inch line from the compressor to the accumulator tank; the 200-gallon accumulator tank; the gas line pressure regulator which drops pressure from 30 to 35 psig to 12 to 13 psig; the 2-1/2-inch-diameter line to the burner intake; and the flow control butterfly valve in the 2-1/2-inch line where it passes through the control room. Miscellaneous valves are also in the lines so that gas flow can be stopped and components can be isolated at several points.

The natural gas meter was included so the sponsoring project can be billed for gas usage in the AESF. Gas consumption in the AESF is a significant portion of the overall NFESC consumption.

The natural gas compressor is driven by a 10-horsepower, 3-phase, 220-volt electric motor. The compressor capacity is approximately four times larger than necessary to supply gas to the single burner of the AESF. The compressor was procured when the intent was to operate up to four burners in the AESF. Because the compressor has excess capacity, it operates intermittently. A high-low pressure sensor at the compressor outlet controls a switch which turns the compressor on when the pressure drops to a preset level (nominally 28 psig), and turns the compressor off when the pressure increases to a higher pressure (nominally 35 psig). The compressor is also equipped with automatic shutoffs if excessive temperature or vibration are sensed.

Air Supply Subsystem. Figure 4 shows a schematic of the air supply subsystem. The air supply subsystem compresses atmospheric air and delivers it to the burner. The components of the air supply subsystem are: a rotary vane air compressor; a bypass valve to control how much compressor air goes to the burner and how much is diverted back to the atmosphere; a 250-gallon accumulator storage tank; a 4-inch pipe from the tank to the burner; and a butterfly flow control valve in the section of the 4-inch pipe that passes through the control room.

The air compressor is powered by a 30-horsepower, 3-phase, 220-volt electric motor. The compressor is capable of delivering approximately $0.6 \text{ lb}_m/\text{sec}$ of air to the burner at a backpressure of 10 psig in the combustion chamber. Normally, however, the burner is operated at a pressure less than 10 psig. The compressor still pumps $0.6 \text{ lb}_m/\text{sec}$, but it draws less than 30 horsepower from the electric motor.

The simulation of most engines requires that the full output of the compressor be passed through the burner. Therefore, during periods when exhaust flow is directed onto specimens, the bypass valve is set so that all flow goes to the burner, and none is "dumped" to the atmosphere. During startup of the burner, however, ignition will not start unless airflow through the burner is reduced to about $1/3$ of the compressor output. So during startup, the bypass valve is adjusted to "dump" about $2/3$ of the air compressor output to atmosphere.

Burner and Test Enclosure Subsystem. The burner is illustrated in Figure 5. Figure 6 is a photograph of the burner and test enclosure. The function of the burner is to produce an exhaust flow which simulates the exhaust flow of a jet engine and causes convective heat fluxes ($\text{Btu}/\text{ft}^2\text{-sec}$) on test specimens that equal those occurring on airfield pavements heated by actual aircraft engine exhausts.

The test enclosure is simply a steel hood, 60 inches wide by 60 inches deep by 60 inches high. The burner sits on top of the hood and is bolted to the hood at a diameter of 26 inches around a support ring. The hood has a 20-inch-diameter hole, in the center of which is the 2-inch-diameter nozzle through which the exhaust gases from the burner are directed downward onto the test specimens. The 20-inch-diameter hole is large enough so that access and disassembly of the burner can be accomplished from below. The hood is open on the east and west sides, but has solid steel sides on the north and south sides. The hood sits on the

concrete floor of the ell of Building 566, and the two solid steel sides are bolted to the concrete floor.

The burner is a unique apparatus. It was designed by NFESC personnel specifically for the AESF. The dimensions of the basic burner casing are 12 inches in diameter by 36 inches high (note that one of the recommendations of this report is that the burner casing be lengthened to achieve better mixing of the air and combustion products within the burner). The upper 12-inch section of the burner is primarily an inlet and swirl chamber for the air. Air from the 4-inch pipe of the air supply subsystem comes tangentially into the upper chamber of the burner. A baffle forces the air to swirl in the upper chamber. The air passes through a hole in the baffle, then through a 5-inch-diameter hole into the lower chamber, or combustion chamber, of the burner.

Natural gas comes into the burner through a 1-inch vertical pipe which extends from the top of the burner, through the center of the upper chamber, to near the top of the combustion chamber. The natural gas pipe is capped with an injector (Figure 7). The injector has a complex pattern of 36 holes, each 1/8 inch in diameter. The pattern of holes makes the gas leave the injector in a direction generally opposite to that of the airflow, thereby enhancing mixing of the air with the natural gas prior to ignition. Figure 5 shows a slotted, serrated/flared sleeve around the natural gas inlet pipe and injector. The sleeve position can be adjusted about 1 inch in the vertical direction. The function of the sleeve is to modulate the amount of air available to mix with gas between the injector and the igniter. It was determined that too much air at the injector made ignition difficult.

Figure 5 shows the igniter inserted into the upper part of the combustion chamber. The design of the igniter is shown in Figure 8. Basically, the igniter is an electrical resistance heater in which 1 inch of the exposed tip of a silicon-nitride heating element becomes cherry red when sufficient voltage is applied to the plug at the end of the igniter. The cherry-red tip of the igniter is positioned just beneath one edge of the serrated/flared sleeve. The position can be adjusted when the Swagelok fitting attaching the igniter to the burner is loosened. Using a Variac transformer to increase 117-volt line voltage, 135 to 165 volts are applied to the igniter plug. The igniter tip temperature has not been measured, but voltage in the range of 135 to 165 volts has been found to compensate for cooling by the burner airflow and give a tip temperature that consistently ignites the burner.

The combustion chamber of the burner is lined with silica-alumina refractory material. The refractory was cast in four sections (chamber top, chamber side, chamber bottom, and nozzle liner) so the burner can be disassembled or parts of the refractory can be replaced as necessary. The interior volume of the combustion chamber is a cylinder, 22 inches high by 10 inches in diameter (again, note that a recommendation of this report is to increase the length by 12 inches). The refractory surrounding the interior volume is an effective insulator for the steel shell of the burner. There are two penetrations of the steel shell and refractory liner of the combustion chamber. One is for a thermocouple, and one is for a pressure probe. Both penetrations are sealed with Swagelok fittings which prevent flow out the penetrations.

The nozzle of the burner is a 2-inch-diameter hole centered at the bottom of the combustion chamber. The nozzle liner section of refractory material is an annulus 2-inch I.D. and a 5-inch O.D. which protects the steel in the bottom plate of the combustion chamber from heating by flow through the nozzle.

The bottom plate of the burner is held in place by four bolts, each of which partially compresses a spring. The bottom plate will act as a pressure relief valve in case of explosion in the combustion chamber. If there is excessive pressure in the combustion chamber, the bottom plate can move downward by further compressing the springs. When the springs have compressed about 1-1/2 inches, gas from the combustion chamber can escape around the perimeter of the bottom plate, as well as through the normal escape route through the nozzle.

Monitoring and Control Subsystem. Figure 9 shows the control panel located in the control room of the AESF. The control panel contains the circuitry for the safety features of the AESF, and has digital displays of operating parameters of the facility. Specifically, the control panel displays eight parameters: (1) natural gas flow to the burner; (2) airflow to the burner; (3) pressure in the natural gas accumulator tank; (4) pressure in the air accumulator tank; (5) pressure in the natural gas line between the gas accumulator tank and the burner; (6) pressure in the air line between the air accumulator tank and the burner; (7) pressure in the combustion chamber of the burner; and (8) temperature in the combustion chamber of the burner.

Measurements for the control panel displays are made with the following types of meters or transducers:

1. Natural gas flow: Fluid Components Inc. Model LT81A Mass Flowmeter.
2. Airflow: Fluid Components Inc. Model AF88 Air Flowmeter.
3. Pressure in the natural gas accumulator tank: Omega Engineering Pressure Transducer Model PX425-0306V.
4. Pressure in the air accumulator tank: Omega Engineering Pressure Transducer Model PX425-0306V.
5. Pressure in the natural gas line: Omega Engineering Pressure Transducer Model PX425-0306V.
6. Pressure in the air line: Omega Engineering Pressure Transducer Model PX425-0306V.
7. Pressure in the burner combustion chamber: Omega Engineering Pressure Transducer Model 242PC05G.
8. Temperature in the burner combustion chamber: Omega Engineering Thermocouple Probe, Model undetermined.

Several automatic safety features are included in the design of the AESF. The circuitry of the control panel automatically stops or holds operations when any safety criterion is

violated. Figure 10 is the circuit diagram of the control panel. The built-in safety features are:

1. Proper ignition sequence must be followed. The airflow to the burner must be on for 5 seconds before the igniter can be turned on. This ensures that the combustion chamber is purged of combustibles before there is an ignition source. Then the igniter must be on for 20 seconds before the natural gas solenoid valve opens to start gas flow into the burner. This ensures that the igniter has time to heat up before gas is introduced.

2. Natural gas is shut off in case of igniter failure. The igniter is on continuously while the burner is operating. In case of igniter failure, or loss of power to the igniter, the solenoid valve controlling flow of natural gas to the burner is closed. Once the solenoid closes due to igniter failure, the control panel switch must be reset manually before the solenoid will open. This is to prevent loss of ignition due to a short power outage, then having the ignition sequence restart automatically and possibly out of sequence when power is restored. (It is noteworthy that tests have shown that, after combustion has started in the burner, combustion continues if gas and air flows are continued after the igniter is turned off. However, the igniter is left on continuously during operations as an added safeguard.)

3. A "panic button" is available for emergency shutdown. If emergency shutdown is required, a "panic button" on the control panel immediately cuts off power to the igniter, immediately closes the solenoid valve controlling flow of natural gas to the burner by turning off power to the solenoid, immediately turns off power to the natural gas compressor, and turns off power to the air compressor after a 5-second delay. The delay in turning off the air compressor allows a short period to purge the combustion chamber of combustible gases. After the panic button is pushed, a reset switch on the control panel must be manually reset before operations of any of the affected components can be resumed. This ensures that nothing restarts automatically, and that the operator can correct the emergency situation while there is an electrical "lockout" by the control panel.

4. The natural gas compressor is turned off in case of accumulator tank overpressure. If the pressure in the natural gas accumulator tank exceeds 50 lb_f/in.² gauge pressure, electrical power to the natural gas compressor is turned off. The compressor has a separate high-low type switch which cycles the off-on operation of the compressor to keep the accumulator tank pressure within the range 30 to 35 lb_f/in.². In case of failure of the high-low switch, however, the compressor would be turned off when tank pressure reaches 50 lb_f/in.². The tank itself is rated for internal pressures of 125 lb_f/in.².

5. The igniter and natural gas flow are turned off in case of excessive burner temperature. If the temperature in the burner exceeds 2,200°F, the igniter is turned off and natural gas flow to the burner is shut off by closing the solenoid controlling the fuel flow. The limiting temperature is approximately the upper temperature limit for the refractory lining of the combustion chamber.

Data Acquisition Subsystem. There are two sets of instrumentation for data acquisition. Set 1, called the Calibration Data Acquisition Subsystem, is used to determine the performance parameters of the AESF. The data presented in this report were acquired with the Calibration Data Acquisition Subsystem. The purpose of the Calibration Data Acquisition Subsystem is to verify that the design criteria have been met and that theoretically predicted performance can be achieved.

Set 2, called the Simulation Testing Data Acquisition Subsystem, is used for acquisition of data during routine testing of specimens. The purpose of the Simulation Testing Data Acquisition Subsystem is to monitor the conditions to which the specimens are exposed, and to detect when the specimens become damaged or fail.

Calibration Data Acquisition Subsystem. Instrumentation in the calibration data acquisition subsystem includes: (a) a thermocouple and a total pressure probe mounted on a rig which can position the thermocouple or the pressure probe at any desired point in the jet exhaust plume; (b) a 24-inch-diameter steel plate with 18 static pressure ports in one radial direction and 5 static pressure ports in a radial direction 90 degrees from the first; and (c) two concrete specimens, one 18 inches by 18 inches square by 4 inches thick, and one 24 inches in diameter by 6 inches thick, with thermocouples imbedded in a prescribed pattern at various radial positions and depths from the surface. These are discussed below:

1. Figure 11 shows the rig with the thermocouple and pressure probe for measuring flow properties in the plume. The thermocouple is attached to the end of a 3-foot-long boom made of 2-inch by 2-inch angle iron. The pressure probe is also attached to the boom, but is 2 inches away from the thermocouple to avoid interference of one measurement with the other. The angle iron is inverted to shield and protect the leads from the probes to the signal processing and recording equipment. The boom is clamped in a vise mounted on a mill table, which in turn is mounted on a hand-operated forklift. The forklift raises or lowers the probes to any desired distance below the nozzle exit plane. After leveling, the mill table permits precise placement of the probes anywhere in a horizontal plane through the plume. Linear position switches are attached to the mill table to measure both x and y positions from an established reference point. At a given horizontal plane, e.g., 6 inches below the nozzle exit plane, x and y positions and the temperature and pressure readings are monitored and recorded. The procedures for calibrating the temperature and pressure instrumentation, and for processing the data signals from the instrumentation, are described in Appendix B of Reference 19.

2. Figure 12 shows the locations of static pressure taps on the 1/4-inch steel plate used to determine pressure distributions of surfaces placed in the jet exhaust plume. The instrumented plate is placed in the plume at various distances between 6 inches and 24 inches from the nozzle exit plane. The center of the instrumented plate is put directly beneath the center of the nozzle exhaust.

The pressure taps are made by drilling 1/8-inch-diameter holes centered at the designated locations. Each hole is countersunk on the top surface of the plate to 1/8-inch depth, with sides at 15 degrees to the vertical centerline. Two-foot lengths of 1/8-inch copper

tubing are pressed into each hole from the bottom until they slightly protrude above the top surface of the plate. The tubes have been flared to prevent retraction, and a grinding wheel has been used to smooth the pressure taps and top surface of the plate. Tygon plastic tubes are attached to the ends of the copper tubes 2 feet beneath the plate, where the copper tubes are cool enough so that tygon is not damaged. The tygon tubes are in turn attached to the ports of a Scanivalve Corporation Model 48J9-2270 Scanning Valve. The scanning valve opens and closes valves in a programmed sequence so that, within 2 seconds, the pressure at each port is measured by a pressure transducer installed to the Scanning Valve. The sequence is repeated at intervals of 5 seconds. The procedure for calibrating and processing the data signals from the pressure transducer is described in Appendix B of Reference 19.

3. Figure 13 shows the approximate locations of thermocouples in the concrete specimens used to determine performance parameters of the AESF. The specimens are made of Portland cement concrete with river bed aggregate. Density of the specimens is about 147 lb_m/ft³. The thermocouples are type K, chromel-alumel.

The connections were made by twisting the dissimilar wires together so that contact is made throughout a length of 1/8 inch or more. The thermocouples were positioned in space within the empty forms before the concrete was poured, with the leads routed out the bottom of the forms. The thermocouples could move slightly while the concrete was being poured. Once the concrete was poured, it was not possible to verify the exact positions of the thermocouples. Therefore, the locations shown in Figure 13 are only approximate. The thermocouple wires from the bottom of the specimens are terminated in banana plugs, which allow connections to leads extending to a Campbell Scientific Instruments 21X datalogger, or detachment so the specimens can be removed.

Simulation Testing Data Acquisition Subsystem. The data acquisition subsystem instrumentation used during the repetitive exposure of samples to simulated jet exhaust flows includes: (a) thermocouples in some of the concrete specimens being tested, and (b) an Impact Echo Fault Detector which is used to detect incipient spalling of the specimens. These are discussed below:

1. The discussion of thermocouples placed in the specimens of the Set 1 data acquisition system applies here. Thermocouple locations may be different or fewer, however, and thermocouples are usually placed only in a few of the specimens.

2. The Impact Echo Fault Detector is shown in Figure 14. It is used to detect subsurface cracks parallel to the heated surface of a specimen. Spalled concrete beneath F/A-18 APU exhausts has the appearance of scale, approximately 1/4 inch thick. This leads to the conclusion that the concrete was probably cracking beneath the surface before failure became visually apparent at the surface. Techniques for detection of subsurface cracks were considered and evaluated. The Impact Echo Fault Detector has been successfully used by highway and bridge inspectors to locate subsurface cracks or flaws in bridges or other concrete structures. Previous applications of the Impact Echo Fault Detector were in search of cracks or flaws much deeper than 1/4 inch. The principle of operation is that a spring-loaded plunger

impacts the surface of the concrete, imposing a compressive wave. The wave moves through the concrete until it is reflected by a flaw, crack, or back surface. The reflected wave returns to the impacted surface, where a transducer detects it. The wave re-reflects from the impacted surface, goes again to the flaw or back surface, re-reflects, etc. The transducer detects a series of reflections until the wave attenuates. From the time between peaks indicating arrival of the wave at the impacted surface, and knowing the speed of sound in concrete, the depth of the crack or flaw can be calculated. NFESC purchased an Impact Echo Fault Detector modified to detect cracks or flaws at an approximate 1/4-inch depth. Detailed information about the Impact Echo Fault Detector can be obtained from Reference 20.

Specimen Handling and Preconditioning Subsystem. The specimen handling and preconditioning subsystem consists of: (a) the NCEL cold chamber which is used to bring the specimens to a predetermined temperature before each exposure to the jet exhaust; (b) carts on which the specimens are moved between the cold chamber and the AESF hood; and (c) a hand-operated hydraulic forklift to raise and lower the specimens for testing, and to hold the specimens at the desired distance below the exhaust plane of the nozzle during testing.

As noted in the Background section of this report, field observations of damage to pavements due to impingement revealed a history of spalling occurring more rapidly in cold climates. Stress analyses showed that stresses are higher in the jet impingement zone if the pavement temperature is lower before impingement starts. Therefore, one of the test capabilities established for the AESF was to be able to cool the specimens to various temperatures before exposure to the simulated jet. Building 566 was ideal for this because it already housed the NCEL cold chamber. The cold chamber is a refrigerated environmental test chamber, 27.5 feet long, 12 feet wide, and 8 feet high. It is capable of cooling its contents to approximately -50°F. It is equipped with double doors, 9.5 feet wide by 8 feet high, at the front of the chamber. Either door or both doors can be opened to move contents in and out of the chamber. The cold chamber was used to cool the specimens to 0°F for some tests and about 32°F for others. Other tests were conducted with the specimens initially at atmospheric temperature. By experimentation with the calibrated slabs, it was determined that a specimen would cool to reasonably uniform preconditioned temperature (less than 5°F variation) in about 4 hours if left to cool naturally in still air. However, if air were blown over the specimens with fans, the same level of uniformity could be reached in 2 to 2.5 hours. A bank of fans was mounted in the cold chamber to circulate air over the specimens, which allowed three complete cycles of testing for each specimen during an 8- to 9-hour test day.

To move the specimens between the cold chamber and the burner/jet exposure area, each specimen was rigidly mounted on its own dedicated 4-wheel steel laboratory cart. The carts were approximately 25 inches wide, 34 inches long, and 34 inches high, and had two shelves. Specimens were placed on the flat top shelves. Four holes were drilled through each top shelf just outside the circumference of the specimens. Four 1/2-inch steel rods were threaded at one end, dropped through the holes and bolted to the top shelf so that they stood vertically, then the top ends were bent over the specimen so that each specimen could not slide off the shelf during movement of its cart. The carts eliminated the transfer of specimens from surface to surface during the cycle of testing, transport to the cold chamber, cooling in the chamber, transport again to the burner/jet assembly, and preparation for testing again.

Elimination of the transfers reduced or eliminated the probability for droppage and breakage, as well as the potential for chipping of the surface during handling which could be misinterpreted as spalling.

When a laboratory cart with specimen was rolled beneath the burner and nozzle, it had to be raised so that the distance between the nozzle exit plane and the top surface of the specimen was that for the test. The tines of a hand-operated hydraulic forklift were placed beneath the top shelf of the cart, and the cart/specimen combination was lifted to the desired height. The heating effects of the jet exhaust did not damage the carts or the forklift.

CONSIDERATIONS IN THE DESIGN OF THE NFESC AVIATION ENGINE SIMULATION FACILITY

Design Philosophy

Design of the NFESC AESF required analyses of the flow parameters throughout the system. The design objective was to provide a facility which will repetitively create the same convective heat fluxes (\dot{q} , Btu/ft²-sec) on test specimens as those that occur on spalling pavement at operational airfields. In this way, specimens of various mix designs can be tested under controlled conditions to determine which mix design will be likely to survive longest under exposure to jet exhaust flows in the field.

As explained in the Background section of this report, when the design of the NFESC AESF began, there were differing opinions as to the basic cause of damage to the pavements. Convective heating of the pavements contributes to the damage, whether thermal stress buildup in the pavements is considered to be the cause of damage, or whether chemical reactions between hydraulic fluids and esters are deemed to be the cause. Convective heating causes localized increase in temperature in the area of impingement of a jet exhaust. A localized temperature increase can certainly cause a buildup of thermal stresses in the pavement, which can lead to "scaling" of material from the surface if the stresses are high enough. If reactions between fuel and lubricants spilled on the pavement and compounds in the pavements can occur, the temperature increases may also increase the rate of the reactions. The design of the AESF allows investigators to repetitively simulate conditions in the impingement zone of the jet exhaust plumes, and to test whichever hypothesis they wish.

Design Approach

The convective heat flux is affected by the temperature and velocity of the exhaust flow and by the temperature of the surface upon which the flow impinges. The temperature and velocity of the exhaust flow are functions of temperature and pressure in the combustion chamber, size of the nozzle, and distance between the nozzle exit and the heated surface. The temperature of the heated surface depends on convective heat transfer and the thermal properties of the pavement material. Because of these functional dependencies, it was necessary to start the design analyses with the combustion chamber of the burner, and to

follow the flow through its impingement on the specimens. It was also necessary to predict the temperature response of the specimens due to flow impingement.

Specimens will have the same temperature history as operational pavements if they are exposed to the same convective heat fluxes, and have the same thermal properties (density, thermal conductivity, specific heat, and radiant emissivity). Since temperatures are easily measured, but convective heat fluxes are not, comparisons of temperature histories between operational airfields and specimens with the same thermal properties are used to verify that desired convective heat fluxes have been achieved.

To accomplish the AESF design and predict behavior of the flow field impinging on specimens, it was necessary to consider the flow field and specimens to be composed of six different sections. The six sections are:

1. The combustion chamber of the burner
2. The nozzle of the burner
3. The turbulent plume of hot gases moving vertically from the nozzle to the specimen
4. The boundary layer which forms when the plume strikes the specimen and the flow turns in a horizontal direction parallel to the specimen surface
5. The specimen itself, which is heated by the hot exhaust gases
6. Stress analysis of the concrete or analysis of chemical reactions in concrete (analysis procedures for these are not included in this report)

The theoretical bases and mathematical procedures for solution are discussed in detail in the Appendix.

In the analyses of failure conducted at NFESC, the time-dependent temperature distributions predicted in step 5 were used as input for a stress analysis program. Results and conclusions from one of the stress analysis studies is reported in Reference 6. Therefore, one might consider the last step in the analysis process to be step 6. Step 6 can be an analysis of stress as conducted by NFESC, or an analysis of temperature-dependent chemical reactions, if that is the hypothesis being examined.

Scaling Factor

The equipment of the NFESC AESF is necessarily smaller than an aircraft engine. At the time of the design of the AESF, NFESC was tasked to test at conditions simulating the F/A-18 APU engine. After the facility was built and testing had started with the simulated F/A-18 APU engine parameters, NFESC was authorized to plan for testing at conditions simulating the AV-8B Harrier. Because the F/A-18 APU engine and the AV-8B Harrier engine are of vastly different sizes, and they are located at different heights above the ground, and the parameters (temperature, velocity) of the flow are different for the flow leaving each engine, it is certainly essential to consider how to model each situation appropriately.

The fact that the AESF nozzle, plume, and specimens are smaller than their full-scale counterparts introduces the concept of a "scaling factor" into the modeling process. The significance and the procedure for calculating the scaling factor were questioned during the design process. The fundamental question was whether or not the scaling factor was a term that would occur naturally in the mathematical simulations of the flow fields, the heating of the concretes, the stress buildups, and the postulated chemical reactions. It was finally recognized that the scaling factor does not occur in all of the mathematical simulations. What does happen is that the heated area on specimens will be smaller than the heated area on operational airfields. It will be possible to get stagnation point heat fluxes for specimens that are equal to those at operational airfields. Radially outward from the stagnation points, the convective heat fluxes decrease toward a negligible value on both the AESF specimens and operational airfields (actually, the specimens are not large enough so that convective heat flux becomes negligible before the boundary layer flow reaches the edge of the specimen). The resulting radial temperature gradients, $(\partial T / \partial r)_z$, are higher on specimens than on operational airfields. However, the temperature gradients normal to the surface, $(\partial T / \partial z)_r$, are the same on specimens and on full scale airfields. So obviously the temperature gradients normal to the surface are not affected by the scaling factor. The temperature gradients normal to the surface are substantially higher than the radial temperature gradients. The temperature gradients normal to the surface create stresses in the specimens equal to those in operational pavements, and cause chemical reactions (if any) in specimens just as in operational pavements.

Based on the reasoning above, the issue of the facility and specimens being smaller than a full scale engine and landing pad or parking apron was handled as follows:

1. The flow parameters at the exit plane of the nozzle of the full scale engine would be met as closely as possible at the exit plane of the nozzle of the AESF.

2. An approximate "scaling factor" would be calculated,

$$\Phi = D_{\text{AESF Nozzle}} / D_{\text{Full Scale}}$$

where Φ = the scaling factor, dimensionless

D = diameter, or hydraulic diameter, of the nozzle exit, inches.

The subscript designates which nozzle.

3. The distance between the AESF nozzle and the specimens would be determined so that the convective heat flux at the stagnation point of the impingement zone would be equal to that of the convective heat flux at the stagnation point of the full scale engine. Unfortunately, there does not appear to be an explicit mathematical expression for calculating the distance. Instead, the distance is determined implicitly based on the following assumptions and approximations.

The initial step is to require that the convective heat flux at the specimen stagnation point be equal to that of the full scale system:

$$q_{0, AESF \text{ Nozzle}} = h_{0, AESF \text{ Nozzle}} (T_{aw} - T_w)_{0, AESF \text{ Nozzle}}$$

$$q_{0, Full \text{ Scale}} = h_{0, Full \text{ Scale}} (T_{aw} - T_w)_{0, Full \text{ Scale}}$$

$$\frac{q_{0, AESF \text{ Nozzle}}}{q_{0, Full \text{ Scale}}} = 1 = \frac{h_{0, AESF \text{ Nozzle}} (T_{aw} - T_w)_{0, AESF \text{ Nozzle}}}{h_{0, Full \text{ Scale}} (T_{aw} - T_w)_{0, Full \text{ Scale}}}$$

where q = convective heat flux rate between flow and surface, Btu/ft²-sec

h = convective heat transfer coefficient between flow and surface,
Btu/ft²-sec-°F

T_{aw} = adiabatic wall temperature of the flow, °F

T_w = temperature of the surface being heated, °F

subscript "0" designates the stagnation point

4. The next step is to express the convective heat transfer coefficients in terms of flow parameters. It is shown in the Appendix, Section A.4, that the convective heat transfer coefficients can be expressed as follows:

$$h_0 = \left(\frac{k}{\delta} \right)_0 = \frac{k_0}{\left(\frac{\mu_0 \Lambda_0}{\rho_0 b_1} \right)^{1/2}}$$

where k = thermal conductivity of the flow, Btu-ft/ft²-sec-°F

δ = boundary layer thickness, ft

μ = dynamic viscosity of the flow, lb_m/ft-sec

ρ = density of the flow, lb_m/ft³

Λ = parameter used in the boundary layer solution, dimensionless.

(It is shown in the appendix that the parameter always has the value 4.71600030 at the stagnation point of an axisymmetric impingement zone, regardless of the size. Therefore,

$$\Lambda_{0, AESF \text{ Nozzle}} = \Lambda_{0, Full \text{ Scale}} \cdot)$$

$b_1 = (dU/dx)_0$ = change in the radial velocity at the outer edge of the boundary layer with respect to distance at the stagnation point, 1/sec.

5. The flow properties (k , μ , and ρ) are all functions of flow temperature. It can be assumed with reasonable accuracy that the flow temperature in the vicinity of the stagnation point of an AESF specimen is about the same as the corresponding flow temperature in the vicinity of the stagnation point at an operational airfield. Therefore, the flow property terms divide out of the equation in which the ratio of convective heat fluxes was set equal to one. The parameter Λ also divides out, since it has the same value for the AESF and for the full scale case. The equation for the ratio of convective heat fluxes reduces as follows:

$$\frac{q_{0, AESF \text{ Nozzle}}}{q_{0, Full \text{ Scale}}} = 1 = \left(\frac{b_{1, AESF \text{ Nozzle}}}{b_{1, Full \text{ Scale}}} \right)^{1/2} \frac{(T_{aw} - T_w)_{0, AESF \text{ Nozzle}}}{(T_{aw} - T_w)_{0, Full \text{ Scale}}}$$

6. The velocity gradient " b_1 " at the stagnation point is different for the scale model (AESF) from that of the full scale situation. It is higher because the changes in velocity have to take place within much smaller distances. The Appendix, Section A.4, discusses the fact that the velocity at the outer edge of the boundary layer changes from zero at the stagnation point to a maximum value at the radial distance where the pressure at the outer edge of the boundary layer decreases to atmospheric pressure. This radial distance is designated as " L ".

An assumption can be made at this point that the velocity gradients are proportional to the maximum velocities divided by the respective L 's:

$$b_{1, AESF \text{ Nozzle}} \propto \left(\frac{U_{Max}}{L} \right)_{AESF \text{ Nozzle}}$$

$$b_{1, Full \text{ Scale}} \propto \left(\frac{U_{Max}}{L} \right)_{Full \text{ Scale}}$$

The ratio of convective heat fluxes becomes

$$\frac{q_{0, AESF \text{ Nozzle}}}{q_{0, Full \text{ Scale}}} = 1 = \left(\frac{U_{Max, AESF \text{ Nozzle}}}{U_{Max, Full \text{ Scale}}} \right)^{1/2} \left(\frac{L_{Full \text{ Scale}}}{L_{AESF \text{ Nozzle}}} \right)^{1/2} \frac{(T_{aw} - T_w)_{0, AESF \text{ Nozzle}}}{(T_{aw} - T_w)_{0, Full \text{ Scale}}}$$

The ratio of $L_{Full \text{ Scale}}/L_{AESF \text{ Nozzle}}$ is a ratio of radial distances. It is reasonable to assume that the distances " L " scale like the ratio of nozzle diameters:

$$\frac{L_{Full \text{ Scale}}}{L_{AESF \text{ Nozzle}}} = \frac{1}{\Phi}$$

$$\frac{q_{0, AESF \text{ Nozzle}}}{q_{0, Full \text{ Scale}}} = 1 = \left(\frac{U_{Max, AESF \text{ Nozzle}}}{U_{Max, Full \text{ Scale}}} \right)^{1/2} \left(\frac{1}{\Phi} \right)^{1/2} \frac{(T_{aw} - T_w)_{0, AESF \text{ Nozzle}}}{(T_{aw} - T_w)_{0, Full \text{ Scale}}}$$

7. The next step requires that data be found or measured for the full scale system. Specifically, it is necessary to have data that permits one to calculate $U_{\max, \text{ Full Scale}}$ and to estimate $T_{\text{aw}, \text{ Full Scale}}$.

In the Appendix, Section A.3, it is shown that $U_{\max, \text{ Full Scale}}$ can be estimated from data from the exhaust plume. The data needed are P_{CL} and T_{CL} .

$$U_{\text{Max, Full Scale}} = a_{\text{CL}} M_{\text{CL}}$$

$$a_{\text{CL}} = \left(g_c \gamma R T_{\text{stat, CL}} \right)^{1/2}$$

$$T_{\text{stat, CL}} = \frac{T_{\text{CL}} + 460}{1 + \frac{\gamma - 1}{\gamma} M_{\text{CL}}^2} - 460$$

$$M_{\text{CL}} = \left[\left(\left(\frac{P_{\text{CL}} + 14.7}{14.7} \right)^{\frac{\gamma - 1}{\gamma}} - 1 \right) \frac{2}{\gamma - 1} \right]^{1/2}$$

where P_{CL} = maximum, i.e., centerline, total pressure in the plume at the impingement distance below the full scale nozzle, $\text{lb}_f/\text{in.}^2$ gauge

T_{CL} = maximum, i.e., centerline, total temperature in the plume at the impingement distance below the full scale nozzle, $^{\circ}\text{F}$

In the Appendix, Section A.4, an argument is presented for making the value of T_{aw} at distance "z" below the nozzle equal to the value of T_{CL} at a distance "z+L" below the nozzle.

$$T_{\text{aw}}(z) = T_{\text{CL}}(z + L)$$

where z = distance between the exit plane of the nozzle and the stagnation point of the impingement area, ft.

8. Arbitrarily give T_w the value of 75°F , which is normal room temperature. T_w is the temperature of the surface being heated. Although T_w increases throughout the period of jet impingement, it starts at a temperature approximately equal to the ambient temperature, which is taken as 75°F for this analysis.

9. The equation for equal convective heat fluxes on the AESF system and the full scale system can be rearranged as follows:

$$\left(U_{\text{Max, AESF Nozzle}} \right)^{1/2} (T_{\text{aw}} - T_w)_{\text{AESF Nozzle}} = \Phi^{1/2} \left(U_{\text{Max, Full Scale}} \right)^{1/2} (T_{\text{aw}} - T_w)_{\text{Full Scale}}$$

Using the definition of ϕ from item 2 and the formulas and the assumptions discussed in item 7 above, the terms on the right-hand side of the equation can be calculated. To achieve the desired simulation of the full scale system with the AESF, the left-hand side must equal the right-hand side. The terms on the left-hand side of the equation can be calculated in the same manner as the corresponding terms on the right-hand side, i.e., by use of the procedures presented in item 7 above. Input for the expressions are $P_{CL, AESF Nozzle}$ and $T_{CL, AESF Nozzle}$, which are the total pressure and the total temperature at the centerline of the plume of the AESF system.

$P_{CL, AESF Nozzle}$ and $T_{CL, AESF Nozzle}$ are both functions of the distance from the exit plane of the AESF nozzle. If values of $P_{CL, AESF Nozzle}$ and $T_{CL, AESF Nozzle}$ from close to the nozzle are used to calculate the left-hand side of the expression immediately above, the left-hand side will be greater than the right-hand side. If values of $P_{CL, AESF Nozzle}$ and $T_{CL, AESF Nozzle}$ from far below the nozzle are used to calculate the left-hand side of the expression, the left-hand side will be less than the right-hand side. There is one set of values of $P_{CL, AESF Nozzle}$ and $T_{CL, AESF Nozzle}$ which makes the left-hand side equal the right-hand side. Experimental data from the AESF plume have to be taken and used to determine the scaled distance "z" which yields the total pressure and total temperature at the plume centerline to produce the same convective heat flux as occurs at operational airfields.

PERFORMANCE DATA AND DESIGN VERIFICATION DATA FOR THE NFESC AVIATION ENGINE SIMULATION FACILITY

Summary of Design of the Burner and Nozzle

Table 1 presents a summary of the flow parameters and design features of the AESF burner and nozzle for both the F/A-18 APU engine and the AV-8B engine rear nozzle. Column 1 of Table 1 identifies the flow variable or design parameter for each row. Columns 2 and 4 give the values for the full scale engines, where applicable. Columns 3 and 5 give the values for the simulated F/A-18 APU and the simulated AV-8B rear nozzle, respectively.

Basically, Table 1 follows the six steps recommended in the section above. It is noted that these steps lead to the conclusion that the nozzle exit diameter for the simulated F/A-18 APU engine should be 1.27 inches, and the diameter for the simulated AV-8B should be 1.1 inches. When the burner and nozzle were fabricated before testing began on the simulated F/A-18 APU engine, the nozzle diameter was made 2.0 inches. With a nozzle diameter of 2.0 inches, the air compressor of the airflow subsystem is unable to pump enough air to make conditions (temperature, pressure, and flow velocity) at the exit of the nozzle equal to those of the full scale engine. To compensate for the effects of the larger diameter, the burner was operated so that the total temperature and the total pressure at the nozzle exit were a bit higher than those at the nozzle exit of the full scale engine. After some experimentation, settings were found which gave the desired convective heat fluxes on specimens located about 21 inches below the exit plane of the 2.0-inch-diameter nozzle.

For future testing where the objective is to simulate a specific engine, the six steps outlined in the previous section, and illustrated in Table 1, are recommended. The experience at NFESC with simulation of the F/A-18 APU engine has shown that the design of the burner and nozzle is flexible enough so that one can deviate from the recommended steps and still get the

desired convective heat fluxes. However, the search for acceptable settings is much less structured if the recommended steps are not followed.

When NFESC was authorized to plan for tests to simulate the AV-8B engine rear nozzle, the only nozzle available was the one that was 2.0 inches in diameter. NFESC was already in the middle of tests in which various specimens were being repetitively exposed to the simulated F/A-18 APU convective heat fluxes. The need to continue with the simulated F/A-18 APU engine tests precluded fabrication of a new nozzle (1.1 inches in diameter) and burner baseplate, and changeover to run with the new configuration. Therefore, using the 2.0-inch-diameter nozzle, the burner was again operated at so that total temperature and total pressure at the nozzle exit plane exceeded those of the full scale engine.

Repetitive exposure of specimens to F/A-18 APU convective heat fluxes is being done simultaneously with the writing of this report. The burner uses the 2.0-inch nozzle and the conditions listed in Table 1. Repetitive exposure of specimens to AV-8B convective heat fluxes has not begun. Although preliminary data for the simulation of the AV-8B has been obtained with the 2.0-inch-diameter nozzle, and is reported below, it is recommended that the repetitive testing be done with a nozzle of 1.1 inches in diameter, and that a shortened period of "recalibration" with the smaller nozzle be scheduled.

Results from Attempted Simulations of the F/A-18 APU Engine and the AV-8B Rear Nozzle

Characteristics of the Plume of the Simulated F/A-18 APU Engine. With chamber pressure and temperature set at conditions to simulate the F/A-18 engine, the probe shown in Figure 11 was used to measure pressure and temperature at numerous positions throughout the exhaust flow. The approach was to fix the tips of the pressure probe and thermocouple at a known distance below the nozzle exit plane, and then move the probes within the fixed plane to measure pressures and temperatures at various positions and distances from the plume centerline. The x and y positions of the pressure probe and thermocouple were recorded, as well as the pressures and temperatures themselves. Measurements were taken at distances of $z = 0.5, 6, 12, 18,$ and 21 inches below the exit plane of the nozzle. Measurements at 21 inches were not complete, and are not presented in this report.

The scaled distance between the nozzle exit plane and surface for the F/A-18 APU engine is approximately 18 inches (see Table 1).

The geometrical centerline of the plume was established by dropping a plumb bob from the center of the nozzle, and reading the x and y positions of the tips of the pressure probe and thermocouple when they coincided with the tip of the plumb bob. Of course the plumb bob centerline was established when there was no flow through the AESF. After the flow was turned on, it was found that the maximum pressure and temperature readings were up to 3/8 inch off center at 20 inches below the nozzle exit plane. This can be attributed to any or all of the following possible causes:

1. The exhaust flow leaves the nozzle at a slight angle with respect to the vertical due to the internal design of the burner.

2. Ventilation of Building 566 to prevent buildup of exhaust gases within the building results in a crossflow which makes the exhaust plane curve.

3. The force of the flow on the probes causes them to flex somewhat, resulting in the tip of the probes being slightly displaced from the indicated x,y position. (This was seen to occur when the thermocouple probe was near the exhaust plane of the nozzle.)

4. The maximum temperature and/or pressure does not occur at the geometrical center of the plume because of incomplete mixing of the flow within the combustion chamber. (The temperature data give evidence that this is a possible cause.)

During reduction and analysis of the measured data, the plume centerline was assumed to be where maximum pressure and temperature occurred, which did not always coincide with the geometrical centerline.

Profiles of Total Pressure in the Plumes of the Simulated F/A-18 APU Engine. Figures 15, 16, 17, and 18 show the profiles of total pressure versus radial distance from the centerline at increasing distances below the exit plane of the nozzle. The total pressure is the sum of the static pressure (atmospheric pressure which is exerted throughout the entire plume from the exit plane of the nozzle and below) plus the dynamic pressure (pressure due to isentropically stopping the velocity of the flow). In Figures 15 through 18, the total pressure is expressed in psig (lb_f/in^2 , gauge). Numerically, the total pressures shown in Figures 15 through 18 are equal to the dynamic pressures.

Figures 15 through 18 show expected trends for the pressure distribution within the F/A-18 APU exhaust plume. Specific trends are as follows:

1. Near the nozzle exit ($z = 0.5$ inch), the pressure is almost constant across the plume until the edge of the nozzle is reached. At the edge, the pressure drops sharply to atmospheric pressure because there is no flow past the edge of the nozzle.

2. As distance below the nozzle increases, the plume spreads. Friction between the plume flow and the surrounding still air causes the plume to spread. Turbulence in the plume flow contributes most to the friction. The edge of the plume is considered to be the radius at which the total pressure drops to a negligible psig value. The plume radii increase from about 1 inch at $z = 0.5$ inch below the nozzle, to 1.5 inches at $z = 6$ inches, and to 3 inches at $z = 18$ inches.

3. The maximum pressures (i.e., the centerline pressures) within the plume decrease as distance below the nozzle increases. The decrease in centerline pressure is due to friction in the plume, which reduces velocity of the faster-moving flow in the center of the plume. Turbulence in the plume increases frictional effects.

Profiles of Total Temperature in the Plumes of the Simulated F/A-18 APU Engine. Figures 19, 20, 21, and 22 show the profiles of total temperature versus radial

distance from the centerline at distances of $z = 0.5, 6, 12$, and 18 inches below the exit plane of the nozzle. The total temperature is the sum of the static temperature (due to random motion of the exhaust flow particles) plus dynamic temperature (due to ordered motion, i.e., flow velocity in the plume). In Figures 19 through 22, the total temperature is expressed in degrees Fahrenheit.

As with the pressure profiles, the temperature profiles show some expected trends. However, one undesirable characteristic showed up in the temperature profiles, although it was not totally unexpected. The two expected trends are summarized first, followed by the undesirable characteristic:

1. As distance below the nozzle increases, the thermal plume spreads. The edge of the thermal plume is considered to be the radius at which the total temperature drops to approximately the same temperature as the air throughout the room housing the burner. Precise boundaries of the plume were difficult to determine, but the thermal plume radii increase from about 1 inch at $z = 0.5$ inch below the nozzle, to 2 inches at $z = 6$ inches, and to 4 inches at $z = 18$ inches. It should be noted that the thermal plume radii are slightly larger than the radii indicated by the pressure distribution plots and by the velocity distribution plots. Reference 21 presents theoretical derivations of the distributions of both the temperature and velocity profiles in turbulent axisymmetric jets. In Reference 21, the theoretical temperature profiles are shown to drop off more slowly to the value of the ambient air around the jet (the temperature distribution function is the square root of the velocity distribution function, which is presented below).

2. The maximum temperatures (i.e., the centerline temperatures) within the plume decrease as distance below the nozzle increases. As with pressure, the decrease in centerline temperature is due to turbulence in the plume, which mixes the hot gases at the plume centerline with cooler gases from the outer portions of the plume. Friction also reduces velocity of the faster moving flow in the center of the plume, thus reducing the dynamic temperature component.

3. The undesirable characteristic of the temperature data was observed at $z = 0.5$ inch. There, the temperature profile indicates that the flow did not become mixed well in the combustion chamber. If the flow had been mixed well, the temperature profile of Figure 19 would have been more or less flat from $r = 0$ to $r = 1$ inch, then would drop off rapidly to atmospheric temperature. In other words, the shape would be similar to that of the pressure profile at $z = 0.5$ inch shown in Figure 15. The fact that there is a high temperature at the center of the plume and continuously decreasing temperatures out to the edge of the nozzle indicates that the burner and nozzle design should be altered to obtain a more uniform temperature distribution across the nozzle. Recommended design changes are given in the Conclusions and Recommendations of this report.

Profiles of Velocity in the Plumes of the Simulated F/A-18 APU Engine.

Using the procedures of the Appendix, Section A.3, the flow velocity at a point can be calculated from the total pressure and total temperature at the point. Since there is

considerable scatter in the total pressure and total temperature data, and because pressures and temperatures were not taken at the same location simultaneously, "averaged" curves were drawn through the plots of pressure and temperature data. Then values from the "averaged" curves were used to calculate the "averaged" velocity profiles. Figures 23, 24, 25, and 26 present the velocity profiles for distances of $z = 0.5, 6, 12,$ and 18 inches below the exit plane of the nozzle.

Trends seen in the velocity profiles are similar to those seen in the temperature data:

1. The velocity profiles spread as the distance from the exit plane of the nozzle increases.
2. The maximum velocity along the centerline of the plume decreases as the distance from the exit plane of the nozzle increases.
3. The velocity profile at $z = 0.5$ inch is not constant across the plane of measurement. A more or less constant profile is desired. With good mixing of the flow in the combustion chamber, a more constant velocity profile would have been expected.
4. Figure 26 compares the "averaged" velocity profile for $z = 18$ inches, which is based upon the experimental data, with the theoretical profile of a fully developed turbulent jet. The "averaged" velocity profile is indicated by the small squares. The theoretical profile is shown as the solid line. The theoretical profile is derived in Reference 21, and is calculated from the equation:

$$\frac{V}{V_{Max}} = e^{\left(-\frac{\eta^2}{2}\right)}$$

where $\eta = r/b$

$r =$ radial distance from jet centerline, inches

$b =$ jet momentum radius, inches (determined to be 1.44 inches for simulated F/A-18 jet at $z = 18$ inches)

$V_{max} =$ velocity of flow at jet centerline, ft/sec (determined to be 420 ft/sec for simulated F/A-18 jet at $z = 18$ inches)

The theoretical profile is for a fully developed turbulent profile, which has had time to form at the position $z = 18$ inches. Good agreement is seen between the theoretical profile and the "averaged" profile based on experimental data. The good agreement is one indication of the validity of the analysis procedure. It is also an indication that the effects of incomplete mixing within the combustion chamber become less important farther away from the nozzle exit because mixing continues within the exhaust plume, eventually reaching a fully developed profile for turbulent flow regardless of the initial profile.

Characteristics of the Plume of the Simulated AV-8B Engine Rear Nozzle. Figures 27 through 41 present characteristics of the plume of the simulated AV-8B engine rear nozzle. The measurements for the AV-8B engine were taken several months after those for the F/A-18 APU engine. However, the instrumentation and approach for making the measurements were essentially the same. For the AV-8B engine, measurements were taken at distances of $z = 0.5, 6, 9, 12, 15,$ and 18 inches below the exit plane of the nozzle. Data taken 18 inches from the exit plane of the nozzle were not completely reduced and are not included in this portion of the report, primarily because the scaled distance between the nozzle exit plane and the surface is approximately 6 inches (see Table 1), and the data for 18 inches are well outside the area of concern.

In general, the patterns observed and conclusions drawn from the F/A-18 APU data apply to the AV-8B data. As with the F/A-18 APU data, the AV-8B data produced maximum temperature and pressures that were slightly offset from the centerline indicated by a plumb bob. Also, the general development of the plume (such as spreading, slowing of the centerline velocity, cooling of the centerline flow) is similar for both engines. However, the temperature in the combustion chamber of the burner was higher during the attempted simulation of the AV-8B engine. This resulted in higher temperatures in the plume at corresponding positions. The higher chamber temperature in turn gave higher velocity to the flow leaving the nozzle and the plume at corresponding positions. But because total pressures in the combustion chamber were approximately equal for both attempted simulations, pressures in the plumes at corresponding distances below the exhaust plane of the nozzle were about the same for both simulated engines. Also, the spreading rate of the AV-8B plume appears to be about the same as that of the F/A-18 APU plume.

Plots of the pressure, temperature, and velocity in the AV-8B plume at various values of z are discussed below.

Profiles of Total Pressure in the Plumes of the Simulated AV-8B Engine Rear Nozzle. Figures 27, 28, 29, 30, and 31 show the profiles of total pressure versus radial distance from the centerline at increasing distances below the exit plane of the nozzle.

Figures 27 through 31 show expected trends for the pressure distribution within the AV-8B rear nozzle exhaust plume. Specific trends are as follows:

1. Near the nozzle exit ($z = 0.5$ inch), the pressure is almost constant across the plume until the edge of the nozzle is reached. At the edge, the pressure drops sharply to atmospheric pressure because there is no flow past the edge of the nozzle.
2. As distance below the nozzle increases, the plume spreads. The plume radii increase from about 1 inch at $z = 0.5$ inch below the nozzle, to 1.5 inches at $z = 6$ inches, and to 2.7 inches at $z = 15$ inches. These values are approximately the same as for the F/A-18 APU plume.
3. The maximum pressures (i.e., the centerline pressures) within the plume decrease as distance below the nozzle increases. The maximum pressures are about 2.6 psig at $z = 6$

inches, 2.35 psig at $z = 9$ inches, and 1.35 psig at $z = 15$ inches. These values are approximately the same as for the F/A-18 APU plume.

Profiles of Total Temperature in the Plumes of the Simulated AV-8B Engine Rear Nozzle. Figures 32, 33, 34, 35, and 36 show the profiles of total temperature versus radial distance from the centerline at distances of $z = 0.5, 6, 9, 12,$ and 15 inches below the exit plane of the nozzle.

As with the pressure profiles, the temperature profiles show the trends identified in the discussion of the F/A-18 APU data, including the non-uniform temperature distribution at $z = 0.5$ inch:

1. As distance below the nozzle increases, the thermal plume spreads. As with the F/A-18 APU data, precise boundaries of the plume were difficult to determine, but the plume radii increase from about 1 inch at $z = 0.5$ inch below the nozzle, to 2 inches at $z = 6$ inches, and to 4 inches at $z = 15$ inches. These are approximately the same as for the simulated F/A-18 APU.

2. The maximum temperatures (i.e., the centerline temperatures) within the plume decrease as distance below the nozzle increases. The maximum temperatures are about 1,300°F at $z = 6$ inches, 990°F at $z = 9$ inches, 750°F at $z = 12$ inches, and 600°F at $z = 15$ inches. For the F/A-18 APU engine, corresponding values were about 1,000°F at $z = 6$ inches and 600°F at $z = 12$ inches. The higher values for the simulated AV-8B engine are attributed to the higher temperature in the combustion chamber.

3. Figure 32 indicates a very erratic and non-uniform temperature distribution at $z = 0.5$ inch. As with the corresponding data for the simulated F/A-18 APU engine, the data of Figure 32 indicate poor mixing of the flow in the combustion chamber, and a need to redesign the combustion chamber. The fact that the temperature distributions become much less erratic as the flow moves away from the nozzle (see Figures 33 through 36) indicates that turbulent mixing effectively smoothes out the temperature distributions in the plume.

Profiles of Velocity in the Plumes of the Simulated AV-8B Engine Rear Nozzle. Figures 37, 38, 39, 40, and 41 present the velocity profiles for distances of $z = 0.5, 6, 9, 12,$ and 15 inches below the exit plane of the nozzle.

Trends seen in the velocity profiles are similar to those seen in the data for the F/A-18 APU engine:

1. The velocity profiles spread as the distance from the exit plane of the nozzle increases.

2. The maximum velocity along the centerline of the plume decreases as the distance from the exit plane of the nozzle increases. However, the velocities for the simulated AV-8B engine plume are higher than those for the simulated F/A-18 APU engine. For example, the centerline velocities for the AV-8B engine are about 1,000 ft/sec at $z = 6$ inches, 880 ft/sec at

$z = 9$ inches, 695 ft/sec at $z = 12$ inches, and 560 ft/sec at $z = 15$ inches. For the F/A-18 APU engine, the centerline velocities are 880 ft/sec at $z = 6$ inches, 625 ft/sec at $z = 12$ inches, and 425 ft/sec at $z = 18$ inches.

3. The velocity profile at $z = 0.5$ inch is not constant across the plane of measurement.

Impingement of the Exhaust Flow on the Specimens: Pressure Data and Analysis of the Boundary Layer

Pressure Distributions on Specimens Due to Impingement of the Exhaust Flow. To analyze the boundary layer formation on specimens heated by impingement of the exhaust flow, it was necessary to measure the pressure distributions resulting from the impingement. The pressure distributions were not actually measured on the concrete specimens themselves. Instead, the pressures were measured with the specially designed plate illustrated in Figure 12. The plate measures static pressure because the opening for each pressure tap is parallel to the flow. At the stagnation point, static pressure and total pressure are the same.

Pressure Distributions for the Simulated F/A-18 APU Engine Flow. Figures 42, 43, 44, 45, and 46 show static pressure distributions resulting from impingement of the simulated F/A-18 APU exhaust at distances of $z = 6, 9, 12, 15,$ and 18 inches below the exit plane of the nozzle. Things to note about the pressure distributions include the following:

1. The maximum (i.e., stagnation point) pressure decreases as the distance from the exit plane of the nozzle increases.

2. Comparisons of Figures 42 and 16, Figures 44 and 17, and Figures 46 and 18 reveal that the maximum pressures in the undisturbed plume and on the impingement plate are approximately equal. This is expected since both measurements are of the pressure resulting from stopping the centerline flow.

3. The area over which there are pressures greater than atmospheric increases as distance from the exit plane of the nozzle increases. This results from the spreading of the plume as the exhaust flow gets further from the nozzle.

Pressure Distributions for the Simulated AV-8B Rear Engine Nozzle. Figures 47 through 51 show the static pressure distributions on specimens due to the impingement of the simulated AV-8B rear nozzle flow. Observations made about the data for the F/A-18 APU engine apply for this simulation as well.

Calculated Characteristics of the Boundary Layers Formed in the Impingement Zone. Pressure distributions for two of the sets of data in Figures 42 through 51 were used to calculate the growth of the boundary layer and the subsequent convective heating of the specimens due to impingement of exhaust flow. The boundary layer calculations were made

by using the procedures described in the Appendix, Section A.3, to get the velocity distribution at the outer edge of the boundary layer, then by using the solution derived in the Appendix, Section A.4, to get the boundary layer characteristics. The boundary layer characteristics of primary interest were the heat transfer coefficient and the adiabatic wall temperature. These were the terms needed to calculate the heat transfer to the specimens. Other boundary layer characteristics (specifically, the velocity along the outer edge of the boundary layer, the boundary layer parameter Λ , and the boundary layer thickness δ) had to be calculated first, however. Results of the boundary layer calculations are discussed below.

Boundary Layer Characteristics, F/A-18 APU Engine Simulation, $z = 18$ Inches. Calculations were made for $z = 18$ inches for the F/A-18 APU simulation because this was the scaled distance which corresponded closest to the full scale distance between the airfield pavement and the nozzle exit plane for which an entire set of AESF test data was available.

Figure 52 shows the velocity at the outer edge of the boundary layer as a function of radial distance from the stagnation point. At the stagnation point, the velocity is zero both by definition and by calculation. At about a 4-inch radius, the velocity reaches a maximum of about 450 ft/sec, and should remain approximately constant between there and the outer diameter of the specimen.

Figure 53 shows the radial distribution of the dimensionless parameter Λ . For an axisymmetric flow, the value of Λ at the stagnation point is always 4.7160003. As the flow moves away from the stagnation point and the boundary layer develops, the parameter Λ decreases and reaches zero where $dU/dx=0$.

Figure 54 shows the boundary layer growth as a function of radial position. It should be noted that the boundary layer thickness is not zero at the stagnation point. The non-zero thickness is a bit difficult to visualize at the location where the flow velocity is zero, but the non-zero value is consistent with the assumption of mathematical continuity of the boundary layer equations at the stagnation point. The boundary layer thickness increases with radial distance.

Figure 55 shows the radial distribution of the convective heat transfer coefficient, which is shown in the Appendix, Section A.4, to be a function of the parameter Λ and the boundary layer thickness. The convective heat transfer coefficient decreases somewhat as the flow moves radially outward.

The adiabatic wall temperature is the other term necessary for calculation of temperatures of heated specimens. It is explained in the Appendix, Section A.4, that determination of the adiabatic wall temperature is not a straightforward matter. Classical solutions of the boundary layer equations exist for flow situations in which the temperature is uniform above the boundary layer, i.e., in which the flow above the boundary layer acts as an infinite source of energy to replace heat transferred from the boundary layer to the heated surface. In the case of an impinging jet, the upper edge of the boundary layer ($y=\delta$) is where the maximum temperature occurs in a plot of $T(y)$, where y is the distance above the surface of the specimen. At values of $y > \delta$, temperatures decrease toward atmospheric temperature. Therefore, heat is transferred in both directions from the upper edge of the boundary layer. The classical solution of equating adiabatic wall temperature to total temperature at the upper

edge of the boundary layer does not apply for the jet impingement problem. No appropriate classical solution was located. Derivation of a completely new solution was not possible within the constraints of time and budget for this report. Instead, a heuristic argument is presented for consistently and quantitatively adjusting the total temperature at the outer edge of the boundary layer to account for energy loss to the atmosphere. The argument is as follows.

For a specimen located a distance z below the exit plane of the AESF nozzle, assume that the flow has traveled a distance $z+L$, where L is the radial distance between the stagnation point and the point where $\Lambda=0$. For the AESF with a 2-inch-diameter nozzle, L typically equals about 4 to 5 inches. From experimental data, determine the stagnation temperature of the unobstructed plume at a distance $z+L$ below the exit plane of the nozzle. Use that temperature as the adiabatic wall temperature for convective heat transfer at distance z .

For the F/A-18 APU, data were not available for z distances greater than 18 inches. The available data were extrapolated, resulting in the assumption of an adiabatic wall temperature of 400°F for the simulated F/A-18 APU at $z = 18$ inches.

Boundary Layer Characteristics, AV-8B Rear Nozzle Simulation, $z = 6$ Inches. Calculations were made for the simulated AV-8B rear nozzle at $z = 6$ inches, which is the closest scaled separation distance for that engine. Graphical results for the AV-8B rear nozzle are presented in Figures 56 through 59.

Compared to the F/A-18 APU results, the velocities at the edge of the boundary layer for the AV-8B simulation are quite a bit higher. The velocity reaches 980 ft/sec for the AV-8B, as seen in Figure 56. The maximum velocity for the F/A-18 APU is 450 ft/sec.

Also, the effects of the impingement are stronger in, and more concentrated toward, the center of the specimen in the case of the AV-8B. For the AV-8B, Figure 57 shows the boundary layer parameter decreasing from 4.7160003 at the stagnation point to a value of about 0.2 at $r = 2.5$, then finally going to 0.0 at a distance of $L = 4.5$ inches. The comparable distance for the F/A-18 APU was $L = 5.0$ inches, but at a more steady rate.

Comparison of Figures 58 and 54 show that the boundary layer thicknesses for both simulations are about the same.

Similar comparison of Figures 59 and 55 show that the convective heat transfer coefficients also have about the same magnitudes. However, the AV-8B has higher values at the stagnation point and lower values toward the outer diameter of the specimen.

The major difference between the AV-8B and F/A-18 boundary layer conditions is in the adiabatic wall temperatures. At $z = 6$ inches, the stagnation point temperature for the AV-8B case is about 1,200 to 1,220°F. This was adjusted as described in the Appendix, Section A.4, and summarized in the previous subsection of this report. The adiabatic wall temperature for the AV-8B case was determined to be approximately 900°F.

Transient Temperatures of the Specimens During Impingement of the Exhaust Flow: Experimental Data and Predicted Values

Validation of the analysis procedures and verification of the design of the NFESC AESF included tests to induce temperature histories in specimens which match those

experienced by airfield pavements. To measure the temperature histories, several specimens were instrumented with thermocouples. Two specimens cast of Portland cement concrete and river rock aggregate were used as "calibration slabs." One was 24 inches in diameter, 6 inches thick, and had 15 thermocouples located as shown on Figure 13. Another was 18 inches square, 4 inches thick, and had 14 thermocouples. Other instrumented specimens were of various concrete and aggregate materials. However, they typically had six or fewer thermocouples which were monitored periodically to compare how the various materials affected the temperature histories. Measurements from the calibration slabs were used to verify the design of the NFESC AESF and to validate the analysis procedures.

Basically, validation of the analysis procedures and verification of the design of the AESF were two different evaluations. For the validation of the analysis procedures, temperature histories measured in the calibration specimens were compared to temperature histories predicted using the transient temperature analysis equations presented in the Appendix, Section A.5. A FORTRAN computer program was written, for which the inputs were thermal properties of the concrete specimens and the convective heat transfer coefficients and adiabatic wall temperatures presented and discussed in the previous subsection of this report. The analysis procedures were considered to be validated by good agreement between temperatures measured in the calibration slabs and temperatures predicted by the FORTRAN program.

Verification of the design of the AESF was dependent on obtaining temperature histories in the calibration slabs which matched those occurring in pavements at operational airfields, while the AESF was being operated to achieve flow conditions at the nozzle exit plane equal to those of the full scale engine, and the specimen was located at the predetermined scaled distance from the exit plane of the nozzle. To perform the verification of the design as prescribed, one must have: (1) the flow conditions at the exit plane of the nozzle; and (2) temperature histories from operational airfield pavement. These data were available for the F/A-18 APU engine (Refs 5, 6, and 22). Only partial data were available for the AV-8B engine, however.

No measurements were found of airfield pavement temperatures during impingement of the AV-8B exhaust flow. One of the recommendations of this report is to determine if such data have been measured, and to obtain the data if it exists. References 22 and 23 present data for the AV-8B engine. Reference 23 specifically gives the exhaust flow temperature and velocity. Reference 22 gives the exhaust gas temperature, mass flow rate, and exit plane area for each nozzle. Temperature data from the two references do not agree. Reference 22 also presents engine thrust, fuel consumption, and positions of the nozzles relative to the AV-8B center of gravity. These data permitted a set of equations to be set up for thrust, fuel consumption, and stability of the aircraft during vertical takeoff and landing. The equations could be solved for flow velocity at the nozzle exit. The velocity from the solution did not agree with Reference 23. Another recommendation of this report is to resolve the discrepancy by obtaining definitive data for the flow conditions at the exit planes of the AV-8B nozzles.

The discussions below are: (a) of the data for the F/A-18 APU, which includes validation of the analysis procedures and verification of the NFESC AESF design; and (b) of the data for the AV-8B rear nozzle, which only includes validation of the analysis procedures.

Transient Temperatures Induced by Impingement of the F/A-18 APU Engine Exhaust. Figures 60 through 67 compare the measured temperature histories of eight thermocouples with calculated temperatures under conditions for the simulated F/A-18 APU engine exhaust. Four of the comparisons are for thermocouples located at the surface, and four are for subsurface thermocouples. The measurements were made with the 18-inch-square, 4-inch-thick calibration slab. The calibration slab actually has 14 thermocouples imbedded in it. Temperatures were calculated for all 14 of the thermocouple locations, and the measured and calculated temperatures were compared for all. Only eight comparisons are shown in this report because they are sufficient to show the patterns of data and to illustrate the conclusions that were drawn.

Ostensibly, the positions of the thermocouples for which data are presented were: (a) at 0, 1, 2, and 4 inches from the stagnation point, for the thermocouples at the surface; and (b) at 1/4, 1/2, 1, and 2 inches below the surface directly beneath the stagnation point, for the subsurface thermocouples. The adverb "ostensibly" is added because the precise locations of the thermocouples were not known, and the junctions for the thermocouples were typically at least 1/8 inch long. These factors were discussed above in the subsection of the report entitled, Calibration Data Acquisition Subsystem. The comparisons between measured and calculated data shown in Figures 60 through 67 are based on the assumption that the thermocouples were located precisely where they were intended to be. It will be seen, however, that agreement between the measured and calculated data was not satisfactory for some of the thermocouples if they were in fact at the intended locations. An argument is made that some of the thermocouple junctions were actually displaced as much as 1/8 inch vertically from their intended locations. To substantiate the argument, comparisons are made between the measured data and calculated temperatures assuming that some thermocouples are 1/8 inch farther from the heated surface of the specimen than they were supposed to be. The revised comparisons are included in the appropriate figures. The revised comparisons show much closer agreement between measured and calculated temperatures.

Validation of the Analysis Procedures with Simulated F/A-18 APU Data. Observations and conclusions drawn from Figures 60 through 67 include the following:

1. Figures 60 through 63 apply to the thermocouples ostensibly located at the surface. Each of the figures includes a curve for the calculated temperature history assuming the thermocouple is actually located at the surface. If one focuses attention on these calculated temperatures, one sees that the maximum temperatures reached after 900 seconds of heating are predicted to be: (a) 378°F at $r = 0$ inch (stagnation point); (b) 375°F at $r = 1$ inch; (c) 365°F at $r = 2$ inches; and (d) 328°F at $r = 4$ inches. The decrease with increasing r is expected. One can also see that the rate of temperature rise ($\partial T/\partial t$) at the beginning of impingement (about 80 seconds) is greater at the stagnation point, and progressively decreases as distance from the stagnation point increases. These effects are due to the decrease of convective heat transfer coefficient, h , as the radius increases. The maximum calculated temperatures at the surface are lower than the adiabatic wall temperature, which they must be. The maximum temperatures are asymptotically approaching a value less than the adiabatic wall

temperature of 420°F. The asymptote is less than the adiabatic wall temperature because of radiation to the environment and conduction to the interior from the surface of the specimen.

2. The measured surface temperatures in Figures 60 through 63 individually seem reasonable, but collectively they do not show the patterns pointed out above for the calculated temperatures, and only Figures 60 and 63 show acceptable agreement between measured and calculated temperatures. The maximum measured temperatures reached after 900 seconds of heating are: (a) 378°F at $r = 0$ inch (stagnation point); (b) 403°F at $r = 1$ inch; (c) 342°F at $r = 2$ inches; and (d) 329°F at $r = 4$ inches. Also, the slopes of the temperature-time curves, i.e., $(\partial T/\partial t)$, do not steadily decrease as r increases.

3. The temperatures in Figure 61 are higher than the calculated surface temperatures. This was the only thermocouple in both calibration slabs for which measured temperatures consistently exceeded the maximum calculated temperatures even at the stagnation point.

4. Comparisons of temperatures for subsurface thermocouples are shown in Figures 64 through 67. Each of these figures includes a curve for the calculated temperature history assuming the thermocouple is actually located at the intended distance below the surface. Focusing attention on these temperatures in these figures, it is seen that: (a) the maximum temperatures reached after 900 seconds of heating decrease as distance from the surface increases, (b) there is a delay from the time of first impingement of the jet (80 seconds) until the temperature at a subsurface location starts rising, and the delay increases as the distance from the surface increases, and (c) the slopes of the temperature-time curves, $(\partial T/\partial t)$, decrease as distance from the heated surface increases. These are the expected trends, or patterns, for the temperature data for the subsurface thermocouple locations. The measured data of Figure 60 could be included to see that they follow the patterns as well, since the thermocouple of Figure 60 is in the vertical line with the thermocouples of Figures 64 through 67.

5. The measured data of Figures 64 through 67 follow the trends and patterns described above for the subsurface thermocouples. If examined without comparison to calculated temperatures, the data would seem reasonable. However, there is not acceptable agreement between the measured and calculated temperatures in Figures 64 and 65.

The differences between measured and calculated temperatures in Figures 61, 62, 64, and 65 initially raised doubts about the validity of the analysis procedure. Several sources of error were considered, but attention was focused on the uncertainty of thermocouple locations because: (a) not all comparisons between measured and calculated data were unacceptable, as would be expected with an error in an earlier stage of the entire analysis procedure; and (b) the differences in Figures 62, 64, and 65 all had the characteristic pattern of predictions for a thermocouple assumed to be nearer the surface than it actually was, i.e., that the calculated temperatures were higher than the measured temperatures, and the slopes $(\partial T/\partial t)$ during the initial period of heating were greater; and (c) the error caused by uncertainty in thermocouple locations could be quantified. To assess the effects of uncertainty in thermocouple locations, it was assumed that the thermocouple junctions in Figures 62, 64, and 65 were 1/8 inch farther from the heated surface than specified. The calculated temperature-time history for each

deeper location was compared to the measured temperature-time history. The results are included as a third curve in Figures 62, 64, and 65. In all three cases, excellent agreement between the measured and calculated temperatures resulted.

In Figure 61, which is for the surface thermocouple at $r = 1$ inch from the stagnation point, the difference between measured and calculated temperatures does not follow the same pattern as the other three. The measured temperatures are higher than the predicted. The proposed explanation for the difference in Figure 61 is that the thermocouple is actually measuring the temperature of the flow above the surface of the specimen. During testing with the 18-inch-square calibration slab, it had been observed that one of the thermocouples protruded above the surface. The calibration slab was discarded before this section of the report was drafted, so it could not be verified that the protruding thermocouple was the one at $r = 1$ inch. The measured maximum temperature of 403°F was about 28°F above the expected concrete surface temperature, but it was just 17°F less than the adiabatic wall temperature, and is about the expected temperature of the airflow.

Based on the acceptable agreement between measured and calculated temperatures for four of the thermocouple locations considered in Figures 60 through 67, and based on the explanation and resolution of differences for the other four, the conclusion is that the experimental data from the F/A-18 APU engine simulations validate the analytical procedures for modeling the various parts of the system.

Verification of the Modeling Procedures with Full Scale F/A-18 APU Data.

The Naval Air Propulsion Center (NAPC) and the Naval Air Warfare Center (NAWC) have measured temperatures of concrete during exposure to exhaust flow from full scale F/A-18 APU engines. The measurements are reported in References 5, 6, and 25. Surface temperatures were measured with infrared cameras. Subsurface temperatures were measured with an array of thermocouples, each with its junction 3/8 inches below the heated surface.

The concrete pavement was heated by exhaust flow from full scale APU engines. The engines were operated in a variety of modes that occur during preflight preparation of F/A-18 aircraft. The various modes are: (a) Ready-To-Load (RTL), which is a reduced power setting while awaiting the initiation of the other modes; (b) Main Engine Startup (MES), during which the APU drives a compressor that supplies air to rotate and start the main engine; (c) powering the Environmental Control System (ECS), and (d) providing power for Ground Maintenance Checkout (GMC). The exhaust flow conditions are less severe during the RTL mode. During the other three modes, exhaust flow conditions are similar to each other, but the ECS mode causes the most severe heating of the pavement.

Typical preflight preparations require about 15 minutes. During the testing reported in References 5, 6, and 25, the engines were fired as long as 46 minutes. The test series of Reference 6 was undertaken to determine if a modification to the APU engine would reduce the pavement heating and reduce the consequent damage. It was determined that the modifications would not significantly reduce pavement heating, so the recommendation was to continue operating the APU engines unmodified.

The data of Reference 5 do not include temperature-time histories. Instead, the data are presented as: (a) temperature distributions over the entire heated area after several minutes of impingement of the jet; and (b) the maximum temperature measured within the heated area.

These two types of data are presented for the surface and for the plane 3/8 inch below the surface. Reference 25 does include a temperature-time history measured during one of the NAWC tests, but the location of the thermocouple is not given. Also, the engine was operated in four different modes during the data acquisition, but not in the ECS mode.

Since temperature-time histories are not available for a test in which the engine operating mode was held constant, only the maximum temperatures are plotted in Figures 60 and 64 for comparison with comparable data measured and calculated by NFESC. The maximum temperature measured at the surface by NAPC was 354°F (see Figure 60). The NAPC data showed the maximum temperature to be at the stagnation point of the impingement zone, and lower temperatures to be arranged in ovals around the stagnation point. The isotherms were ovals rather than circles because impingement was oblique in the NAPC tests. The pattern is consistent with the NFESC analyses. The maximum temperature was about 24°F lower than the maximum calculated and measured by NFESC.

Figure 64 shows the highest temperature measured by NAPC at 3/8 inches below the surface to be 239°F. This is about 60°F lower than the temperature calculated by NFESC, and about 45°F lower than measured. Of course, a major part of the discrepancy of 60°F is due to the discrepancy between surface temperatures.

Closer agreement between the NFESC data and the measurements from the full scale APU tests was desired. However, differences of 24 to 60°F are not excessive considering the complexities of scale model testing and of mathematically predicting the combustion, flow, and heat transfer processes which take place. At this point, no changes are recommended in the AESF testing or modeling procedures because of the differences between NFESC data and full scale data from the F/A-18 APU tests. The recommendation to proceed with simulation of the F/A-18 APU engine as described in Table 1 is based on the following reasons:

1. The AESF conditions seem slightly conservative compared to full scale data, but not excessively so.
2. Because of the absence of temperature-time histories from the full scale tests, it is not possible to compare rates of temperature increase ($\partial T/\partial t$) during the initial periods of heating. In determining the thermal stress buildup within the concrete, this term is as important as the maximum temperature reached.
3. Data such as thermal properties of the concrete and possible contact resistance between the imbedded thermocouples and the concrete were not available in References 5, 6, and 25. It was not possible to calculate the contributions these variables had on the differences in the data.

Transient Temperatures Induced by Impingement of the AV-8B Engine Rear Nozzle Exhaust. Figures 68 through 75 compare the measured temperature histories of eight thermocouples with calculated temperatures for the same thermocouples under conditions of the simulated AV-8B engine rear nozzle exhaust. As with the F/A-18 APU engine, four of the comparisons are for thermocouples located at the surface, and four are for subsurface thermocouples aligned vertically beneath the stagnation point. The measurements were made

with the calibration slab illustrated in Figure 13. It is 24 inches in diameter, 6 inches thick, and has 15 imbedded thermocouples. Data from only eight of the thermocouples are presented because they are representative and sufficient for conclusions. Comparisons between measured and calculated data were also made for the other seven thermocouples.

Validation of the Analysis Procedures with Simulated AV-8B Engine Data.

Observations made and conclusions drawn from the data for the AV-8B simulations are similar to those from the F/A-18 APU simulations. They include the following:

1. When temperatures were measured during simulated AV-8B conditions, full exposure of the specimen began about 400 seconds after the specimen was placed in the test enclosure. During the first 400 seconds, the specimen was covered with a heat resistant fabric. However, there was slight heating of the specimen before the fabric cover was removed. For the calculations, the pre-exposure heating was neglected, and the initial temperature of the specimen was assumed to be 65°F. This accounts for the differences between measured and calculated temperatures before and immediately after the beginning of the heating of the specimen. During testing at simulated F/A-18 APU conditions, the specimen was also initially covered with the heat resistant fabric. During the testing at F/A-18 APU conditions, the fabric was removed 80 seconds after the specimen went into the test enclosure. No noticeable heating of the specimen occurred prior to removing the fabric because: (a) 80 seconds was not sufficient time for a significant amount of heat to penetrate the fabric; and (b) the convective heat transfer rates from the simulated F/A-18 plume have been seen to be significantly less than those from the simulated AV-8B plume.

2. Figures 68 through 71 apply to the thermocouples that were supposed to be located at the surface of the specimen. One can see in Figures 68, 69, and 70, however, that the calculated surface temperatures become quite a bit higher than the measured temperatures during the early period of exposure of the specimen (just after 400 seconds). In Figure 71, there was acceptable agreement between the measured temperatures and the temperatures calculated for the surface. In fact the measured temperatures were slightly higher than the calculated values. If one considers the pattern of calculated temperatures for the surface locations, it is seen that after 900 seconds of exposure to the AV-8B jet exhaust, they were 799°F at $r = 0$ inch (stagnation point), 786°F at $r = 1$ inch, 740°F at $r = 2$ inches, and 641°F at $r = 4$ inches. The radial distribution of calculated surface temperatures is consistent with an adiabatic wall temperature of 900°F and the calculated radial distribution of heat transfer coefficients.

3. If one considers the pattern of measured temperatures after 900 seconds of heating, it is seen that they are 744°F at $r = 0$ inch, 772°F at $r = 1$ inch, 758°F at $r = 2$ inches, and 698°F at $r = 4$ inches. The stagnation point temperature (Figure 68) is lower than expected throughout the entire 900 second period of heating. At $r = 1$ inch and $r = 2$ inches (Figures 69 and 70), the measured temperatures are lower than expected during the initial period of exposure to the jet exhaust, but the calculated and measured temperatures become almost equal after 900 seconds. The measured temperatures in Figures 68, 69, and 70 demonstrate the

characteristics of thermocouples that are slightly below the surface, specifically: (a) the slopes of the measured temperature-time curves ($\partial T/\partial t$) are initially too low, and (b) measured temperatures eventually approach the calculated surface temperatures after the calculated surface temperatures approach their asymptotic limit.

Figures 68, 69, and 70 include curves of calculated temperatures assuming the thermocouples to be 1/8 inch below the surface. Much better agreement between the calculated temperatures and the measured temperatures is found in Figures 68 and 69. In Figure 70, the calculated temperatures at $z = 0$ inch are higher than measured, and those at $z = 0.125$ inch are lower than measured. No temperatures were calculated for an intermediate subsurface distance, e.g., 0.0625 inch.

4. Figures 72 through 75 compare calculated and measured temperatures for four thermocouples supposedly located at distances of 0.25, 0.5, 1, and 4 inches below the surface directly beneath the stagnation point. Expected trends seen in both the calculated and measured data are: (a) as distance from the surface increases, there is an increasing delay before temperatures of the thermocouples begin to rise; (b) once the temperatures do begin to rise, the rate of increase ($\partial T/\partial t$) is highest near the surface and lowest further from the surface; and (c) the temperature reached after 900 seconds of exposure decreases as distance from the surface increases. In Figures 72 and 73, there is unacceptable agreement between the measured temperatures and the temperatures calculated for the presumed locations of the thermocouples. For these cases, calculated temperatures are included assuming that the thermocouples are actually located 1/8 inch farther from the surface than specified. Agreement between these calculated temperatures and the measured temperatures is acceptable.

In Figures 74 and 75, agreement between the originally calculated temperatures and the measured temperatures is acceptable.

As with the F/A-18 APU simulations, there is acceptable agreement between the experimental data taken during simulations of the AV-8B engine rear nozzle and the calculated data based upon AV-8B parameters. Acceptable agreement is dependent on the assumption that some of the thermocouple junctions in the 24-inch round calibration specimen were as much as 1/8 inch from their specified locations. The agreement is not quite as good for the AV-8B simulations as it is for the F/A-18 APU simulations.

Requirements for Verification of Modeling Procedures with AV-8B Engine Data. No references have been found that present data for verification of the AV-8B modeling and mathematical simulation. The goal was to find measurements of pavement temperatures for comparison with the temperatures calculated using the analysis procedures of this report and with the temperatures measured in the calibration slab.

Since the data needed for verification are not available, a discussion is given of important parameters and considerations for the best possible simulation of the AV-8B engine and the heat transfer from its plume to the pavement:

1. For the calibration tests, the duration of exposure of the calibration specimen to the simulated AV-8B exhaust was more than 900 seconds. The extended lengths of exposure were

done to acquire data comparable to that for the F/A-18 APU. At operational airfields, an F/A-18 APU engine typically runs for 900 seconds or more while the aircraft is stationary and is being prepared for flight. However, an AV-8B aircraft is not held stationary for 900 seconds (15 minutes) with its engine at full thrust and its nozzles directed vertically. At operational airfields, the time of exposure of the pavements to the direct vertical flow from the nozzles is much shorter than 900 seconds.

2. Also, if the aircraft is lifting off a takeoff/landing pad, it is at ground level only a few seconds after the nozzles are rotated to vertical. As the plane rises, there is increasing distance between the nozzle exit plane and the takeoff/landing pad, which results in less severe convective heat transfer rates to the operational pad than those of the simulation described in this report. Temperatures on the surface of the pavement are lower than the temperatures reached in the simulation described in this report.

3. Transient conditions occur during both vertical lift-offs and landings. Thermal stresses induced in the pavement are higher during lift-offs than during landings. In both cases, the pavement is initially at a uniform temperature, approximately that of the ambient atmosphere and/or the surrounding soil. During vertical takeoffs, the aircraft taxis onto the pad, then turns the nozzles vertically and increases engine power to full throttle. This causes a very rapid increase in the temperature at the surface of the concrete, but there is a delay before heat is conducted and the temperature begins to increase below the surface. The large temperature difference between the surface and the concrete below the surface creates high stresses in the pavement, leading to spalling. During vertical landings, jet impingement on the pavement begins when the aircraft is high above the pad. Impingement while the aircraft is descending causes the surface of the concrete to slowly heat up, and allows time for heat to conduct from the surface to the interior of the concrete. The result is that the surface temperatures probably reach approximately the same maximum during vertical takeoffs and landings, but the temperature differences and resulting stresses in the vertical direction in the concrete are highest during takeoffs. Therefore, it is more important to repetitively test at conditions that replicate the vertical lift-offs rather than vertical landings.

The realistic simulation of the AV-8B impingement conditions requires that the following information be obtained: (a) determination of the correct temperature and velocity of the flow at the exit plane of the nozzle during vertical lift-off; (b) the duration of exposure of the pavement before vertical lift-off begins, and the typical trajectory (height versus time) of the aircraft after lift-off; and (c) if available, temperature-time histories actually measured at an operation airfield. Regarding item (b), Reference 24 presents graphs of aircraft altitude versus maximum dynamic pressure and aircraft altitude versus maximum total temperature within the area of impingement of the plume on the pavement as the aircraft ascends. This is helpful information, but it does not include the altitude versus time. The relationship back to time is essential in a transient temperature analysis.

At present, the NFESC AESF is not equipped to simulate the transient plume conditions to which the pavement is exposed as the AV-8 aircraft rises. Three possible approaches for taking into account the transient conditions are: (a) to change the burner conditions as a function of time; (b) to change the distance between a specimen and the nozzle

exit plane as a function of time; and (c) to determine a constant condition for the testing, where the constant condition produces the same final result as the transient conditions. The first approach is not recommended because changing the burner conditions deviates from the basic concept of the simulation (which is to establish the same nozzle exit velocity and temperature as exist on the full scale engine), and because extensive modifications to the burner controls would be required to automatically and repetitively change the burner conditions during tests. Consideration should be given to both of the other approaches. At the present time, a clear preference for one over the other is not evident. To accomplish the second approach, probable changes to the system would be: (a) modify the laboratory carts used to carry the specimens between the burner and the cold chamber so that the specimens can be removed; (b) modify the manual forklift, or design or procure a mechanism on which a specimen can be placed and moved to the closest scaled distance below the nozzle for the beginning of tests, then lowered at a prescribed rate as the tests are underway. To accomplish the third approach, no changes in the hardware are anticipated, but the theoretical approach is not immediately evident for determination of a constant condition that produces the same result as transient conditions.

If repetitive testing of pavement mixes to withstand the heating effects of the AV-8B engine is undertaken in the future, a recommendation of this report is that the transient effects of the aircraft lift-off be considered. The recommendation is also to decide between two different ways to take the transient effects into account, specifically, to modify the system to actually move the specimens away from the nozzle during testing, or to determine if a constant test condition can be established which gives the same heating and stress to the specimens as the transient conditions.

CONCLUSIONS

The following conclusions can be drawn regarding the NFESC Aviation Engine Simulation Facility:

1. The original design criteria, which are listed in the section of this report entitled, Description of the NFESC Aviation Engine Simulation Facility, were met or exceeded. Operation of the facility, including operation during shakedown, during calibration, and during repetitive testing of specimens, has demonstrated that the facility does meet or exceed the original design criteria.

2. The original design objective for the NFESC AESF was to give a laboratory simulation of the conditions to which airfield concrete is exposed in the areas of spalling. That is, the objective was to subject concrete specimens in the AESF to the same convective heat fluxes (and resulting thermal stresses) that occur to concretes at operational airfields. Data in this report show that the convective heat fluxes occurring at operational airfields can be simulated in the NFESC AESF.

3. A theoretical basis for design of the NFESC AESF and for predicting the thermal response (temperature histories) of the specimens has been established. The theory can be

used for analysis and interpretation of test data. The theoretical basis is explained in the Appendix. The Background section of this report discusses other facilities which have been built to subject concrete specimens to thermal loads simulating those at operational airfields, and other burners designed for other purposes which have been used for the testing of concrete specimens. But the NFESC AESF is unique in that a complete theoretical analysis accompanied the design, the facility and specimens were built to accurately reproduce the airfield environment and effects, and the testing parameters have shown that the facility does so.

4. Thus far, taskings to NFESC have been to test specimens under a simulated F/A-18 APU engine exhaust, and to determine settings for the AESF which will simulate the flow from a rear nozzle of the AV-8B engine. Almost immediately after completion of fabrication of the AESF, calibration and design verification data were taken at conditions which simulate the F/A-18 APU engine. Several months later, calibration and design verification data were taken at conditions which simulate the AV-8B engine rear nozzles. The data are included in this report.

For several months following calibration at the F/A-18 APU engine conditions, various concrete specimens were repetitively exposed to the exhaust plume of the simulated F/A-18 APU engine. The repetitive testing confirmed achievement of several of the design criteria, e.g., continuous flow of 8 hours or more, unattended control panel after setting flow parameters, and proper functioning of the automated safeties. Also, the testing confirmed that failure of the type witnessed at operational airfields can be reproduced in the specimens after repeated exposures.

5. An initial decision was made to fabricate the burner with a 2-inch-diameter nozzle. It was later determined that the air compressor that could be procured for the AESF will not pump enough air for all flow parameters (static pressure, static temperature, flow velocity) at the exit plane of the 2-inch nozzle to equal those at the exit plane of a full scale engine. This is true for simulation of the F/A-18 APU engine and the rear nozzle of the AV-8B engine. Table 1 shows that, with the current air blower of the AESF, the nozzle should have a diameter of about 1.25 inches to match the flow parameters at the exit plane of the full scale F/A-18 APU engine, and should have a diameter of about 1.1 inches to match the flow parameters at the exit plane of the rear nozzle of the full scale AV-8B engine.

Data and discussions in the report show that, even with the 2-inch-diameter nozzle, test conditions can be changed so that the same convective heat transfer rates can be imposed on specimens by the AESF as are imposed on airfield pavements by full scale engines. The flexible design of the AESF enables one to change the convective heat transfer rate by changing the combustion chamber temperature, combustion chamber pressure, and/or the distance between the specimen and the exit plane of the nozzle.

6. Figures 19 and 32 show the temperature distributions across the exit plane of the nozzle for attempted simulations of the F/A-18 APU engine and the rear nozzle of the AV-8B engine, respectively. The distributions are not uniform. The non-uniform distributions indicate inadequate mixing in the combustion chamber between the products of combustion and

the excess cooling air. The combustion chamber should be lengthened to increase the time and distance for mixing to occur.

7. The data of Figures 15 through 41 show that the plumes from the AESF develop as expected for turbulent axisymmetric plumes. By the time the exhaust flow has moved far away (several nozzle exit diameters) from the nozzle exit plane, the plume takes the shape and flow characteristics of a classical turbulent jet with uniform flow at the origin. The effects of non-uniform flow at the nozzle exit plane cannot be seen after the flow has moved well away from the nozzle.

8. The analysis procedures presented in the Appendix are validated by comparing calculated results with measured data from the AESF. In particular, measured data validate the following: (a) the solution of the boundary layer equations to calculate boundary growth on specimens; (b) the use of Reynolds' Analogy to get heat transfer coefficients; (c) the estimation of adiabatic wall temperature based on an effective distance over which turbulent mixing has acted to reduce the temperature of the streamline at the edge of the boundary layer; and (d) the finite difference solutions of the heat transfer equations to calculate temperature-time histories of nodes throughout the specimens. Wherever possible, test data from the AESF were compared with calculations from the analysis procedures of the Appendix. Satisfactory agreement was obtained between the measured data and the calculated results for both the simulated F/A-18 APU engine and the simulated AV-8B engine rear nozzle. The close agreement shown in Figures 60 through 75 validated the analysis procedures.

It is noted, however, that there were uncertainties in the locations of thermocouples. Satisfactory agreement between measured data and calculated results depended upon the assumption that some of the thermocouple junctions were approximately 1/8 inch from their specified locations.

9. Quantitative verification of the numerical accuracy of the scale model testing procedures comes from satisfactory agreement between temperature-time histories in the specimens exposed to a simulated jet exhaust, and the temperature-time histories in operational airfield pavements that are exposed to the full scale engine exhaust. If the specimens have thermal properties (density, specific heat, thermal conductivity) approximately equal to those of the operational airfield pavement, comparable temperature-time histories indicate comparable convective heat transfer rates. Quantitative verification of the scale model testing procedures, therefore, depends upon acquisition of temperatures from airfield pavements during exposure to full scale engine exhaust flow.

Qualitative verification of the scale model testing procedures comes from producing failures in specimens that resemble the failures at airfield pavements, and occur after approximately the same number of cycles of heating and cooling. Precise records are not kept at airfields on the number of cycles of heating and cooling that pavements experience before spalling begins. Estimates can be made based on the number of flight operations during which the airfield pavement was heated. If the scale model tests include specimens with the same concrete mix design as the airfield pavement, the parameters of the scale model tests should be such that specimens spall after approximately the same number of heating and cooling cycles as the airfield pavement.

10. Limited temperature data are available for pavements subjected to full scale F/A-18 APU exhaust flow. Comparison with the AESF data show the temperatures from the full scale system to be 24 to 60°F lower than those from the AESF.

11. Temperature measurements were not available for pavements subjected to the AV-8B jet exhaust. Therefore, the results in this report do not include verification of the scale model testing procedures based upon AV-8B data.

12. Simulation of the AV-8B will require other information as well. This includes: (a) clarification of flow conditions (temperature and velocity) at the exit plane of the rear nozzles; (b) typical time versus altitude history during vertical lift-off, beginning at the time of rotation of the nozzles to the vertical position; and (c) previous measurements and/or calculations of temperature-time histories of pavements subjected to the full scale AV-8B exhaust flow.

Values of temperature and velocity at the exit plane of the AV-8B rear nozzles are shown in Table 1. The values in Table 1 are deduced from Reference 22. They are consistent with nozzle exit conditions which will give the correct thrust, stability, and rate of fuel consumption during vertical takeoff and landing of the AV-8B. However, they do not agree with values of temperature and flow velocity presented in Reference 23. There may be more than one combination of nozzle flow conditions which will also give correct thrust, stability, and fuel flow. Therefore, it will be advisable to verify whether the nozzle exit conditions in Table 1 are correct.

RECOMMENDATIONS

The following recommendations are made for future modification of and testing with the NFESC AESF:

1. Additional data should be sought for the AV-8B engine. The specific data or information needed are: (a) clarification of flow conditions (temperature and velocity) at the exit plane of the rear nozzles; (b) typical time versus altitude history during vertical lift-off, beginning at the time of rotation of the nozzles to the vertical position; and (c) previous measurements and/or calculations of temperature-time histories of pavements subjected to the full scale AV-8B exhaust flow.

The recommended source for the needed data and information is D. G. Dobbs, who is the author of the memoranda cited as References 23 and 24. Other potential sources include: (a) manuals for the F402 engine; (b) a manufacturer's representative from the Rolls-Royce company, which manufactures the F402 engine; (c) a manufacturer's representative from McDonnell-Douglas, the licensee to produce the AV-8B in the United States; or (d) a representative from the AV-8B program office either at the Naval Air Systems Command or at the Marine Corps.

2. Verify that the data for the AV-8B engines in Table 1 are accurate, for both full scale and the AESF simulation. If so, proceed with fabrication of a nozzle with diameter =

1.1 inches for use in subsequent AV-8B simulations. Operate the burner with the combustion chamber pressure and temperature shown in Table 1.

If the data in Table 1 are not accurate, substitute correct values, recompute the nozzle diameter, and fabricate the nozzle for subsequent AV-8B simulations. Compute and use the correct combustion chamber pressure and temperature.

3. To provide more time for the fuel in the combustion chamber to burn, and to improve mixing between the combustion products and the excess air used for cooling, add 12 inches to the length of the burner between the igniter and the nozzle.

4. After the length of the burner has been increased, move the chamber pressure and chamber temperature probes so they are no farther from the nozzle than shown in the original burner.

5. After the modifications recommended above have been made to the burner, conduct the startup/shutdown of the modified facility in the following sequence:

(a) Do the initial light-off with the extended combustion chamber in place, but without any bottom plate and nozzle. In other words, re-establish the light-off sequence and stable combustion with the bottom of the combustion chamber completely open to the atmosphere.

(b) After the light-off sequence is re-established, attach the original bottom plate with its 2-inch-diameter nozzle at the bottom of the combustion chamber. Confirm that safe light-off and stable combustion are still achieved with the 2-inch-diameter nozzle.

(c) As the final step, replace the bottom plate and 2-inch-diameter nozzle with the new bottom plate and 1.1-inch-diameter nozzle. Again confirm that safe light-off and stable combustion are achieved with the 1.1-inch-diameter nozzle.

6. Evaluate and compare the alternatives for simulating or taking into account the transient convective heat input from the AV-8B exhaust plume due to the increasing distance between the nozzle exit plane and the pavement as the aircraft takes off. Alternatives discussed in the previous section of the report were: (a) to modify the AESF so that the specimens can be lowered at a predetermined rate during the tests; or (b) to determine an average test condition that produces the same result as the transient test conditions. Plan the test series based on the decision made for simulating or taking into account the transient heating.

7. Conduct a truncated calibration test series to confirm that the expected test conditions and results are being attained. To recommend a plan for the truncated calibration tests is not appropriate here, because the plan will depend on which alternative is selected during recommendation 6.

REFERENCES

1. Naval Civil Engineering Laboratory. Technical Memorandum M-53-85-01: Test and evaluation master plan for materials resistant to effects of V/STOL aircraft on pavements and support facilities, by G.Y. Wu. Port Hueneme, CA, Nov 1984.
2. Naval Civil Engineering Laboratory. Technical Memorandum M-53-85-02: Initiation decision report (IDR) on fiber reinforced concrete (FRC) airfield pavement, by G.Y. Wu. Port Hueneme, CA, Nov 1984.
3. Naval Facilities Engineering Command. Military Handbook MIL-HDBK-1021/4: Rigid pavement design for airfields, Section 6.2, Heat resistant concrete for F/A-18 aircraft. Alexandria, VA, 30 Apr 1987.
4. Naval Civil Engineering Laboratory. Task No. E-7: High temperature pavements, by M.C. Hironaka. Presentation for the 1993 Shore Facilities Materials Program Review. Port Hueneme, CA, 1993.
5. Naval Air Warfare Center Aircraft Division. Technical Report No. SA-162R-91: Evaluation of an F/A-18 auxiliary power unit modified nozzle, by S.W. Houck, D.N. Gordge, and C.A. Hadfield. Patuxent River, MD, 23 Jan 1992.
6. Naval Air Propulsion Center. Report No. NAPC-LR-90-18: F-18 auxiliary power unit exhaust gas footprint evaluation test, by M.L. Houck, A.J. Cifone, and J.F. Thaler. Trenton, NJ, Nov 1990.
7. L.J. Malvar and M.C. Hironaka. "Heat resistant concrete for airfield pavements: Preliminary numerical study," Computers & Structures, vol 40, no. 2 (printed in Great Britain), 1991, pp 303-311.
8. C.A. Kodres. "Moisture induced pressures in concrete airfield pavements," Journal of Materials in Civil Engineering, vol 8, no. 1, Feb 1996, pp 41-50.
9. P.A. Abeloff, W.R. Van Dalsem, and F.C. Dougherty. "Thermal interaction between an impinging hot jet and a conducting solid surface," AIAA 8th Applied Aerodynamics Conference, Portland, OR, 20-22 Aug 1990
10. M.C. McVay, C.W. Manzione, and J. Murfree. "Damage to military aprons from hydraulic fluid engine lubricants and heat," Transportation Research Record, no. 135, Jan 1993, pp 86-92.
11. Naval Construction Battalion Center. Final Report: Heat resistant materials for the FA-18 pavement, by V. Ramakrishnan, W. Krause, W. Groves, H.A.F. Shafai, and S Rajpal. Port Hueneme, CA, P.O. No. N62583/88MX784, South Dakota School of Mines and Technology (undated).

12. Naval Construction Battalion Center. Final Report: Cyclic heating (to 400°F) and cooling effects on concrete strength, by V. Ramakrishnan. Port Hueneme, CA, P.O. No. N6258388P2206, South Dakota School of Mines and Technology (undated).
13. Naval Construction Battalion Center. Final Report: Cyclic heating (to 280°F) and cooling effects on concrete strength, by V. Ramakrishnan. Port Hueneme, CA, P.O. No. N6258389MM710, South Dakota School of Mines and Technology (undated).
14. Naval Construction Battalion Center. Final Report: Protective coating heat resistant pavement materials for FA-18 pavement, by V. Ramakrishnan, W. Krause, W. Groves, H.A.F. Shafai, and S. Rajpal. Port Hueneme, CA, P.O. No. N625838P0336, South Dakota School of Mines and Technology, Nov 1989.
15. Naval Construction Battalion Center. Final Report: Evaluation of heat and thermal shock resistant materials for airfield pavement applications, by R. Aman, V. Ramakrishnan, and W. Krause. Port Hueneme, CA, P.O. No. N6258389P1087, South Dakota School of Mines and Technology, Nov 1989.
16. Naval Construction Battalion Center. Final Report: Evaluation of heat and thermal shock resistant materials for airfield pavement applications (A Supplement report), by R. Aman, V. Ramakrishnan, and W. Krause. Port Hueneme, CA, P.O. No. N6258389P1087, South Dakota School of Mines and Technology, Oct 1989.
17. Tyndall Air Force Base. Videotape of British Aerospace Corporation tests of jet impingement on various airfield pavement specimens, High Temperature Pavements Coordination Meeting between J. Rish (AFESC) and E. Cooper (NCEL), 1992.
18. High Temperature Pavements Coordination Meeting between J. Rish, Mr. J. Murfree (AFESC), E. Cooper, and M. Hironaka (NCEL). Tyndall AFB, 1993.
19. Naval Civil Engineering Laboratory. Technical Note N-1788: Experimental examination of the aerothermal performance of the T-10 test cell at NAS, Cubi Point, by C.A. Kodres and E.E. Cooper. Port Hueneme, CA, Sep 1988.
20. Cornell University. Structural Engineering Report No. 92-2M: Theory and operation manual for the impact-echo field system, volume I, second edition, by M. Sansalone and D.G. Pratt. Gormann Instruments, Evanston, IL, Jan 1993.
21. H. Schlichting. Boundary layer theory. Fourth Edition, pp 590-611, 137-140, 243-251, and 303-306. New York, NY, McGraw-Hill Book Company, 1960.
22. Naval Facilities Engineering Command. P-918: Aviation test facilities, aircraft and engine data, final submission. Alexandria, VA, Jan 1989.

23. D.G. Dodds. Informal Memorandum to Larry Close: AV-8B nozzle exhaust plume characteristics, AV-8B Propulsion 344/270E/5/ms106 of McDonnell-Douglas, 29 Feb 1988.
24. D.G. Dodds. Informal Memorandum to Larry Close: AV-8B nozzle exhaust plume characteristics, AV-8B Propulsion 344/270E/5/ms106 of McDonnell-Douglas, 1 Mar 1988.
25. D. Gorge. Naval Air Warfare Center, FAX to C. Kodres, Naval Civil Engineering Laboratory, subject: Concrete test data, production nozzle, 27 Feb 1992.

Table 1. Nozzle and Combustion Chamber Conditions to Simulate the F/A-18 APU and the AV-8B Rear Nozzle.

Flow Variable or Design Parameter	Value for Full Scale F/A-18 APU Engine	Value for F/A-18 APU Engine Simulated with AESF	Value for Full Scale AV-8B Rear Nozzle	Value for AV-8B Rear Nozzle Simulated with AESF
Nozzle Exit Static Pressure, P_{exh} lb_f/in^2 , absolute	14.7	14.7	14.7	14.7
Nozzle Exit Total Pressure, lb_f/in^2 , gauge	0.92	See Figure 15	1.96	See Figure 27
Nozzle Exit Static Temperature, T_{exh} , deg F	1026	Not Uniform	1300	Not Uniform
Nozzle Exit Total Temperature, Deg F	1052	See Figure 19	1364	See Figure 32
Nozzle Exit Flow Velocity, ft/sec	560	See Figure 23	879	See Figure 37
Speed of Sound at Nozzle Exit, ft/sec $a_{exh} = (g_c \gamma R T_{exh})^{1/2}$	1889	Not Uniform	2056	Not Uniform
Mach Number, dimensionless $M_{exh} = \frac{V_{exh}}{a_{exh}}$	0.296	Not Uniform	0.427	Not Uniform

Table 1 (Cont'd). Nozzle and Combustion Chamber Conditions to Simulate the F/A-18 APU and the AV-8B Rear Nozzle.

Flow Variable or Design Parameter	Value for Full Scale F/A-18 APU Engine	Value for F/A-18 APU Engine Simulated with AESF	Value for Full Scale AV-8B Rear Nozzle	Value for AV-8B Rear Nozzle Simulated with AESF
AESF Combustion Chamber Pressure, lb/in ²	N/A	Actual 2.60 Needed 0.92	N/A	Actual 2.62 Needed 1.92
$P_{CC} = P_{exh} \left[1 + \frac{\gamma - 1}{2} M_{exh}^2 \right]^{\frac{\gamma}{\gamma - 1}} - P_{atm}$				
AESF Combustion Chamber Temperature, Deg F	N/A	Actual 1100 Needed 1043	N/A	Actual 1425 Needed 1347
$T_{CC} = T_{exh} \left[1 + \frac{\gamma - 1}{2} M_{exh}^2 \right]$				
AESF Air Flow Rate, lbm/sec	N/A	0.117	N/A	0.117
AESF Theoretical Natural Gas Flow Rate, lbm/sec	N/A	0.0147	N/A	0.0214
$\dot{m}_g = \frac{\dot{m}_{air} [c_{pCC}(T_{CC} - 75)]}{HV_g - c_{pCC}(T_{CC} - 75)}$				
AESF Actual Natural Gas Flow Rate, lbm/sec	N/A	0.0039	N/A	0.0044

Table 1 (Cont'd). Nozzle and Combustion Chamber Conditions to Simulate the F/A-18 APU and the AV-8B Rear Nozzle.

Flow Variable or Design Parameter	Value for Full Scale F/A-18 APU Engine	Value for F/A-18 APU Engine Simulated with AESF	Value for Full Scale AV-8B Rear Nozzle	Value for AV-8B Rear Nozzle Simulated with AESF
AESF Theoretical Nozzle Diameter, in $D_{exh} = \left[\frac{4 (\dot{m}_{air} + \dot{m}_g)}{\pi \rho_{exh} V_{exh}} \right]^{\frac{1}{2}}$	N/A	1.27	N/A	1.10
AESF Actual Nozzle Diameter, inches	N/A	2.00	N/A	2.00
Full Scale Nozzle Exit Area, in ²	39.4	N/A	542	N/A
Full Scale Nozzle Hydraulic Diameter, in	7.08	N/A	26.3	N/A
Scaling Factor, dimensionless $\Phi = \frac{D_{AESF \text{ Nozzle}}}{D_{Full \text{ Scale Nozzle}}}$	N/A	0.282	N/A	0.076
$Z_{Full \text{ Scale Nozzle}} - \text{Concrete, inches}$	N/A	77	N/A	85
$Z_{AESF \text{ Nozzle}} - \text{Specimen, inches}$ $= \Phi * (Z_{Full \text{ Scale Nozzle}} - \text{Concrete})$	N/A	21.7	N/A	6.5

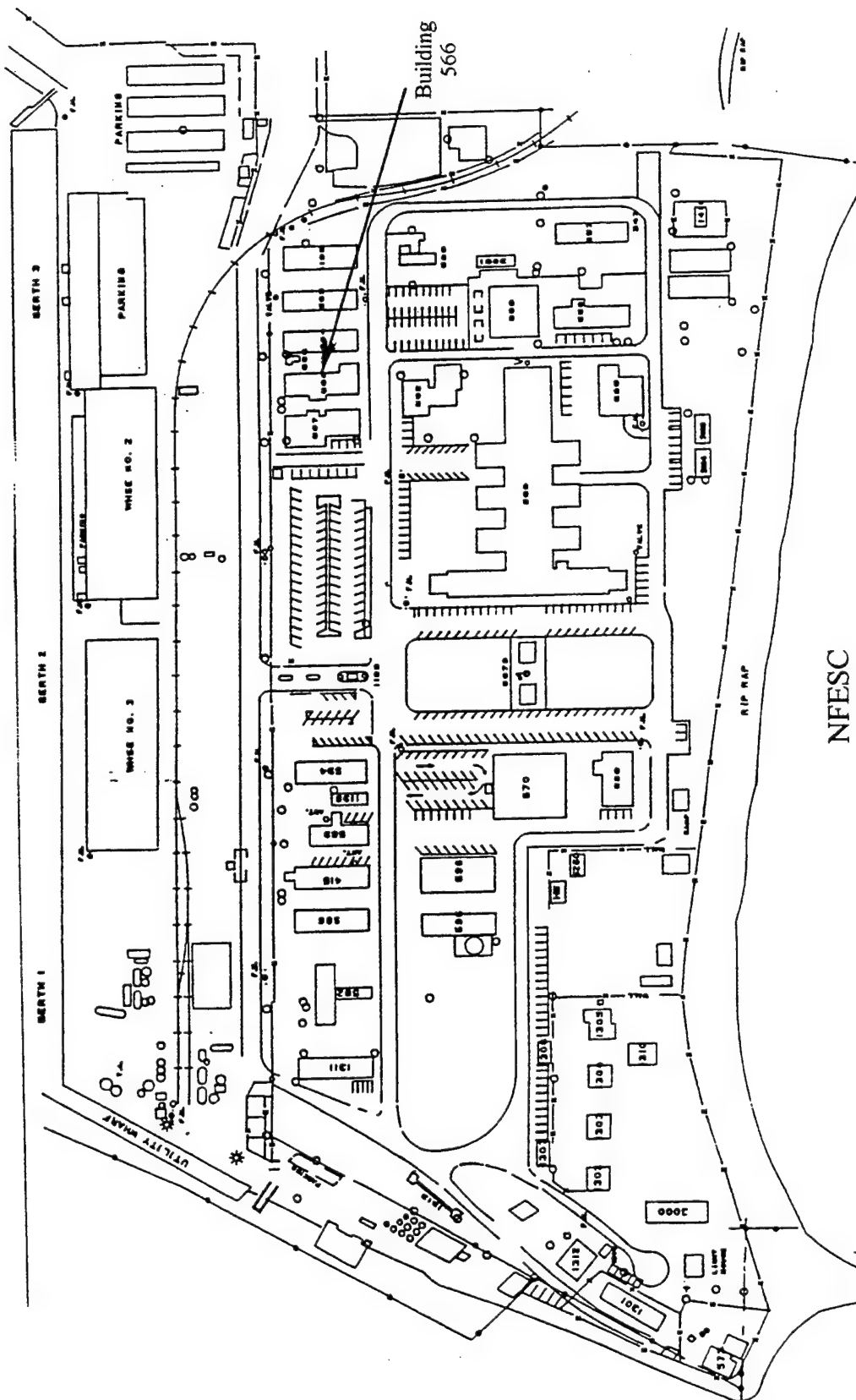


Figure 1. NFESC compound, showing location of Building 566 and the AESF within the compound

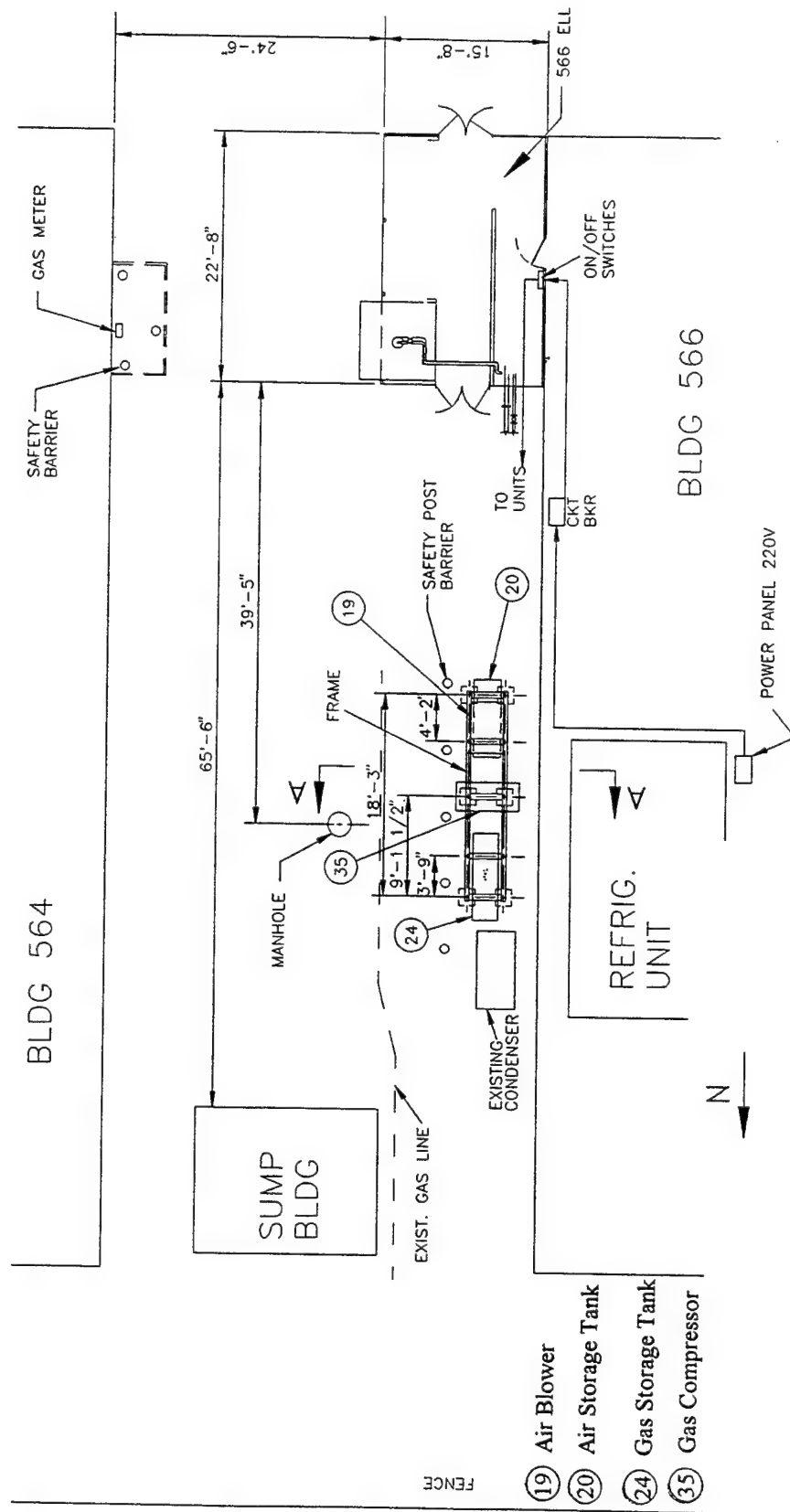


Figure 2. Layout of the Aviation Engine Simulation Facility at Building 566

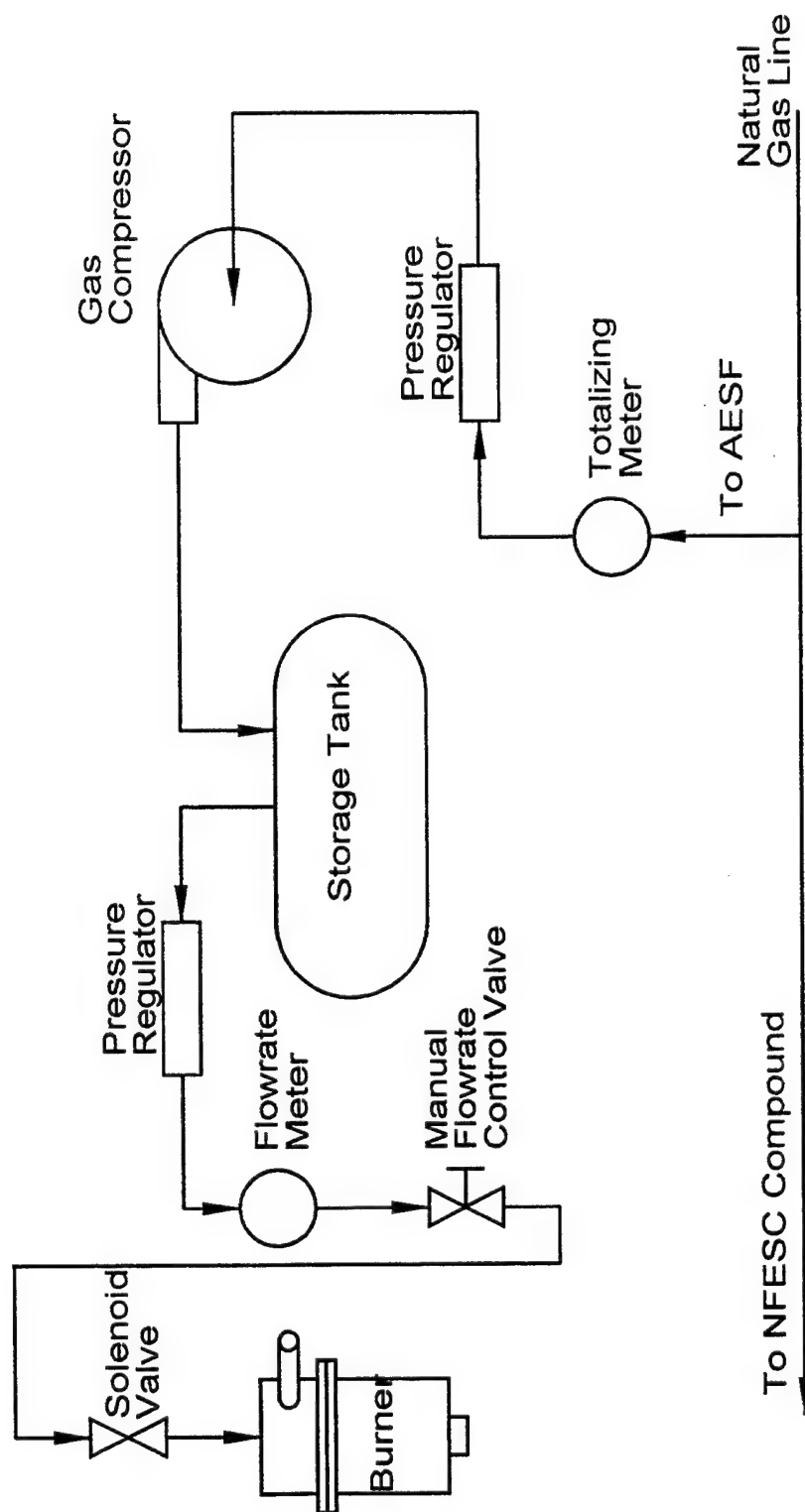


Figure 3. Schematic Diagram of the Natural Gas Supply Subsystem

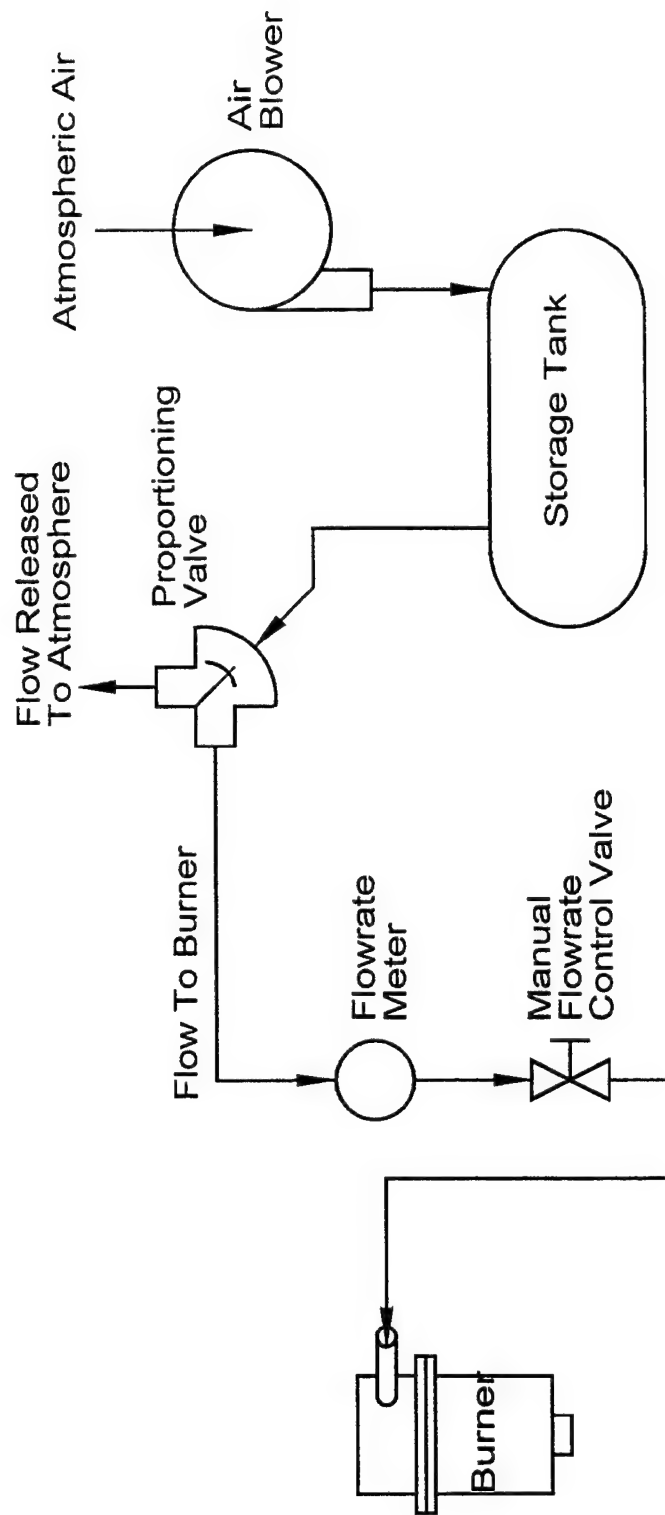


Figure 4. Schematic Diagram of the Air Supply Subsystem

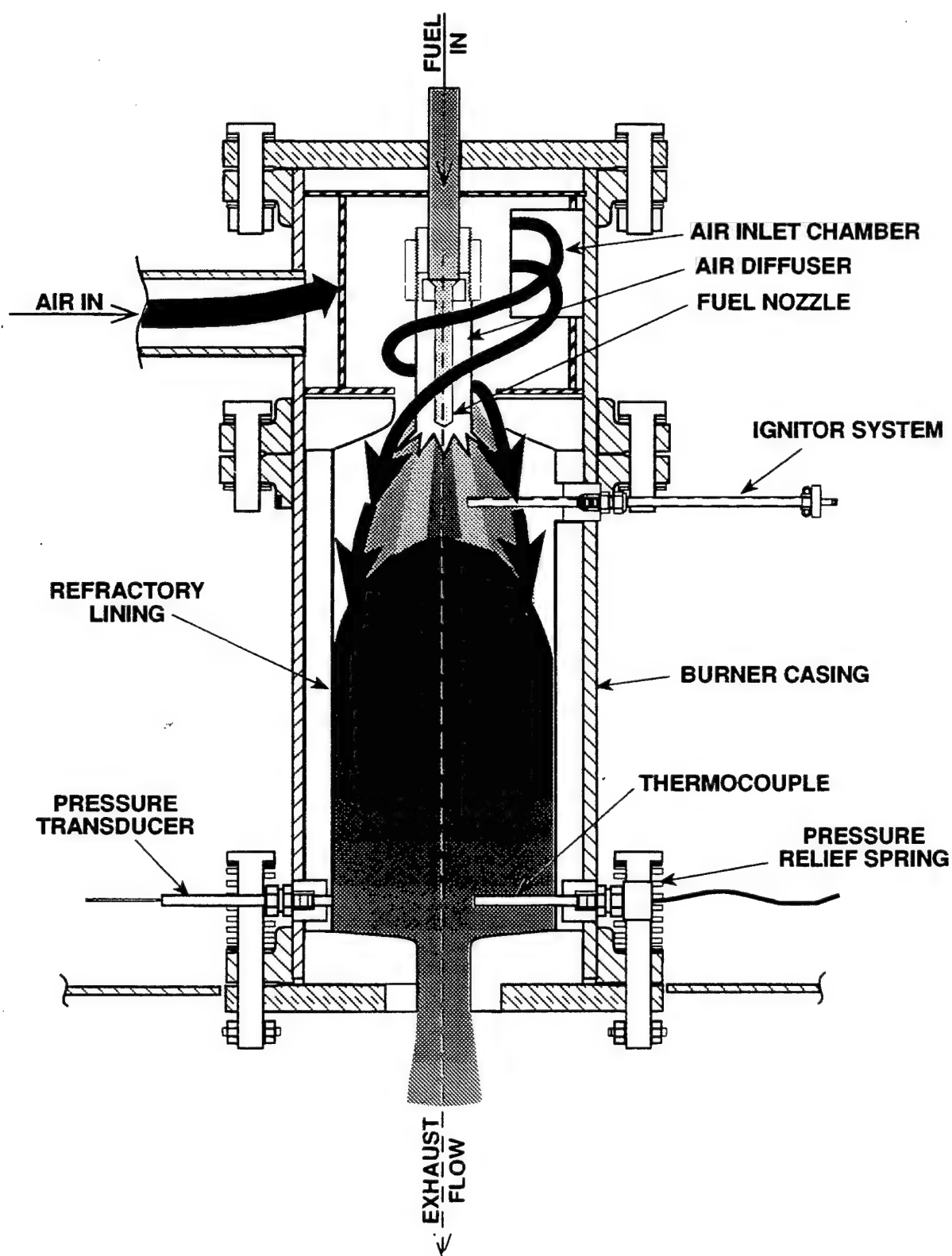


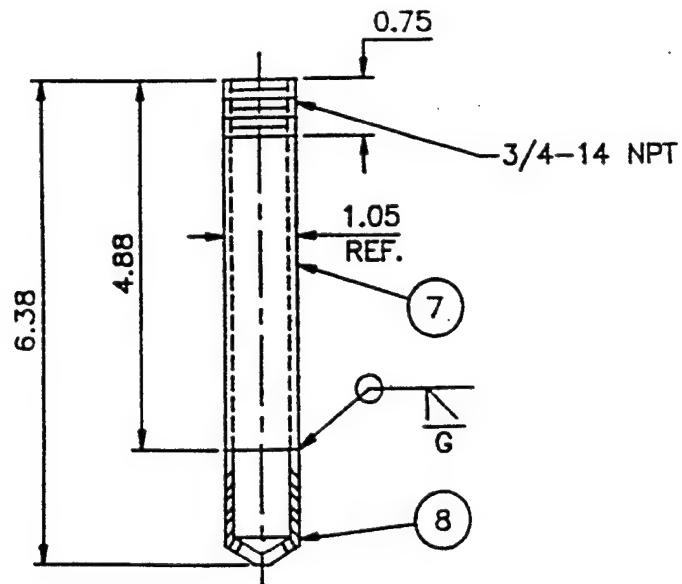
Figure 5. Section view of the AESF burner, showing the general flow pattern within the burner



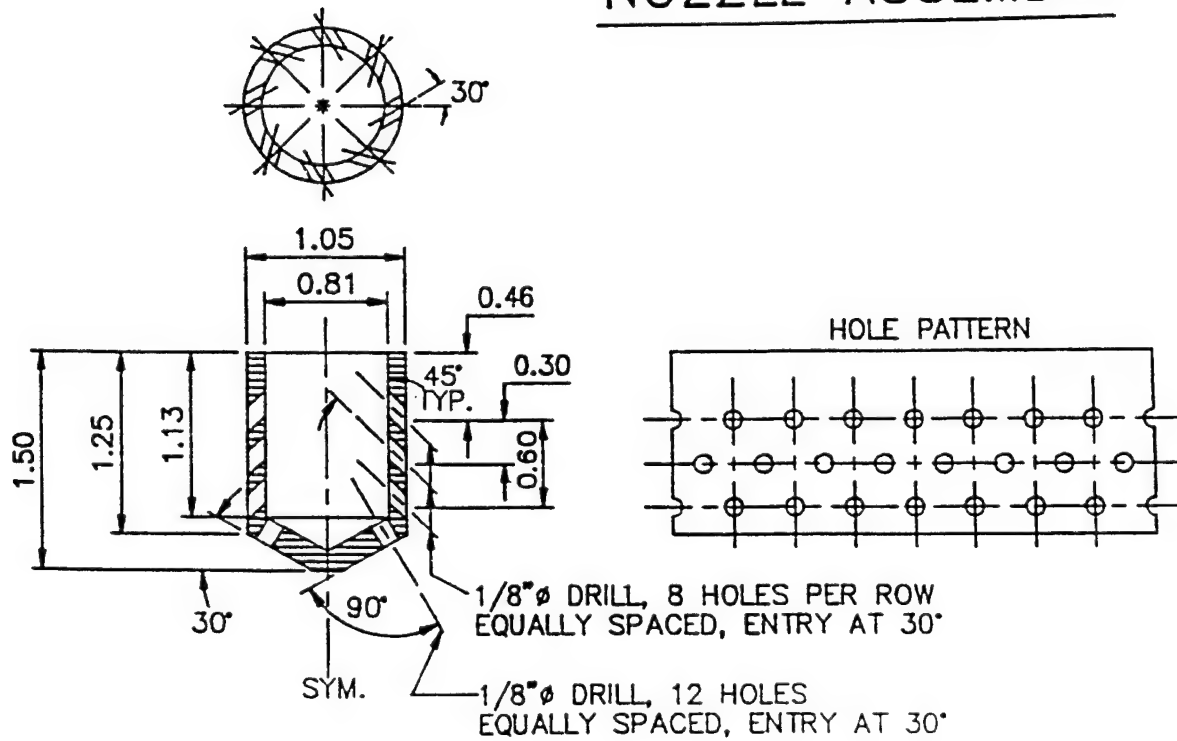
Figure 6. Burner and test enclosure of the NFESC Aviation Engine Simulation Facility

⑦ 3/4" pipe, sch. 40 seamless

⑧ nozzle tip

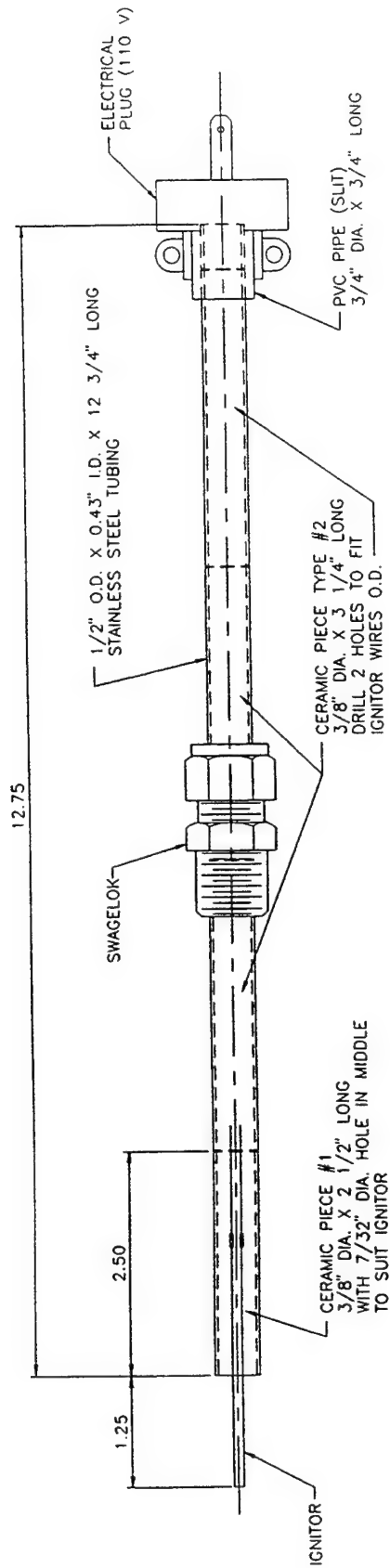


NOZZLE ASSEMBLY



NOZZLE TIP

Figure 7. Design of the natural gas injector in the burner of the AESF



NOTE: USE CERAMIC CEMENT AS NEEDED.

Figure 8. Design of the ignitor of the burner of the NFESC Aviation Engine Simulation Facility

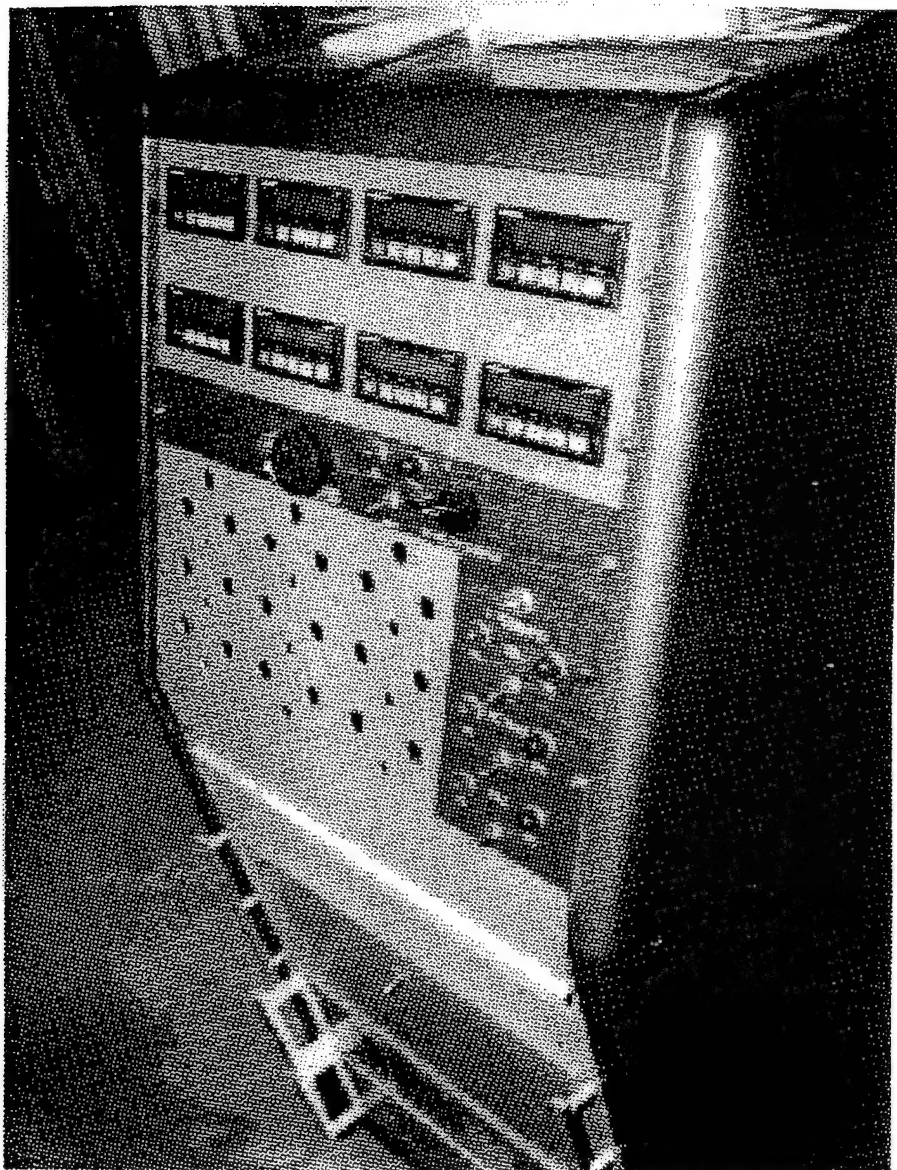


Figure 9. Control panel of the NFESC Aviation Engine Simulation Facility

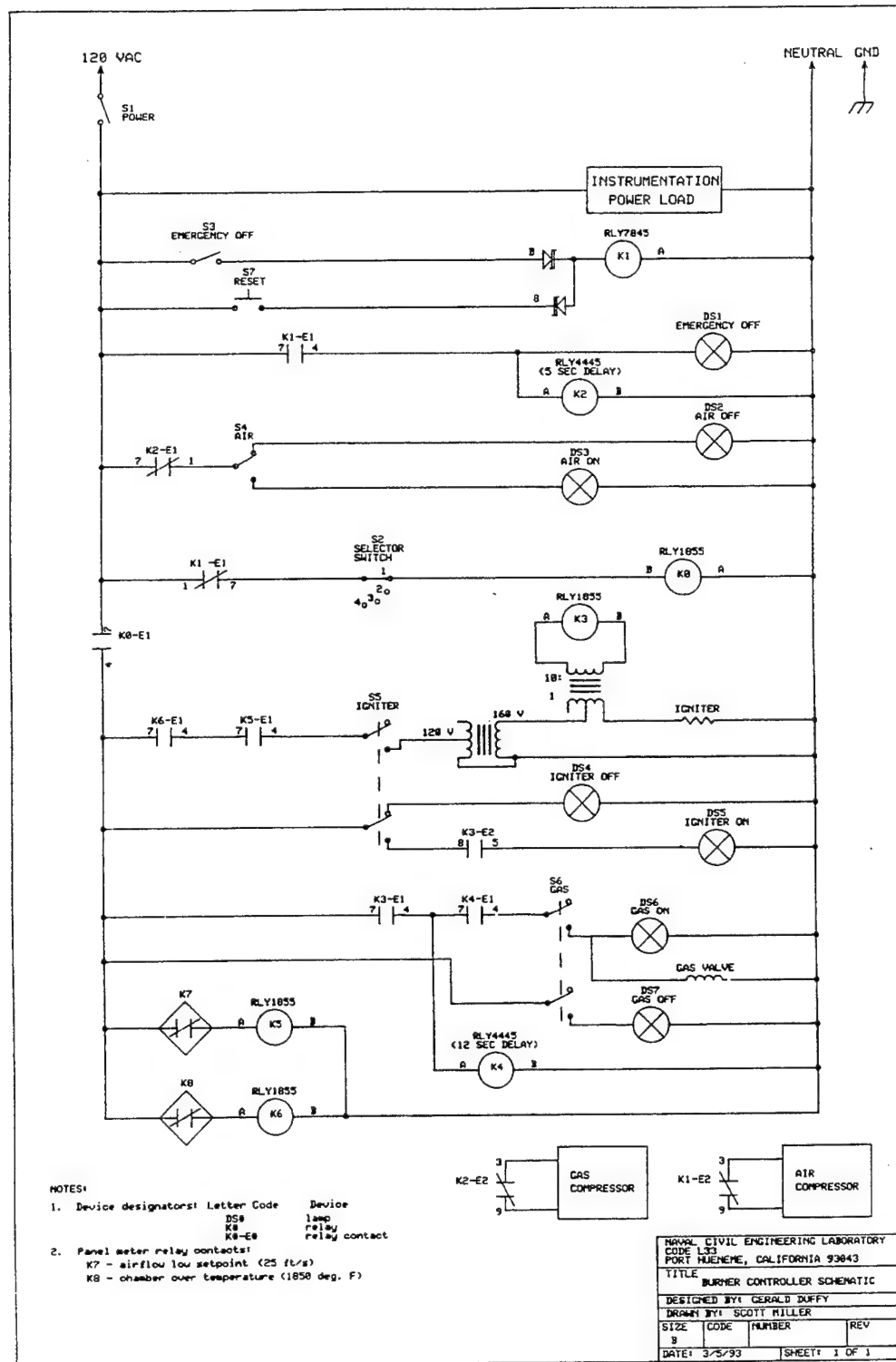


Figure 10. Circuit diagram for the control panel of the NFESC Aviation Engine Simulation Facility

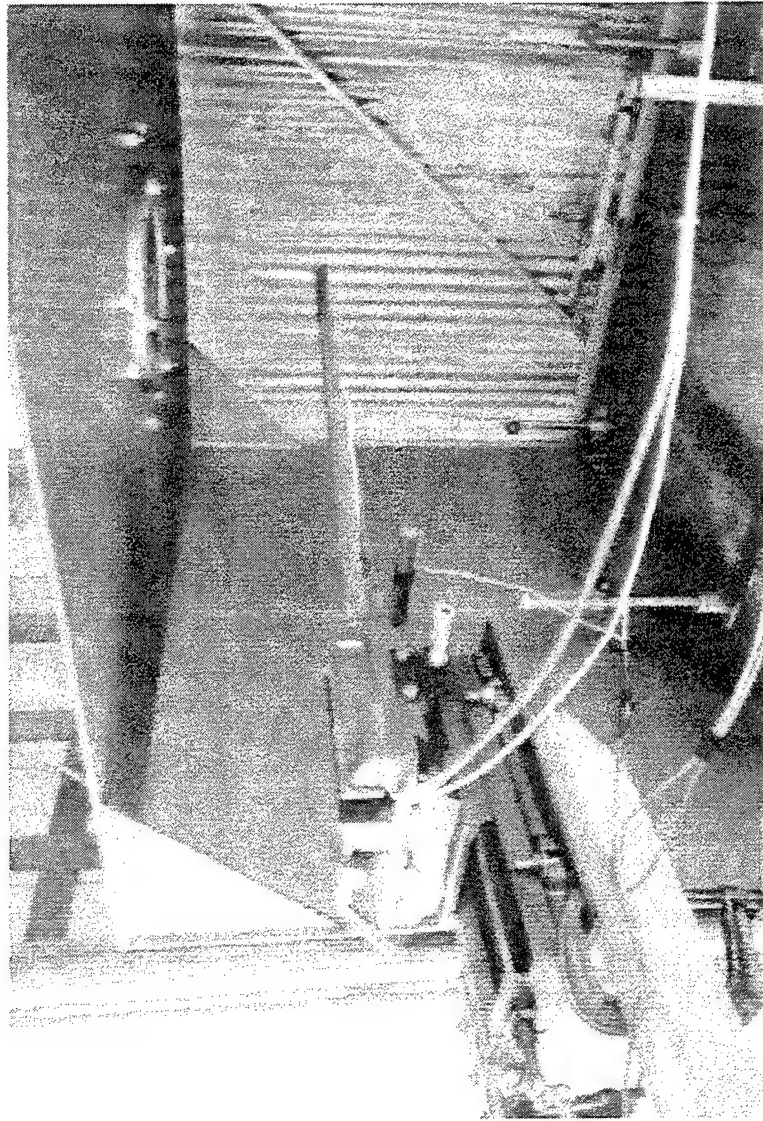


Figure 11. Rig to measure temperatures and pressures in the plumes of the NFESC Aviation Engine Simulation Facility

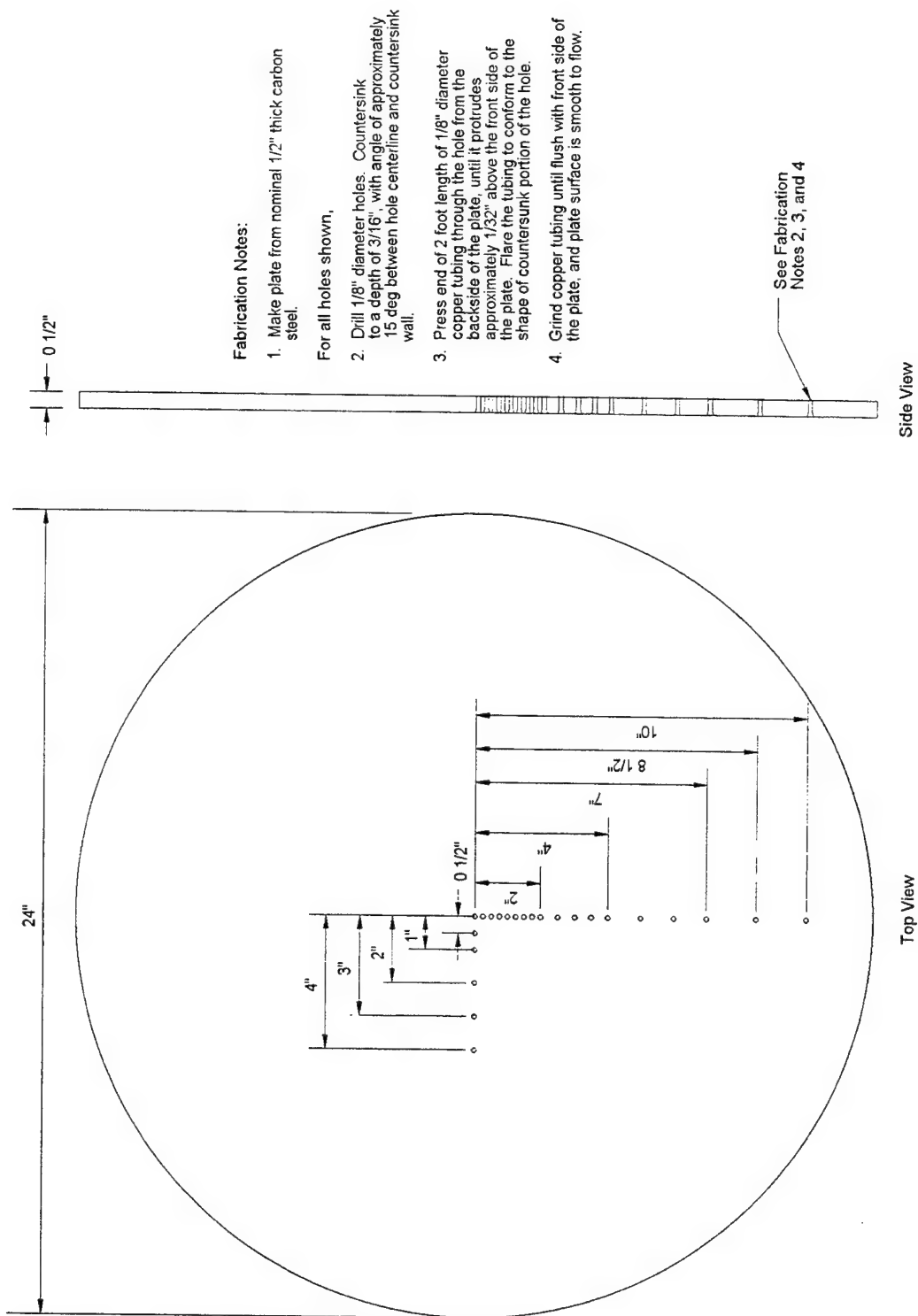


Figure 12. Design of plate to measure surface pressure distribution on specimens due to plume impingement on the specimens

- Notes:
1. Place thermocouples 0", 1/4", 1/2", 1", 2", and 4" below top surface of specimen.
 2. Place thermocouples 0", 1/4", and 1" below top surface of specimen.
 3. Place thermocouples 0", 1/4", and 1/2" below top surface of specimen.
 4. Place thermocouples 0" and 1/2" below top surface of specimen.
 5. Place thermocouple 0" below top surface of specimen.
 6. Fabricate thermocouples of chromel-alumel thermocouple wires. Silver solder or weld tips. Trim tips and beads to <1/8" length.
 7. Pre-position thermocouples within molds, with leads out the bottom side. Wrap each vertical group of thermocouples with tape for stiffness and to maintain relative position. Hold surface thermocouple stationary while concrete is poured into mold, and adjust to surface level before concrete hardens.
 8. Various concrete mix designs are to be specified.

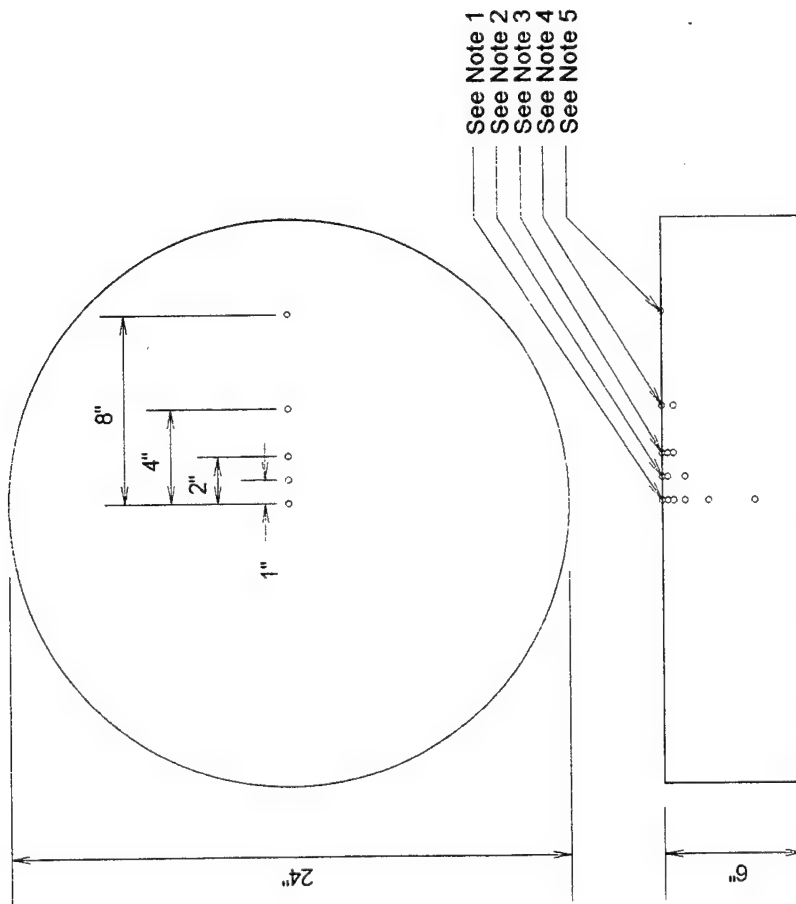


Figure 13. Design of instrumented concrete specimens to measure temperature distributions resulting from impingement of the jet flow on the concrete

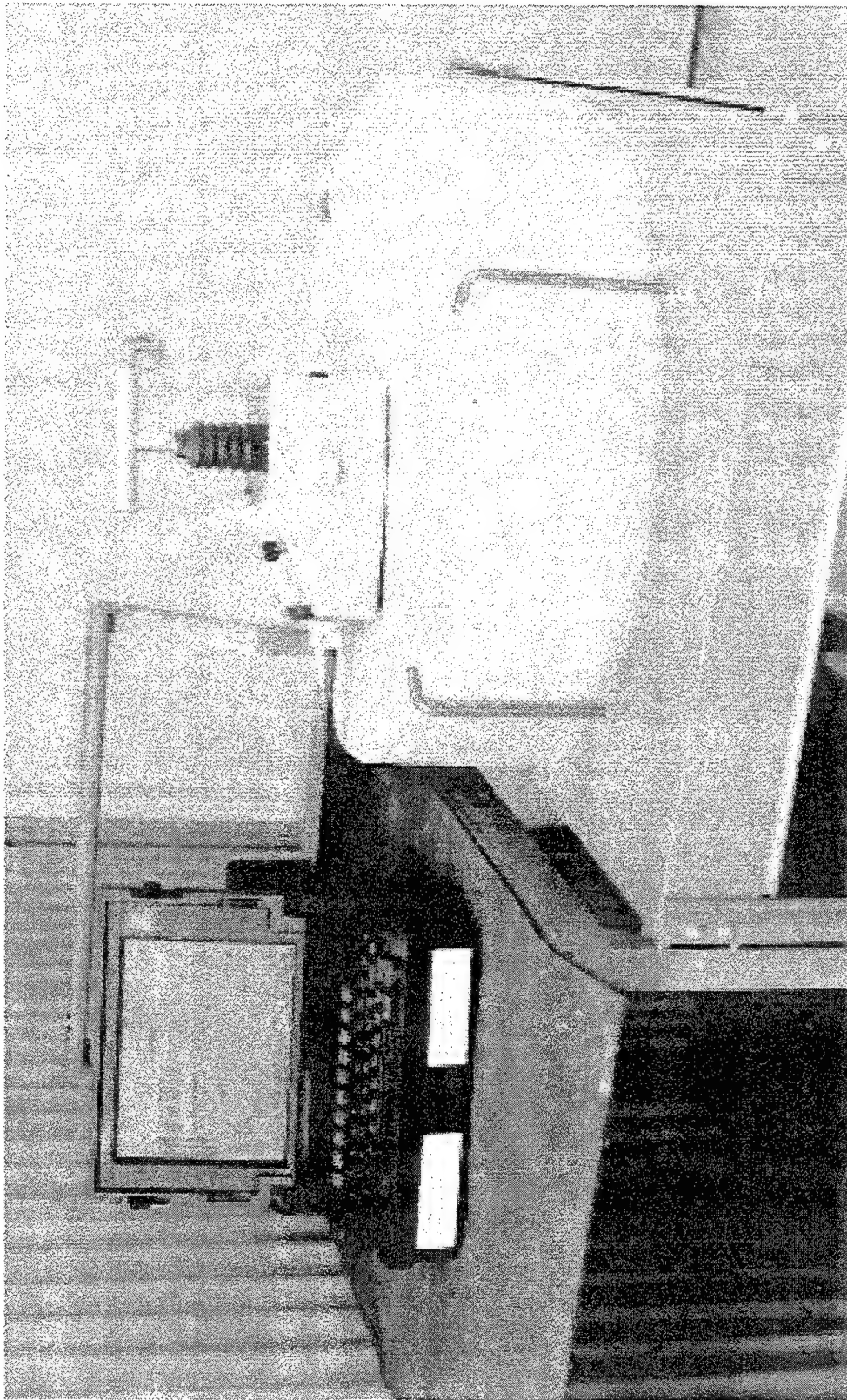


Figure 14. The impact echo fault detector used to determine when subsurface cracks have formed parallel to the heated surface of a specimen.

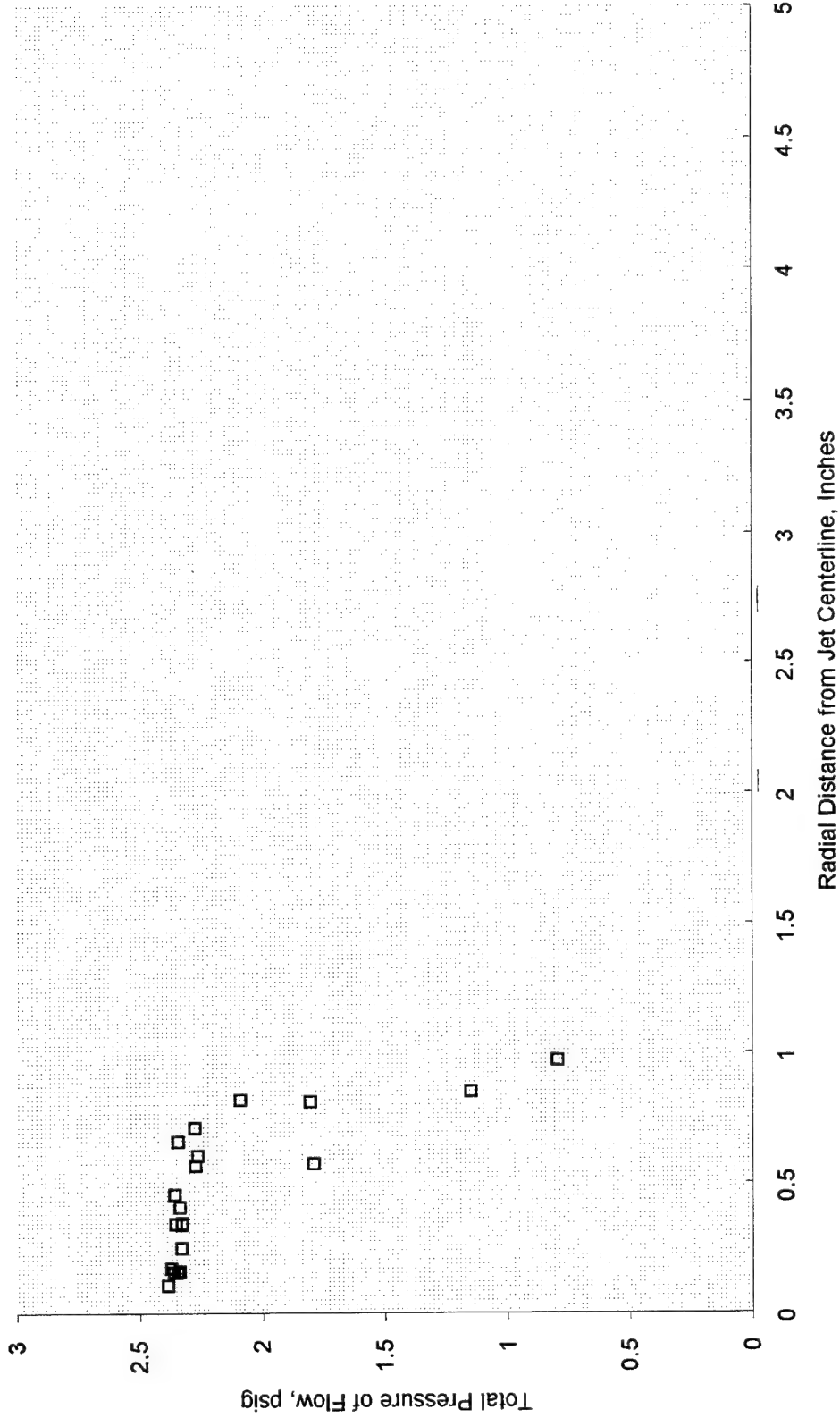


Figure 15. Profile of total pressure in attempted simulation of
F/A-18 APU exhaust plume, Z=0.5"

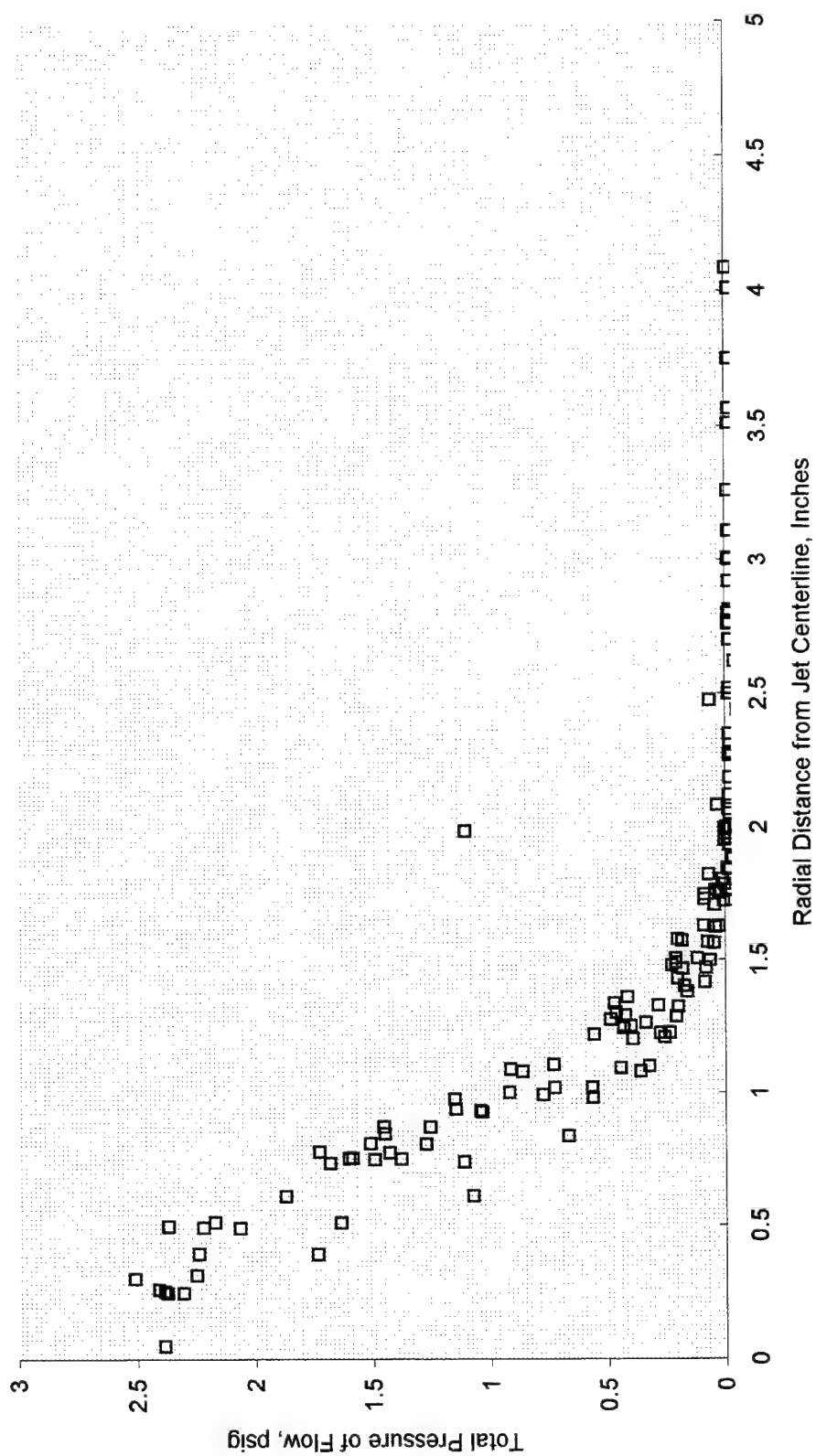


Figure 16. Profile of total pressure in attempted simulation of F/A-18 APU exhaust plume, Z=6"

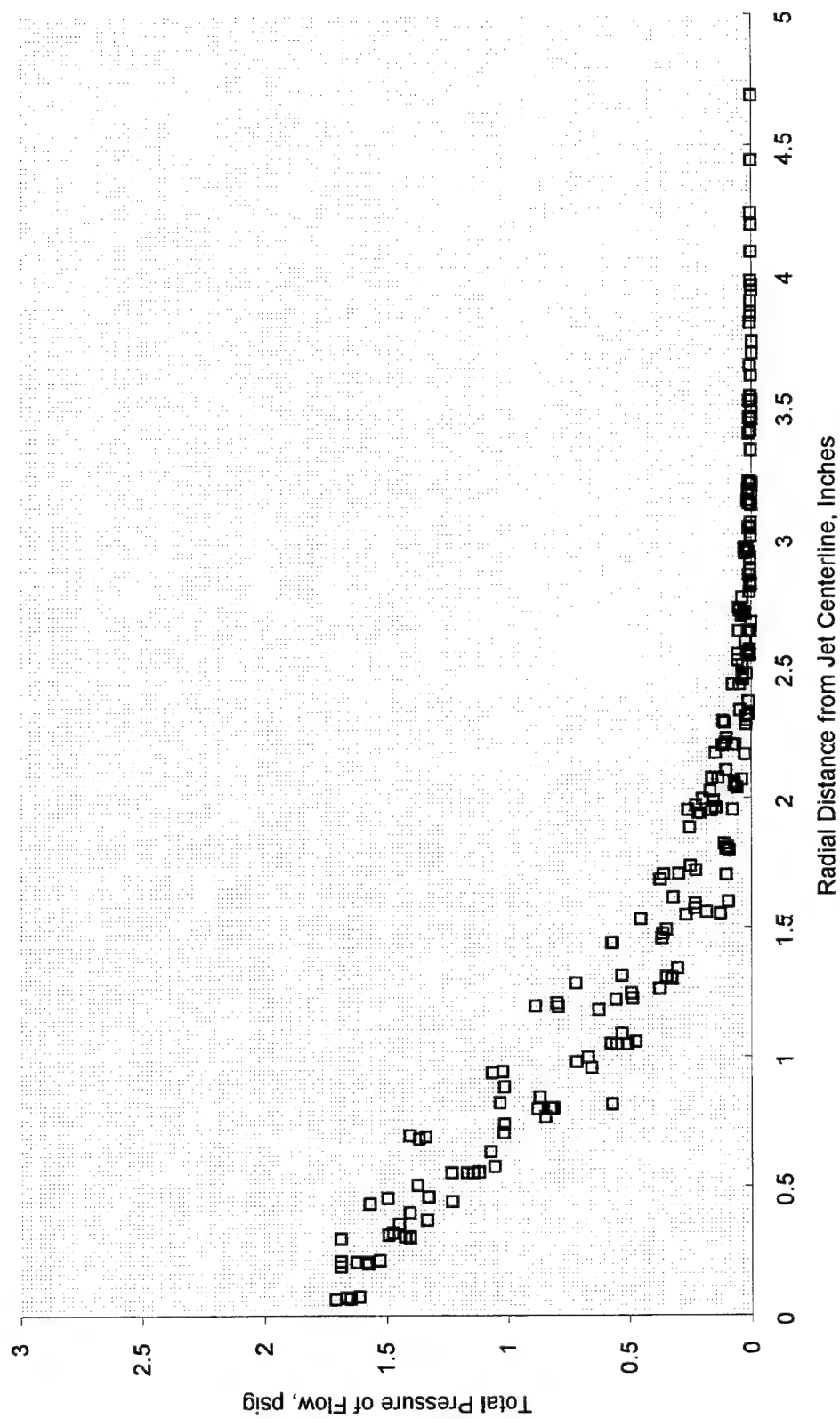


Figure 17. Profile of total pressure in attempted simulation of F/A-18 APU exhaust plume, Z=12"

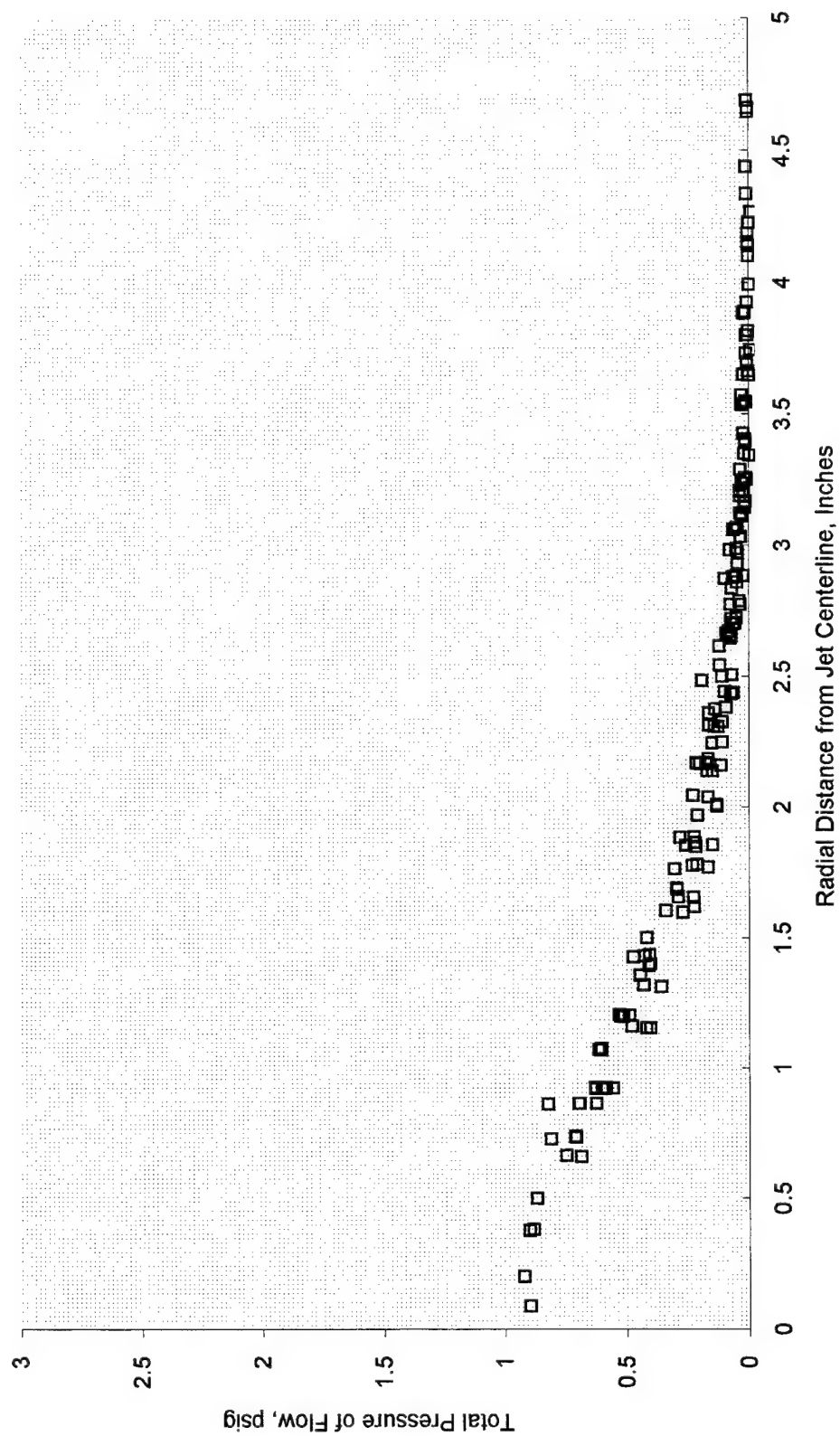


Figure 18. Profile of total pressure in attempted simulation of
F/A-18 APU exhaust plume, Z=18"

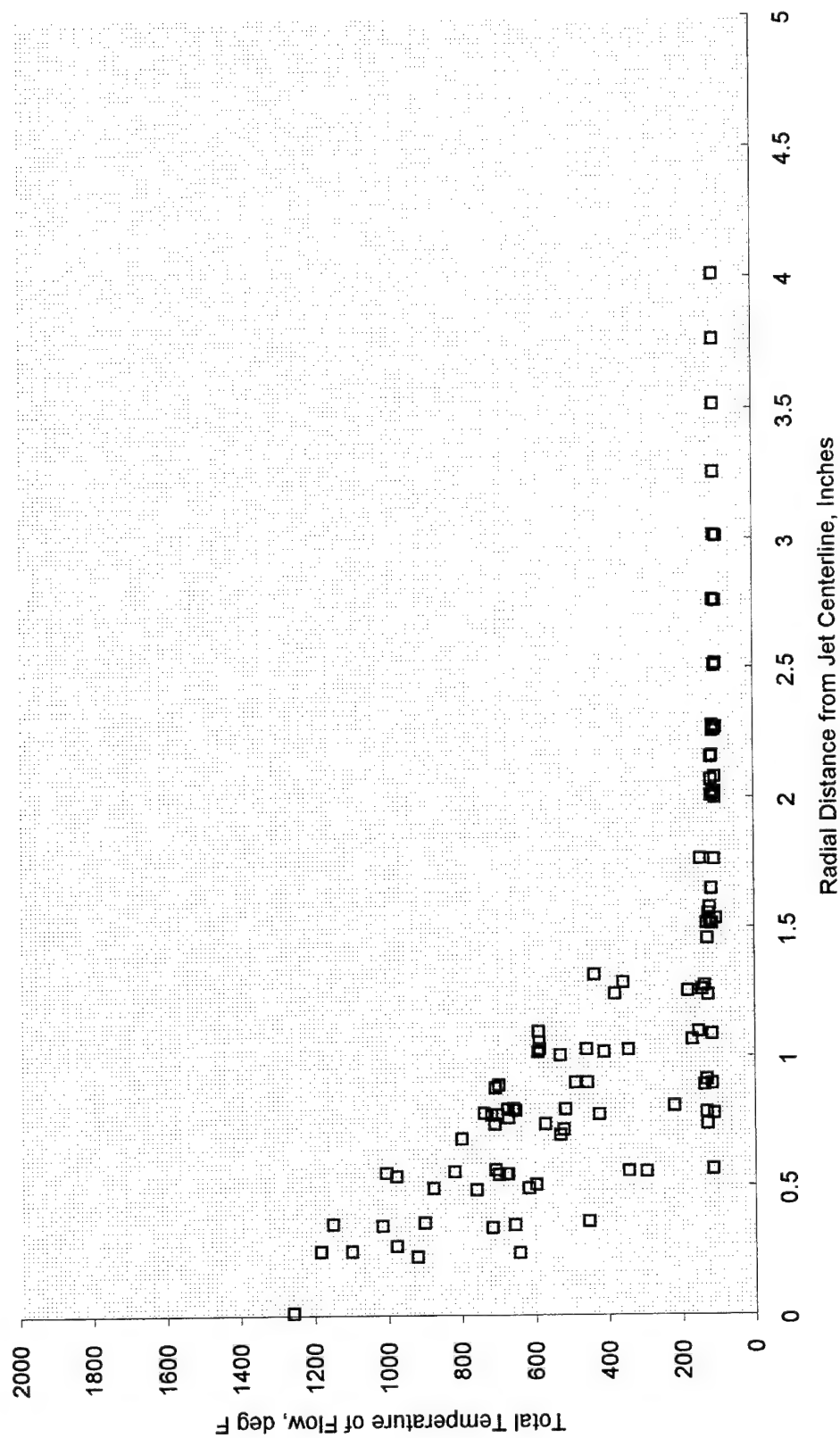


Figure 19. Profile of Total Temperature in attempted simulation of F/A-18 APU exhaust plume, Z=0.5"

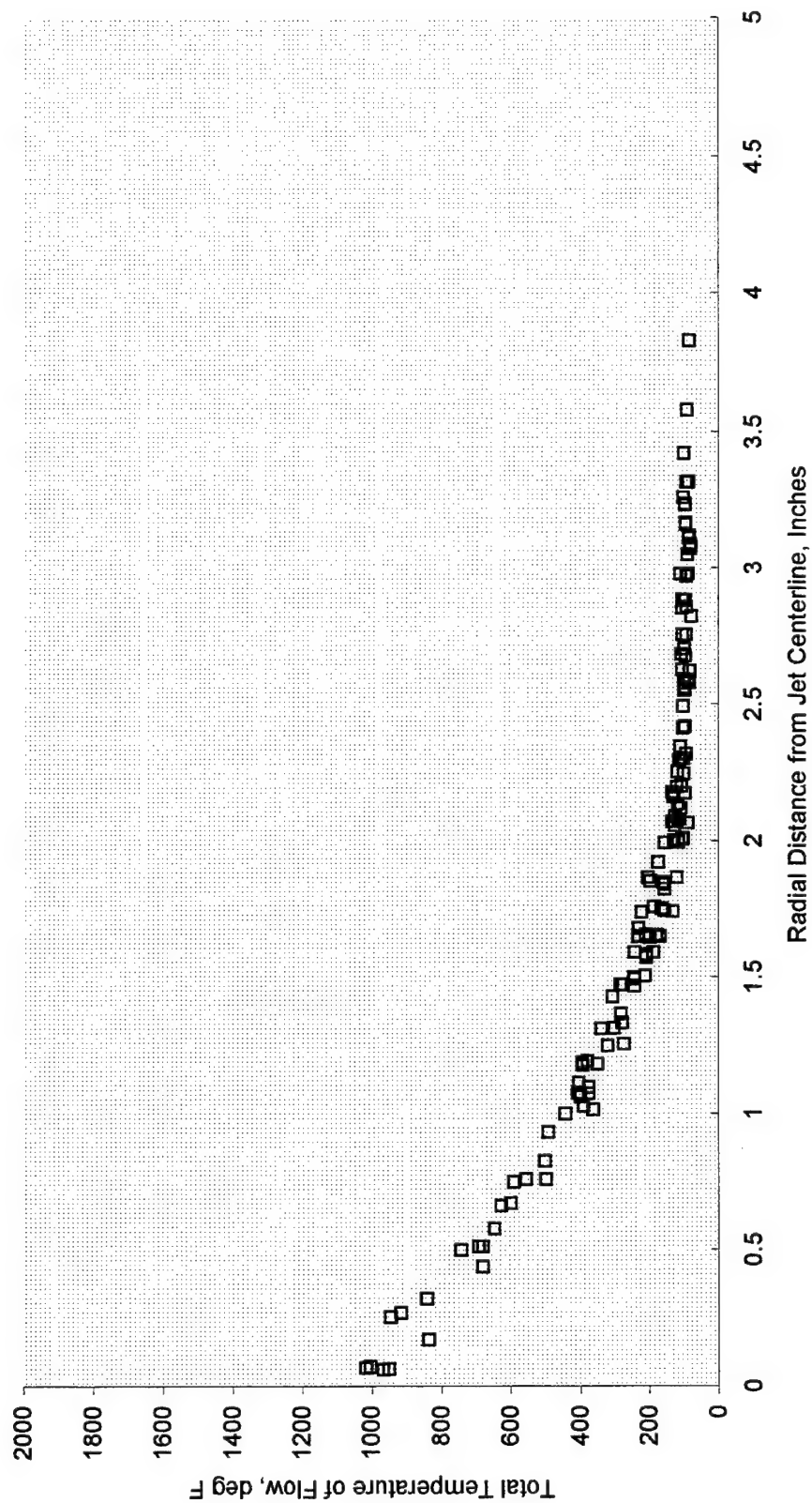


Figure 20. Profile of total temperature in attempted simulation of
F/A-18 APU exhaust plume, Z=6"

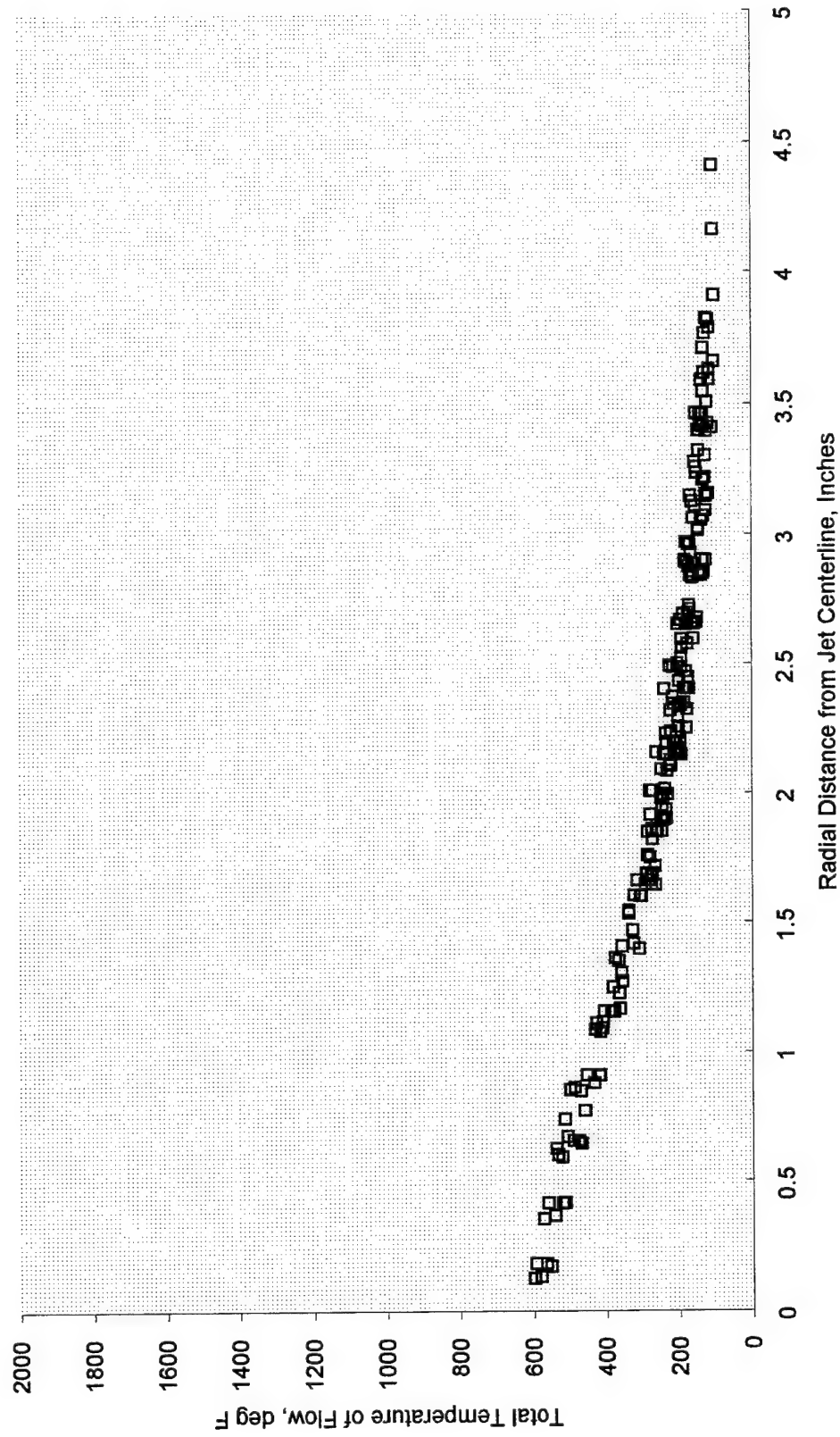


Figure 21. Profile of total temperature in attempted simulation of
F/A-18 APU exhaust flow, Z=12"

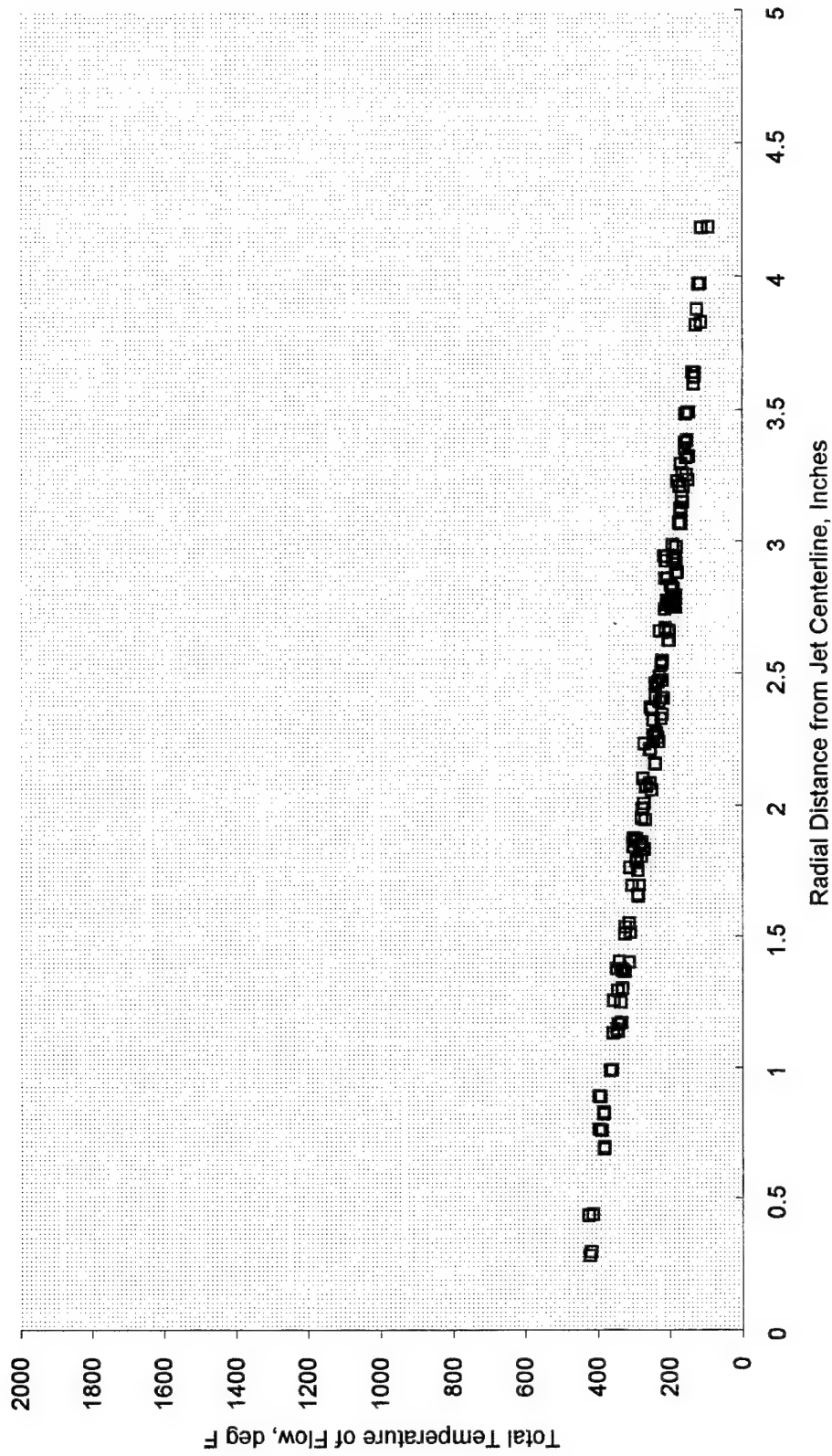


Figure 22. Profile of total temperature in attempted simulation of F/A-18 APU exhaust plume, Z=18"

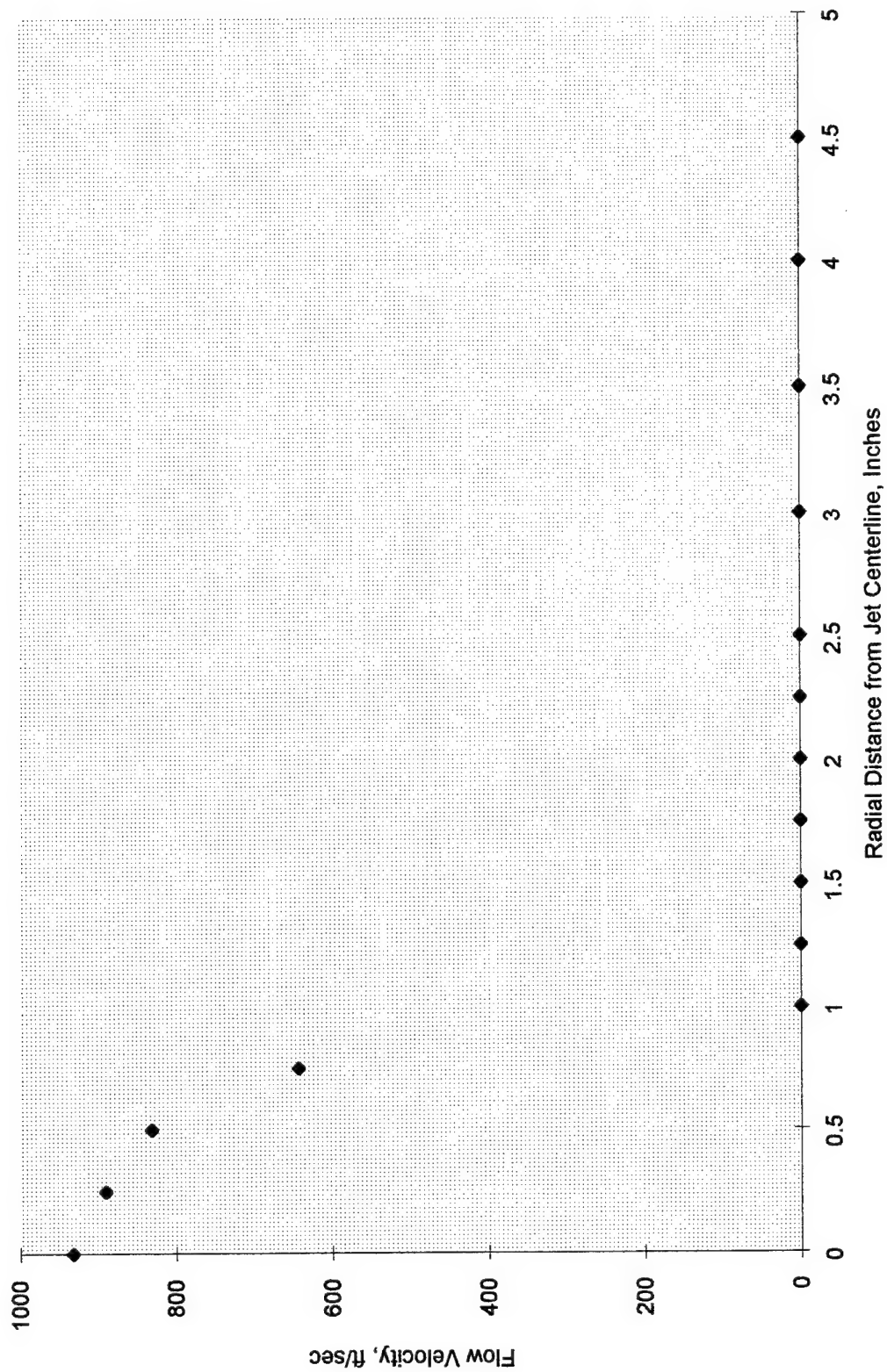


Figure 23. Profile of velocity in attempted simulation of F/A-18 APU exhaust plume, $Z=0.5$ "

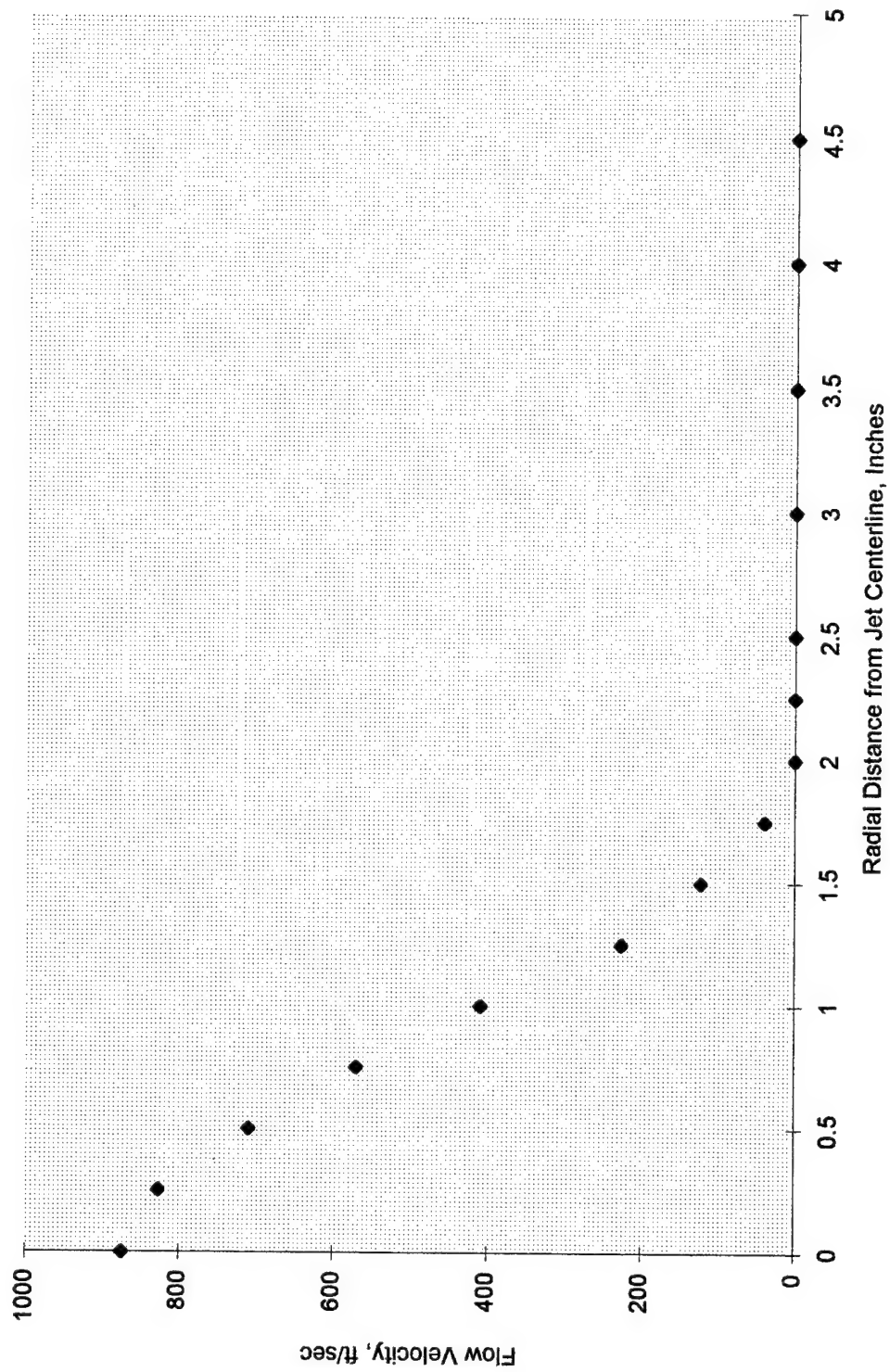


Figure 24. Profile of velocity in attempted simulation of F/A-18 APU exhaust plume, Z=6"

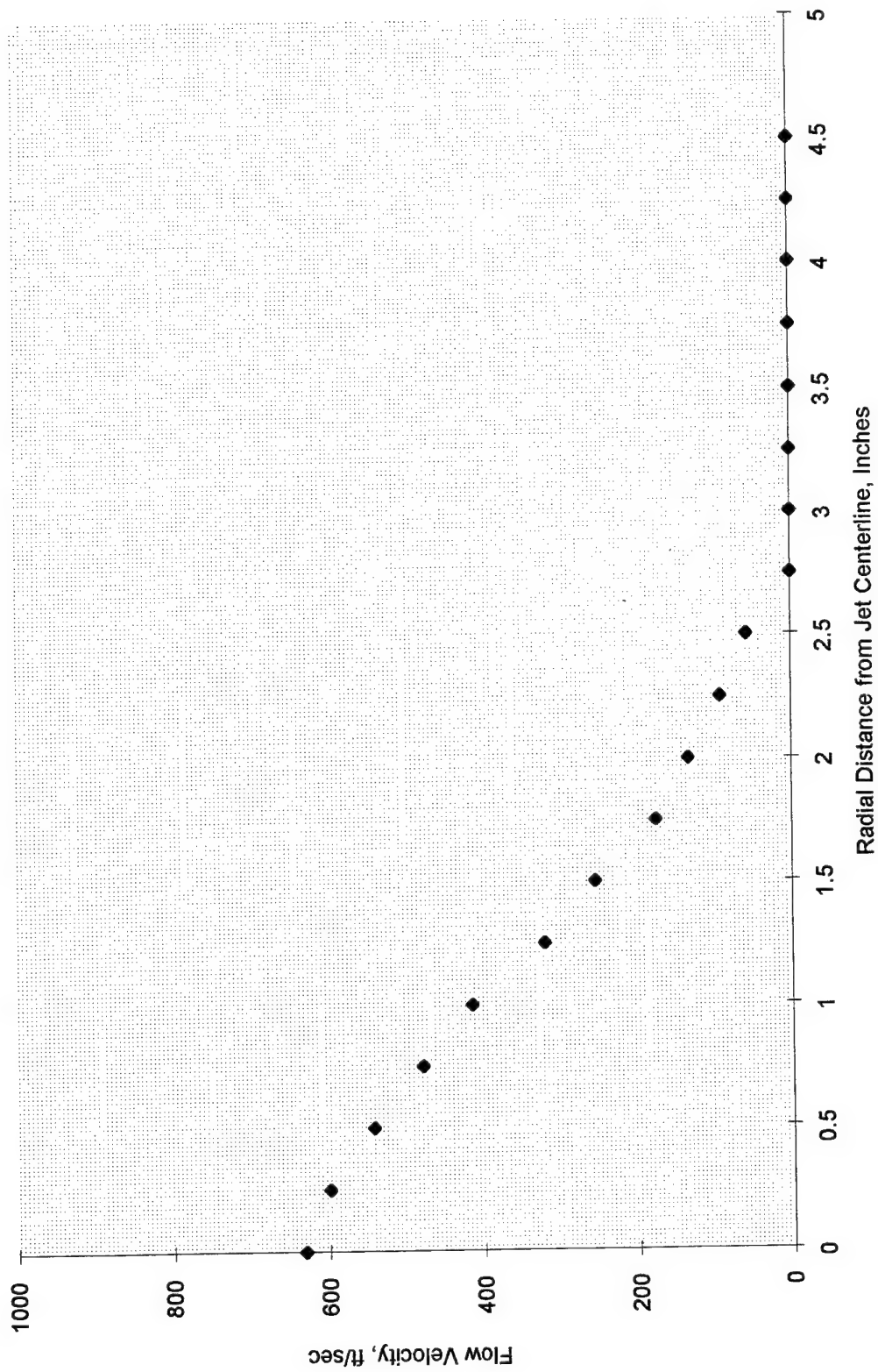


Figure 25. Profile of velocity in attempted simulation of F/A-18 APU exhaust plume, Z=12"

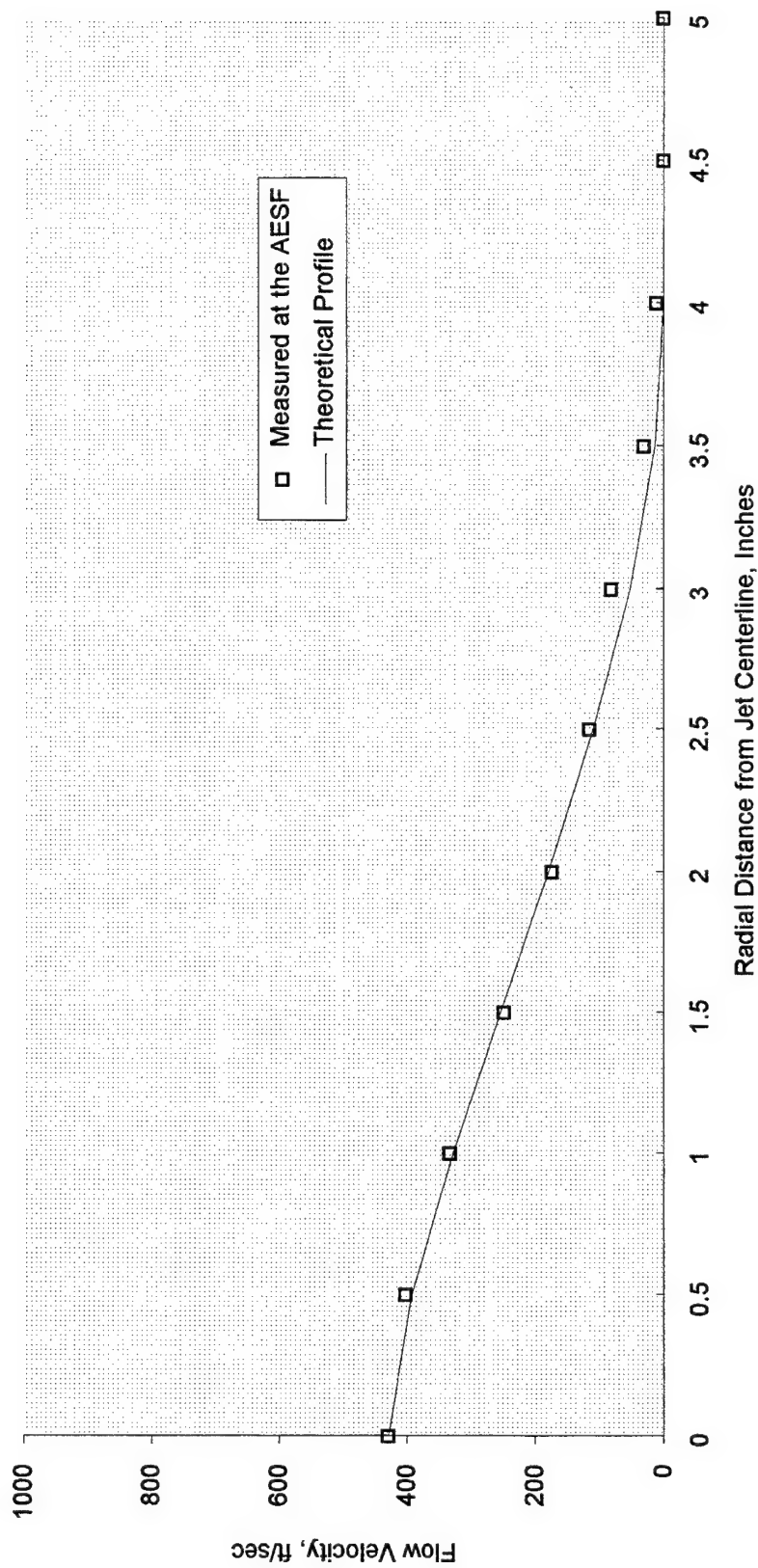


Figure 26. Profile of velocity in attempted simulation of F/A-18 APU exhaust plume, Z=18"

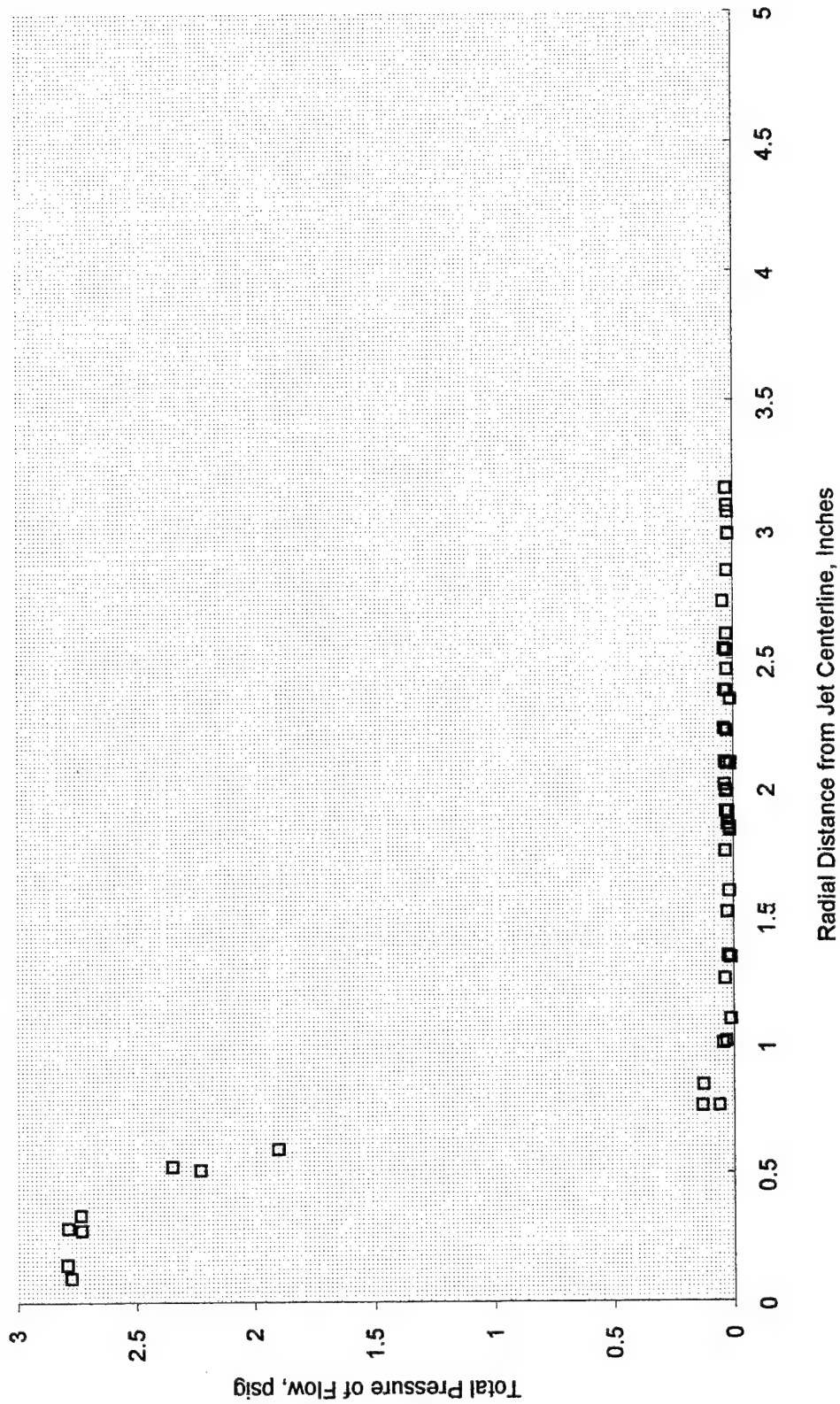


Figure 27. Profile of total pressure in attempted simulation of AV-8B exhaust plume, $Z=0.5$ "

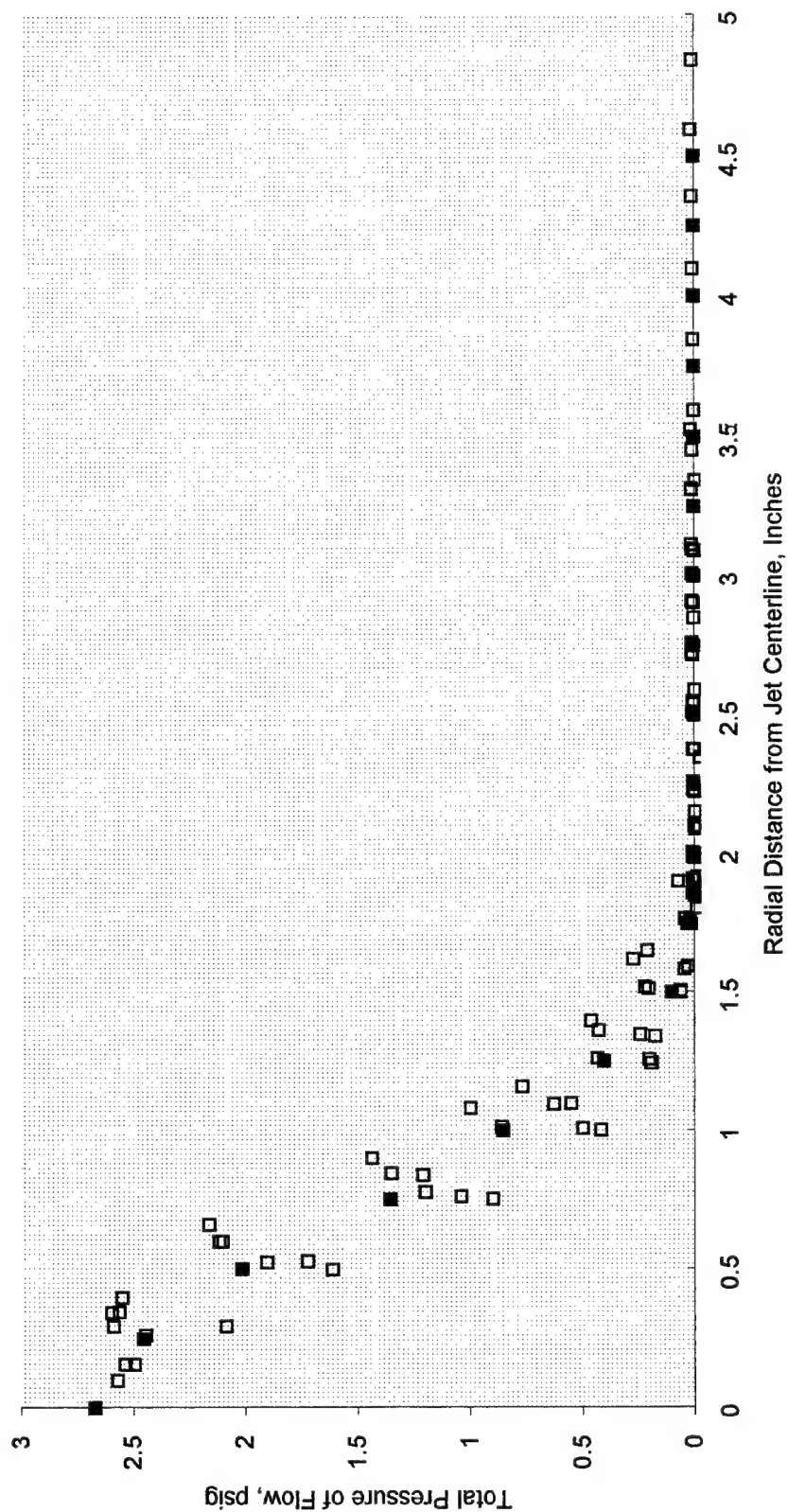


Figure 28. Profile of total pressure in attempted simulation of AV-8B exhaust plume, Z=6"

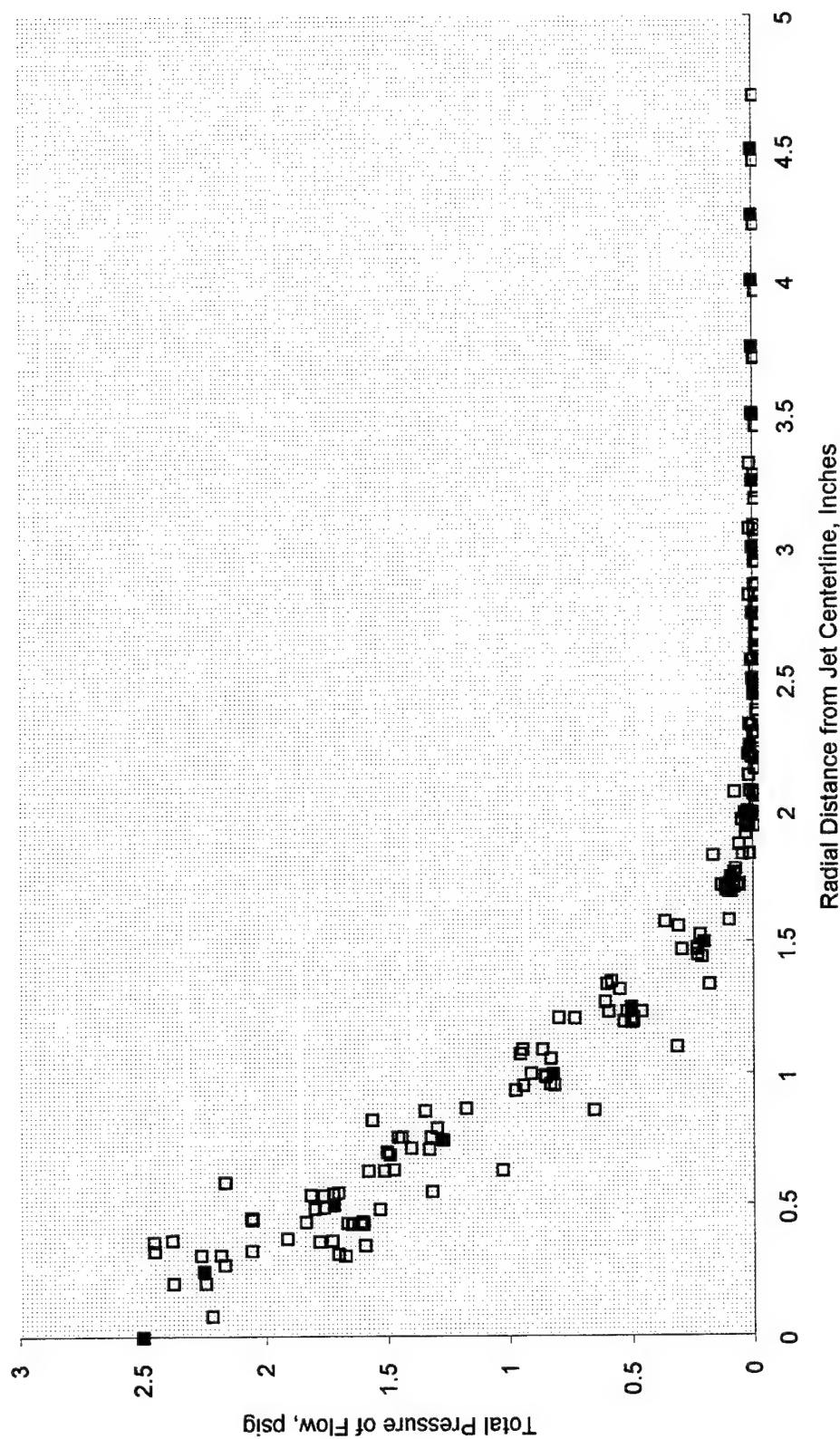


Figure 29. Profile of total pressure in attempted simulation of AV-8B exhaust plume, Z=9"

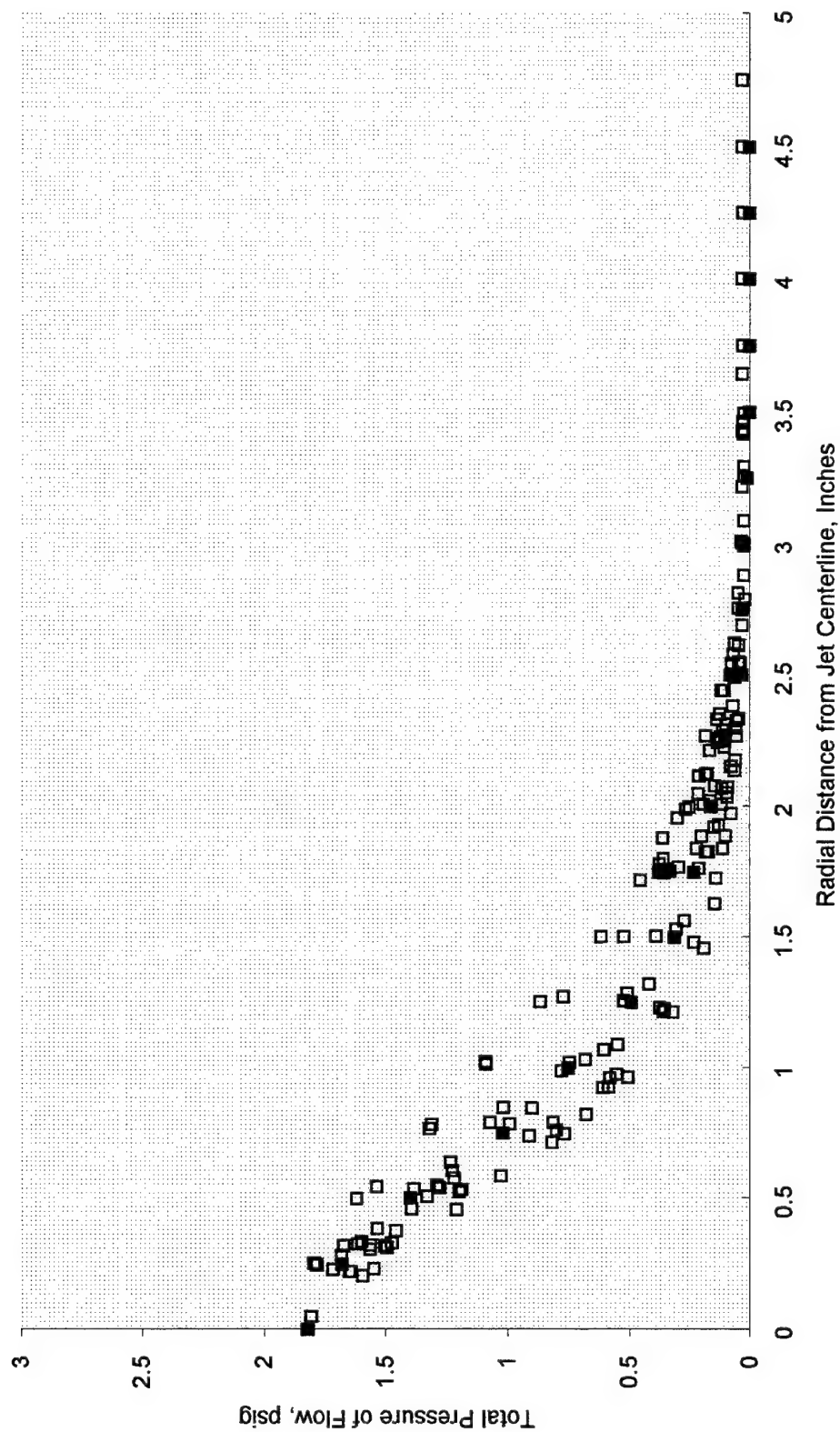


Figure 30. Profile of total pressure in attempted simulation of
AV-8B Exhaust Plume, Z=12"

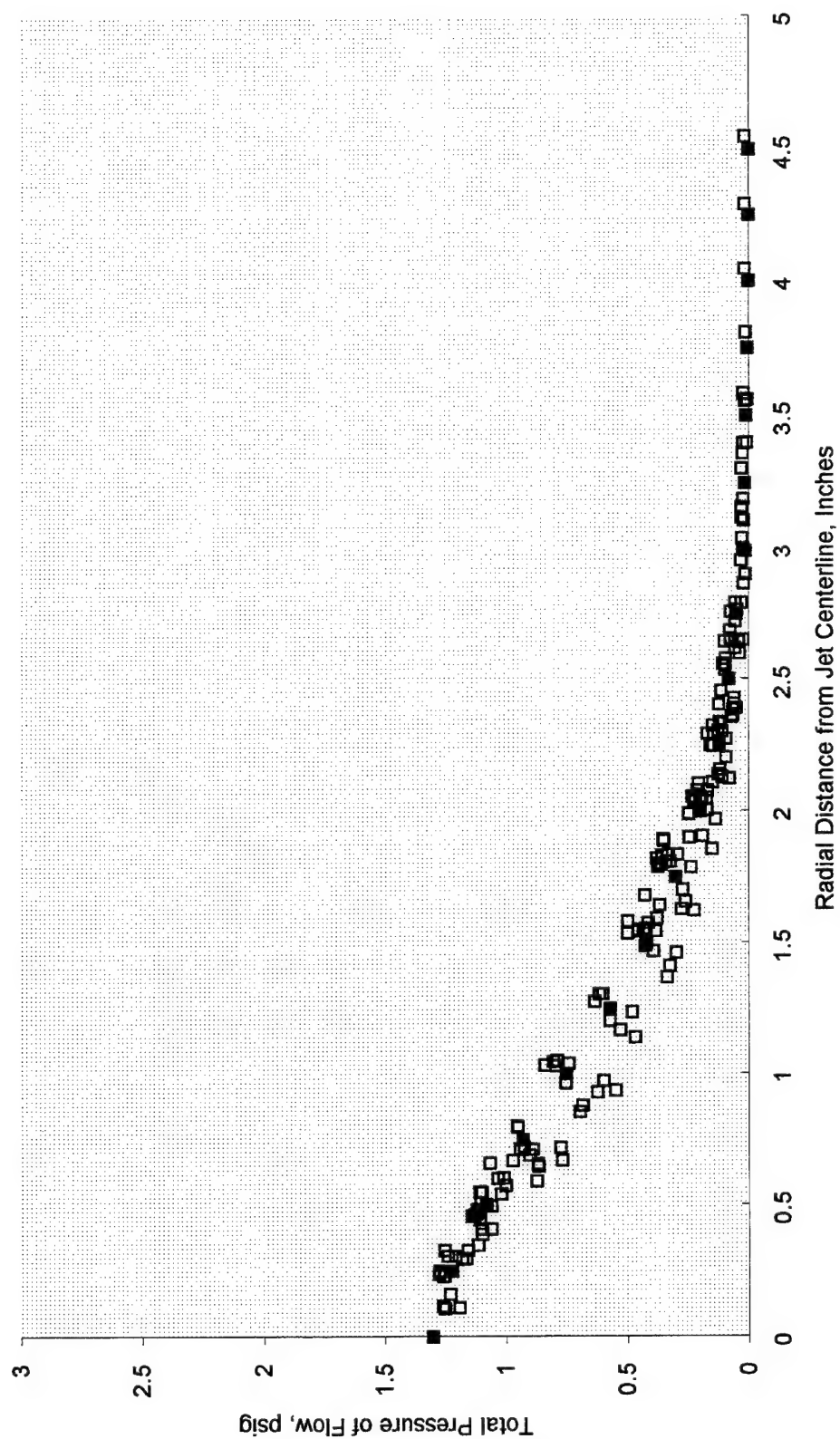


Figure 31. Profile of total pressure in attempted simulation of AV-8B exhaust plume, Z=15"

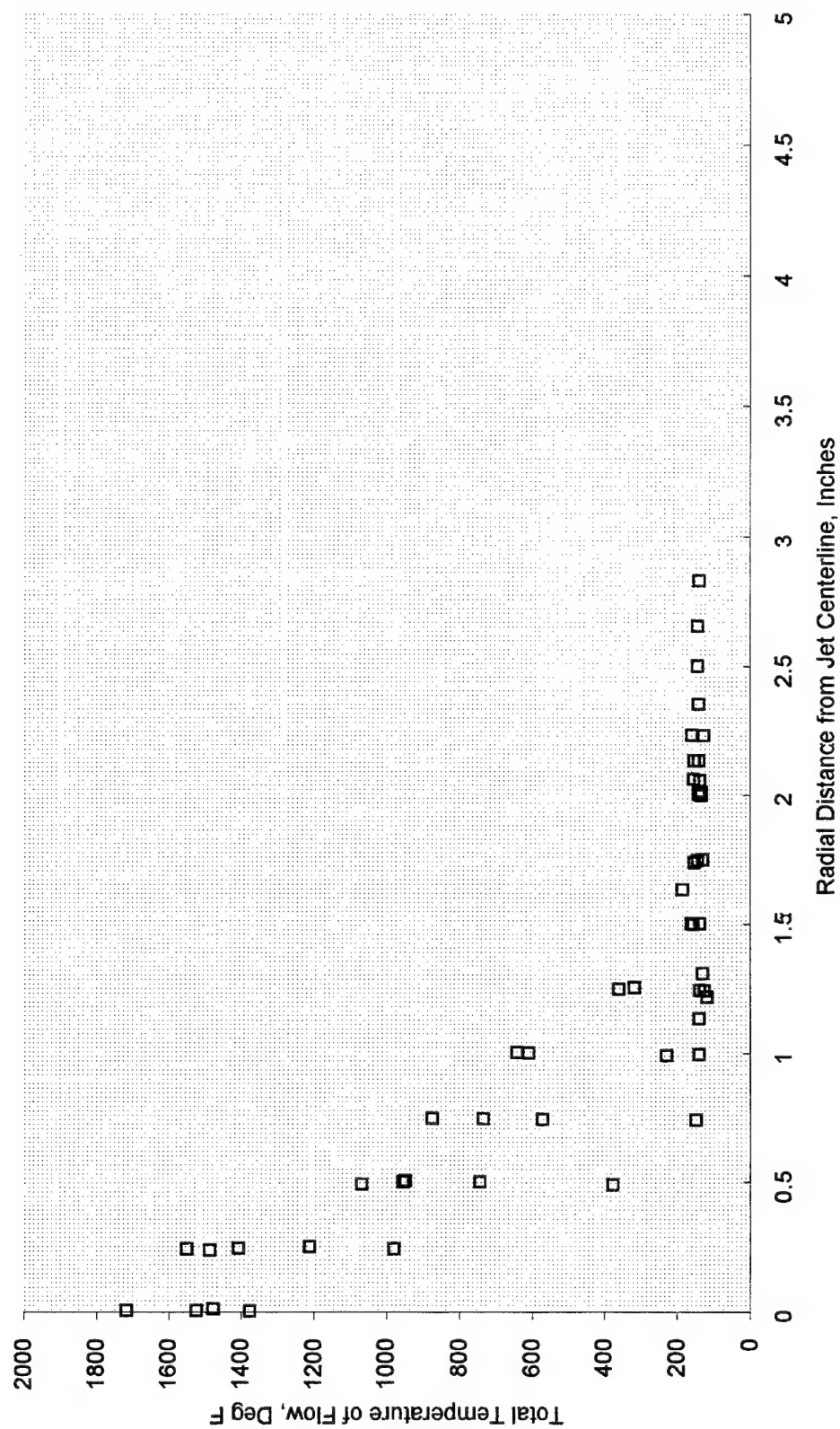


Figure 32. Profile of total temperature in attempted simulation of AV-8B exhaust plume, Z=0.5"

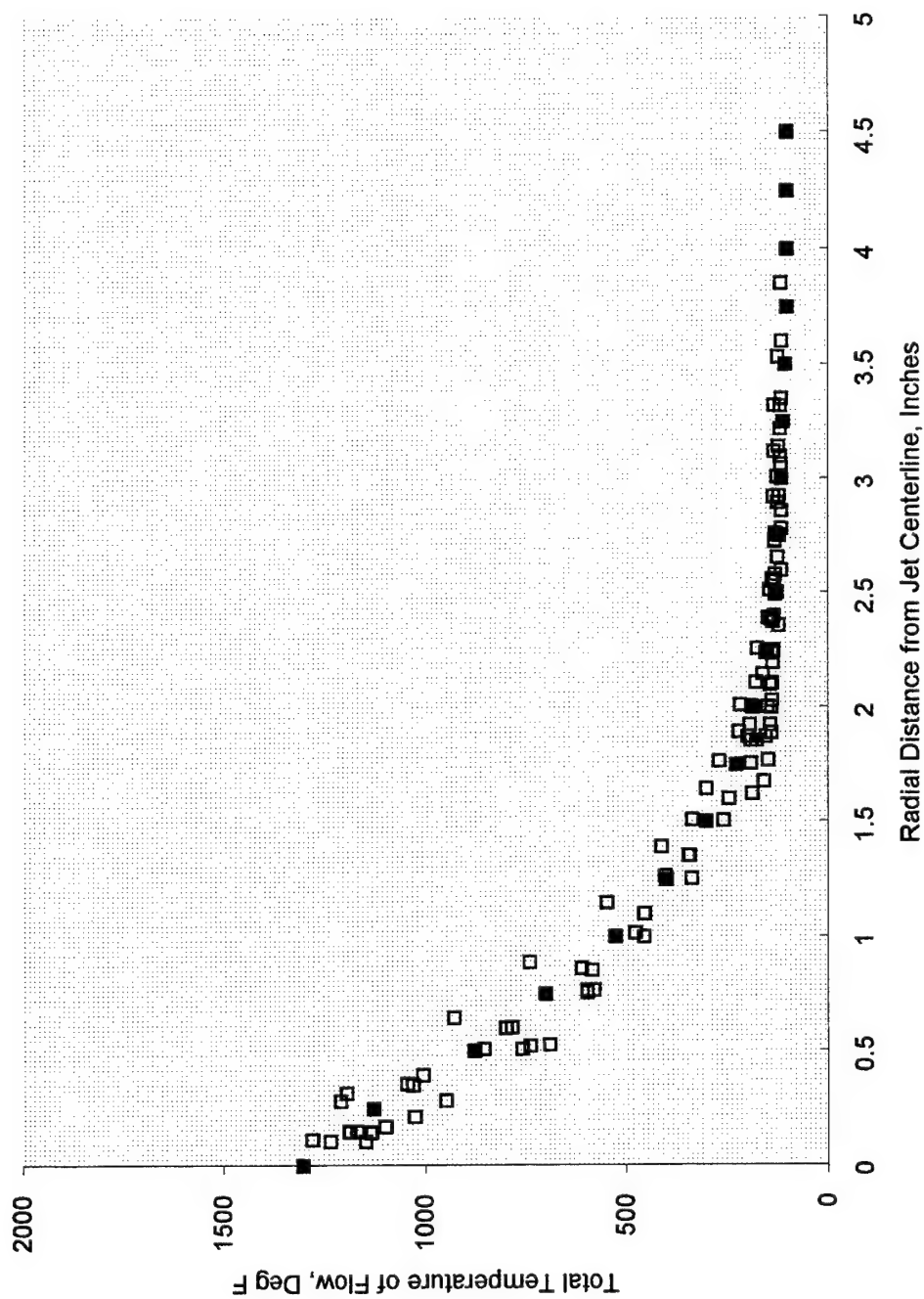


Figure 33. Profile of total temperature in attempted simulation of
AV-8B exhaust plume, Z=6"

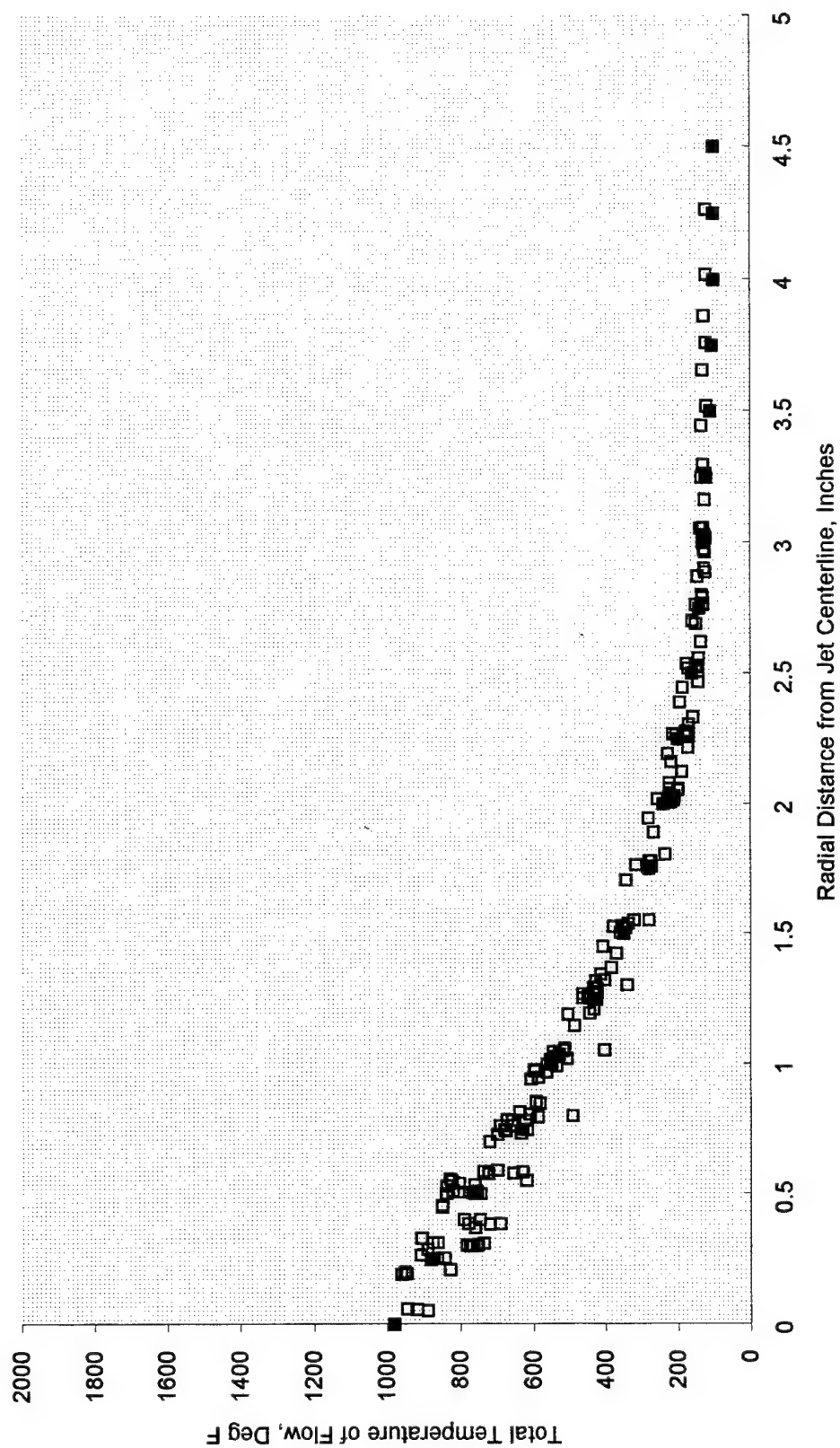


Figure 34. Profile of total temperature in attempted simulation of AV-8B Exhaust Plume, Z=9"

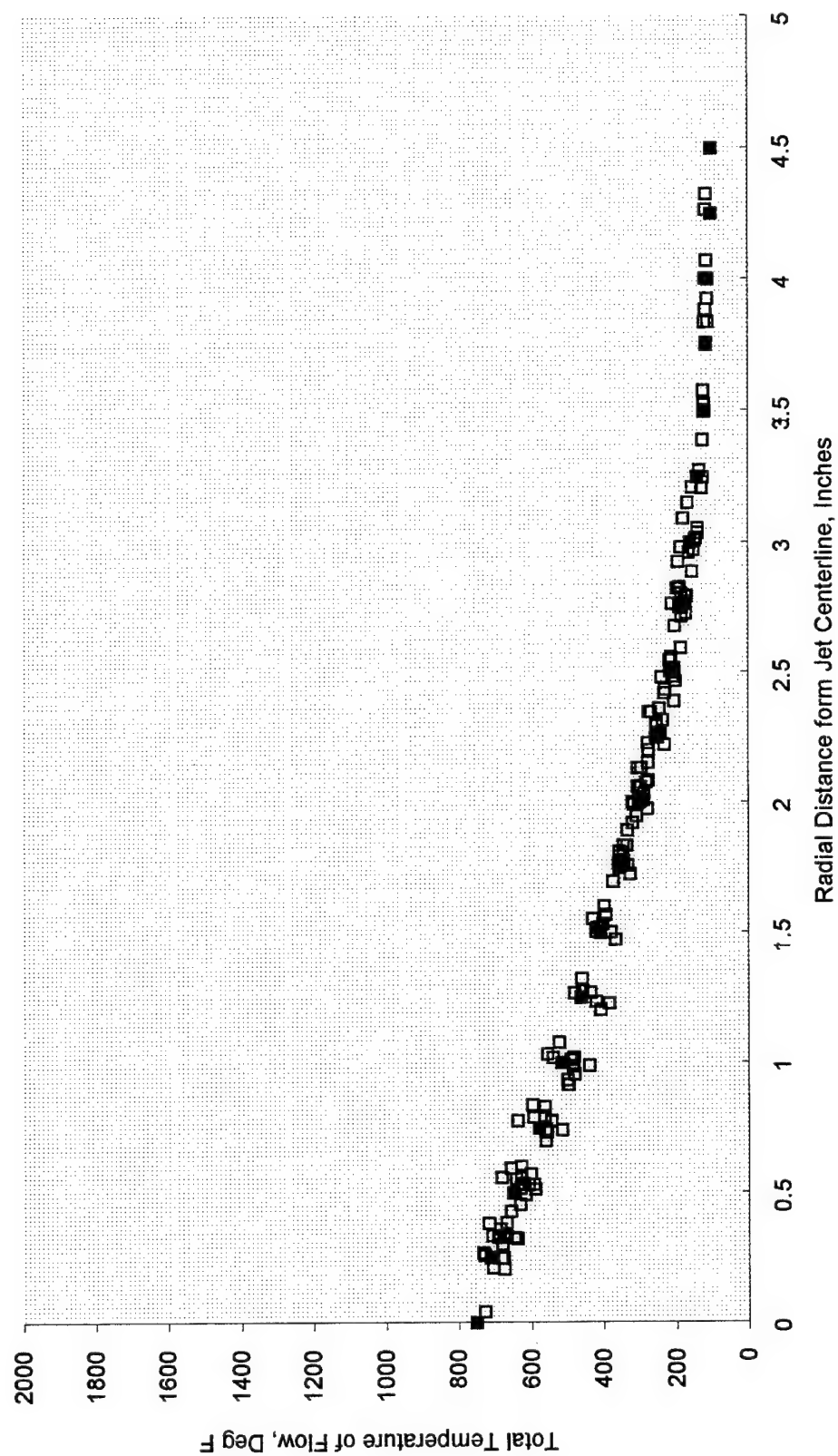


Figure 35. Profile of total temperature in attempted simulation of AV-8B Exhaust Plume, Z=12"

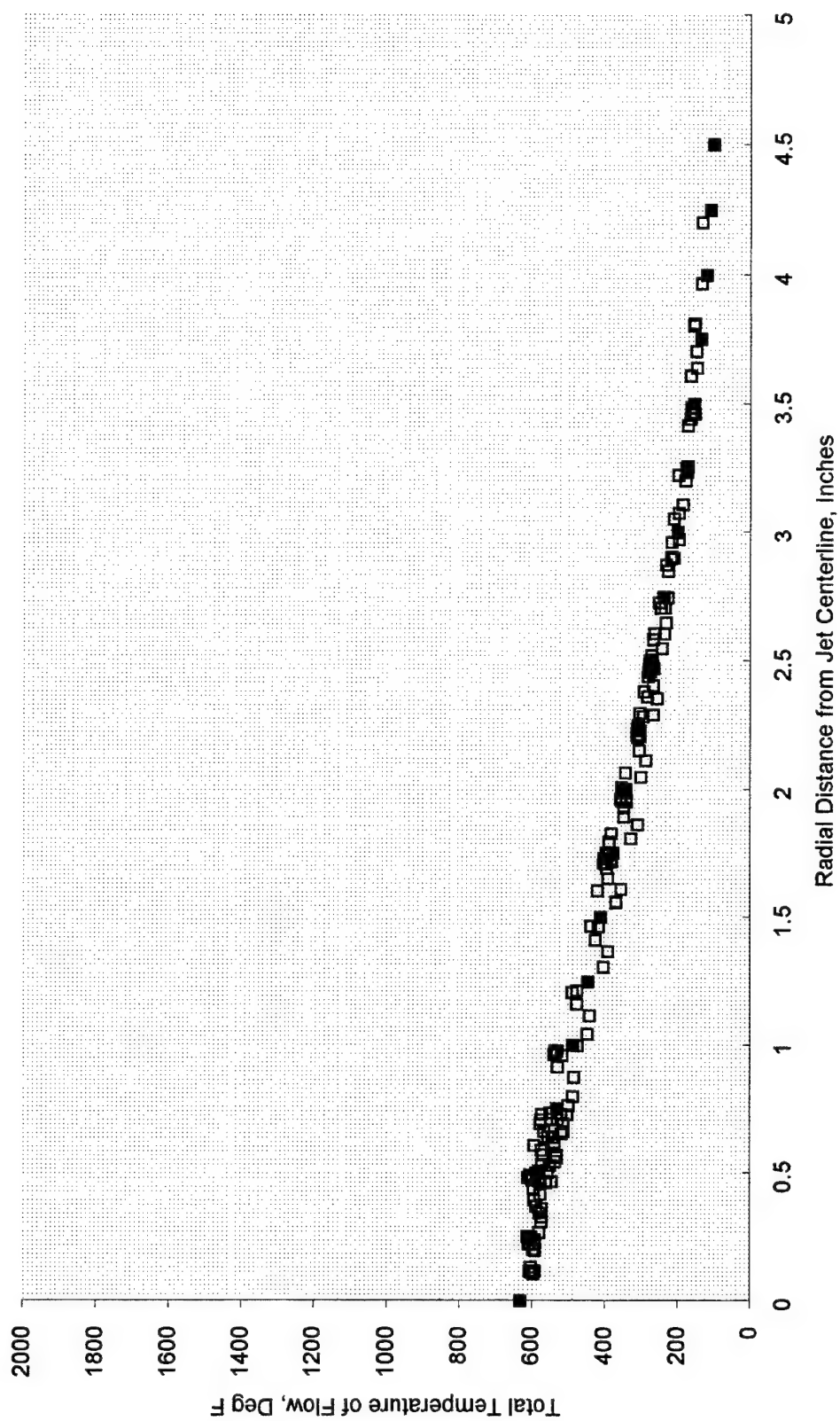


Figure 36. Profile of total temperature in attempted simulation of AV-8B exhaust plume, Z=15"

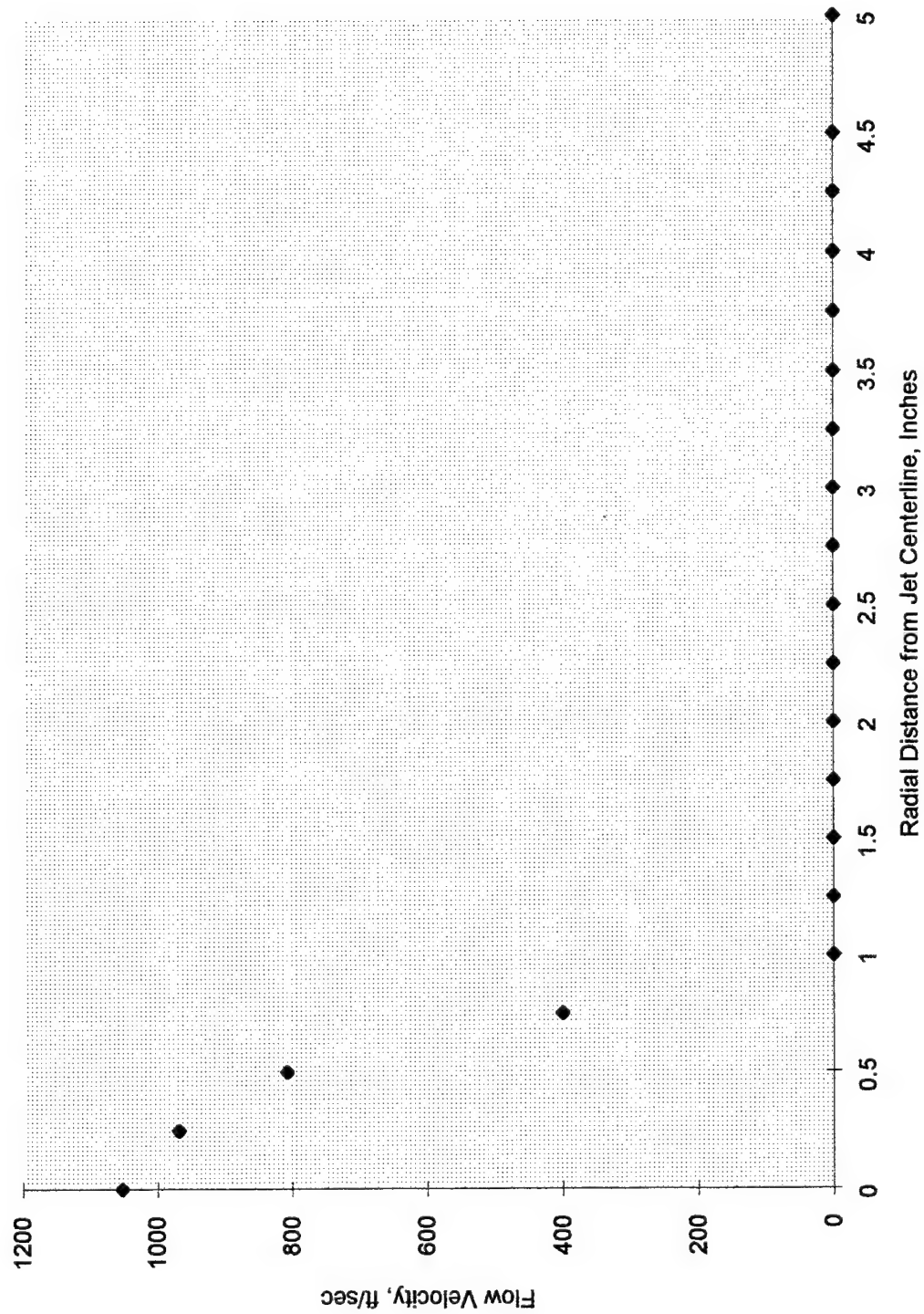


Figure 37. Profile of velocity in attempted simulation of AV-8B exhaust plume, $Z=0.5''$

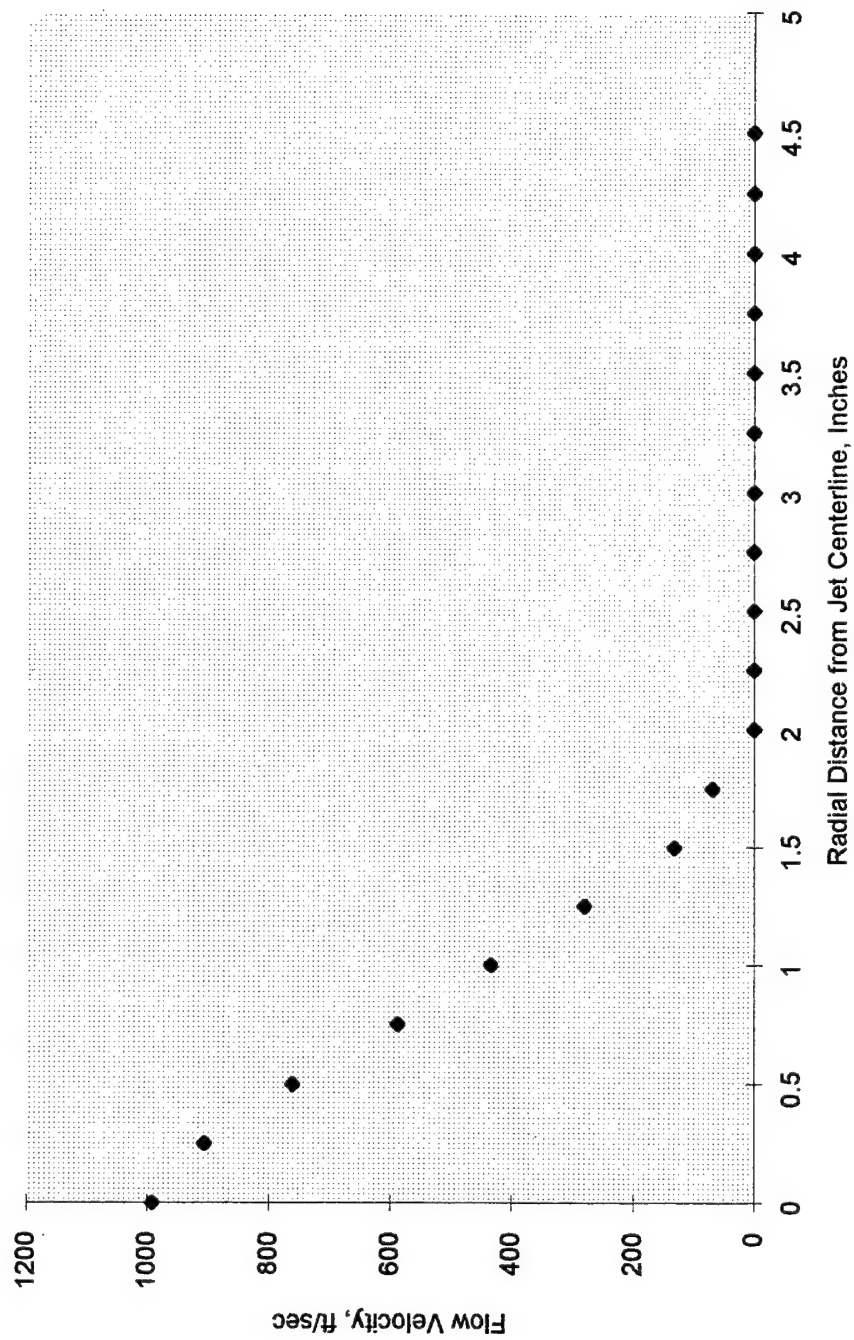


Figure 38. Profile of velocity in attempted simulation of AV-8B exhaust plume, Z=6"

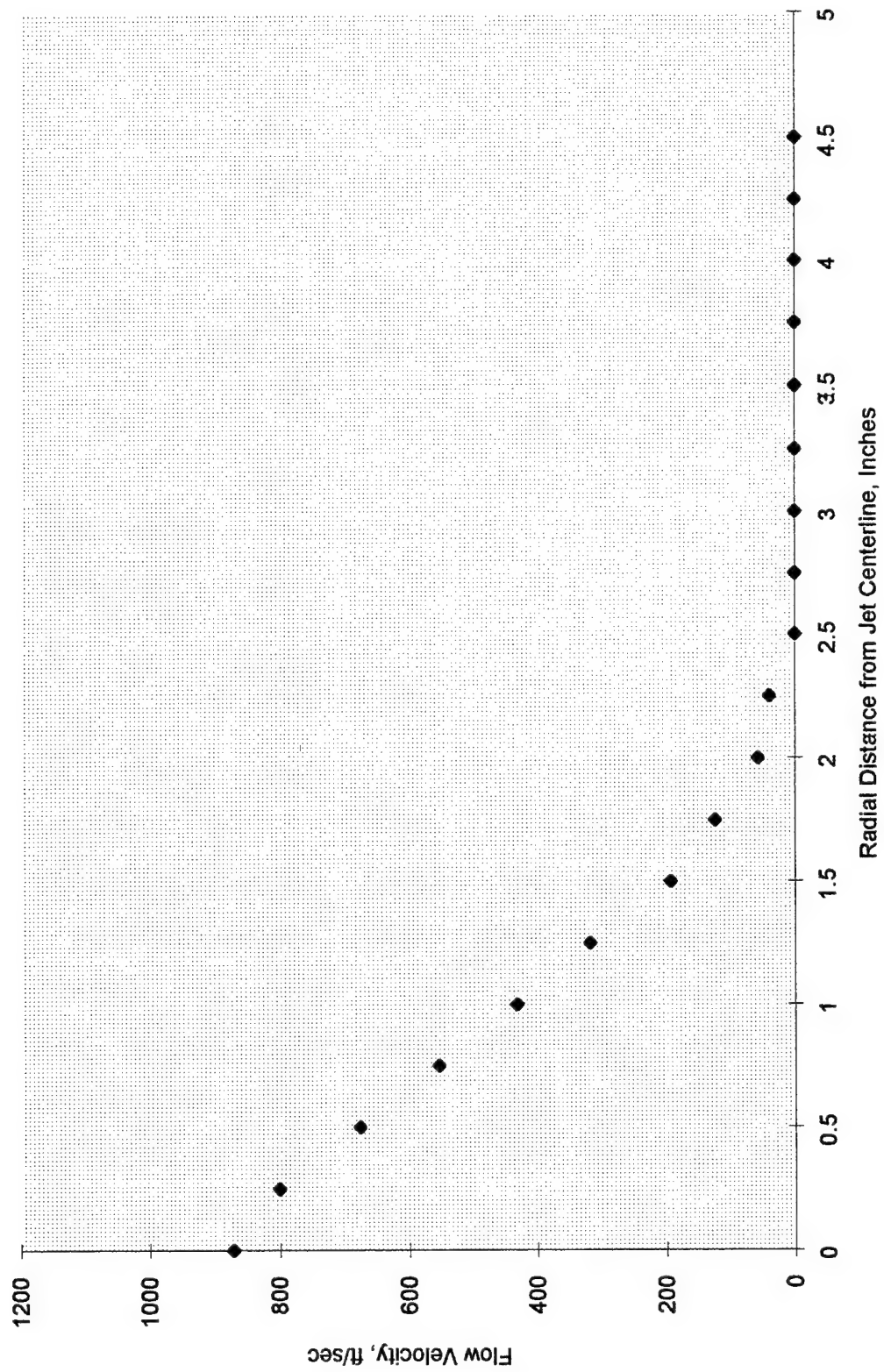


Figure 39. Profile of velocity in attempted simulation of AV-8B exhaust plume, Z=9"

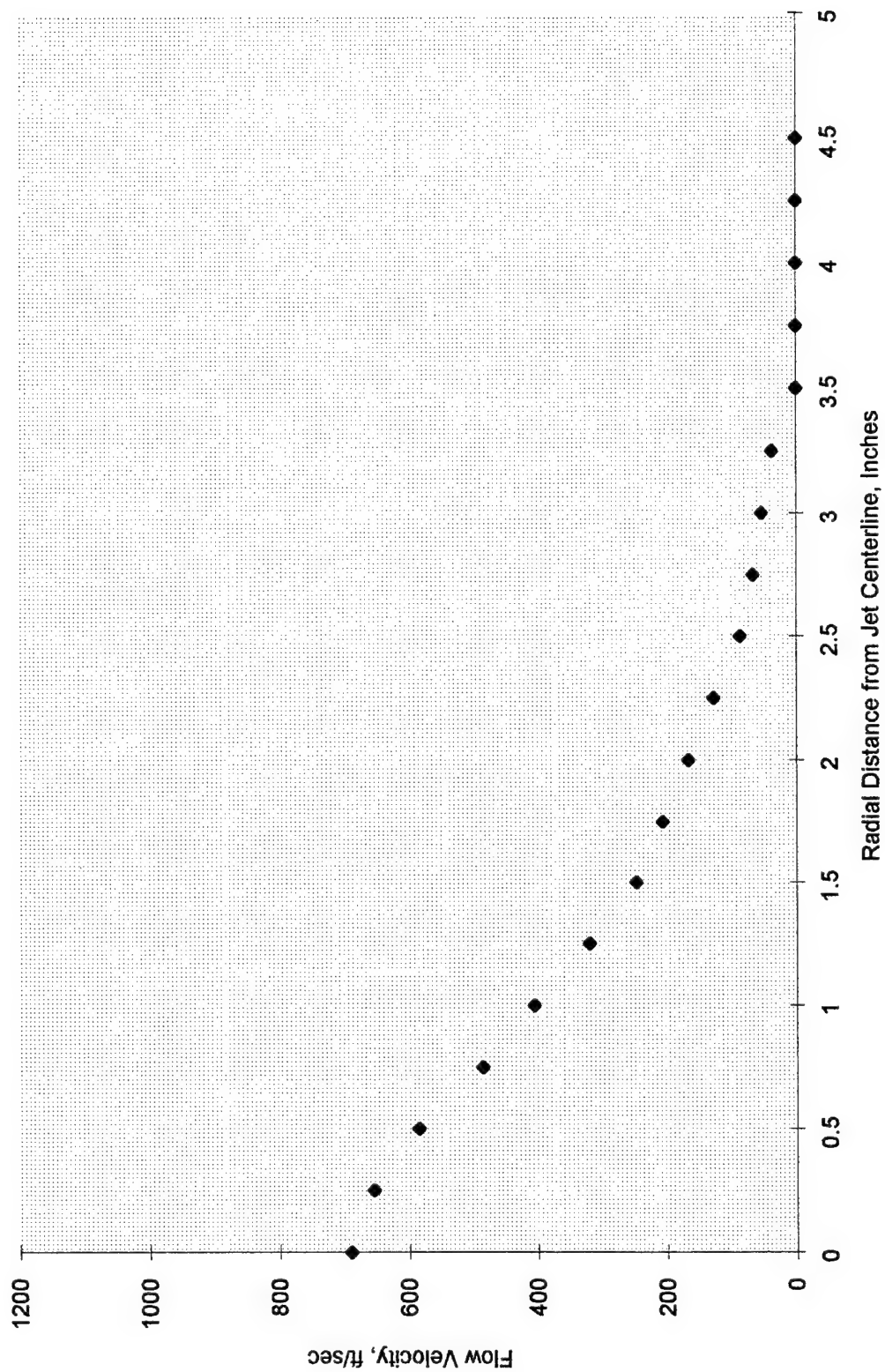


Figure 40. Profile Of velocity in attempted simulation of AV-8B exhaust plume, Z=12"

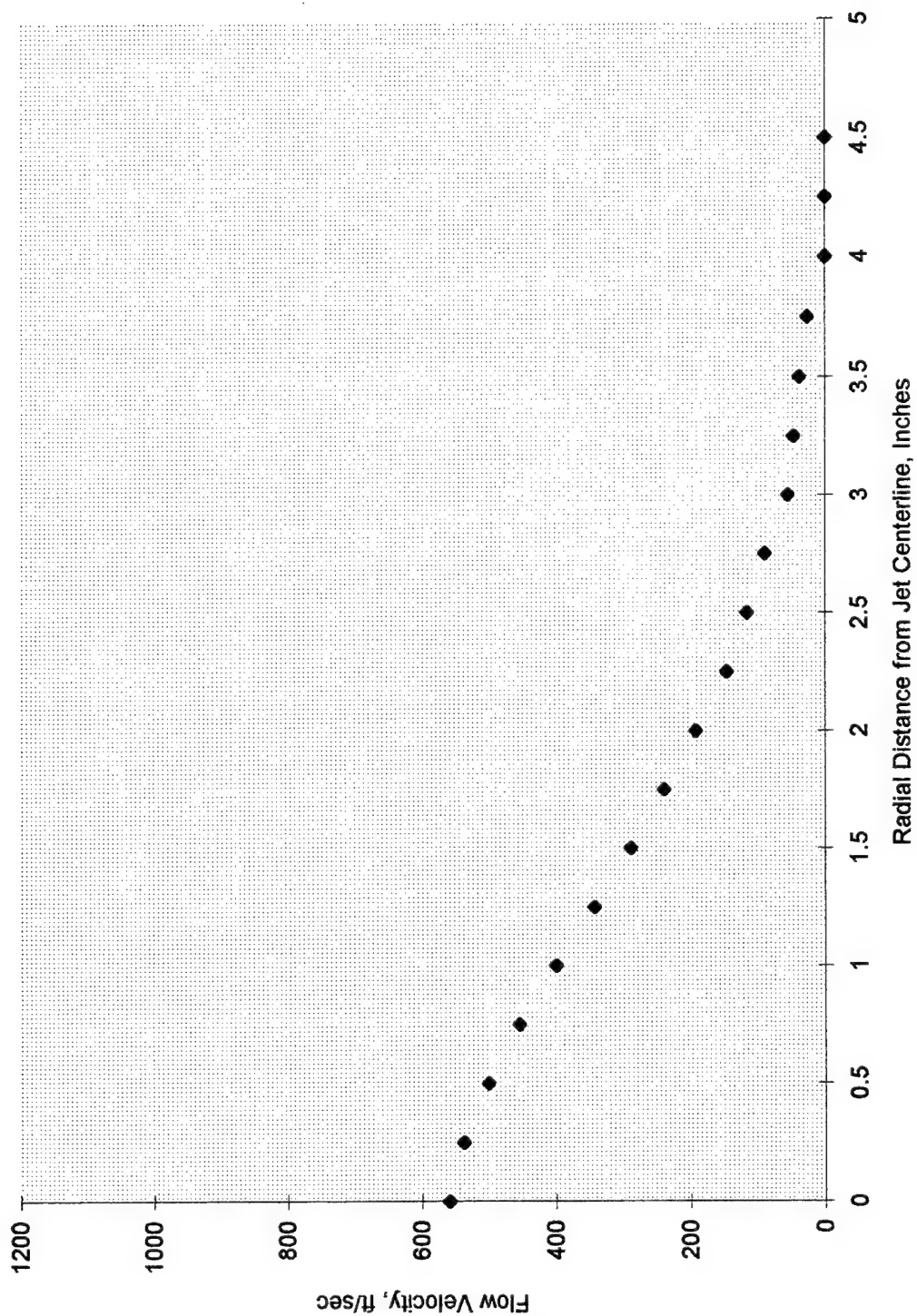


Figure 41. Profile of velocity in attempted simulation of AV-8B exhaust plume, Z=15"

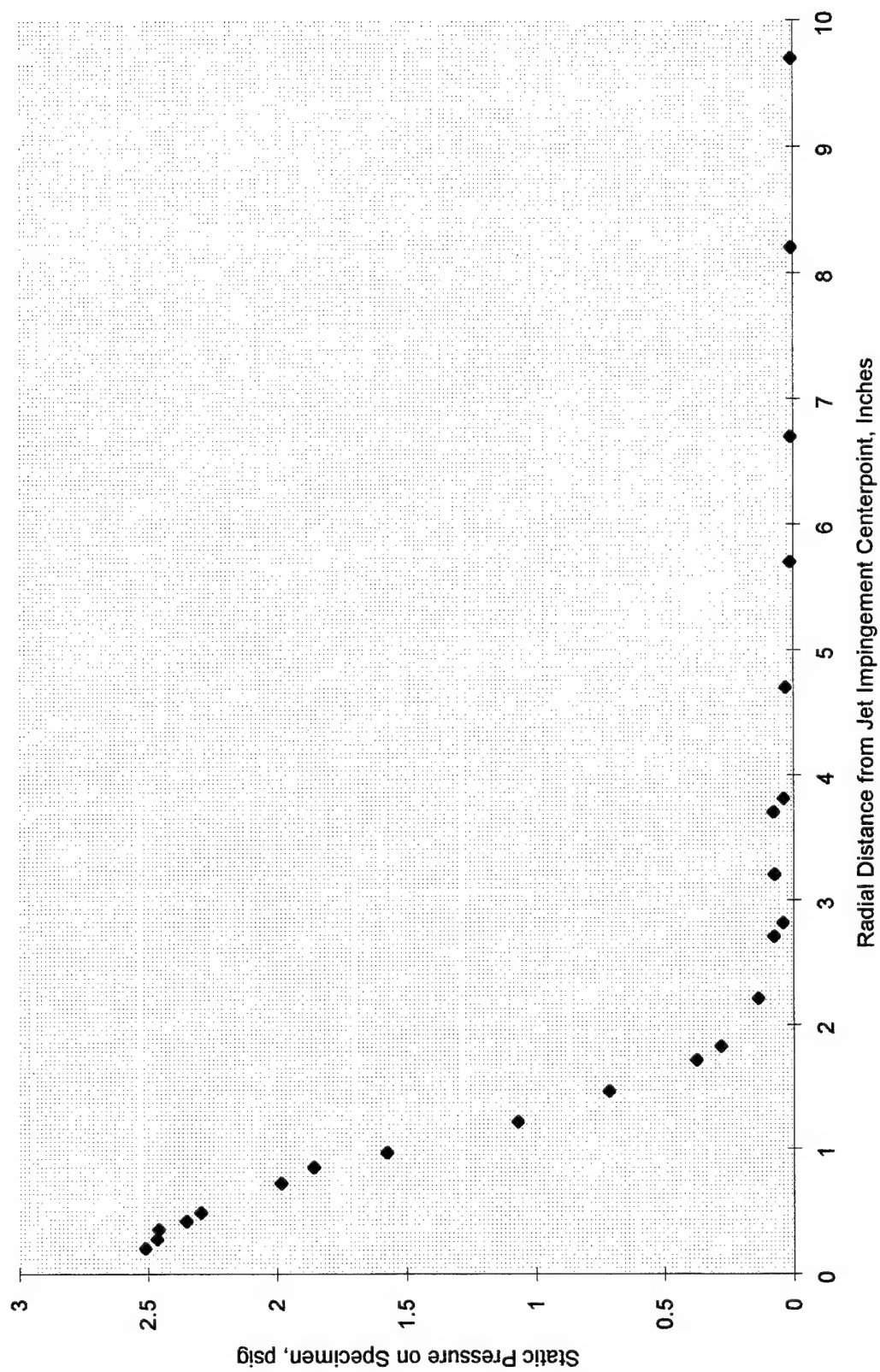


Figure 42: Static pressure as a function of distance from stagnation point on concrete specimens exposed to the simulated F/A-18 APU plume, Z=6"

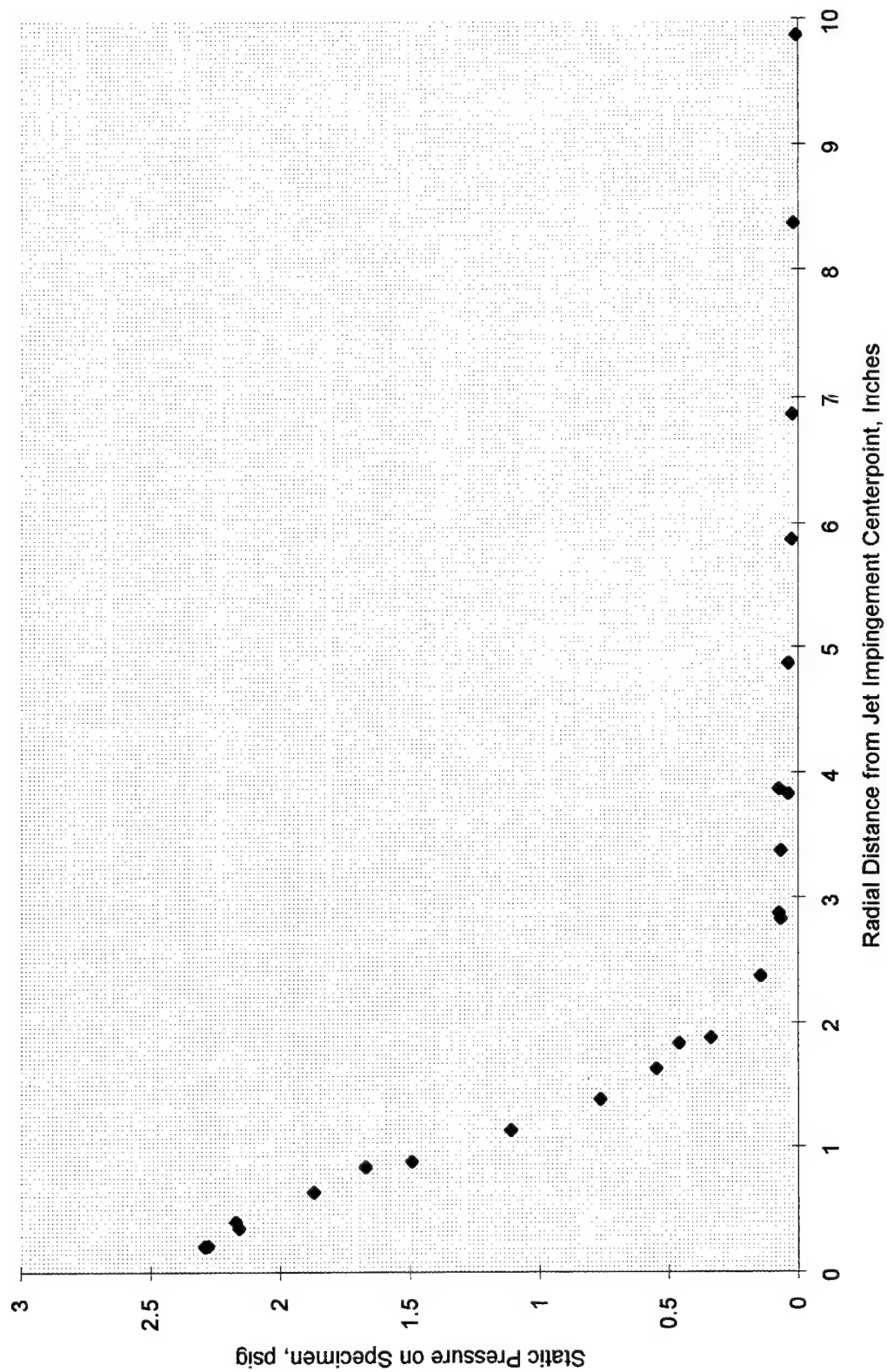


Figure 43: Static pressure as a function of distance from stagnation point on concrete specimens exposed to the simulated F/A-18 APU plume, Z=9"

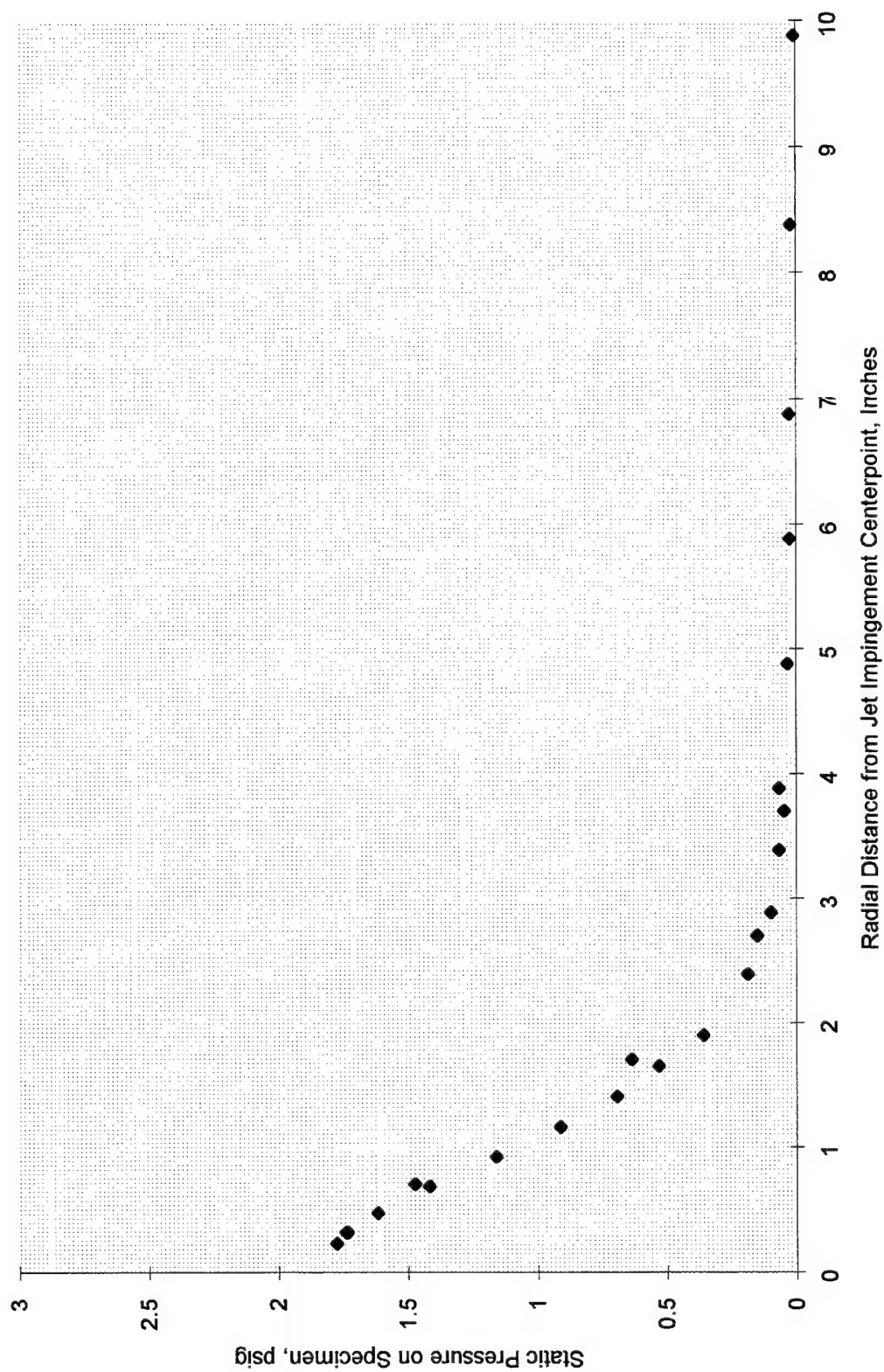


Figure 44: Static pressure as a function of distance from stagnation point on concrete specimens exposed to the simulated F/A-18 APU plume, Z=12"

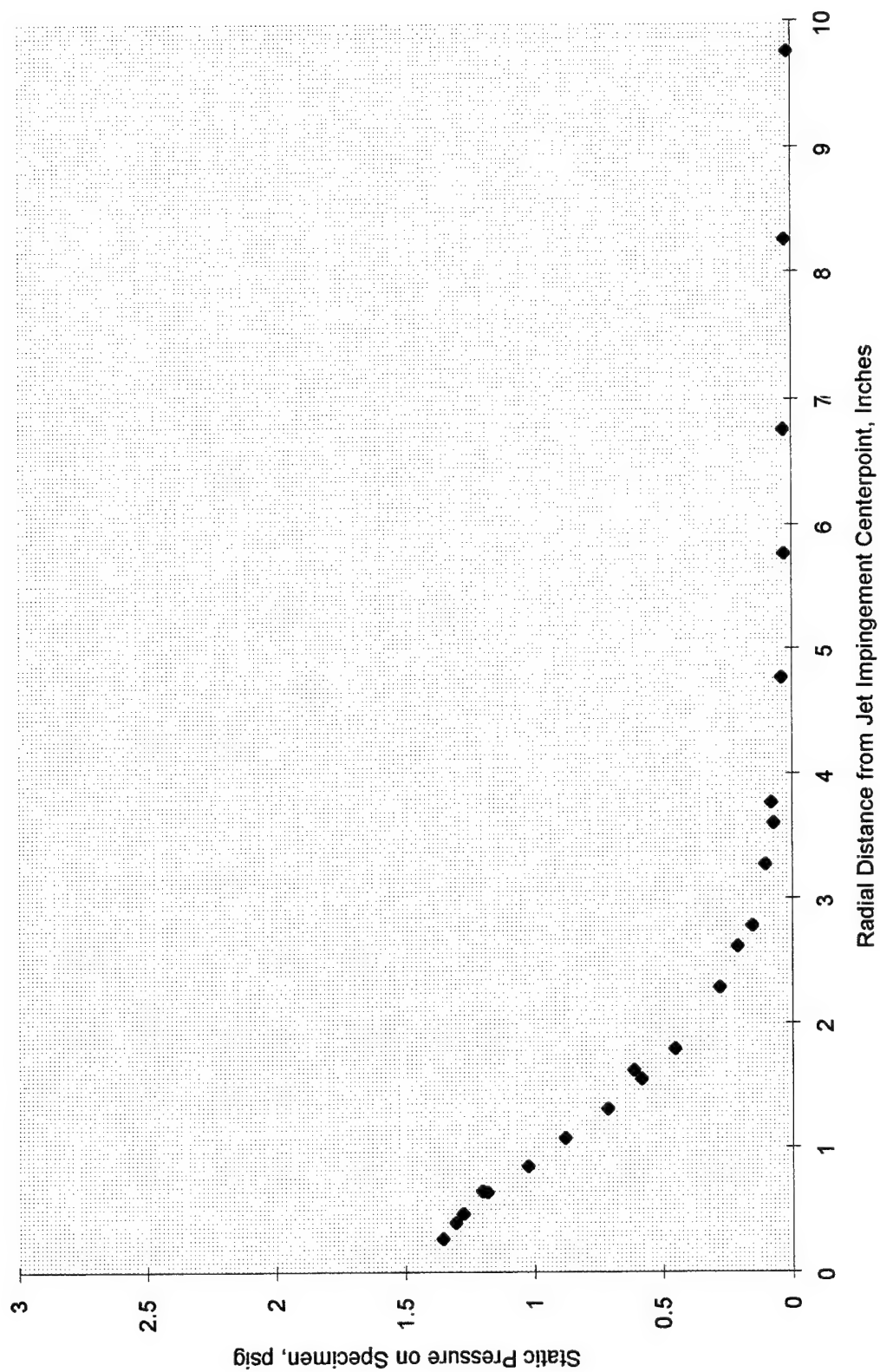


Figure 45: Static pressure as a function of distance from stagnation point on concrete specimens exposed to the simulated F/A-18 APU plume, $Z=15"$

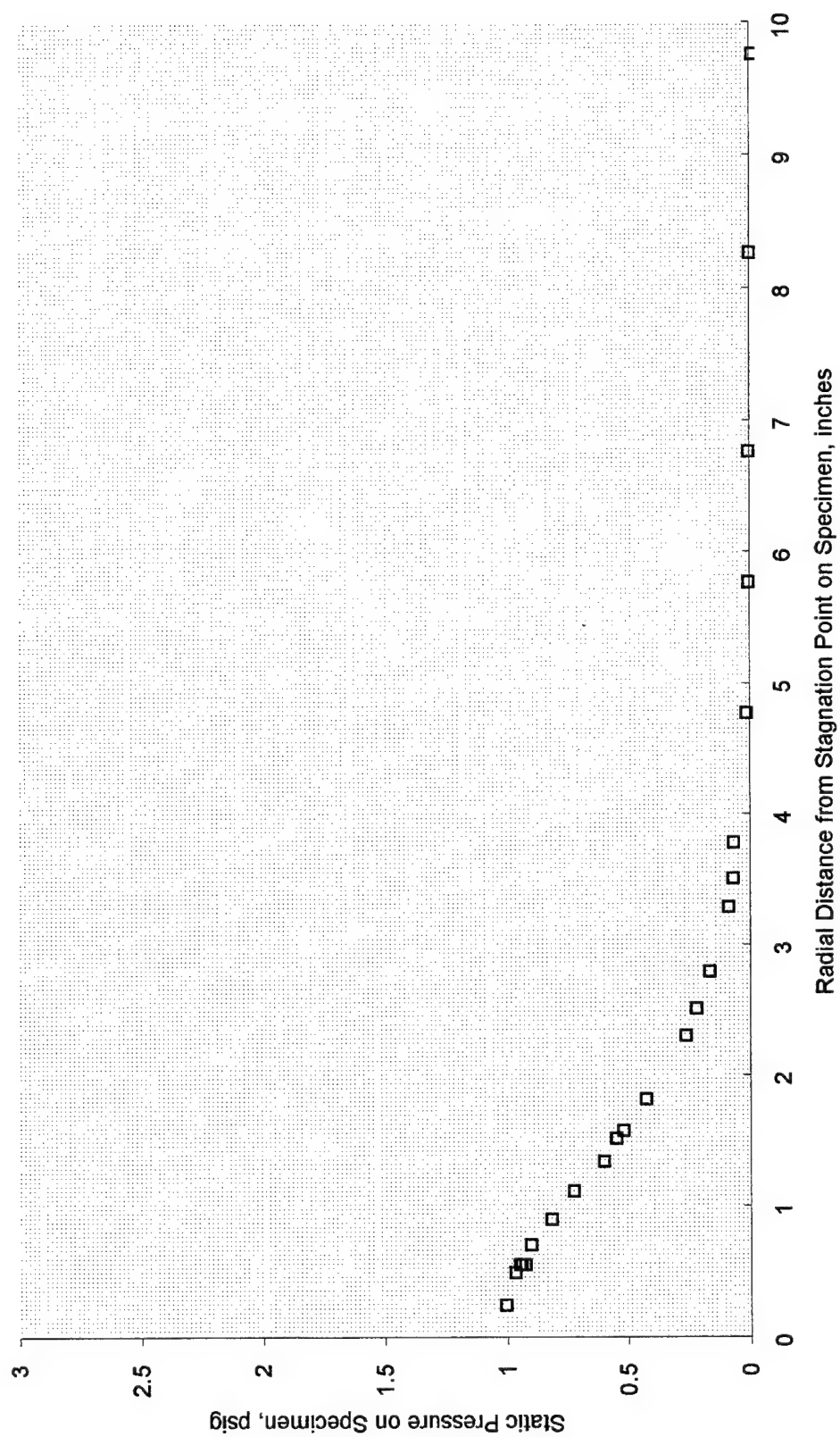


Figure 46. Static pressure as a function of distance from stagnation point on concrete specimens exposed to the simulated F/A-18 APU plume, $Z=18"$

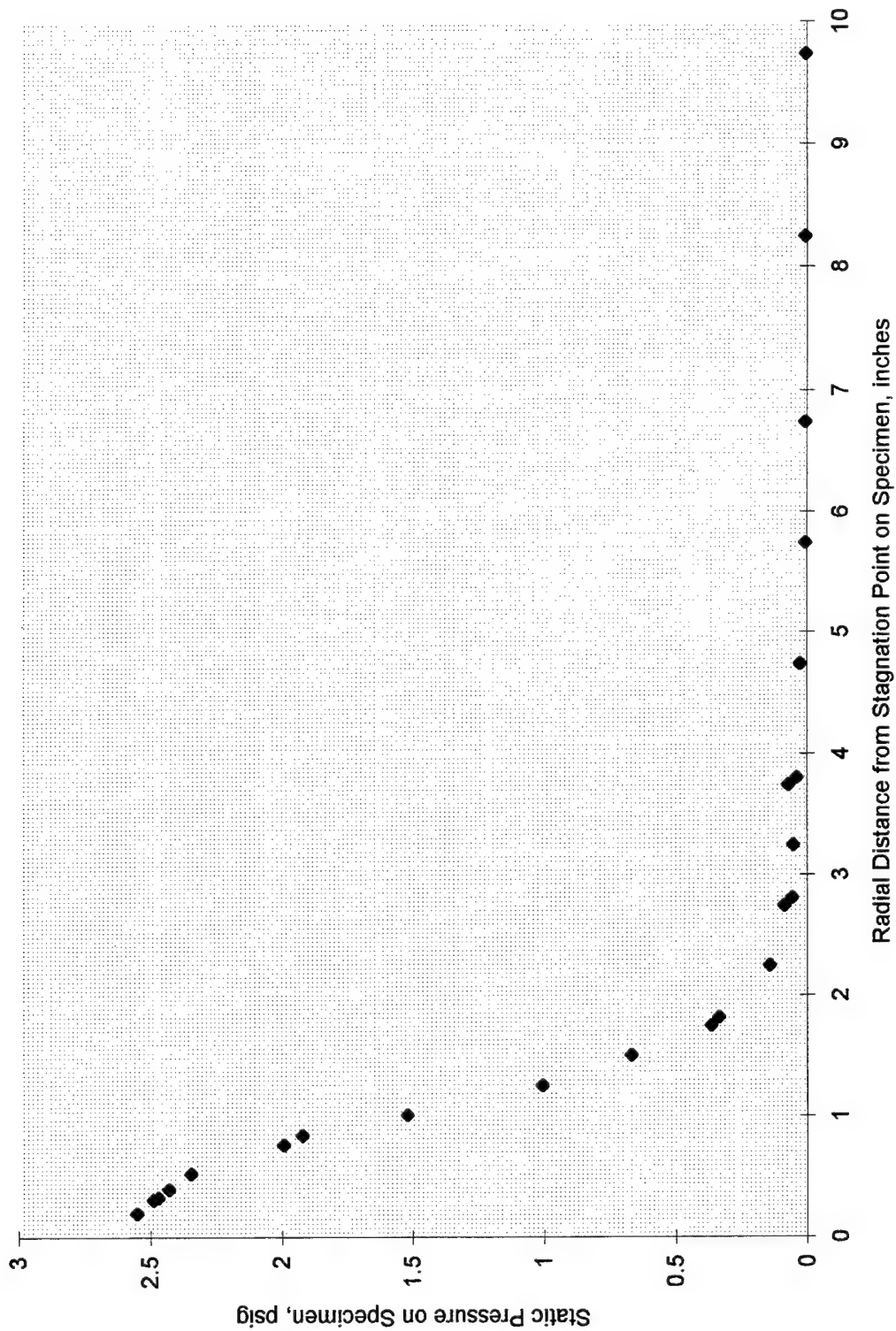


Figure 47. Static pressure as a function of distance from stagnation point on concrete specimens exposed to the simulated AV-8B plume, Z=6"

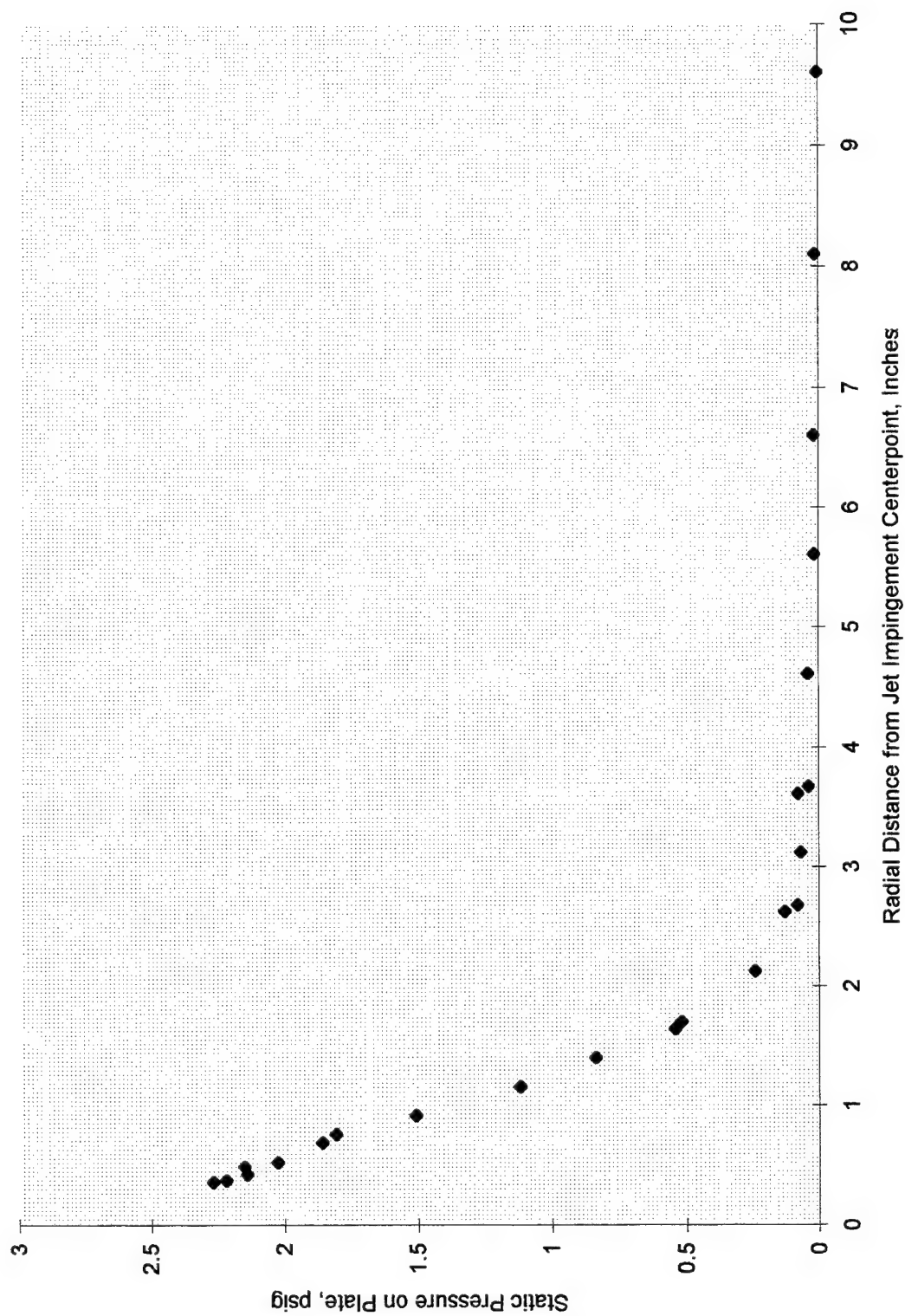


Figure 48: Static pressure as a function of distance from stagnation point on concrete specimens exposed to the simulated AV-8B plume, $Z=9''$

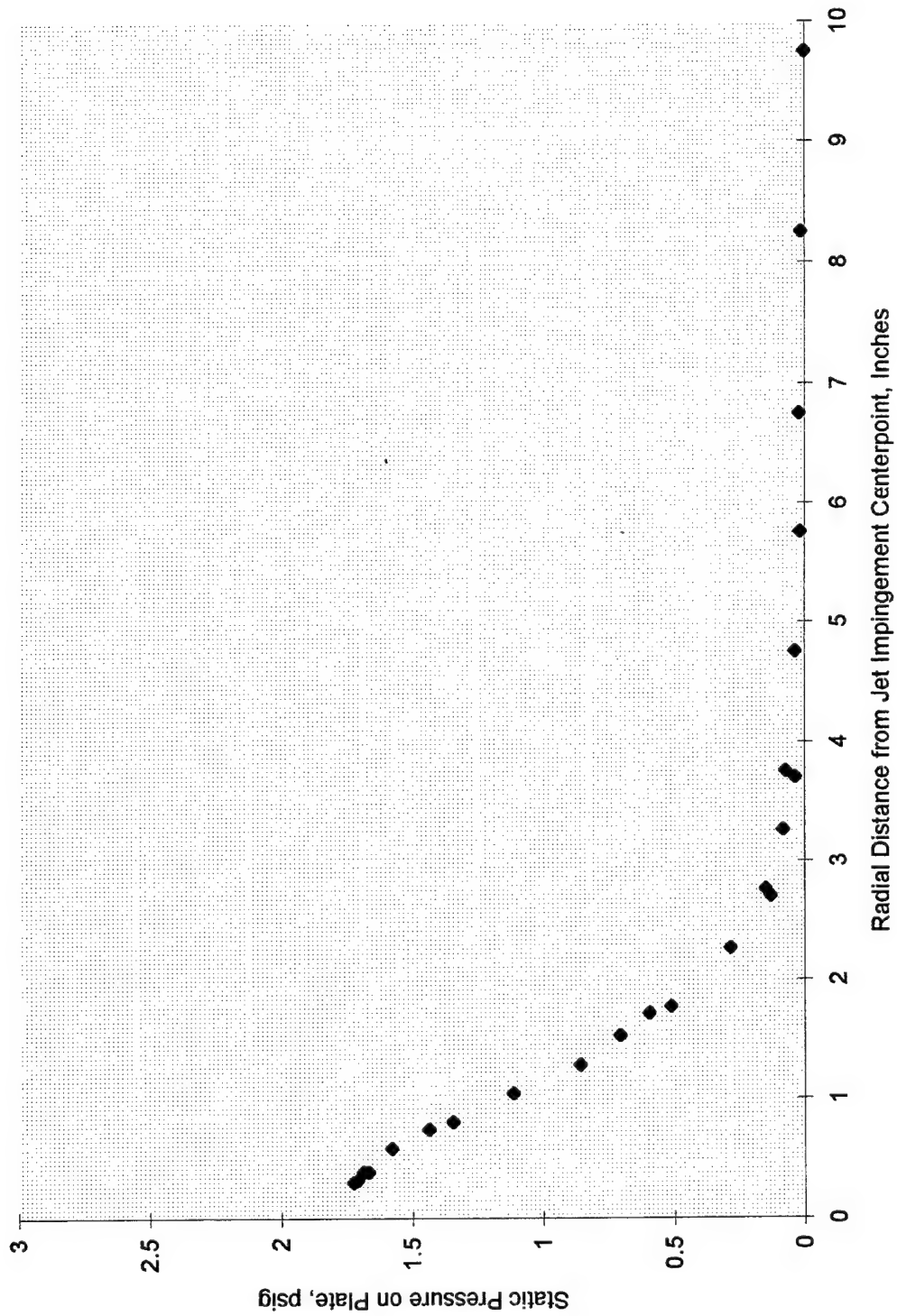


Figure 49: Static pressure as a function of distance from stagnation point on concrete specimens exposed to the simulated AV-8B plume, Z=12"

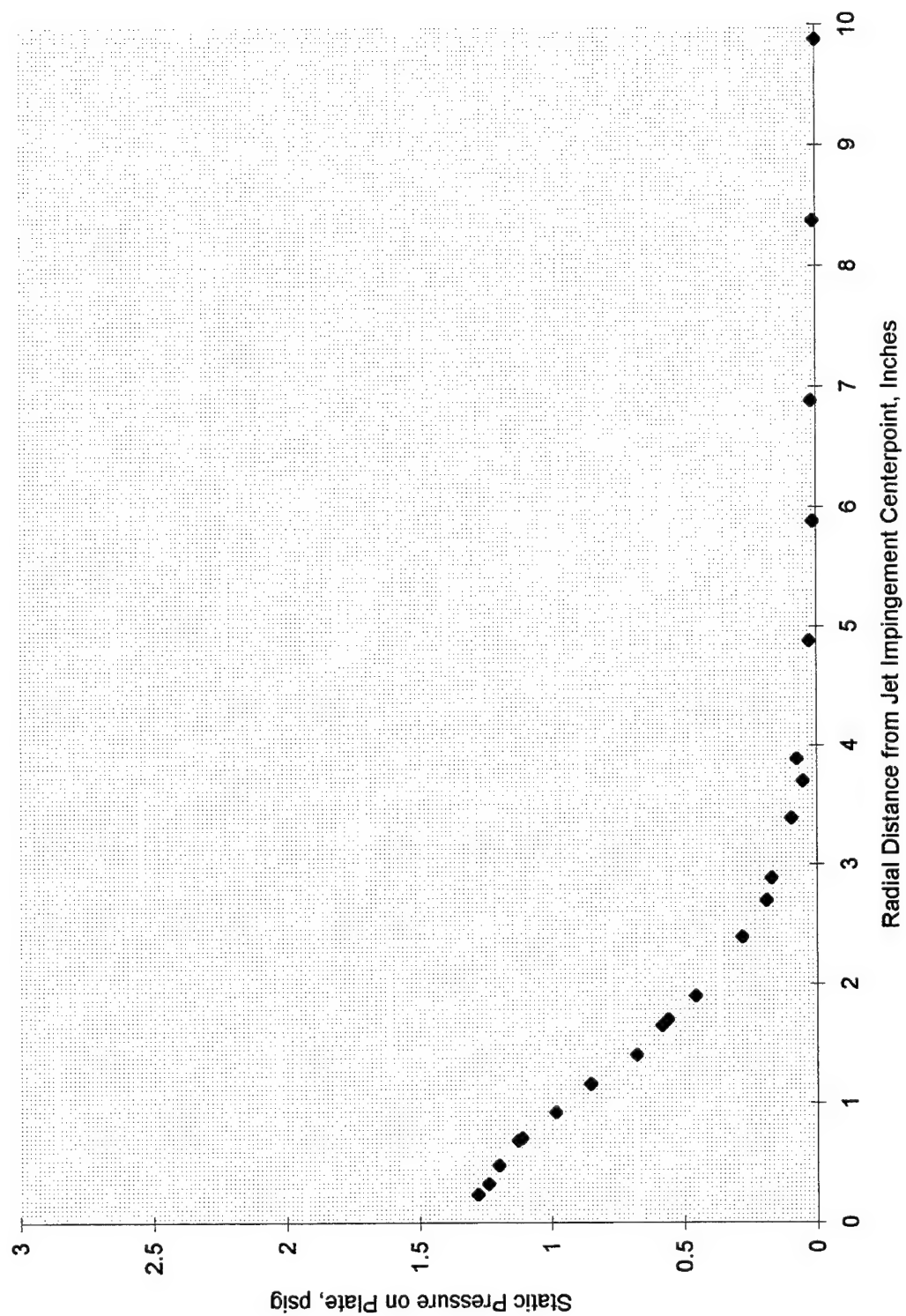
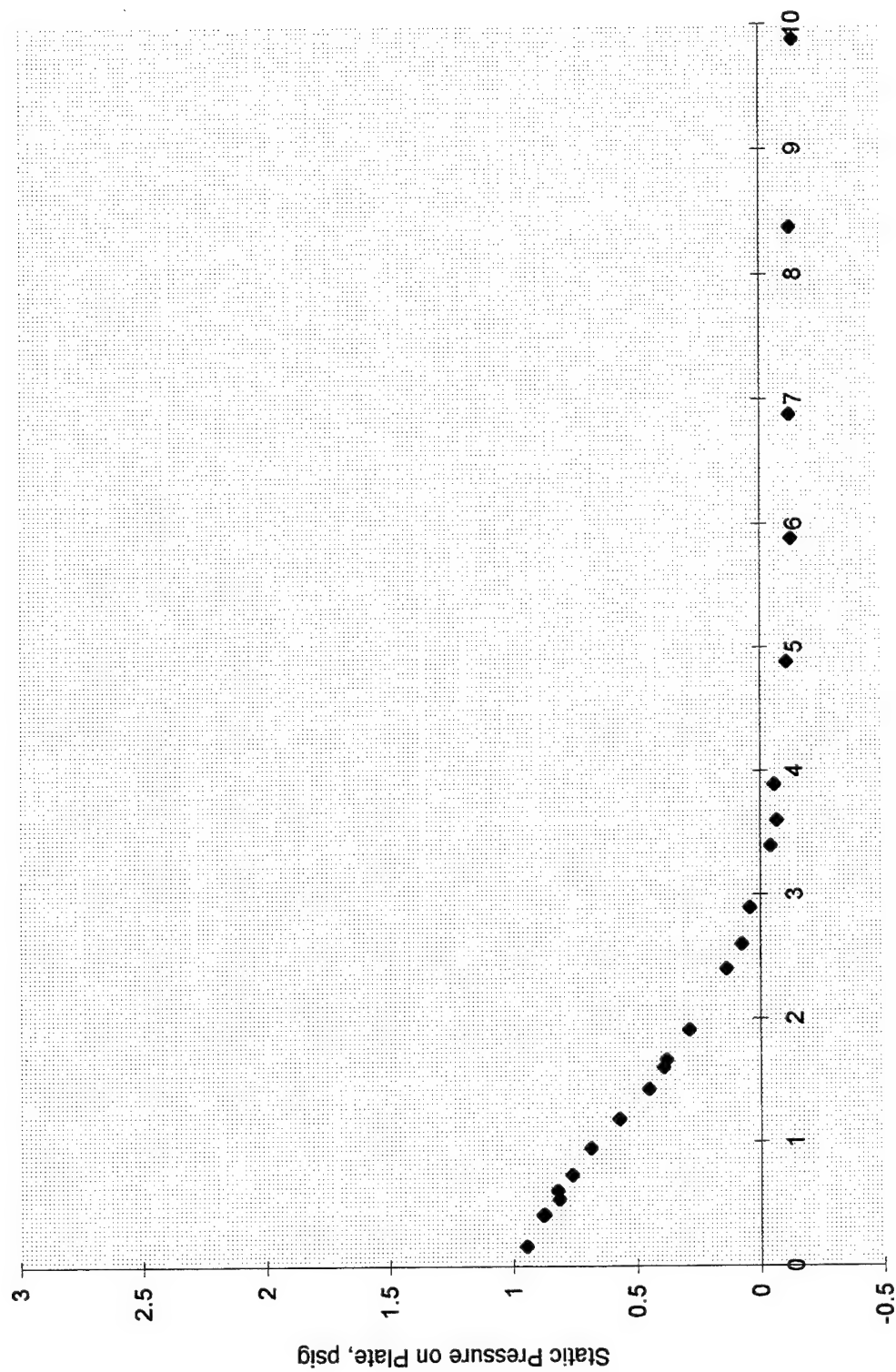


Figure 50: Static pressure as a function of distance from stagnation point on concrete specimens exposed to the simulated AV-8B plume, Z=15"



Radial Distance from Jet Impingement Centerpoint, Inches

Figure 51: Static pressure as a function of distance from stagnation point on concrete specimens exposed to the simulated AV-8B plume, Z=18"

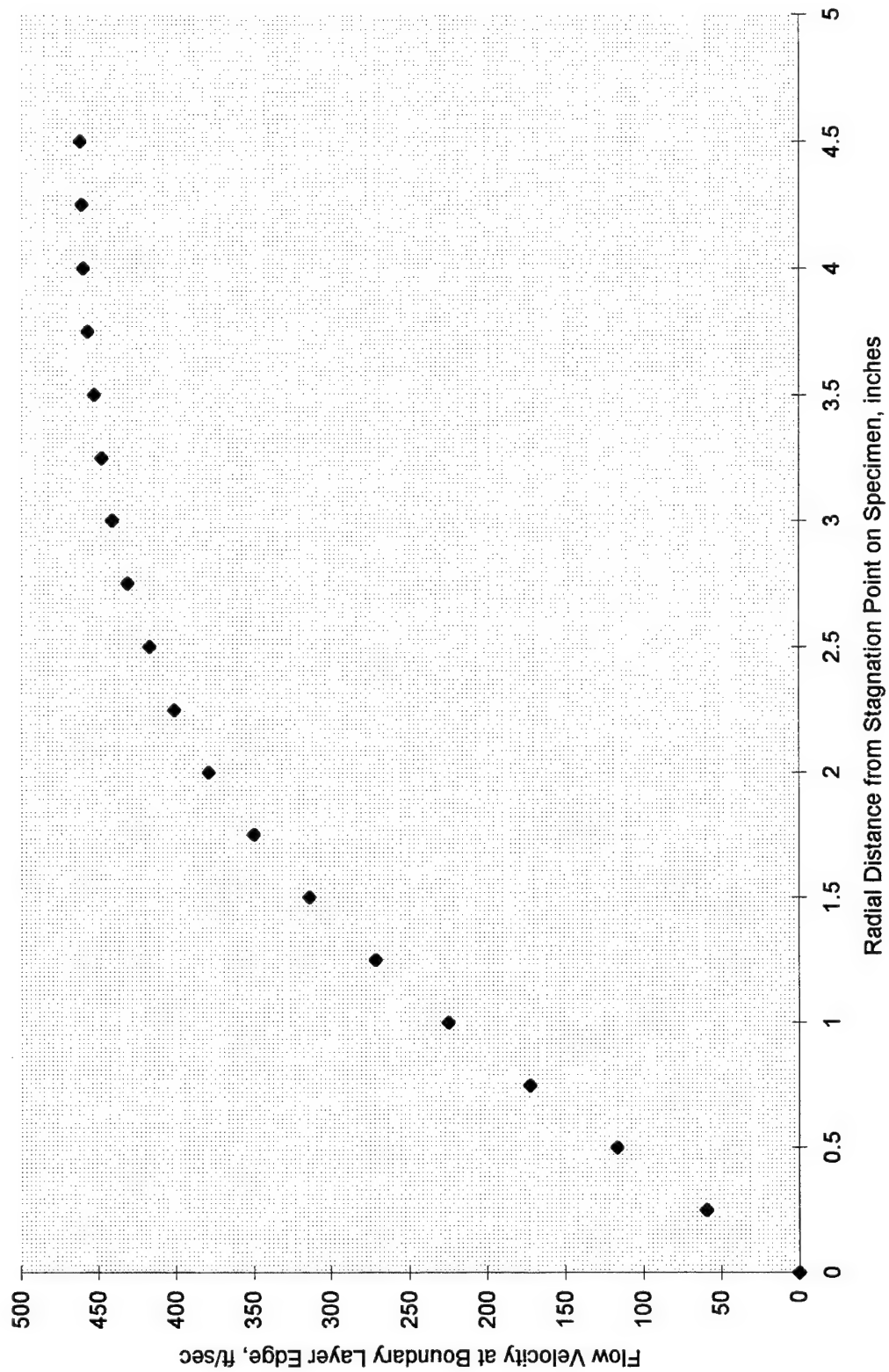


Figure 52. Flow velocity at the edge of the boundary layer on concrete specimens exposed to the simulated F/A-18 APU plume, $z=18"$

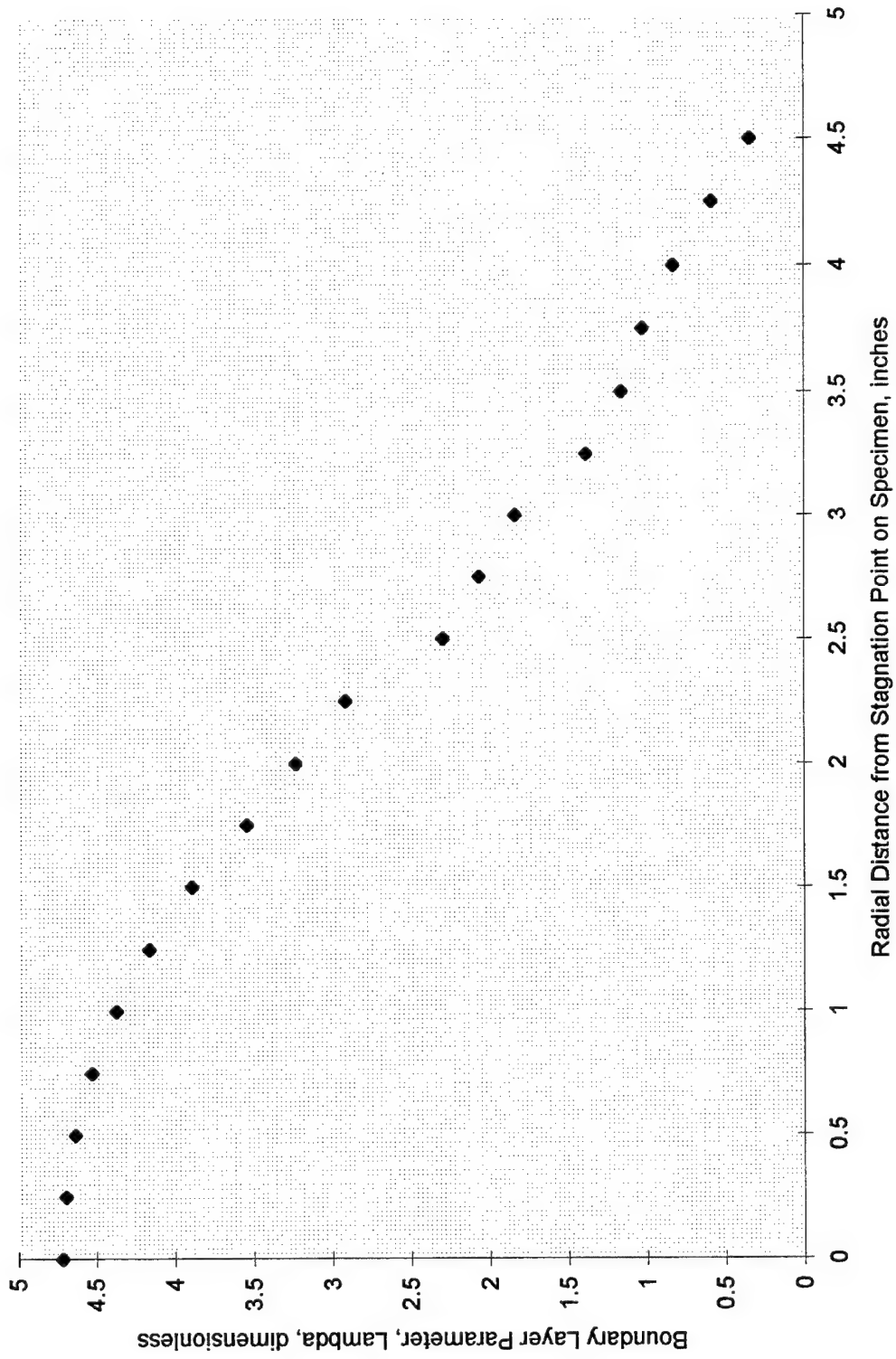


Figure 53. Radial distribution of boundary layer parameter (λ) on concrete specimens exposed to the simulated F/A-18 APU plume, $Z=18"$.

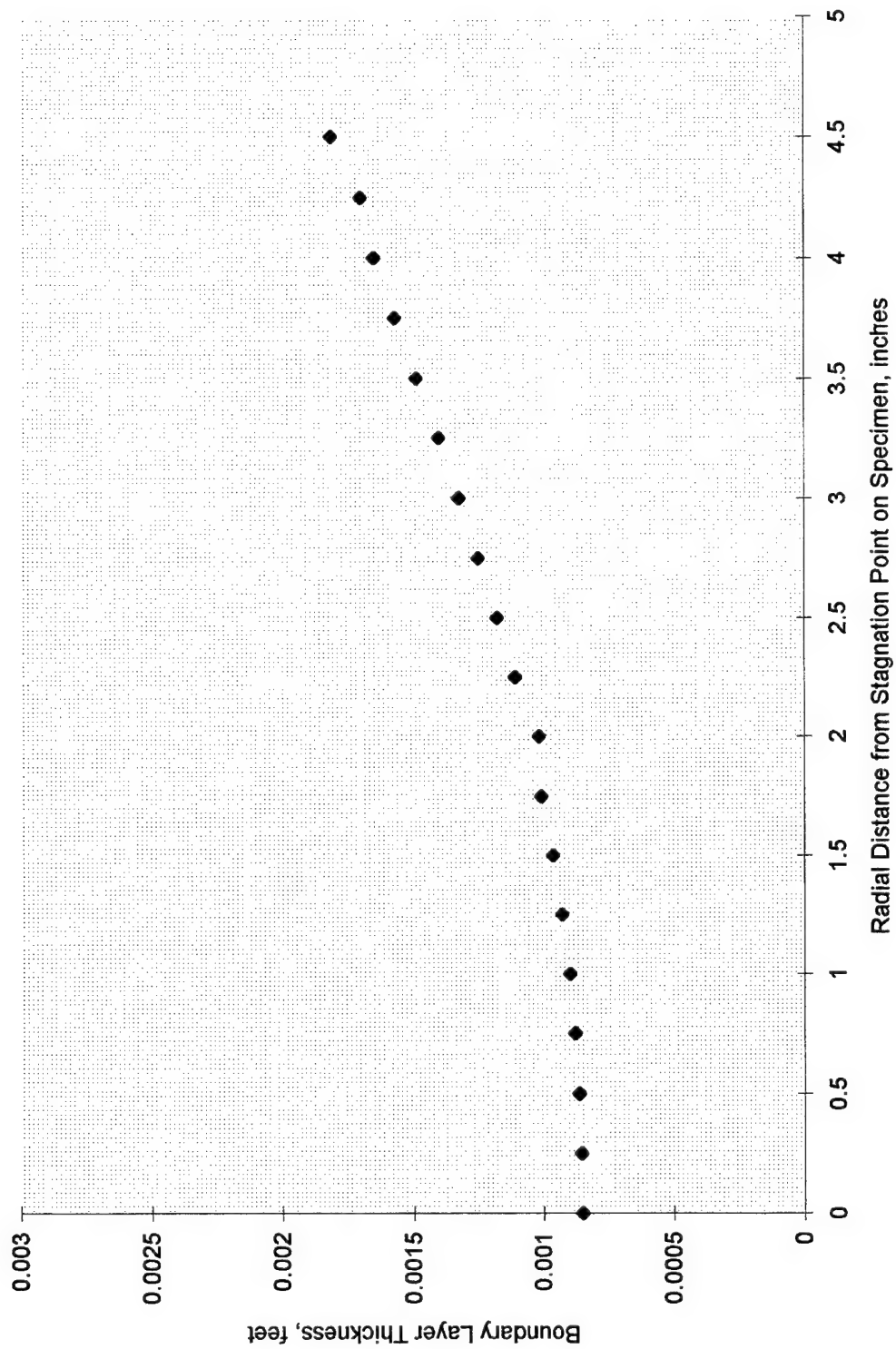


Figure 54. Radial distribution of boundary layer thickness on concrete specimens exposed to the simulated F/A-18 APU plume, $Z=18''$.

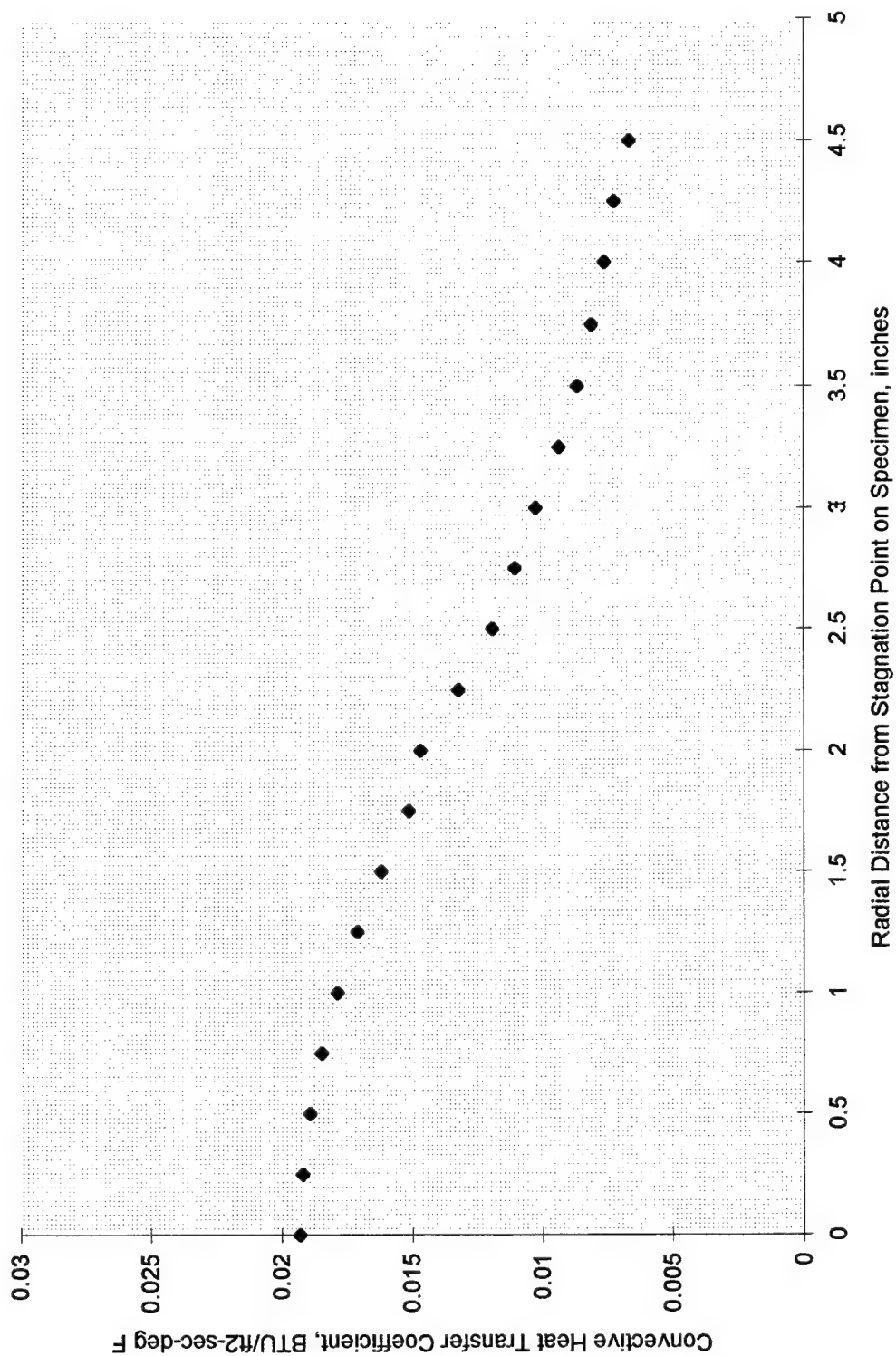


Figure 55. Radial distribution of convective heat transfer coefficients on concrete specimens exposed to the simulated F/A-18 APU plume, Z=18".

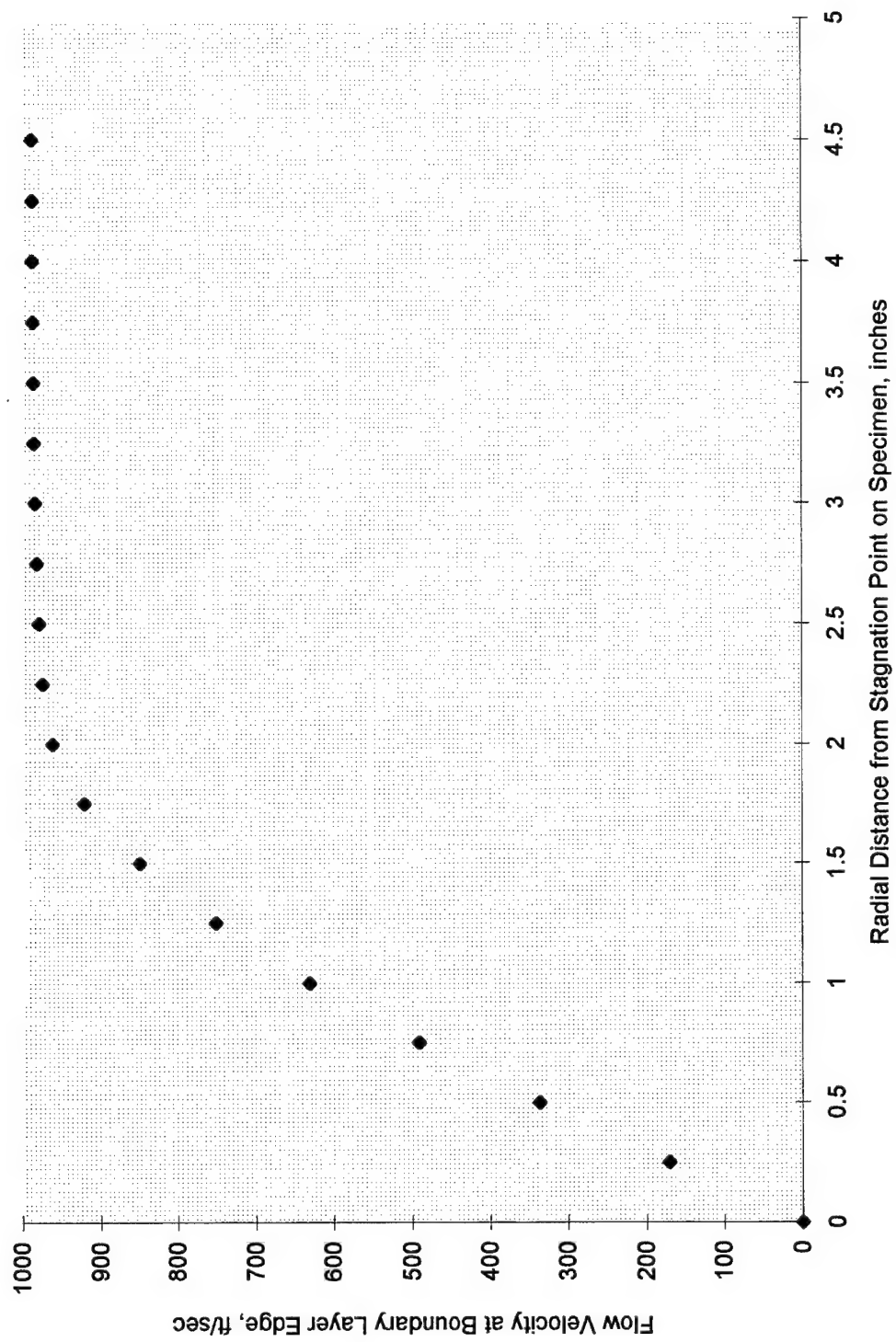


Figure 56. Flow velocity, at the edge of the boundary layer on concrete specimens exposed to the simulated AV-8B plume, $Z=6''$.

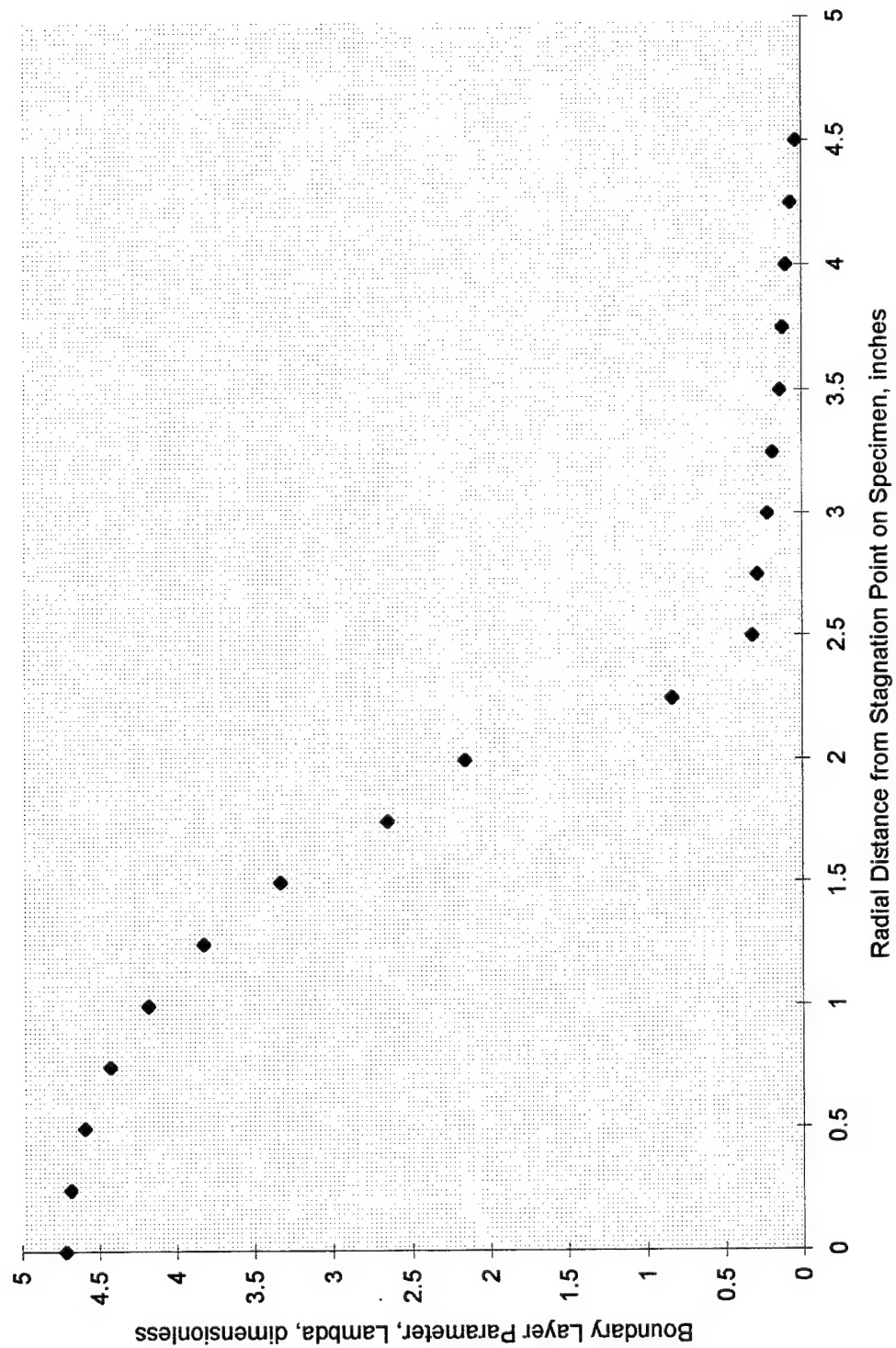


Figure 57. Radial distribution of boundary layer parameter (λ) on concrete specimens exposed to the simulated AV-8B plume, $Z=6''$.

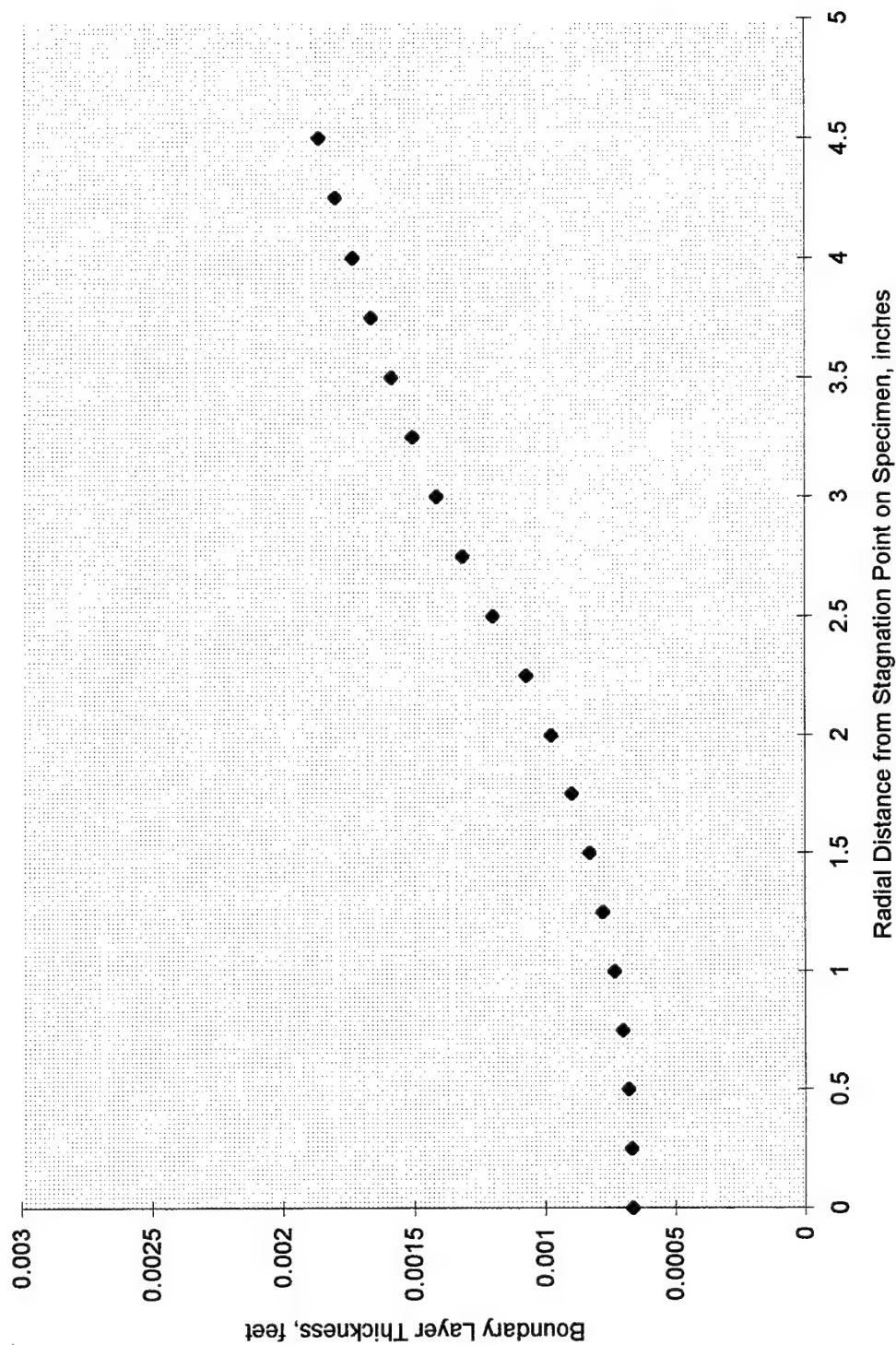


Figure 58. Radial distribution of boundary layer thickness on concrete specimens exposed to the simulated AV-8B plume, $Z=6''$.

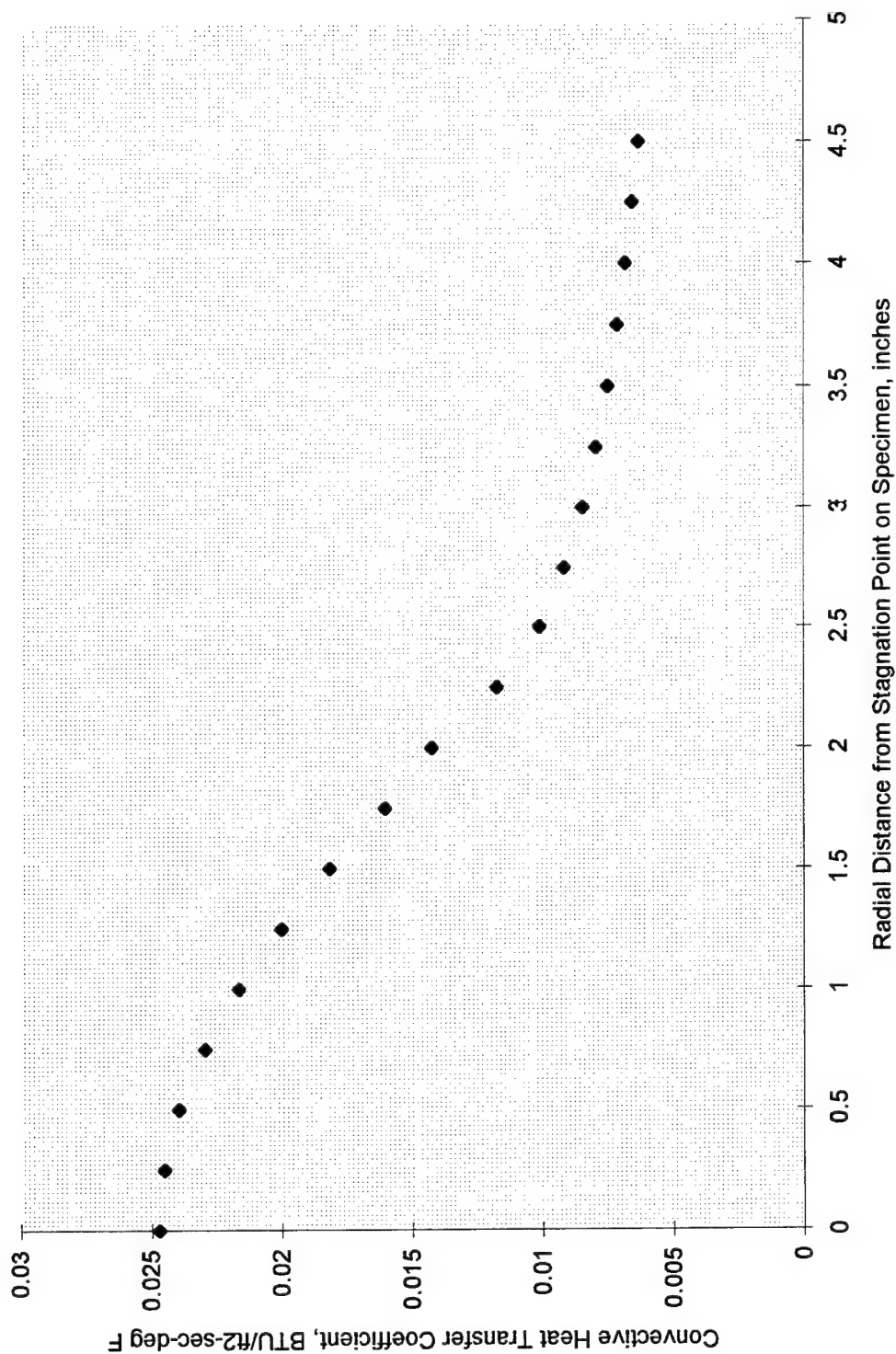


Figure 59. Radial distribution of convective heat transfer coefficients on concrete specimens exposed to the simulated AV-8B plume, Z=6".

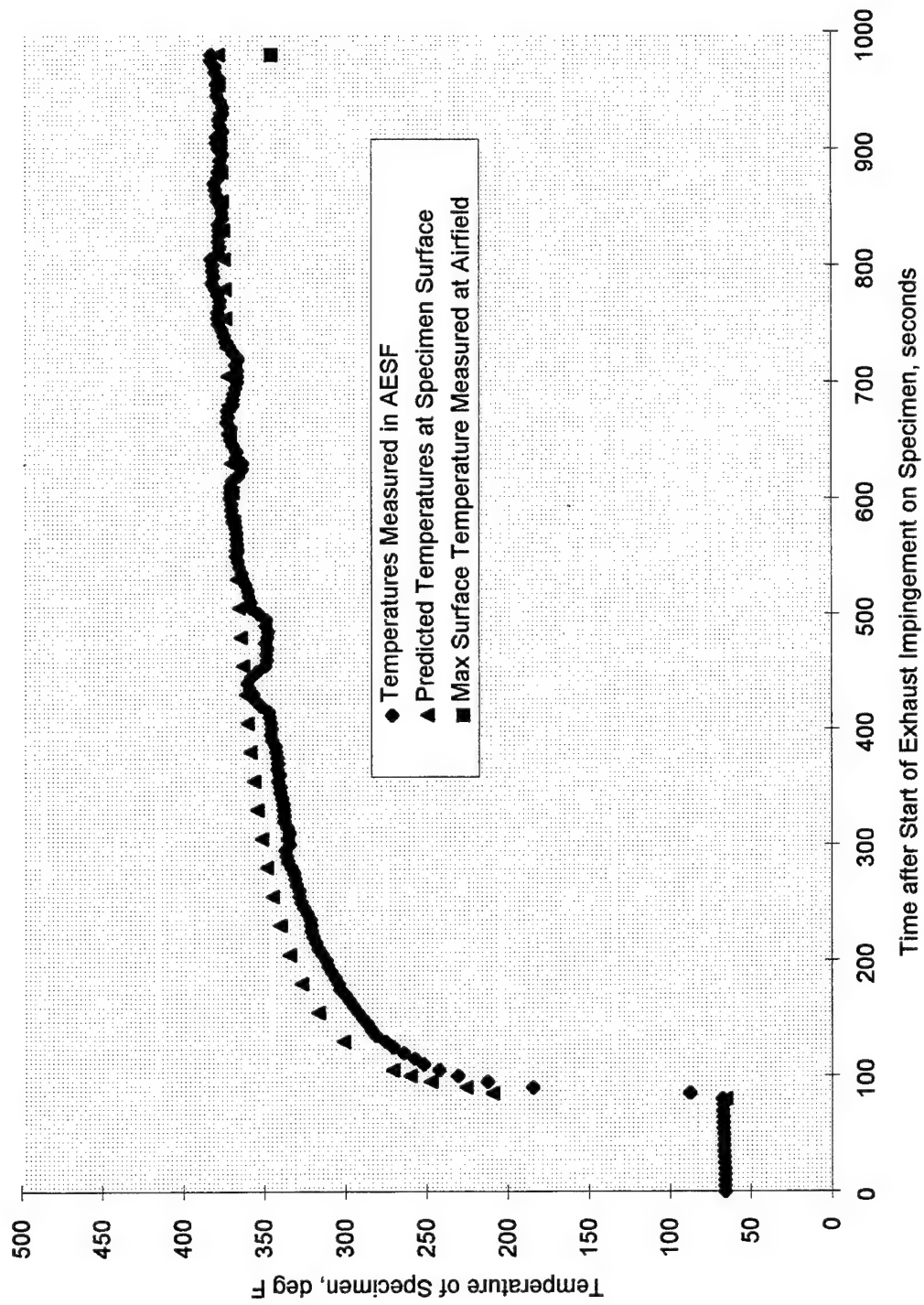


Figure 60. Comparison of measured and predicted temperatures of a concrete specimen exposed to the simulated F/A-18 APU exhaust, $z=18''$ (surface, $r=0''$).

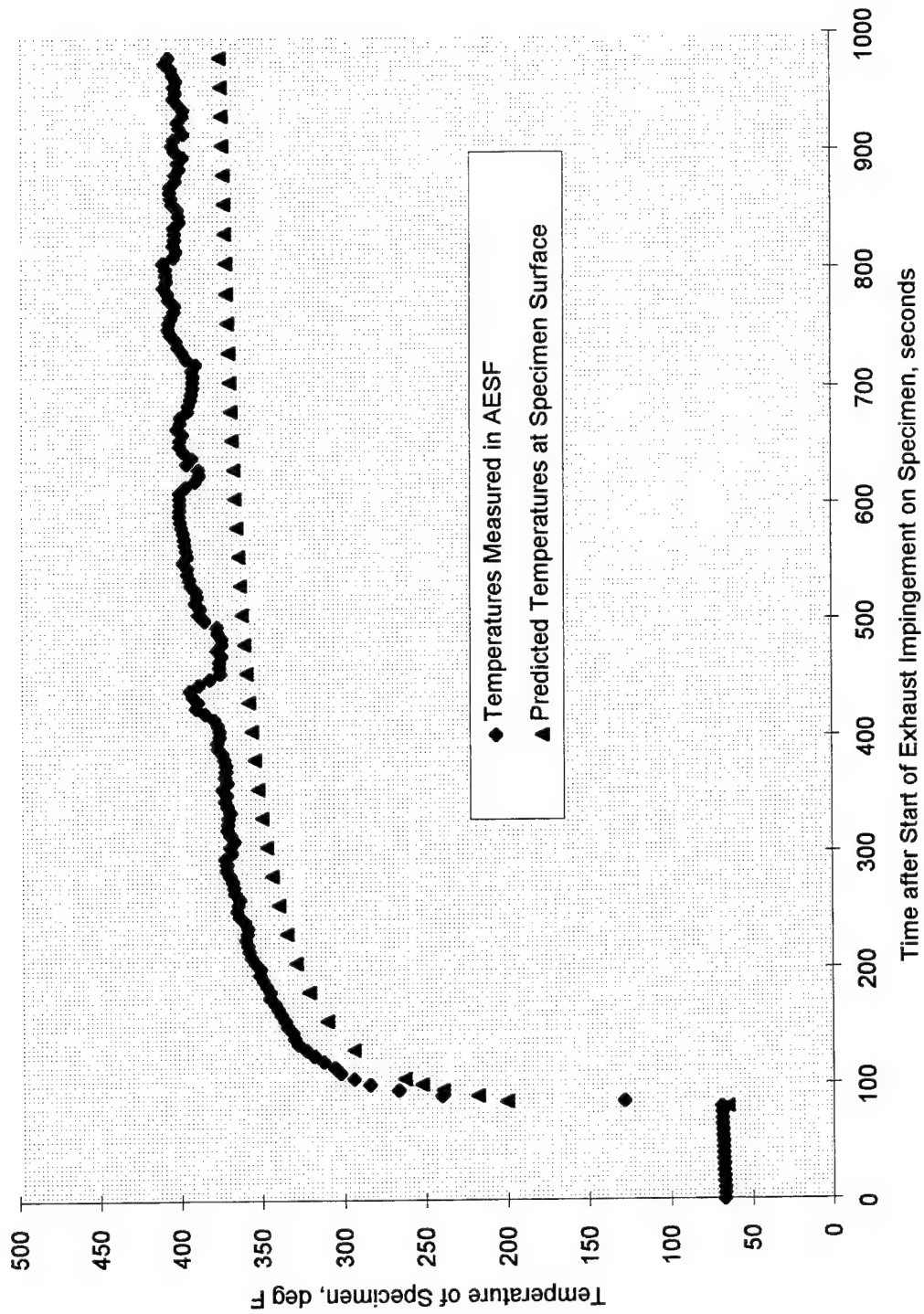


Figure 61. Comparison of measured and predicted temperatures of a concrete specimen exposed to the simulated F/A-18 APU exhaust, z=18" (surface, r=1").

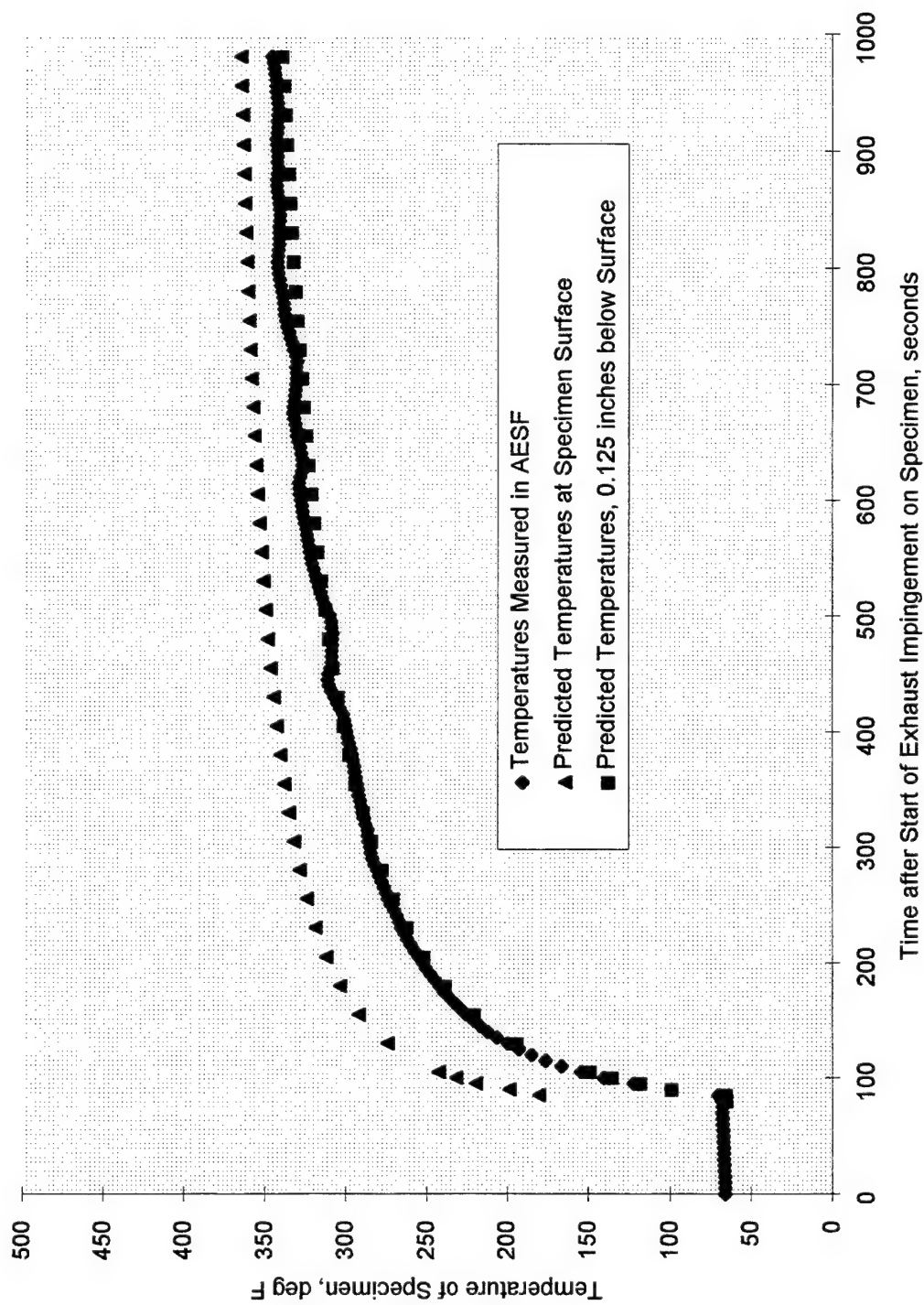


Figure 62. Comparison of measured and predicted temperatures of a concrete specimen exposed to the simulated F/A-18 APU exhaust, $z=18''$ (surface, $r=2''$).

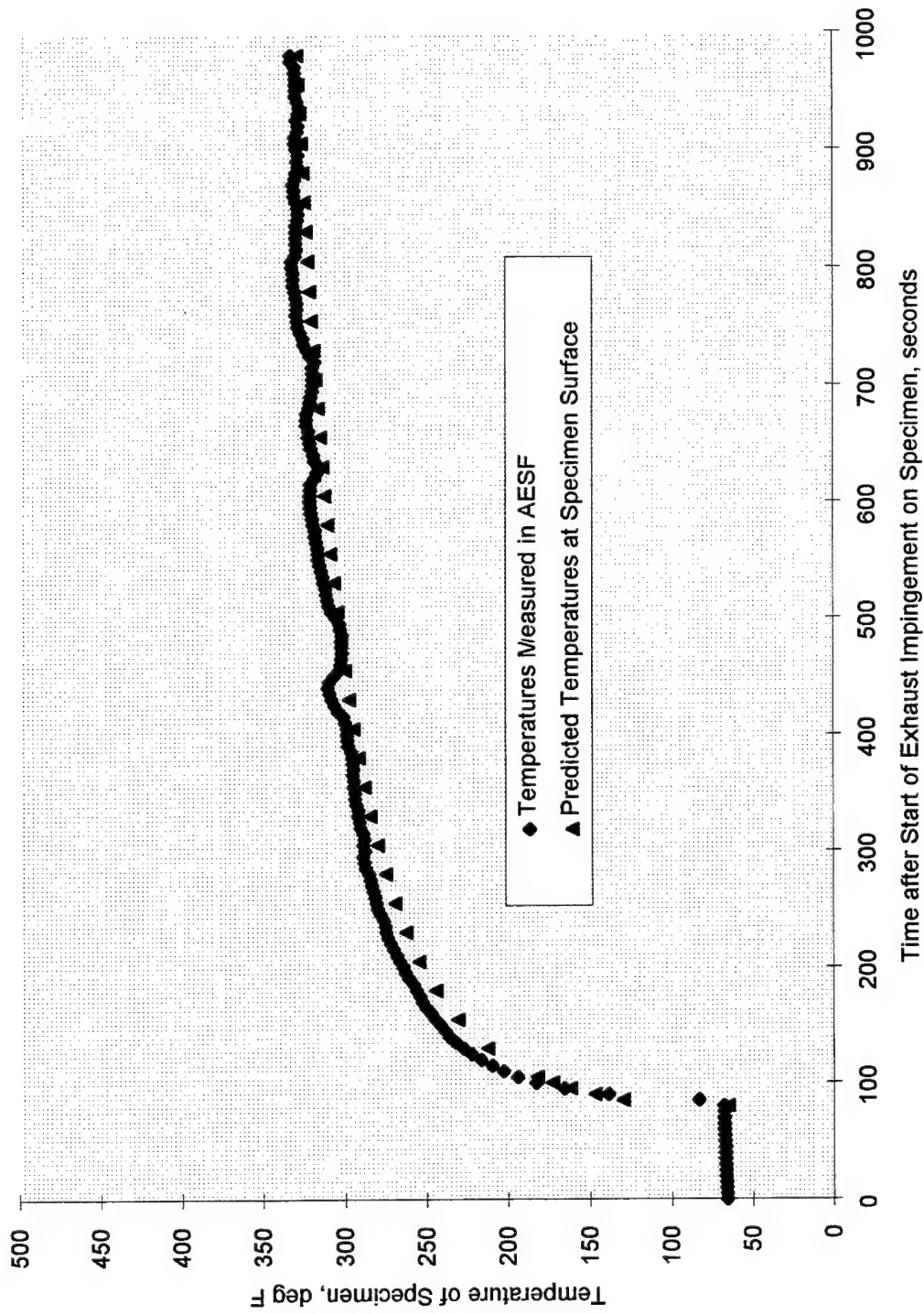


Figure 63. Comparison of measured and predicted temperatures of a concrete specimen exposed to the simulated F/A-18 APU exhaust, $z=18"$ (surface, $r=4"$).

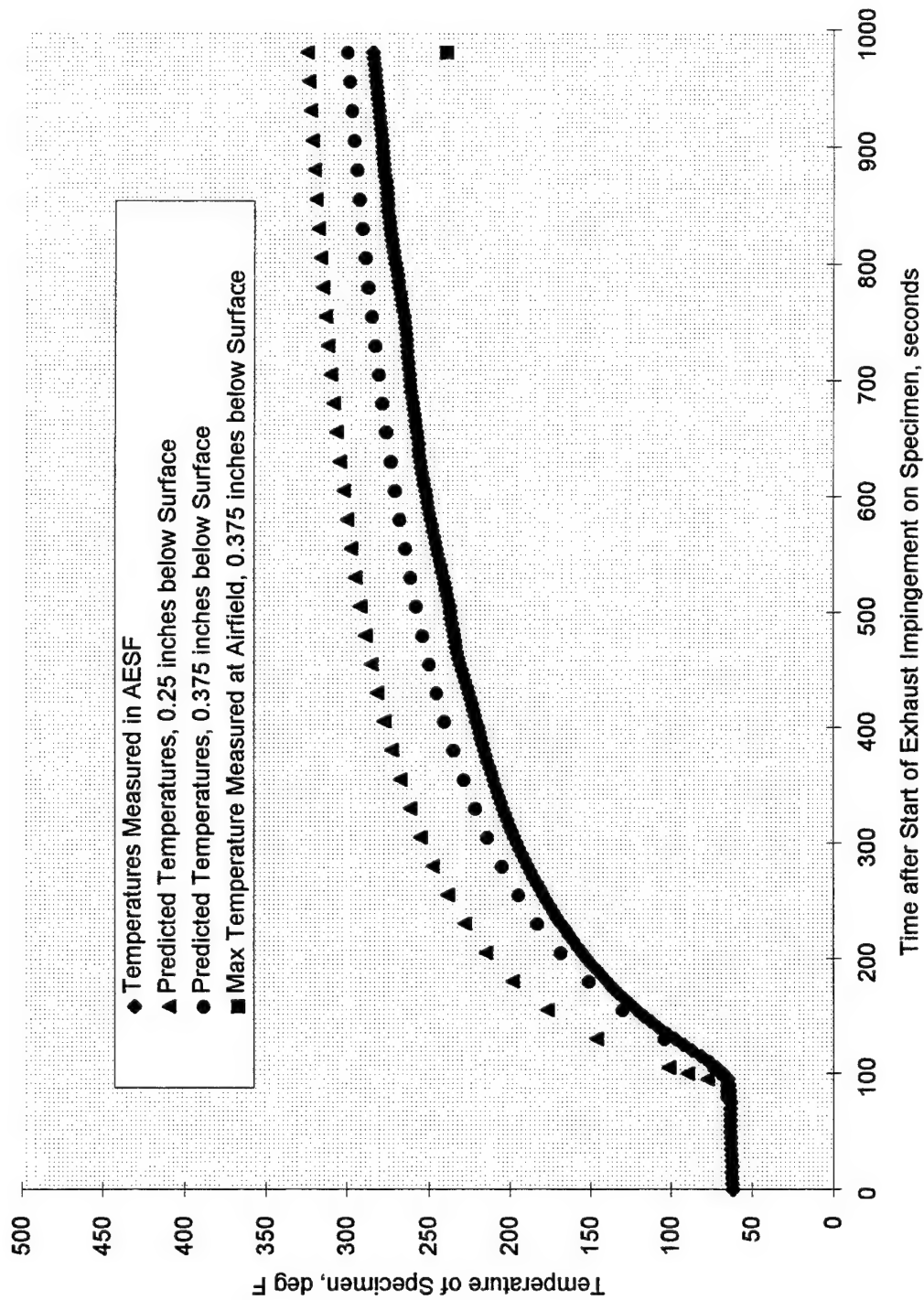


Figure 64. Comparison of measured and predicted temperatures of a concrete specimen exposed to the simulated F/A-18 APU exhaust, $z=18"$ ($0.25"$ below surface, $r=0"$).

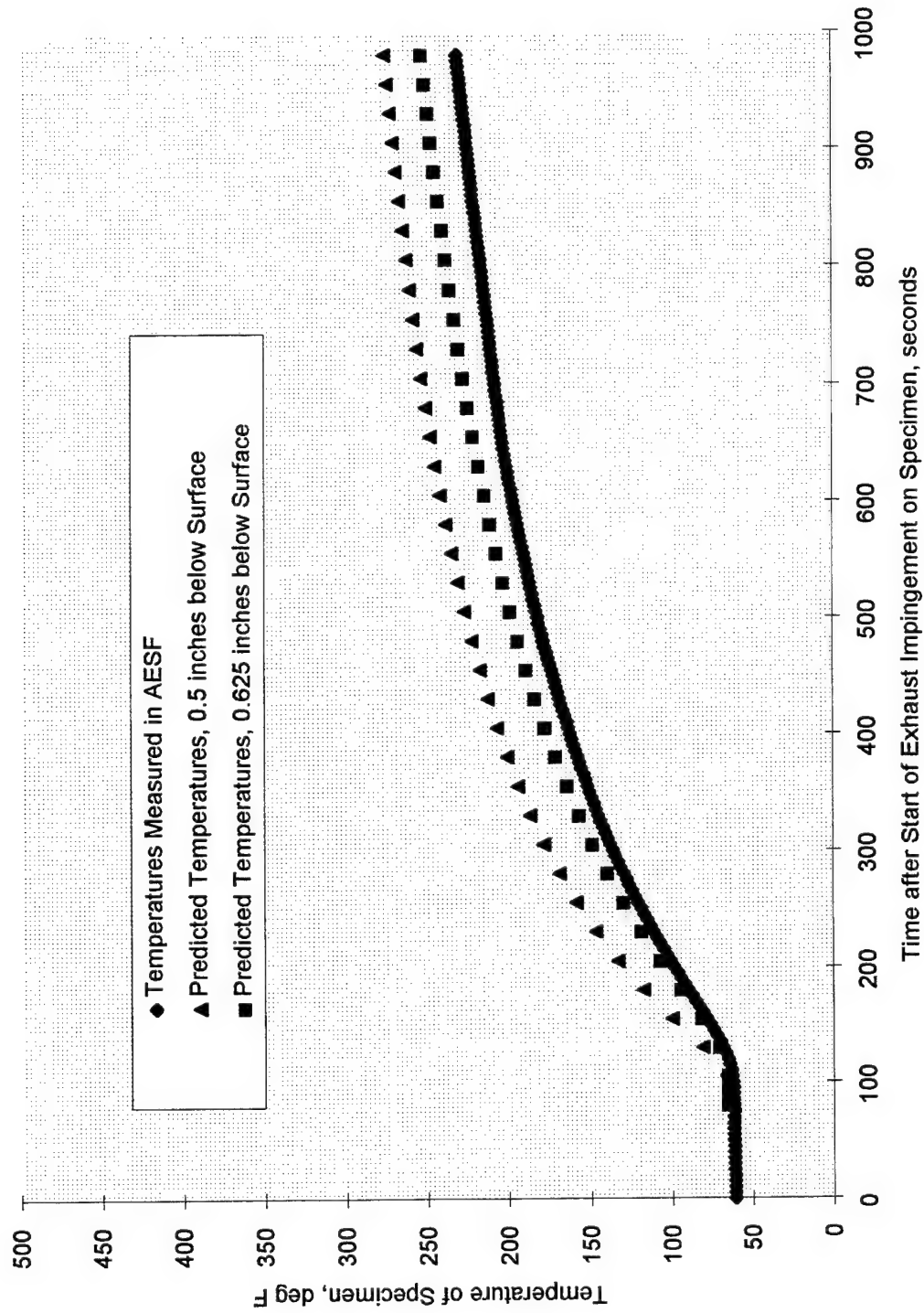


Figure 65. Comparison of measured and predicted temperatures of a concrete specimen exposed to the simulated F/A-18 APU exhaust, $z=18''$ (0.5" below surface, $r=0''$).

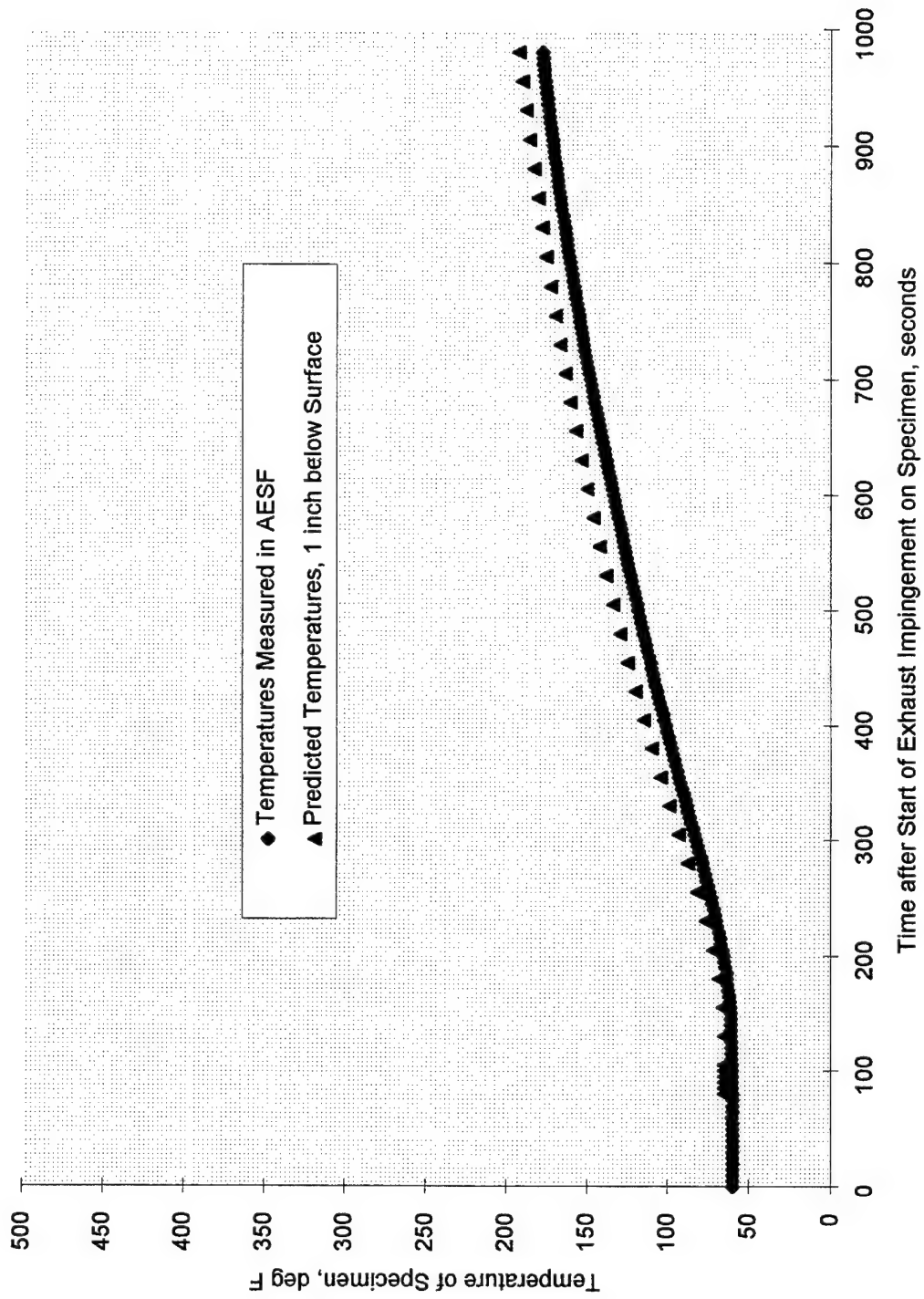


Figure 66. Comparison of measured and predicted temperatures of a concrete specimen exposed to the simulated F/A-18 APU exhaust, $z=18"$ (1" below surface, $r=0"$).

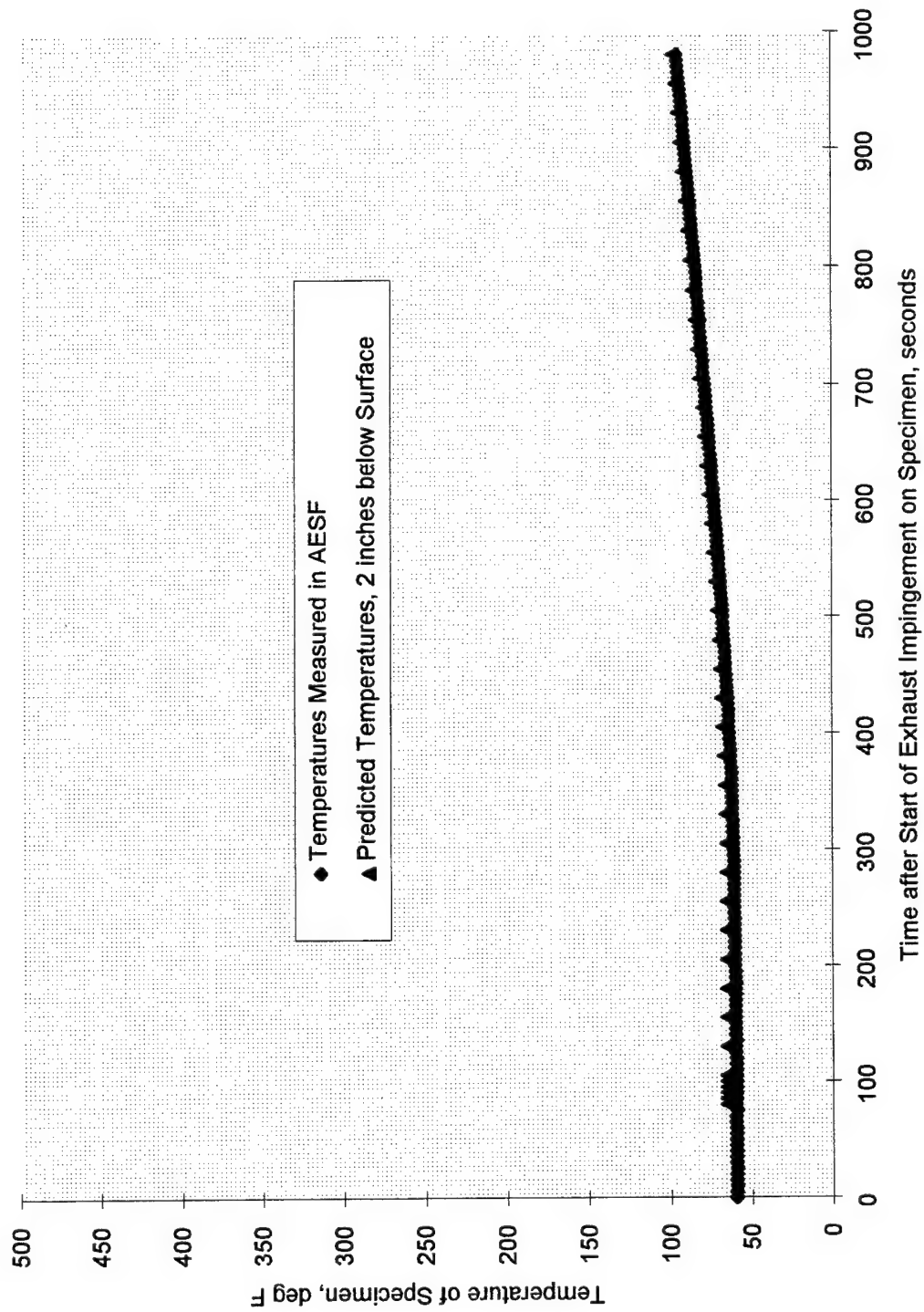


Figure 67. Comparison of measured and predicted temperatures of a concrete specimen exposed to the simulated F/A-18 APU exhaust, $z=18"$ (2" below surface, $r=0"$).

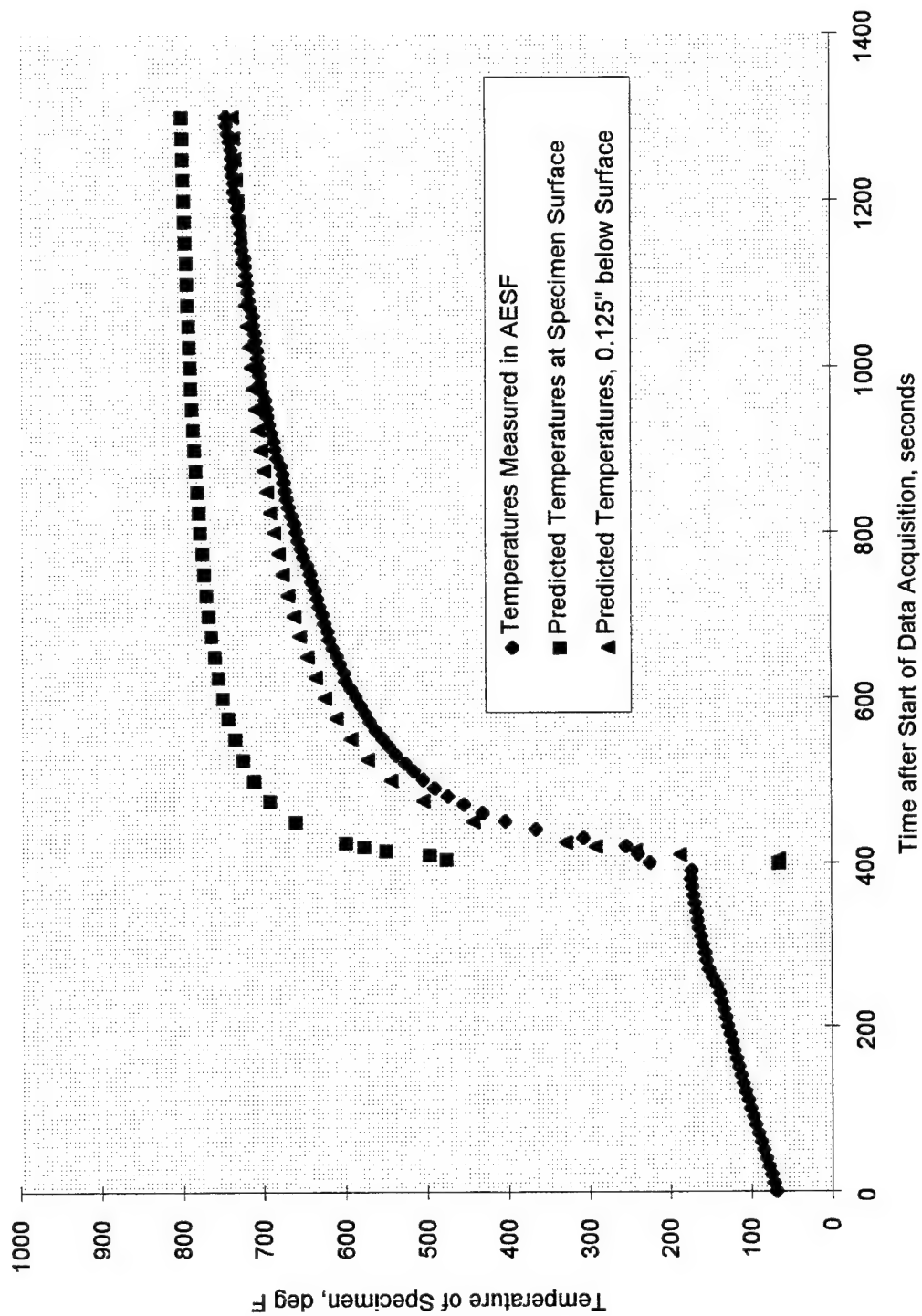


Figure 68. Comparison of measured and predicted temperatures of a concrete specimen exposed to the simulated AV-8B rear nozzle exhaust, $z=6"$ (surface, $r=0"$)

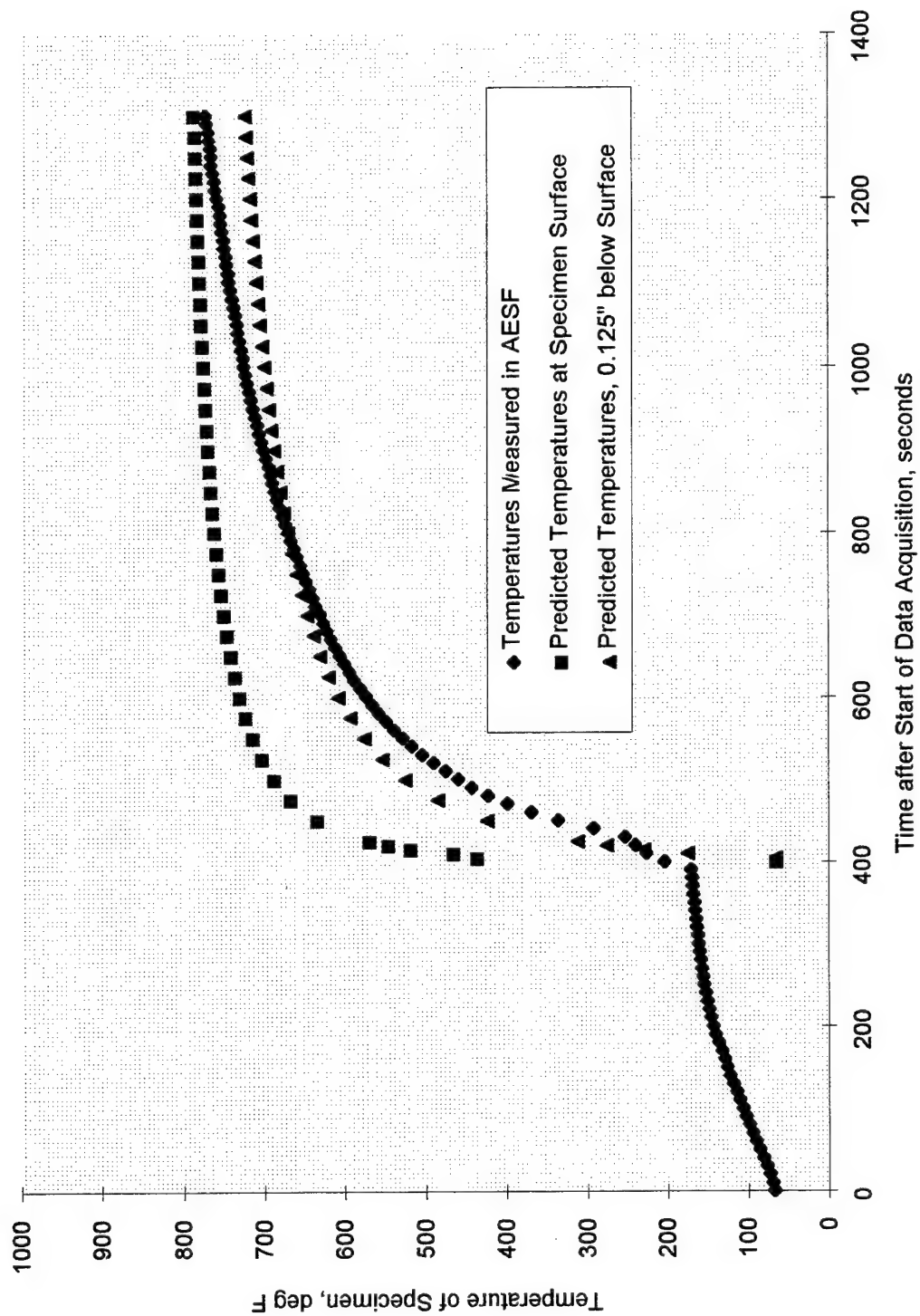


Figure 69. Comparison of measured and predicted temperatures of a concrete specimen exposed to the simulated AV-8B rear nozzle exhaust, $z=6"$ (surface, $r=1"$)

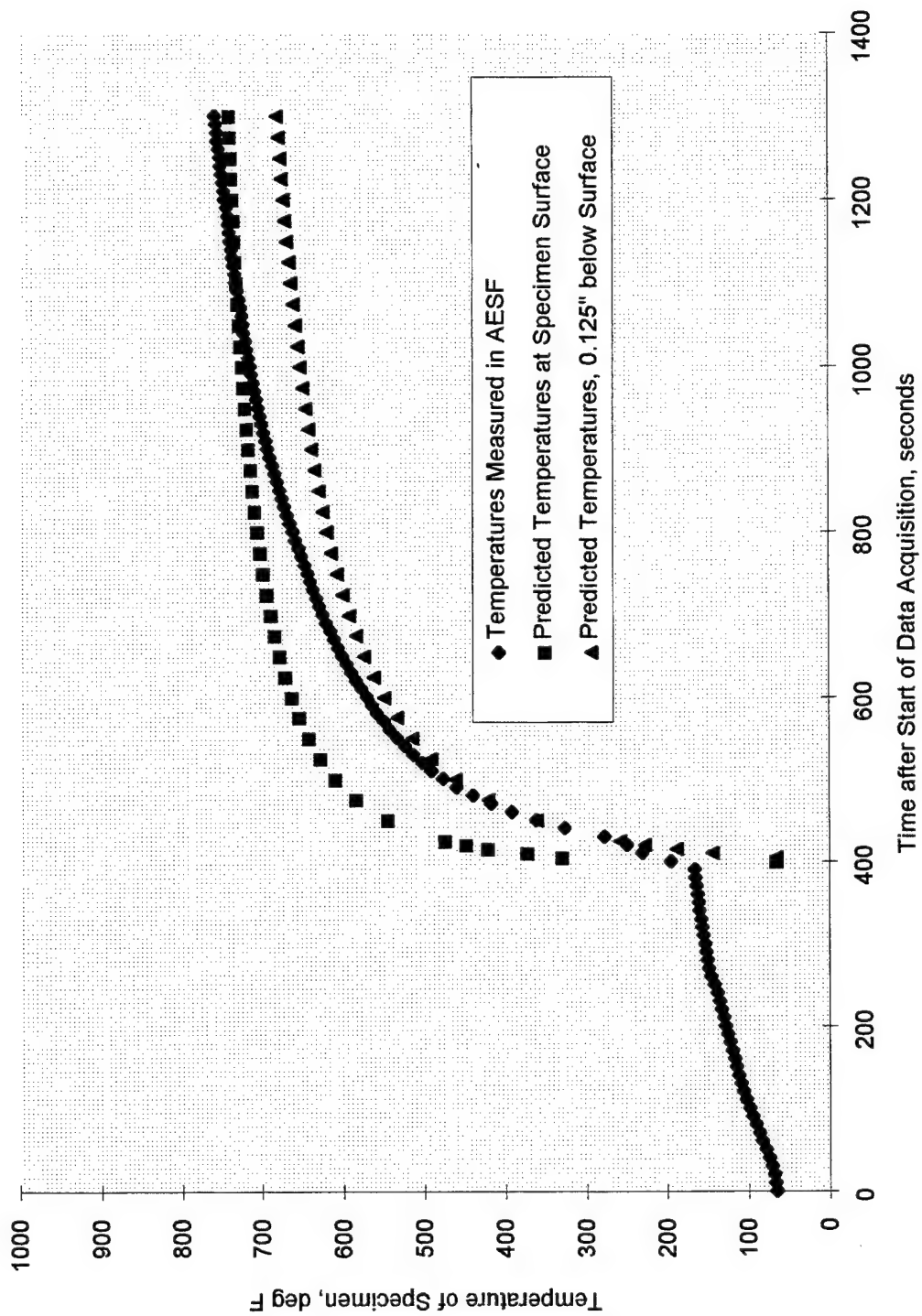


Figure 70. Comparison of measured and predicted temperatures of a concrete specimen exposed to the simulated AV-8B rear nozzle exhaust, $z=6"$ (surface, $r=2"$)

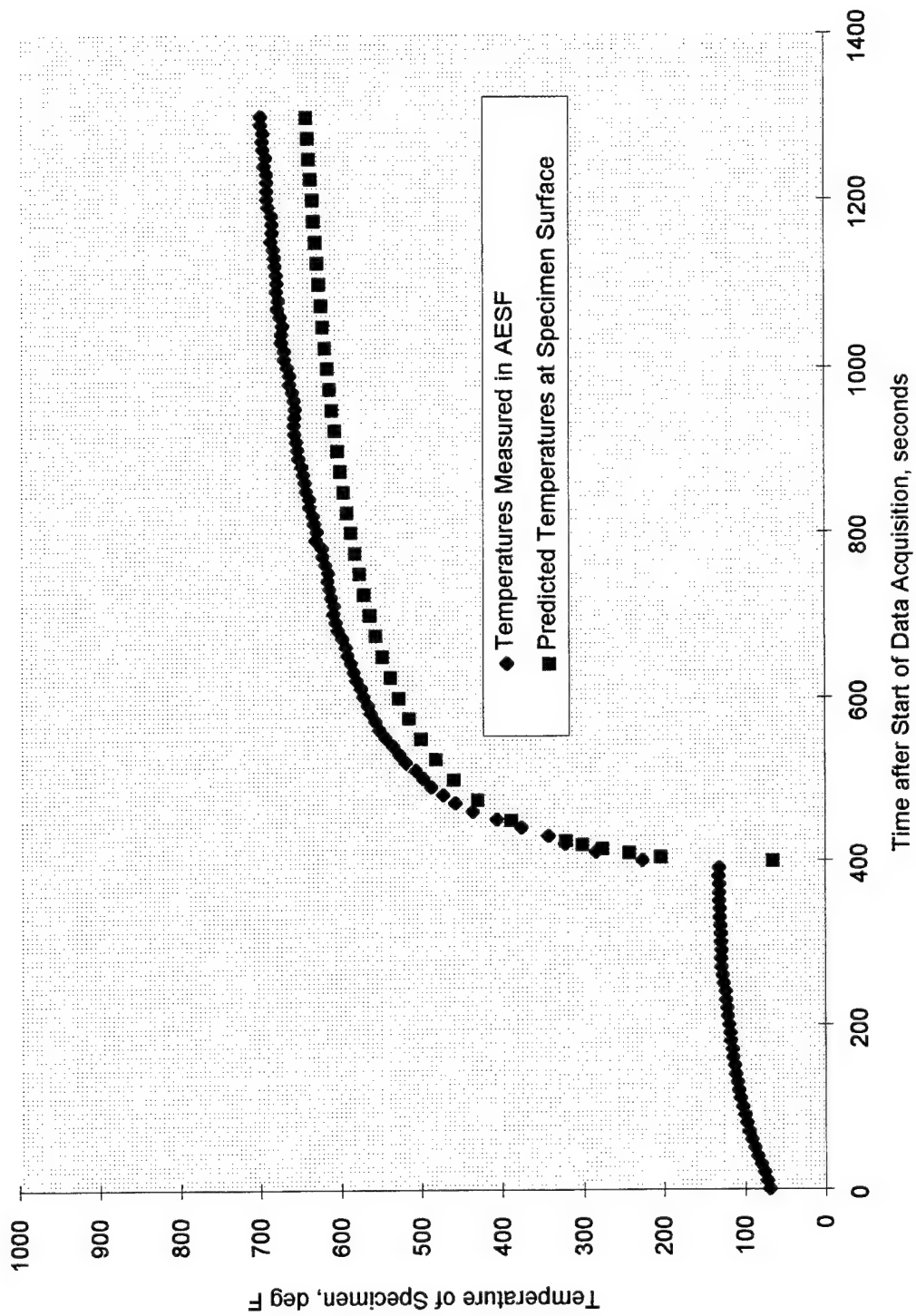


Figure 71. Comparison of measured and predicted temperatures of a concrete specimen exposed to the simulated AV-8B rear nozzle exhaust, z=6" (surface, r=4")

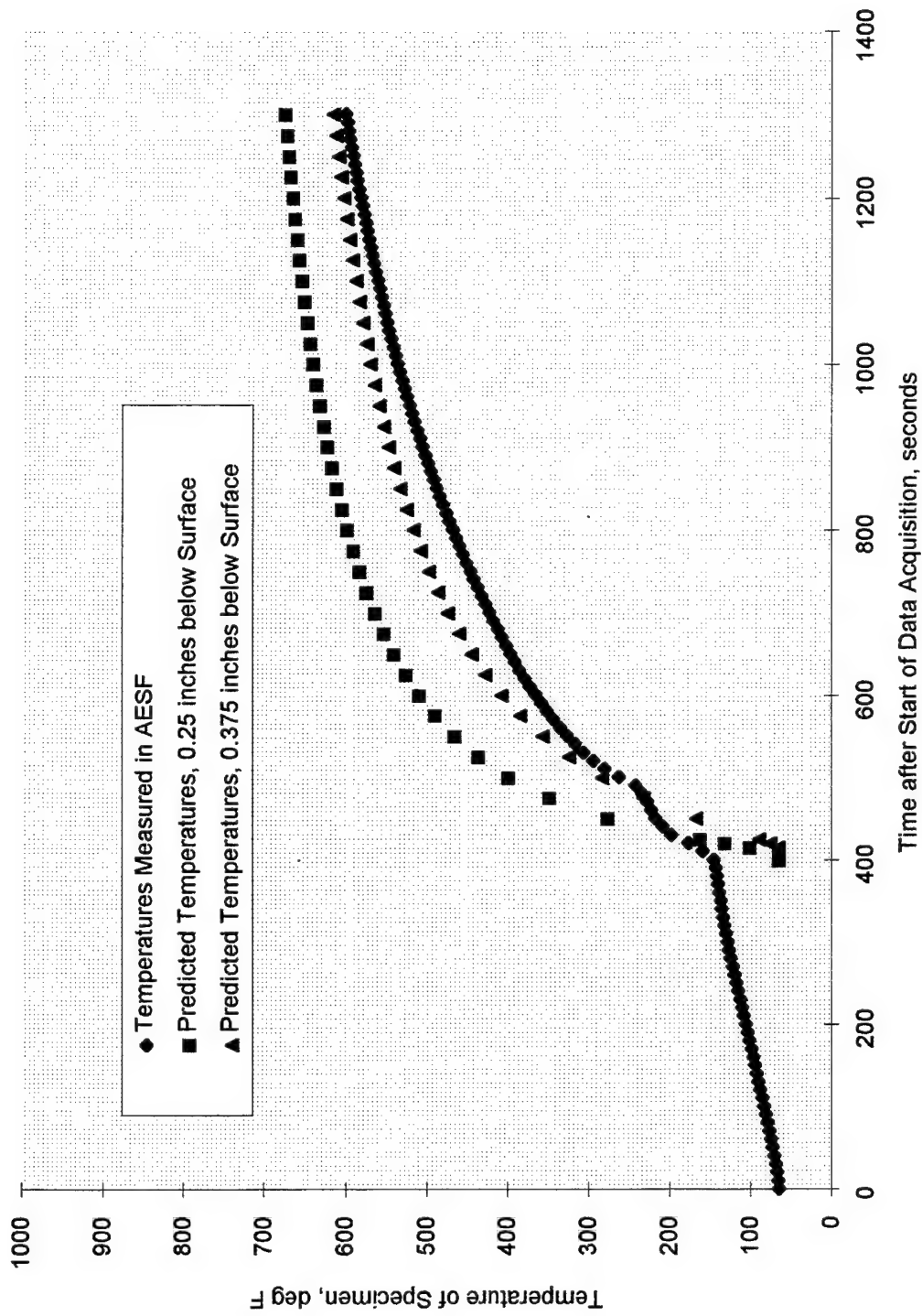


Figure 72. Comparison of measured and predicted temperatures of a concrete specimen exposed to the simulated AV-8B rear nozzle exhaust, $z=6"$ ($0.25"$ below surface, $r=0"$)

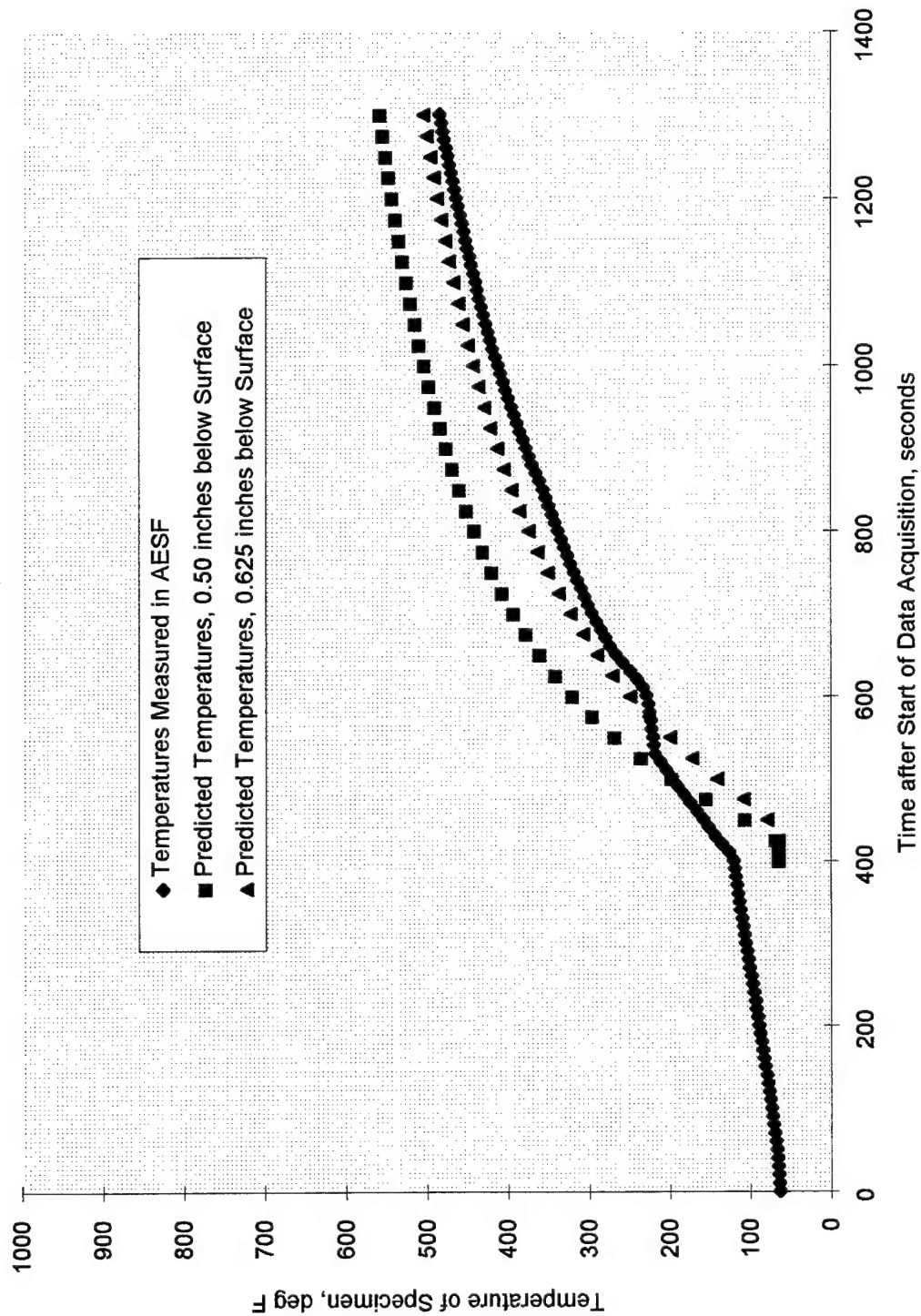


Figure 73. Comparison of measured and predicted temperatures of a concrete specimen exposed to the simulated AV-8B rear nozzle exhaust, $z=6"$ (0.5" below surface, $r=0"$)

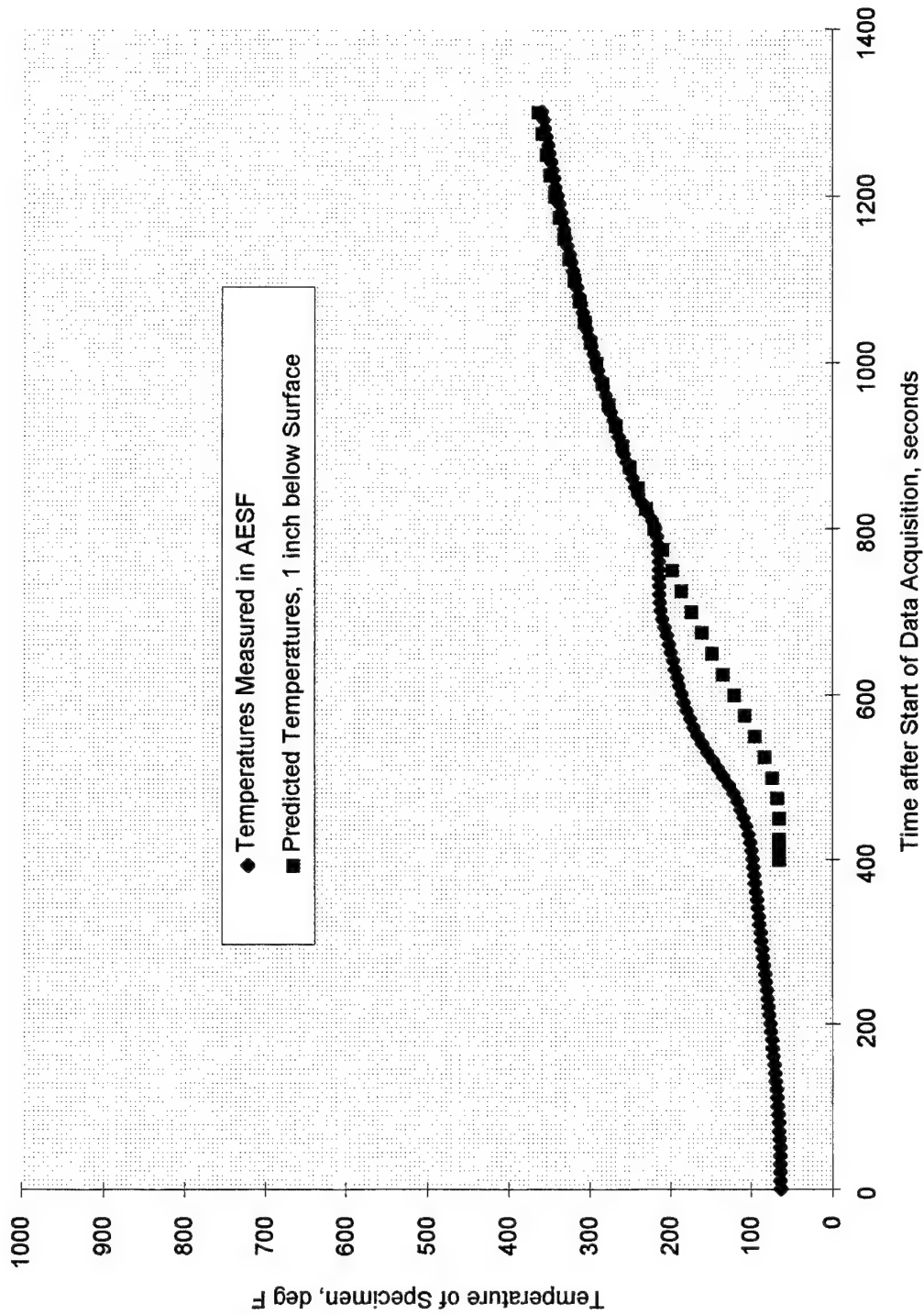


Figure 74. Comparison of measured and predicted temperatures of a concrete specimen exposed to the simulated AV-8B rear nozzle exhaust, $z=6$ " (1" below surface, $r=0$ ")

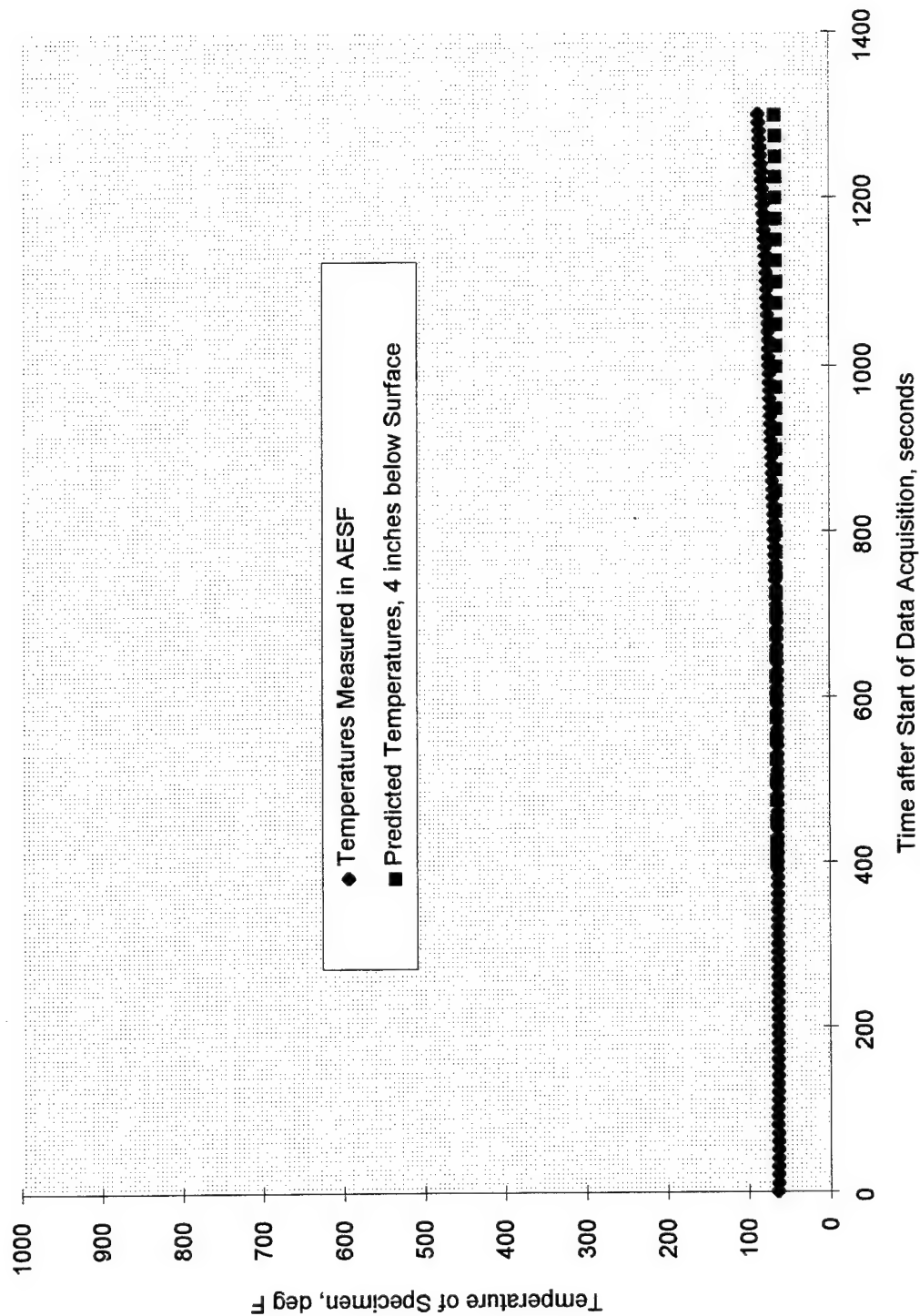


Figure 75. Comparison of measured and predicted temperatures of a concrete specimen exposed to the simulated AV-8B rear nozzle exhaust, $z=6"$ (4" below surface, $r=0"$)

APPENDIX A

**THEORY AND ANALYSIS PROCEDURES FOR DESIGN
OF THE NFESC AVIATION ENGINE SIMULATION FACILITY**

A.1 COMBUSTION ANALYSIS

Combustion of Natural Gas (Methane) in Air.

Natural gas is primarily methane, CH_4 . The stoichiometric reaction of methane with oxygen produces carbon dioxide and water, according to the following reaction equation.

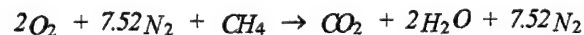


The reaction equation represents one mole of methane (molecular wt = 16 $\text{lb}_m/\text{lb}_{\text{mole}}$) reacting with two moles of oxygen (molecular wt = 32 $\text{lb}_m/\text{lb}_{\text{mole}}$) to produce one mole of carbon dioxide (molecular wt = 44 $\text{lb}_m/\text{lb}_{\text{mole}}$) and two moles of water (molecular wt = 18 $\text{lb}_m/\text{lb}_{\text{mole}}$). The Law of Conservation of Mass states that the mass of the reactants equals the mass of the products.

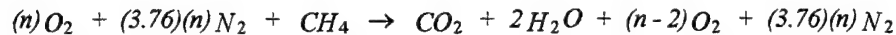
$$\begin{aligned} \left(2 \text{ lb}_{\text{mole}}\right) \left(32 \frac{\text{lb}_m}{\text{lb}_{\text{mole}}}\right) + \left(1 \text{ lb}_{\text{mole}}\right) \left(16 \frac{\text{lb}_m}{\text{lb}_{\text{mole}}}\right) = \\ \left(1 \text{ lb}_{\text{mole}}\right) \left(44 \frac{\text{lb}_m}{\text{lb}_{\text{mole}}}\right) + \left(2 \text{ lb}_{\text{mole}}\right) \left(18 \frac{\text{lb}_m}{\text{lb}_{\text{mole}}}\right) \end{aligned}$$

For the combustion of methane in air, the nitrogen in the air must be taken into account, although it passes through the combustion zone without reacting. (Note: A very small amount of the nitrogen does react, and the reaction is important when considering air pollutant emissions. However, for this part of the analysis, which is to determine the heat release and the temperature and pressure after combustion, the slight formation of NO_x is neglected.) If we neglect trace elements, dry air is 79% nitrogen by volume and 21% oxygen. That is, for every 100 molecules of air, 79 are nitrogen molecules and 21 are oxygen molecules. For one mole of oxygen, there are 79/21 (=3.76) moles of nitrogen. For two moles of oxygen, there are 7.52 moles of nitrogen.

The equation for the stoichiometric reaction of methane in air is:



Most combustion processes are not stoichiometric, but instead are completed with excess air. Excess air is desirable because a deficiency of air results in the production of dangerous CO rather than CO_2 . Consider the reaction in which excess air is provided to burn 1 mole of methane. Let the excess air have n moles of oxygen, where $n > 2$.



The application of the Law of Conservation of Mass to the reaction equation with excess air gives the following equality.

$$\begin{aligned} (n) \left(32 \frac{\text{lb}_m}{\text{lb mole}} \right) + (3.76)(n) \left(28 \frac{\text{lb}_m}{\text{lb mole}} \right) + (1 \text{ lb mole}) \left(16 \frac{\text{lb}_m}{\text{lb mole}} \right) = \\ (1 \text{ lb mole}) \left(44 \frac{\text{lb}_m}{\text{lb mole}} \right) + (2 \text{ lb mole}) \left(18 \frac{\text{lb}_m}{\text{lb mole}} \right) + \\ (n-2) \left(32 \frac{\text{lb}_m}{\text{lb mole}} \right) + (3.76)(n) \left(28 \frac{\text{lb}_m}{\text{lb mole}} \right) \end{aligned}$$

The "excess air" is defined as the percent of air in excess of that required for stoichiometric combustion. The computation of percent excess air is as follows:

$$\% \text{ Excess Air} = \frac{\text{Actual Air Flow} - \text{Stoichiometric Air Flow}}{\text{Stoichiometric Air Flow}} \times 100\% =$$

$$\frac{(n-2)[32 + (3.76)(28)]}{(2)[32 + (3.76)(28)]} \times 100\% = \frac{(n-2)}{2} \times 100\%$$

The amount of excess air can be used to control the temperature of the flow after combustion. During the combustion process, the amount of fuel controls the amount of heat released. The release of heat raises the temperature of all gases in the output stream. When there is excess air, more gas is present to be heated than there would be if only stoichiometric air were provided. Thus, the higher the % of excess air, the lower the combustion temperature.

The heat released during combustion can be calculated from the heats of formation for the various reactants and products of the reaction. Heats of formations for the reactant and products for combustion of methane have been obtained from Reference A.1. They are listed in Table A-1. They are based on the arbitrary, but most common, assumption of a scale which sets the enthalpy of diatomic gasses such as O_2 and N_2 at 0 Btu/lbm-°F at temperature = 25°C = 77°F.

$$\text{Heat Release} = Q_{rel} = - \sum_{\text{Pr oducts}} (\eta_p)(H_{f,p}) + \sum_{\text{Re ac tan ts}} (\eta_r)(H_{f,r})$$

where: Q_{rel} = heat release, BTU

η = number of moles, lb_{mole}

H_f = heat of formation, BTU/lb_{mole}

subscript p designates product compounds

subscript r designates reactant compounds

The heat released during the reaction causes the temperature and enthalpy of the products to increase. If we assume that the products initially form at 77°F, and that there is no loss of the heat released during the reaction (i.e., all heat released goes to heating the products), then the energy balance equation can be used to calculate the final enthalpy.

$$Q_{rel} = \sum_{\text{Pr oducts}} [\eta_p] \left[h_p(P_{cc}, T_{cc}) \right] - \sum_{\text{Pr oducts}} [\eta_p] \left[h_p(P_{cc}, 77^\circ F) \right]$$

where: $h_p(P_{cc}, T_{cc})$ = enthalpy of the product compound
corresponding to the values for pressure and
temperature in the combustion chamber, BTU/lb_{mole}

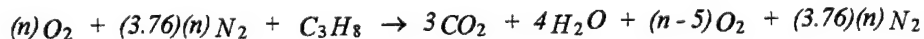
The temperature " T_{cc} " cannot be calculated explicitly. The solution process is: (1) calculate Q_{rel} ; (2) calculate the summation of $[\eta_p] * [h_p(P_{cc}, 77^\circ F)]$; (3) Assume a value of T_{cc} (call it T_{assum}); (4) calculate the summation of $[\eta_p] * [h_p(P_{cc}, T_{assum})]$; (5) Determine if Q_{rel} equals the difference of the summations; and (6) iteratively change T_{assum} until the equality is true.

Figure A-1 presents combustion temperatures for methane-air reaction for various percentages of excess air from 0 to 1000%.

Combustion of Propane in Air.

Propane has the chemical formula C_3H_8 . It is a heavier compound in the same family as methane, i.e., the family of compounds C_aH_{2a+2} .

The procedure for computation of heat released and the combustion temperature for a propane-air reaction is basically the same as for a methane-air reaction. The reaction equation and the equation for percent of excess air are slightly different because of the increased number of carbon and hydrogen atoms. The reaction equation for propane with excess air is as follows:



For stoichiometric combustion, $n = 5$. Therefore, the computation of % excess air for the propane-air reaction is:

$$\% \text{ Excess Air} = \frac{(n - 5)}{5} \times 100\%$$

Heat release and combustion temperature computations are made in the same way for propane-air reactions as for methane-air reactions. Figure A-1 presents propane-air combustion temperatures for 0 to 1000% excess air.

A.2 NOZZLE FLOW ANALYSIS

The initial testing with the NFESC Aviation Engine Simulation Facility will be with subsonic flow (Mach number < 1) discharged from the nozzles and directed onto the concrete samples. Future plans call for sonic (Mach number $= 1$) or supersonic flow (Mach number > 1) from the nozzles. These different flow parameters can be achieved by installing nozzles of different geometry, and varying the pressure upstream of the nozzles.

Figure A-2 illustrates typical nozzle shapes and shows the corresponding ranges of pressures which must be maintained upstream of the nozzles to achieve either subsonic, sonic, or supersonic flow.

Subsonic Flow

As shown in Figure A-2(a), the typical subsonic nozzle will be a converging nozzle. Upstream of the nozzle is a "plenum", where the volume and cross-sectional area are large compared to the nozzle. The "plenum" is the combustion chamber, for which the properties are discussed in the previous section, **COMBUSTION ANALYSIS**. At the exit of the nozzle, the pressure is very near atmospheric. The pressure in the combustion chamber must be greater than the pressure at the nozzle exit. Reference A.2 shows that there is a maximum pressure in the combustion chamber for maintaining subsonic flow at the nozzle exit. If the chamber pressure equals or exceeds the maximum pressure, the flow will become sonic at the nozzle exit. For isentropic flow of air, assumed to be a perfect gas, the limiting pressure in the combustion chamber is $(1.893)P_{exh}$.

$$(1.893)P_{exh} > P_{cc} > P_{exh} = P_{atm}$$

$$\text{where: } P_{atm} = 14.7 \text{ lb}_f/\text{in}^2 = 2117 \text{ lb}_f/\text{ft}^2$$

Reference A.2 explains that, in a subsonic flow, converging flow increases velocity. Flow velocity is very slow in the plenum, but increases as it moves toward the nozzle exhaust. As P_{cc} increases, velocity at the exhaust increases.

Sonic Flow

The case of sonic flow is illustrated in Figure A-2(b). The sonic nozzle is basically the same as the subsonic nozzle. However, to achieve sonic flow at the nozzle exhaust, i.e. mach number $= 1$, at the nozzle exhaust, the combustion chamber pressure is raised above the limits for subsonic flow. For air, sonic flow is achieved when the chamber pressure satisfies the inequality below.

$$P_{cc} \geq (1.893)P_{exh} = (1.893)P_{atm}$$

The subsonic and sonic nozzles both converge to a minimum area at the exhaust. Reference A.2 explains that exhaust velocity increases as P_{cc} increases. Similarly, exhaust mach number increases as P_{cc} increases, until $P_{cc} = (1.893)P_{exh}$. When $P_{cc} = (1.893)P_{exh}$, the mach number at the exhaust is $M_{exh} = 1$. After that, further increases in P_{cc} do not change $M_{exh} = 1$, although the exhaust velocity continues to increase.

The minimum area of a nozzle is called the "throat". If the plenum pressure is high enough, i.e. $P_{cc} \geq (1.893)P_{exh}$, then the mach number at the throat is always $M_{thr} = 1$.

Supersonic Flow

The supersonic nozzle is illustrated in Figure A-2(c). The supersonic nozzle converges to a throat, then slightly diverges. With this shape, the flow is subsonic and increasing in velocity as the nozzle converges from the plenum to the throat, the flow becomes sonic at the throat, then the flow is supersonic and continues to increase in velocity as the nozzle diverges from the throat to the exhaust. To achieve supersonic flow in air,

$$P_{cc} \geq (1.893)P_{exh} = (1.893)P_{atm}$$

Reference A.2 explains how the converging/diverging nozzle creates supersonic flow if the plenum pressure is sufficiently high.

Adiabatic Flow Relationships

The assumption is made that the plenum and nozzle are well insulated. If so, the heat transfer losses will be small, and the assumption of adiabatic flow closely represents the actual flow conditions.

The equation for the conservation of energy (the First Law of Thermodynamics) in the nozzle can be applied to the control volume illustrated in Figure A-2(a). Flow enters the control volume at the lower end of the combustion chamber, and leaves the control volume at the nozzle exit plane. At the lower end of the combustion chamber, the flow temperature = T_{cc} , which can be computed as explained in the previous section, **COMBUSTION ANALYSIS**. Also at the lower end of the combustion chamber, the flow pressure = P_{cc} is regulated to give either subsonic, sonic, or supersonic flow, as desired. Regulation of the pressure will be discussed later, but for now simply assume that the flow pressure, P_{cc} , will be at the desired value.

$$\left(\frac{dE}{dt}\right)_{cv} = Qdot + Wdot + \left(\sum_{Products} \eta_p MW_p\right)_{in} \left[h_{ave}(P_{cc}, T_{cc}) + \frac{V_{exh}^2}{2g_c J} + \frac{gz_{cc}}{g_c J} \right] - \left(\sum_{Products} \eta_p MW_p\right)_{out} \left[h_{ave}(P_{exh}, T_{exh}) + \frac{V_{exh}^2}{2g_c J} + \frac{gz_{exh}}{g_c J} \right]$$

where: $(dE/dt)_{cv} = 0$ Rate of energy change in control volume, BTU/sec ("0" indicates steady state flow)

$Qdot = 0$ Rate of heat transfer between control volume and its environment, BTU/sec ("0" indicates adiabatic flow)

$Wdot = 0$ Rate of transfer of shaft work between the control volume and its environment, BTU/sec ("0" indicates no shaft work)

$\Sigma \eta_p MW_p$ = mass flow rate, lb_m/sec (mass flow rate in = mass flow rate out)

$h(P, T)$ = enthalpy, which is a function of pressure and temperature, BTU/lb_m

V = velocity of flow, ft/sec ($V_{cc} \approx 0$ indicates negligible flow velocity in the combustion chamber)

z = height above a reference plane, ft ($[(gz_{cc}/g_c J) - (gz_{exh}/g_c J)] \approx 0$ indicates negligible potential energy)

g = gravitational constant
= 32.2 ft/sec²

g_c = gravitational conversion constant
= 32.2 ft-lb_m/lb_f-sec²

J = Joules constant
= 778 ft-lb_f/BTU

The equation for the conservation of energy through the nozzle reduces to

$$h_{ave}(P_{exh}, T_{exh}) = h_{ave}(P_{cc}, T_{cc}) - \frac{V_{exh}^2}{2g_c J}$$

The solution process is as follows:

- (1) from engine data for the full scale engine being simulated, determine V_{exh} ;
- (2) use the solution from the previous section to calculate $h_{ave}(P_{cc}, T_{cc})$;
- (3) calculate $h_{ave}(P_{exh}, T_{exh})$.

With two state properties at the nozzle exhaust (i.e., h and p), other state properties can be calculated. The procedure starts by iteratively determining T_{exh} , as follows:

- (1) assume a value of T_{exh} (call it T_{assum});
- (2) calculate $h_{ave}(P_{exh}, T_{assum})$;
- (3) determine if $h_{ave}(P_{exh}, T_{assum}) = h_{ave}(P_{exh}, T_{exh})$; and (4) iteratively change T_{assum} until the equality is true.

At the moderate pressures and temperatures of the flow in the nozzle, the exhaust gas can be treated as an ideal gas. The ideal gas law relates the density, temperature, and pressure of the gas.

$$\rho_{exh} = \frac{P_{exh}}{R_{exh} T_{exh}} = \frac{P_{exh}}{\left(\frac{\mathfrak{R}}{MW_{exh}}\right) T_{exh}}$$

where: ρ_{exh} = mass density of exhaust flow, lb_m/ft^3

R_{exh} = gas constant, $ft-lb_f/lb_m-^{\circ}R$

\mathfrak{R} = universal gas constant = $1545 \text{ ft-lb}_f/lb_{mole}-^{\circ}R$

$$MW_{exh} = \frac{\sum_{Pr\ oducts} [\eta_p [MW_p]]}{\sum_{Pr\ oducts} \eta_p}$$

= molecular weight of the exhaust flow, lb_m/lb_{mole}

η_p = number of moles of compound p , lb_{mole}

Two additional terms of interest for nozzle flow characterization are the speed of sound and the mach number at the nozzle exhaust.

$$a_{exh} = (g_c \gamma R_{exh} T_{exh})^{1/2}$$

$$M_{exh} = \frac{V_{exh}}{a_{exh}}$$

where: a_{exh} = speed of sound at the nozzle exhaust, ft/sec

γ = ratio of specific heats = c_p/c_v , dimensionless

M_{exh} = Mach number at nozzle exhaust, dimensionless

c_p = specific heat at constant pressure, BTU/lb_m-°R

c_v = specific heat at constant volume, BTU/lb_m-°R

The specific heats can be calculated as follows:

$$c_{p,exh} = \frac{\sum_{\text{Products}} [m_p][c_{p,products}(T_{exh})]}{\sum_{\text{Products}} m_p}$$

$$c_{v,exh} = c_{p,exh} - \frac{R_{exh}}{J}$$

The mass flow rate from the nozzle is

$$\dot{m}_{exh} = \rho_{exh} A_{exh} V_{exh}$$

where: A_{exh} = cross-sectional area normal to the direction of flow, ft²

These expressions can be used to calculate the flow conditions at the exhaust of a nozzle, knowing the conditions in the combustion chamber. Of particular interest for this report, the expressions can be used to design a subscale nozzle which simulates the flow from the nozzle of a full scale engine for which we know the exhaust conditions.

A.3 ANALYSIS OF TURBULENT JET FLOW

Exhaust Flow into Still Air, without Impingement on a Specimen

If uniform flow from the nozzle is blowing into still air, with no test specimen in its path, the flow pattern develops as shown in Figure A-3(a). The flow leaves the nozzle at more-or-less uniform velocity, and the static pressure at the exit plane is very close to atmospheric pressure. Taking any streamline at the nozzle exit plane, the total pressure is

$$P_{Total} = P_{cc} = P_{exh} \left[1 + \frac{(\gamma - 1)}{2} M_{exh}^2 \right]^{\frac{\gamma}{\gamma - 1}}$$

As the flow moves downward from the nozzle exit plane, there is friction between the moving fluid of the jet and the still air. A shear layer grows at the outer edge of the jet. In the jet core, outward to the inside edge of the shear layer, the velocity remains the same as at the nozzle exhaust. The outer boundary of the shear layer can be defined in different ways, e.g., where velocity = 0, or where total momentum within the interior of the boundary equals the momentum at the nozzle exit plane. In the jet core, the total pressure remains P_{cc} . In the shear layer, however, the viscous forces cause the total pressure to drop from P_{cc} to P_{atm} . The shear layer and the jet core are identified in Figure A-3(a). The jet core is sometimes called the "inviscid core region" because viscous forces are negligible in that short region. In the inviscid core region,

$$P_{Total} = P_{cc}$$

In the shear layer, at position (z, r)

$$P_{cc} \geq P_{Total} = f(z, r) \geq P_{atm}$$

where $f(z, r)$ = a function to be determined.

Beyond the point where the shear layer extends to the centerline of the jet exhaust, there is no longer an inviscid core. All streamlines of the jet flow are affected by viscosity, and the total pressure of each streamline is reduced below P_{cc} . Downstream of the inviscid core, the total pressure distribution at position (z, r) within the jet plume is

$$P_{cc} \geq P_{Total} = g(z, r) \geq P_{atm}$$

where $g(z, r)$ = another function to be determined.

References A.3 and A.4 give empirical relationships for $f(z,r)$ and $g(z,r)$. These functions can also be derived, as shown in Reference A.3, if one makes the assumptions that the nozzle exit flow is uniform, and that the turbulent mixing length is proportional to the width of the shear layer. In an even more complicated approach, the flow variables throughout the entire flow field can be estimated using Computational Fluid Dynamics (CFD) methods. However, the accuracy of the estimation of flow variables may be dependent on the validity of the assumption that the flow at the nozzle exit is uniform. This must be validated by measurements at or near the nozzle exit. Such measurements were done for the NFESC Aviation Engine Simulation Facility.

Flow at the nozzle exit might not be uniform due to flow patterns and combustion characteristics in the combustion chamber. For example, the swirl imparted to the intake air to increase its residence time in the combustion chamber may make velocities higher toward the inside of the nozzle. Or uneven combustion patterns in the chamber may make velocities higher on one side of the nozzle. The only way to verify the uniformity of the flow at the nozzle exit is to measure the flow. Since these measurements are required at the nozzle exit, it is advisable to also measure the flow properties at other "z" planes. Skewing, unevenness, or non-symmetry of flow, if present, will show up at other "z" planes. These measurements will eliminate the need for empirical relationships or for calculations to get $f(z,r)$ and $g(z,r)$.

Assume that a uniform nozzle exhaust flow and a plume exhaust flow that is symmetrical about the vertical centerline have been achieved. Consider then a streamline, such as the one designated "A" in Figure A-3(a). As flow moves along the streamline, the total pressure drops from P_{cc} to some lower value, $f(z,r)$ or $g(z,r)$, depending upon the path of the streamline. The velocity also decreases from V_{exh} to some lower value. What is constant for the streamline, however, is the mass flow rate inside its surface of revolution about the plume axis.

Exhaust Flow into Still Air, Impinging on a Specimen

Figure A-3(b) depicts the flow from a nozzle impinging on a specimen whose surface is parallel to the nozzle exit plane. Some important characteristics of the impinging flow are:

- (1) The center streamline impinges perpendicularly at the point designated the stagnation point, where theoretically the velocity becomes zero.
- (2) The other streamlines approach the specimen at an angle < 90 degrees and, in the vicinity of the surface of the specimen, turn more or less parallel to the surface.
- (3) The flow moving approximately parallel to the specimen surface creates a boundary layer.
- (4) The distance between the exit plane of the nozzle and the surface of the specimen influences the pressures and the size of the impingement zone. When the jet nozzle is close to the surface, the pressures in the impingement zone will be high and the impingement zone will be small.

When the nozzle is far from the surface, the pressure in the impingement zone will be low and impingement zone will be large.

The presence of a specimen significantly complicates the jet plume flow field. To analyze the flow field with a specimen in place, CFD computer programs are often used. If a CFD program is used, a prohibitively small grid pattern might be required near the specimen surface to accurately predict the boundary layer details. Rather than use CFD, an empirical approach is formulated in this report which relates flow properties measured at points in the plume flow field, without the specimen, to flow properties at corresponding points along the upper edge of the boundary layer when a specimen is placed in the plume. The approach allows us to estimate the boundary layer growth on the specimen, and to proceed with conventional approaches to estimate convective heat fluxes and temperature histories of the specimens.

Measurements Required in the Jet Exhaust Plume and on the Specimen

During experimentation, it is necessary to make measurements which allow calculation of the convective heat transfer rates. The measured data change as nozzles or nozzle exit flow conditions are changed and as the distances change between nozzle exit planes and the samples. The recommended measurements and the recommended approach for using the experimental data to calculate convective heat transfer rates are described below.

- (1) Select a nozzle and exit flow conditions (e.g., the simulated A/F-18 APU nozzle).
- (2) Determine the scaled distance "z" between the nozzle exit plane and the surface of the sample ($z = [\text{diameter of nozzle for tests} / \text{diameter of full scale nozzle}] [\text{full-scale distance from nozzle exit to ground}]$).
- (3) Measure $P_{\text{Total}}(z, r)$ and $T_{\text{Total}}(z, r)$ across the jet plume flowing as a free jet, i.e., without a sample surface placed in the exhaust flow.
- (4) Place a sample in the exhaust flow at a distance z from the nozzle exit plane, and measure static pressure $P(z, x)$ along the surface of the sample. (Note that the radial dimension in a free plume is called "r". But when the plume impinges on the surface of a sample, the radial dimension along the surface of the sample is called "x".)

These data are used to estimate the velocity $U(x)$, which is the component parallel to the specimen surface, occurring along the outer edge of the boundary layer.

Curve Fit of Velocity at Boundary Layer Edge

Analysis of Measurements in the Plume

The pressure measurements are used to determine the velocity at the outer edge of the boundary layer, which is a boundary condition necessary for

the solution of the boundary layer equations. Pressure and velocity in the plume are related by the isentropic equation for total pressure.

$$P_{Total}(z,r) = P(z,r) \left[1 + \frac{\gamma-1}{2} M^2 \right]^{\left(\frac{\gamma}{\gamma-1} \right)}$$

Use the measurements of $P_{Total}(Z_n, r)$ across the jet exhaust flowing as a free jet to determine the total pressure of each streamline. Streamlines are lines of constant flow rate, \dot{m} , where the flow rate is measured as the amount of flow per unit time (lb_m/sec) through the area inside the radial position "r". From the measurements of $P_{Total}(Z_n, r)$, plot $P_{Total}(Z_n, r)$ versus $\dot{m}(Z_n, r)$. The calculation procedure to get the values of \dot{m} in the plume from the experimental data is as follows.

$$M(z,r) = \left\{ \left[\left(\frac{P_{Total}(z,r) + 14.7}{P_{atm}} \right)^{\left(\frac{\gamma-1}{\gamma} \right)} - 1 \right] \left(\frac{2}{\gamma-1} \right) \right\}^{1/2}$$

where $M(z,r)$ = Mach number at position (z,r) , dimensionless

P_{atm} = atmospheric pressure = 14.7 psia

P_{total} = total pressure, psig

γ = ratio of specific heats = 1.4, dimensionless

$$T(z,r) = \frac{T_{Total}(z,r) + 460}{\left[1 + \frac{\gamma-1}{2} M^2(z,r) \right]} - 460$$

where $T_{total}(z,r)$ = total temperature at position (z,r) , deg F

$$c(z,r) = [g_c \gamma R (T(z,r) + 460)]^{1/2}$$

where R = gas constant for the exhaust flow = 53.3 $\text{ft-lb}_f/\text{lb}_m\text{-}^\circ\text{F}$

g_c = gravitational constant units conversion factor = 32.2 $\text{ft-lb}_f/\text{lb}_m\text{-sec}^2$

$$V(z,r) = M(z,r) c(z,r)$$

where $V(z,r)$ = velocity of the flow in the jet exhaust at position (z,r) , ft/sec

$$\rho(z,r) = \frac{P_{atm}}{R(T(z,r) + 460)}$$

where $\rho(z,r)$ = density of the exhaust flow at position (z,r) ,
lb_m/ft³

$$\dot{m}(z,r) = \int_0^r \rho(z,r) V(z,r) \pi(2r) dr$$

where $\dot{m}(z,r)$ = the mass flow rate between the plume centerline
and the radial position r at distance z below
the exit plane of the nozzle, lb_m/sec

The integration for $\dot{m}(z,r)$ must be performed numerically. Figures A-4 and A-5 graphically present typical relationships between " $\dot{m}(z,r)$ " versus " $P_{Total}(z,r)$ " and " $\dot{m}(z,r)$ " versus " $T_{Total}(z,r)$ " in the plume of a turbulent jet.

Analysis to Determine Flow Parameters and Velocity at the Boundary Layer Edge

A specially instrumented plate was fabricated to measure static pressure distributions $P(z,x)$ on specimens placed at a distance " z " from the nozzle exit plane. The static pressures $P(z,x)$ were measured on the surface of the specimen, but, consistent with boundary layer theory, were equal to the static pressures at the edge of the boundary layer at the corresponding location.

Figure A-6 shows a typical variation of static pressure versus radial position on a specimen subjected to perpendicular impingement of a turbulent jet exhaust. The centerline of the plume ($r = 0$) impinges on the specimen at the stagnation point, ($x = 0$). At the stagnation point, the flow velocity and Mach number decrease to zero, and the static pressure and total pressure are equal.

$$P_{Total}(z,r=0) = P_{Total}(z,x=0) = P(z,x=0)$$

At positions away from the stagnation point, the static pressure decreases, until at some position $x = L$, the static pressure and atmospheric pressure are equal. Further away from the stagnation point, the pressure remains constant at atmospheric pressure. At $x = L$, the velocity and Mach number of the flow parallel to the surface of the specimen have become maximum, and remain essentially constant further outward.

Values of $U(z,x)$, dU/dx , and other parameters along the edge of the boundary layer are determined as follows.

First, assume that

$$P_{Total}(z,x) = P_{Total}(z,x=0)$$

$$T_{Total}(z,x) = T_{Total}(z,x=0)$$

This is not exactly valid at x positions well away from the stagnation point, but correction of the assumption can be made later.

Then using the measured static pressures, such as the distribution shown in Figure A-6, calculate mach number, static temperature, speed of sound, and velocities at various radial positions at the outer edge of the boundary layer.

$$M(z, x) = \left\{ \left[\left(\frac{P_{Total}(z, x) + 14.7}{P(z, x)} \right)^{\left(\frac{\gamma - 1}{\gamma} \right)} - 1 \right] \left(\frac{2}{\gamma - 1} \right) \right\}^{1/2}$$

$$T(z, x) = \frac{T_{Total}(z, x) + 460}{\left[1 + \frac{\gamma - 1}{2} M^2(z, x) \right]} - 460$$

$$c(z, x) = [g_c \gamma R (T(z, x) + 460)]^{1/2}$$

$$U(z, x) = M(z, x) c(z, x)$$

$$\rho(z, x) = \frac{P(z, x)}{R(T(z, x) + 460)}$$

$$\dot{m}(z, r) = \int_0^r \rho(z, r) U(z, r) \pi(2r) dr$$

The velocity distributions as functions of x (plural because there is a different distribution for each z and for each simulated engine setting) are needed in the solution of the boundary layer equations. The distributions can be used in tabular form. For the analyses of this report, however, curve fits were made of the distributions. The curve fits were beneficial because: (a) they facilitated calculation of dU/dx, which is also needed in the boundary layer solution; (b) they facilitated calculation of U and dU/dx at points between data points; and (c) they facilitated examination of the "smoothness" of the curves and the ability to make small adjustments necessary to smooth out the effects of experimental error and uncertainty.

The curve fit technique was to express the velocity at the outer edge of the boundary layer as a polynomial function of non-dimensional distance

between the stagnation point and the point where the static pressure equals atmospheric pressure.

$$U(z,x) = b_0 + b_1(x/L) + b_2(x/L)^2 + b_3(x/L)^3 + b_4(x/L)^4 + b_5(x/L)^5 + b_6(x/L)^6 + \dots$$

where: b_0, b_1, \dots are coefficients to be determined from the experimental data. They will change as the "z" position of test specimen is changed, so they are functions of z. The units of each b_n are ft/sec.

L = the distance from the stagnation point at which the static pressure of the impingement flow drops to atmospheric pressure, ft

Experience has shown that a reasonable or logical boundary layer solution, derived and explained in Section A-4, is not obtained unless the velocity profile predicted by the techniques in this Section has the following characteristics: (1) the velocity must monotonically increase in the region $x = 0$ to L ; and (2) the profile must have a $dU/dx > 0$ in the region $x = 0$ to L . A single polynomial curve fit cannot accurately represent the flow velocity in the region $x = 0$ to L , and smoothly match $U = \text{constant}$ at $x > L$. The application of three polynomial curve fits generally has been necessary to give a smooth representation of $U(z,x)$ over the entire specimen. The recommended limits for the curve fits are for the regions $x = 0$ to $0.625L$, $x = 0.625L$ to $0.875L$, and $x = 0.875L$ to L .

Region $x=0$ to $x=0.625L$.

Represent the velocity distribution in this region with the truncated series

$$U(z,x) = b_0 + b_1 (x/L) + b_2 (x/L)^2 + b_3 (x/L)^3$$

At the stagnation point,

$$U(z,0) = 0$$

This yields $b_0 = 0$. The other three coefficients can be found so that the curve plotted from the curve fit will pass through selected values of $U(z,x)$, and will have positive slope dU/dx throughout the region. Experience has shown that these characteristics can be achieved if the curve is forced to pass through $U(z,x=0.25)$ and $U(z,x=0.625)$, and if the slope $dU/dx=0$ at $x=L$. (Note that the point $x=L$ is outside the region of the portion of the curve fit, but forcing the slope to go to 0 at $x=L$ helps with the requirement that dU/dx remain positive.)

The equations to determine b_1, b_2 , and b_3 for the first region are:

$$U(z,x=0.25L) = b_1^{(1)} (0.25) + b_2^{(1)} (0.25)^2 + b_3^{(1)} (0.25)^3$$

$$U(z,x=0.625L) = b_1^{(1)} (0.625) + b_2^{(1)} (0.625)^2 + b_3^{(1)} (0.625)^3$$

$$\left(\frac{dU}{dx}\right)_{(z,x=0L)} = 0 = \left(\frac{1}{L}\right) \left(\frac{dU}{d\left(\frac{x}{L}\right)}\right)_{(z,x/L=1)} = \frac{1}{L} \left(b_1^{(1)} + b_2^{(1)} (1.0) + b_2^{(1)} (1.0)^2\right)$$

The equations can be expressed as a single matrix equation

$$U_{(1)} = C_{(1)} B_{(1)}$$

$$\text{where } U_{(1)} = \begin{pmatrix} U(z, x = 0.25) \\ U(z, x = 0.625) \\ 0 \end{pmatrix}$$

$$C_{(1)} = \begin{pmatrix} 0.25 & 0.0625 & 0.015625 \\ 0.625 & 0.390625 & 0.244140625 \\ 1 & 2 & 3 \end{pmatrix}$$

$$B_{(1)} = \begin{pmatrix} b_1^{(1)} \\ b_2^{(1)} \\ b_3^{(1)} \end{pmatrix}$$

The solution is

$$C_{(1)}^{-1} U_{(1)} = B_{(1)}$$

where $C_{(1)}^{-1}$ = the inverse of matrix $C_{(1)}$

$$= \begin{pmatrix} 0.296296 & -1.89629 & 0.111111 \\ -19.7925 & 8.912592 & -0.62222 \\ 10.42962 & -5.30962 & 0.711111 \end{pmatrix}$$

The matrix inversions and multiplications can be carried out using capabilities in Microsoft EXCEL® or LOTUS 123®.

Region $x=0.625L$ to $x=0.875L$.

Represent the velocity distribution in this region with the truncated series

$$U(z,x) = b_0^{(2)} + b_1^{(2)} \left(\frac{x}{L} \right) + b_2^{(2)} \left(\frac{x}{L} \right)^2$$

The coefficients $b_0^{(2)}$, $b_1^{(2)}$, and $b_2^{(2)}$ can be determined by forcing the curve to go through the calculated values of $U(z,x)$ at three different x positions. Select x/L values of 0.625, 0.75, and 0.875. The resulting equations are:

$$U(z,x=0.625L) = b_0^{(2)} + b_1^{(2)} (0.625) + b_2^{(2)} (0.625)^2$$

$$U(z,x=0.750L) = b_0^{(2)} + b_1^{(2)} (0.750) + b_2^{(2)} (0.750)^2$$

$$U(z,x=0.875L) = b_0^{(2)} + b_1^{(2)} (0.875) + b_2^{(2)} (0.875)^2$$

Values for $U(z,x)$ and dU/dx are determined as for the region $x = 0$ to $x = 0.625L$. Simultaneous solution of the three equations gives coefficients $b_0^{(2)}$, $b_1^{(2)}$, and $b_2^{(2)}$ for the curve fit for the region $x = 0.625L$ to $x = 0.875L$.

Region $x=0.875L$ to $x=1.0L$.

Represent the velocity distribution in this region with the truncated series

$$U(z,x) = b_0^{(3)} + b_1^{(3)} \left(\frac{x}{L} \right) + b_2^{(3)} \left(\frac{x}{L} \right)^2$$

The coefficients $b_0^{(3)}$, $b_1^{(3)}$, and $b_2^{(3)}$ can be determined by forcing the curve to go through the calculated values of $U(z,x)$ at two different x positions ($x=0.875L$ and $x=1.0L$), plus forcing the curve to have zero slope at $x=1.0L$. The resulting equations are:

$$U(z,x=0.875L) = b_0^{(3)} + b_1^{(3)} (0.875) + b_2^{(3)} (0.875)^2$$

$$U(z,x=1.0L) = b_0^{(3)} + b_1^{(3)} (1.0) + b_2^{(3)} (1.0)^2$$

$$\left(\frac{dU}{dx} \right)_{(z,x=1.0L)} = 0 = \left(\frac{1}{L} \right) \left(\frac{dU}{d\left(\frac{x}{L} \right)} \right)_{(z,x/L=1)} = \frac{1}{L} (b_1^{(3)} + b_2^{(3)} (1.0) + b_2^{(3)} (1.0)^2)$$

Values for $U(z,x)$ and dU/dx are determined as for the other two regions. Simultaneous solution of the three equations gives coefficients $b_0^{(3)}$, $b_1^{(3)}$, and $b_2^{(3)}$ for the curve fit for the region $x = 0.875L$ to $x = 1.0L$.

A.4. ANALYSIS OF BOUNDARY LAYER FLOW

The non-linear partial differential equations which represent conservation of mass, momentum, and energy in boundary layers of the specimens are, respectively:

$$\frac{\partial(\rho ur)}{\partial x} + \frac{\partial(\rho vr)}{\partial y} = 0$$

$$\rho u \frac{\partial u}{\partial x} + \rho v \frac{\partial u}{\partial y} = \rho U \frac{dU}{dx} + \frac{\partial}{\partial y} \left(\mu \frac{\partial u}{\partial y} \right)$$

$$\rho c_p \left(u \frac{\partial T}{\partial x} + v \frac{\partial T}{\partial y} \right) = \frac{\partial}{\partial y} \left(k \frac{\partial T}{\partial y} \right) + \frac{\mu}{Jg_c} \left(\frac{\partial u}{\partial y} \right)^2$$

where u = velocity component in the boundary layer, parallel to specimen surface, ft/sec

U = velocity component at the outer edge of the boundary layer, parallel to the specimen surface, ft/sec

v = velocity component in the boundary layer, perpendicular to specimen surface, ft/sec

r = radius of rotation of surface about axis of symmetry, ft

ρ = density, lb_m/ft³

μ = coefficient of viscosity, lb_m/ft-sec

T = temperature, °F

k = thermal conductivity, Btu-ft/ft²-sec-°F

c_p = specific heat at constant pressure, Btu/lb_m-°F

g_c = gravitational conversion constant, 32.2 ft-lb_m/lb_f-sec²

J = Joule's constant, 778 ft-lb_f/Btu

x = distance along surface of specimen, ft

y = distance perpendicular to surface of specimen, ft

Since the boundary layers on the specimens are symmetrical about the stagnation point and the axis of the exhaust plume, the axisymmetric form of the boundary layer equations have been presented. Reference A3 presents several solutions for the boundary layer equations, including solutions for axisymmetric flow and rectilinear flow (flow in which there are no changes in properties in the direction perpendicular to the plane of the paper), solutions for surfaces with pressure gradient (dp/dx and $dU/dx \neq 0$) or without pressure gradient (dp/dx and $dU/dx = 0$), and solutions for incompressible flow ($\rho = \text{constant}$) and compressible flow ($\rho = \rho(x,y)$). For this report, the selected solution is for axisymmetric flow, with a pressure change along the surface, but with assumed incompressible flow. The assumption of incompressible flow can be justified because flow velocities (actually Mach numbers) have been found to be low enough so that compressibility effects are negligible in the boundary layer and along the outer edge of the boundary which forms on specimens during impingement of the jet exhausts on the specimens. Mach numbers are ≤ 0.5 .

An advantage resulting from the assumption of incompressible flow is that the energy conservation equation does not have to be solved simultaneously with the conservation equations for momentum and mass. This is understood by noting that the dependent variables in the conservation of mass and momentum equations are: ρ, r, u, v, U , and μ . However, $r = r(x)$ from the geometry of the axisymmetric body; $U(x)$ comes from the curve fit explained in Section A.3.4; and if $p(x)$ and $T(x)$ at the outer edge of the boundary layer are determined as outlined in **APPENDIX A.3**, then $\rho = P/RT$ and $\mu = \mu(T)$. This only leaves "u" and "v" to be determined from the two equations, conservation of mass and conservation of momentum.

A disadvantage of assuming incompressible flow is that the lack of a solution of the energy conservation equation appears to preclude determination of the convective heat transfer rate between the boundary layer flow and the specimens, which is calculated with the term $k(\partial T/\partial y)_{y=0}$. This apparent difficulty is overcome by using the "Reynolds' Analogy", which is discussed at the end of this section of the **APPENDIX**.

Integral Solution of the Boundary Layer Equations

Of the several types of boundary layer solutions presented in Reference A.3, the "Integral Solution" was selected for analyses of the Aviation Engine Simulation Facility, primarily because the variables defined in the solution are relatively easily associated with physical properties described so far. The starting point for the Integral Solution is the integral form of the boundary layer momentum equation. For any arbitrary position x along the surface, the momentum equation is integrated from the surface ($y=0$) to the outer edge of the boundary layer ($y = \delta$). Details of the derivation can be found in Reference A.3.

$$\int_0^{\delta} u \frac{\partial u}{\partial x} dy + \int_0^{\delta} v \frac{\partial u}{\partial y} dy - \int_0^{\delta} U \frac{dU}{dx} dy = \int_0^{\delta} \frac{1}{\rho} \frac{\partial}{\partial y} \left(\mu \frac{\partial u}{\partial y} \right) dy$$

$$= \frac{1}{\rho} \left[\mu \left(\frac{\partial u}{\partial y} \right)_{\delta} - \mu \left(\frac{\partial u}{\partial y} \right)_0 \right] = - \frac{\tau_0}{\rho}$$

where $\mu(\partial u / \partial y)$ = shear stress, lb_f/ft^2

δ = boundary layer thickness, ft

From the equation for conservation of mass, the velocity "v" can be expressed in terms of "u".

$$v = - \frac{1}{r} \int_0^{\delta} \frac{\partial(ur)}{\partial x} dy$$

After substitution for "v", the second term of the momentum equation can be integrated by parts. With algebraic rearrangement, one gets

$$\int_0^{\delta} \frac{\partial}{\partial x} [u(U - u)] dy + \frac{\partial U}{\partial x} \int_0^{\delta} (U - u) dy + \frac{1}{r} \frac{dr}{dx} \int_0^{\delta} [u(U - u)] dy = \frac{\tau_0}{\rho}$$

Define a "displacement thickness" and a "momentum thickness".

$$\delta^* = \text{displacement thickness} = \int_0^{\delta} \left(1 - \frac{u}{U} \right) dy$$

$$\theta = \text{momentum thickness} = \int_0^{\delta} \frac{u}{U} \left(1 - \frac{u}{U} \right) dy$$

With these substitutions, the integral form of the momentum equation becomes:

$$\frac{d}{dx} (U^2 \theta) + \delta^* U \frac{dU}{dx} + \frac{1}{r} \frac{dr}{dx} U^2 \theta = \frac{\tau_0}{\rho}$$

Reference A.3 summarizes the approach of Pohlhausen, who recommended that the velocity profile of the boundary layer be expressed as a polynomial.

$$\frac{u}{U} = a_0(x) + a_1(x)\eta + a_2(x)\eta^2 + a_3(x)\eta^3 + a_4(x)\eta^4$$

where $\eta = y/\delta$, dimensionless

The terms $a_0(x)$, $a_1(x)$, $a_2(x)$, $a_3(x)$, and $a_4(x)$ are functions to be determined knowing boundary conditions which the velocity profile must satisfy. Those boundary conditions are:

$$\text{At } y = 0: \quad u = 0; \quad \rho U (dU/dx) = -\mu (\partial^2 u / \partial y^2) \quad (\text{momentum eqn at } y=0).$$

$$\text{At } y = \delta: \quad u = U; \quad \partial u / \partial y = 0; \quad \partial^2 u / \partial y^2 = 0.$$

In the solution for $a_0(x), \dots, a_4(x)$, a recurring group of variables is given a special designation.

$$\Lambda(x) = \frac{\rho \delta^2 dU}{\mu dx}, \quad (\text{shape factor, dimensionless})$$

In terms of Λ ,

$$a_0(x) = 0$$

$$a_1(x) = 2 + \frac{\Lambda}{6}$$

$$a_2(x) = -\frac{\Lambda}{2}$$

$$a_3(x) = -2 + \frac{\Lambda}{2}$$

$$a_4(x) = 1 - \frac{\Lambda}{6}$$

The velocity profile is:

$$\begin{aligned}\frac{u}{U} &= (2\eta - 2\eta^3 + \eta^4) + \frac{\Lambda}{6}(\eta - 3\eta^2 + 3\eta^3 - \eta^4) \\ &= F(\eta) + \Lambda G(\eta)\end{aligned}$$

$$\text{where } F(\eta) = 2\eta - 2\eta^3 + \eta^4$$

$$G(\eta) = (1/6)(\eta - 3\eta^2 + 3\eta^3 - \eta^4)$$

The objective of the solution of the equations for conservation of momentum and mass is to calculate $u(x,y)$ and $v(x,y)$ for any coordinate (x,y) in the boundary layer of the specimen. The manipulations made so far have introduced five new variables: Λ , δ , η , θ and δ^* . Five equations have also been introduced: (1) the definition of $\eta = y/\delta$; (2) the series expression for $u/U = f(\Lambda, \eta)$; (3) the definition of δ^* ; (4) the definition of θ ; and (5) the definition of the shape factor Λ . Further manipulations of the momentum equation were recommended by Holstein and Bohlen, Reference A.3, to get a form of the momentum equation that is amenable to numerical solution. The additional manipulations are: (1) as shown below, calculate and substitute the shear stress in terms of the shape factor variable; and (2) introduce a new variable, Z , defined below.

$$\frac{\tau_0}{\rho} = \frac{\mu}{\rho} \left(\frac{\partial u}{\partial y} \right)_0 = \frac{\mu U}{\rho \delta} \left(\frac{d \left(\frac{u}{U} \right)}{d\eta} \right)_{\eta=0} = \frac{\mu U}{\rho \delta} \left(2 + \frac{\Lambda}{6} \right)$$

$$Z = \frac{\theta^2}{\nu}$$

where: $\nu = \mu/\rho$, kinematic viscosity, ft^2/sec

The momentum equation can be rearranged to yield:

$$\frac{dZ}{dx} + \frac{2Z}{U} \frac{dU}{dx} \left[\left(2 + \frac{\delta^*}{\theta} \right) + \frac{U \left(\frac{dr}{dx} \right)}{\left(\frac{dU}{dx} \right)_r} - \frac{\left(2 + \frac{\Lambda}{6} \right)}{\Lambda} \frac{\delta}{\theta} \right] = 0$$

The numerical solution for the momentum equation in this form can be accomplished as follows:

Step 1: Start at the stagnation point, $x=0$. At the stagnation point, $U=0$. Therefore the second term of the rearranged momentum equation is finite only if the bracketed portion of the term also equals zero. Set the bracketed term equal to zero.

$$\left[\left(2 + \frac{\delta^*}{\theta} \right) + \frac{U \left(\frac{dr}{dx} \right)}{\left(\frac{dU}{dx} \right) r} - \frac{\left(2 + \frac{\Lambda}{6} \right)}{\Lambda} \left(\frac{\delta}{\theta} \right) \right]_{x=0} = 0$$

Use the following terms to express δ^*/θ and δ/θ as functions of Λ .

$$\frac{\delta^*}{\delta} = \int_{\eta=0}^{\eta=1} [1 - F(\eta) - \Lambda G(\eta)] d\eta = \frac{3}{10} - \frac{\Lambda}{120}$$

$$\frac{\theta}{\delta} = \int_{\eta=0}^{\eta=1} [F(\eta) + \Lambda G(\eta)] [1 - F(\eta) - \Lambda G(\eta)] d\eta = \left(\frac{37}{315} - \frac{\Lambda}{945} - \frac{\Lambda^2}{9072} \right)$$

For the boundary layer on the specimens, $r = x$. Also, in the vicinity of the stagnation point, $U = b_1 x$. Therefore,

$$\lim_{x \rightarrow 0} \left[\frac{U \left(\frac{dr}{dx} \right)}{\left(\frac{dU}{dx} \right) r} \right] = 1$$

The bracketed term becomes

$$\left[\frac{3\Lambda \left(\frac{37}{315} - \frac{\Lambda}{945} - \frac{\Lambda^2}{9072} \right) + \Lambda \left(\frac{3}{10} - \frac{\Lambda}{120} \right) - \left(2 + \frac{\Lambda}{6} \right)}{\left(\frac{37}{315} - \frac{\Lambda}{945} - \frac{\Lambda^2}{9072} \right)} \right]_{x=0} = 0$$

The solution is $\Lambda_1 = \Lambda(x=0) = 4.71600030$.

Step 2. Having determined the shape factor at the stagnation point, values of other variables can be determined also.

$$\delta_1 = \left(\frac{\rho \Lambda_1}{\left(\frac{dU}{dx} \right)_{x=0} \mu} \right)^{1/2} = \left(\frac{\rho \Lambda_1}{b_1^{(1)} \mu} \right)^{1/2}$$

Note: The boundary layer thickness is not zero at the stagnation point.

$$\theta_1 = \left(\frac{37}{315} - \frac{\Lambda_1}{945} - \frac{\Lambda_1^2}{9072} \right) \delta_1$$

$$Z_1 = \frac{\rho \theta_1^2}{\mu}$$

It can also be shown that

$$\left(\frac{dZ}{dx} \right)_{x=0} = 0$$

Step 3. Having solved for the boundary layer parameters at the stagnation point, the solution is continued by moving a distance Δx from the stagnation point and determining values of the boundary layer parameters there. The values must be obtained by iteration.

Note: The distance Δx is made the same as Δr in **APPENDIX A.5** so that the boundary layer solution and the subsequent convective heat transfer rates are located at the centers of nodes in the finite difference conduction solution.

Assume a value for $\Lambda_{2,asm} = \Lambda_{asm}(x=\Delta x)$. A reasonable initial assumption is $\Lambda_{2,asm} = \Lambda_1$.

Calculate

$$\delta_{2,assm} = \left(\frac{\rho \Lambda_{2,assm}}{\left(\frac{dU}{dx} \right)_2 \mu} \right)^{1/2}$$

$$\theta_{2,assm} = \left(\frac{37}{315} - \frac{\Lambda_{2,assm}}{945} - \frac{\Lambda_{2,assm}^2}{9072} \right) \delta_{2,assm}$$

$$\delta_{2,assm}^* = \left(\frac{3}{10} - \frac{\Lambda_{2,assm}}{120} \right) \delta_{2,assm}$$

$$Z_{2,assm} = \frac{\rho \theta_{2,assm}^2}{\mu}$$

$$\left(\frac{dZ}{dx} \right)_{2,assm} = - \frac{2 Z_{2,assm}}{U_2} \left(\frac{dU}{dx} \right)_2 \left[\left(2 + \frac{\delta_{2,assm}^*}{\theta_{2,assm}} \right) + \frac{U_2 \left(\frac{dr}{dx} \right)_2}{\left(\frac{dU}{dx} \right)_2 r_2} - \frac{\left(\frac{2 + \Lambda_{2,assm}}{6} \right)}{\Lambda_{2,assm}} \left(\frac{\delta}{\theta} \right)_{2,assm} \right]$$

$$Z_{2,calc} = Z_1 + \left[\frac{\left(\frac{dZ}{dx} \right)_1 + \left(\frac{dZ}{dx} \right)_{2,assm}}{2} \right] \Delta x$$

If $|\Lambda_{2,assm} - \Lambda_{calc}| \leq \text{tolerance}$, then $\Lambda_2 = \Lambda_{2,assm}$. Otherwise, change $\Lambda_{2,assm}$. When the tolerance is satisfied, go to step 4. The SOLVER subroutine available in the TOOLS menu of the Microsoft EXCEL® program was used to calculate the Λ 's which satisfied the iteration.

Step 4. Move radially another distance $\Delta x = \Delta r$ and repeat the calculations of Step 3. Continue moving radially until boundary layer solutions are obtained for all radial positions $0, \Delta x, 2\Delta x, 3\Delta x, \dots, N\Delta x$, which correspond to the radial positions used in the finite difference conduction solution

used to get the temperature history of the specimen (see Section A.5).

Note: The boundary layer solution obtained in Steps 1-4 above use the function $U(x) = b_0^{(n)} + b_1^{(n)}(x/L) + b_2^{(n)}(x/L)^2 + b_3^{(n)}(x/L)^3$, where $b_0^{(n)}$, $b_1^{(n)}$, $b_2^{(n)}$, and $b_3^{(n)}$ are calculated by the procedures described in **APPENDIX A.3**. In **APPENDIX A.3**, calculations of the values of $U(z,x)$ used in the curve fitting techniques to get $P_{total}(z,x)$ and $T_{total}(z,x)$ at the outer edge of the boundary layer were constants, and had the same values as $P_{total}(z,x=0)$ and $T_{total}(z,x=0)$. Actually, it is likely that $P_{total}(z,x) < P_{total}(z,x=0)$ and $T_{total}(z,x) < T_{total}(z,x=0)$ because streamlines away from the centerline streamline of the jet arrives at the outer edge of the boundary layer (see Figure A-3). To correct for the effects of different total pressures and temperatures at the boundary layer edge, first calculate the mass flow rate in the boundary layer.

$$\begin{aligned} \dot{m} \text{dotbl}(z,x) &= \int_0^\delta \rho u dy = \rho U \delta \int_{\eta=0}^{\eta=1} \left(\frac{u}{U} \right) d\left(\frac{y}{\delta} \right) \\ &= \rho U \delta \int_0^1 \left[(2\eta - 2\eta^3 + \eta^4) + \frac{\Lambda}{6} (\eta - 3\eta^2 + 3\eta^3 - \eta^4) \right] d\eta = \rho U \delta \left(\frac{7}{10} + \frac{\Lambda}{120} \right) \end{aligned}$$

With the calculated values of $\dot{m} \text{dotbl}(z,x)$, read corrected values of $P_{total}(z,x)$ and $T_{total}(z,x)$ from Figures A-4 and A-5. Recalculate selected values of $U(z,x)$, and decide if the changes from the original values are large enough to warrant new curve fits. If so, repeat the boundary layer solution with the new values and curve fits of $U(z,x)$.

Reynolds' Analogy

The most rigorous, and presumably the most accurate, solution for the rate of heat transfer between the boundary layer flow and the specimen is obtained by simultaneously solving the equations for conservation of mass, momentum, and energy. This is done with Computational Fluid Dynamic solutions. Another approach is explained in Reference A.3, in which several methods are presented for simultaneously solving the boundary layer forms of the complete conservation equations. Due to the complexity of the methods, a third approach was followed in this report. That approach is commonly called the "Reynolds' Analogy".

Reynolds' Analogy takes note of the mathematical similarity between the equations to calculate the rate of heat transfer from the boundary layer to the specimen and the equation to calculate the tangential shear stress between the boundary layer flow and the specimen. The mathematical similarities in the equations (and boundary conditions), leads to the assumption that the mathematical form of the solutions for the energy and momentum equations are similar, i.e., that the solution for $T(x,y)$ is similar to that for $u(x,y)$. A solution for $u(x,y)$ (actually for $u/U = f(\eta)$) was obtained above. With Reynolds' Analogy, one assumes that the solution for $T(x,y)$ is like that for

$u(x,y)$, and uses that assumption as a basis for calculating the rate of convective heat flux into the surface of the specimen. The problem of solving the boundary layer form of the energy equation is avoided entirely.

Refer to Figure A-6. At the surface of a specimen, the boundary layer flow causes shear stress parallel to the flow, and heat transfer from the hot exhaust gases to the specimen. The shear stress is predicted by the expression

$$\tau_w = \frac{\mu}{g_c} \left(\frac{\partial u}{\partial y} \right)_{y=0}$$

The heat transfer is predicted by the expression

$$q_w = k \left(\frac{\partial T}{\partial y} \right)_{y=0}$$

The mathematical forms of the equations are the same.

The shear stress equation can be rearranged as follows

$$\tau_w = \frac{\mu U}{g_c \delta_M} \left(\frac{d \left(\frac{u}{U} \right)}{d \eta_M} \right)_{\eta=0}$$

where: $U = U(z,x)$, the velocity at the edge of the boundary layer, ft/sec

δ_M = the thickness of the velocity boundary layer, ft

$\eta_M = \frac{y}{\delta_M}$, dimensionless

The heat transfer equation can also be rearranged.

$$q_w = \frac{k(T_{aw} - T_w)}{\delta_T} \left(\frac{d \left(\frac{T - T_w}{T_{aw} - T_w} \right)}{d \eta_T} \right)_{\eta=0}$$

where: $T_w = T_w(x)$, the specimen surface temperature, °F

$T_{aw} = T_{aw}(x)$, the "adiabatic wall temperature" for the boundary layer, i.e., the highest temperature which the boundary layer flow can force the specimen surface to reach, °F. The adiabatic wall temperature is approximately equal to the total temperature of the streamline at the outer edge of the boundary layer, i.e.,

$$T_{aw} \approx T(x, \delta_T) \left[1 + \left(\frac{\gamma - 1}{2} \right) M(x, \delta_T)^2 \right]$$

δ_T = the thickness of the thermal boundary layer, ft

It is noted that

$$\frac{u}{U} = 0 \quad , \quad \frac{T - T_w}{T_{aw} - T_w} = 0 \quad \text{at} \quad \eta = 0$$

$$\frac{u}{U} = 1 \quad , \quad \frac{T - T_w}{T_{aw} - T_w} = 1 \quad \text{at} \quad \eta = 1$$

$$\frac{d\left(\frac{u}{U}\right)}{d\eta_M} = 0 \quad , \quad \frac{d\left(\frac{T - T_w}{T_{aw} - T_w}\right)}{d\eta_T} = 0 \quad \text{at} \quad \eta = 1$$

$$\frac{d^2\left(\frac{u}{U}\right)}{d\eta_M^2} = 0 \quad , \quad \frac{d^2\left(\frac{T - T_w}{T_{aw} - T_w}\right)}{d\eta_T^2} = 0 \quad \text{at} \quad \eta = 1$$

These similarities lead to the basic assumption of the Reynolds' Analogy, which is

$$\left(\frac{d\left(\frac{T - T_w}{T_{aw} - T_w}\right)}{d\eta_T} \right)_{\eta=0} = \left(\frac{d\left(\frac{u}{U}\right)}{d\eta_M} \right)_{\eta=0}$$

After making this substitution, q_w can be expressed in terms of the dimensionless velocity gradient.

$$q_w = \frac{k(T_{aw} - T_w)}{\delta_T} \left(\frac{d\left(\frac{u}{U}\right)}{d\eta_M} \right)_{\eta=0}$$

The convective heat flux rate is often expressed in terms of a heat transfer coefficient multiplied by the temperature difference between the boundary layer and the surface.

$$q_w = h(T_{aw} - T_w)$$

where: h = heat transfer coefficient, BTU/ft²-sec-°F

So,

$$h = \frac{k}{\delta_T} \left(\frac{d\left(\frac{u}{U}\right)}{d\eta_M} \right)_{\eta=0}$$

To this point, any solution of the momentum equation can be used to get the dimensionless velocity gradient. The solution available from the previous section of this report is the one from the Karmen-Pohlhausen integral method.

$$\left(\frac{d\left(\frac{u}{U}\right)}{d\eta_M} \right)_{\eta=0} = \left(2 + \frac{\lambda}{6} \right)$$

One further assumption is needed for the solution. That is,

$$\delta_T = \delta_M$$

is also obtained from the solution of the momentum equation.

$$h = \frac{k}{\delta_M} \left(2 + \frac{\lambda}{6} \right)$$

Estimation of the Adiabatic Wall Temperature

The adiabatic wall temperature must also be calculated or determined in order to calculate the convective heat transfer rate. If convective heating transfer is the only mode of heat transfer, the adiabatic wall temperature is the maximum temperature that the heated surface can reach regardless of the length of time that convective heating takes place. When the surface reaches the adiabatic wall temperature, there is no longer any temperature difference that can provide convective heat input to the surface.

The estimation of adiabatic wall temperature is a trivial calculation for classical boundary layers. It is the total temperature of the flow at the outer edge of the boundary layer.

$$(T_{aw})_{Classical} = T_{Total} = T_{Static} + \frac{U^2}{2 g_c J c_p}$$

Basically, this means that the temperature in the boundary layer at the surface can be raised to $T_{aw} = T_{total}$ because the kinetic energy in the flow is converted to sensible heat as the flow is stopped by the frictional effects in the boundary layer.

When heat transfer takes place between the boundary layer and the surface, heat lost from the boundary layer is replaced by energy from the uniform flow above the boundary layer. The flow above the boundary layer is theoretically infinite in height, and has infinite capacity to replace any heat lost from the boundary layer to the surface. Also, the uniformity of the temperature outside the boundary layer dictates that heat will flow in only one direction between the boundary layer and the flow outside the boundary layer.

The temperature distribution in and above the boundary layer in the impingement zone of jet exhausts differs from that of classical theory as illustrated in Figure A-7. At the top of the boundary layer, the temperature is a maximum, which is the static temperature of the jet streamline at the outer edge. Due to its velocity, the streamline has even higher total temperature. Unlike the classical case, however, the total temperature of the outer streamline does not represent the potential of an infinite source of energy that is available to replace all heat transferred from the boundary layer to the surface. The reason is that the static and total temperatures decrease in both directions vertically from the streamline at the top of the boundary layer.

One can consider that the flow in the impingement zone is composed of two parts: (a) the laminar boundary layer, which is immediately above the surface of the specimen; and (b) a turbulent mixing layer which is above the boundary layer. The turbulent mixing layer is a continuation of the turbulent jet exhaust plume. At the upper edge of the boundary layer, the temperature of the boundary layer equals the temperature of the mixing layer, and the slope $(\partial T / \partial y)_{y=\delta} = 0$ in both parts of the flow. The streamline which separates the two parts, i.e., the streamline at the outer edge of the boundary layer, can theoretically be traced back to the nozzle where the exhaust flow becomes the start of the jet plume. Throughout the path of the streamline, it has been affected by the turbulent mixing in the plume and in the mixing layer

above the boundary layer. If we consider the streamline at the outer edge of the boundary layer at $r=x$, then the path length of the streamline at that point is approximately $(z+x)$, where z is the distance of separation between the nozzle exit plane and the specimen. Turbulent mixing has acted on the streamline over the entire length $(z+x)$. Therefore, the static temperature and total temperature at the outer edge of the boundary layer might be approximately that of the streamline in an undisturbed plume (no specimen in the plume) if the temperatures were measured at a distance of $(z+x)$ from the exit plane of the nozzle. Using this reasoning, it was assumed that the temperatures at the outer edge of the boundary layer would be those for the streamline in an undisturbed plume at distance $(z+x)$ below the nozzle.

An alternative to computing convective heat transfer with the expression $h(T_{aw} - T_w)$ is to use the expression $k(\partial T / \partial y)_{y=0}$. This expression requires knowledge of the temperature distribution $T = T(x, y)$ in the boundary layer. Determination of the temperature distribution might be made with computational fluid dynamics (CFD). A CFD solution was not pursued because: (a) the difficulty in predicting T_{aw} was not recognized early in the design effort; and (b) when the difficulty was recognized, it was feared that the time and budget required to acquire and gain proficiency in the use of a suitable CFD program would detract from focus on the other design requirements of the AESF.

Determination of the temperature distribution and $k(\partial T / \partial y)_{y=0}$ might also have been made by combining a boundary layer solution with a solution for turbulent mixing layer. The solutions would be forced to have the same boundary conditions of temperature and $\partial T / \partial y = 0$ where they meet at the outer edge of the boundary layer. No such combination of solutions was found in the literature. Derivation of this combination of solutions was also considered to be outside the scope of this study.

A.5 Analysis of Temperatures of Heated Specimens

Temperature distributions and histories of the specimens exposed to exhaust gas flow have been calculated using finite difference approximations to the heat balance equations described below.

The specimens are circular cylindrical in shape, with diameters of 24 inches and heights of 6 inches. They are made from differing concrete mix designs, so the properties (density, thermal conductivity, specific heat, coefficient of thermal expansion, etc.) vary as the mix design changes.

For the finite difference solution, the specimens are assumed to be divided into "nodes" of various shapes and sizes. The nodes are small enough so that distances (Δr , Δz) between adjacent nodes approximate the infinitesimal distances (dr , dz) in the heat conduction differential equation. Figure A-6 shows the nodal geometries assumed for the circular cylindrical specimens. The nodes are formed by imaginary cuts through the specimens. If a vertical penetration is made through the 6 inch height of a specimen, the penetration encounters (N_z+1) nodes. Each node has thickness Δz , except for the top node which has thickness $\Delta z/2$. Therefore the characteristic thickness of nodes in the z -direction is

$$\Delta z = \frac{H}{N_z + \frac{1}{2}}$$

where: H = height of specimen, ft

$N_z + 1/2$ = number of nodes in the z -direction,
dimensionless

Imaginary annular cuts are also made throughout the 24 inch diameter of the specimens. The annular cuts are spaced so that the number of nodes encountered is (N_r+1) as one moves from the center of the specimen to the outer radius. Therefore all nodes have radial lengths of Δr , except the center nodes which are circular with radii of $\Delta r/2$. The characteristic thickness of nodes in the r -direction is

$$\Delta r = \frac{\frac{D}{2}}{N_r + \frac{1}{2}}$$

where: D = diameter of specimen, ft

$N_r + 1/2$ = number of nodes in the r -direction,
dimensionless

Imaginary cuts are also made radially in the specimens to form the width of the nodes. The radial cuts are not extended to the center of the specimens, but only from the outer diameters of the center nodes to the outer diameter of specimens. This leaves the center nodes as circular cylinders. All other nodes, however, are wedge-shaped. Each of the wedge-shaped nodes has an angular width of

$$\Delta\theta = \frac{2\pi}{N_\theta}$$

where: N_θ = number of nodes in the radial direction, dimensionless

Numbers are assigned to each layer formed by the imaginary cuts through the height H , to each annulus formed by the imaginary annular cuts, and to each wedge section formed by the imaginary cuts along radii. In this way, each node has a unique combination of numbers which locates its position vertically, radially, and angularly. The assumption is made below that heating of the specimens is uniform in the angular direction. If the temperature distribution history is known at one angular position, the same distribution history occurs at all other angular positions. Therefore, temperature distribution histories are calculated for only one wedge-shaped slice out of each specimen. It is necessary to number the nodes in only one slice. The layers are numbered $i = 1$ to (N_z+1) , starting at the upper surface. The annuli are numbered $j = 1$ to (N_r+1) , starting at the center of the specimen. Each node may be located knowing i and j .

The conservation of energy equation is applied to each node to determine its temperature history. The conservation of energy equation for a node is

$$\begin{aligned} \left(\frac{dE}{dt}\right)_{node} &= \frac{\delta Q}{\delta t} + \frac{\delta W_{sh}}{\delta t} + \left(\frac{dm}{dt}\right)_{entering} \left(h_{enth} + \frac{V^2}{2 g_c J} + \frac{g z}{g_c J} \right)_{entering} \\ &+ \left(\frac{dm}{dt}\right)_{leaving} \left(h_{enth} + \frac{V^2}{2 g_c J} + \frac{g z}{g_c J} \right)_{leaving} \end{aligned}$$

Since there is no flow of material into or out of each node, the terms $(dm/dt)_{entering}$ and $(dm/dt)_{leaving}$ both equal zero. Also, there is no shaft work, so $\delta W_{sh}/\delta t = 0$. Therefore,

$$\left(\frac{dE}{dt}\right)_{node} = \frac{\delta Q}{\delta t}$$

In the finite difference solution, one is interested in the heat transfer and the change in energy in the node during a short time interval, Δt . Integrate the above equation between time "t" and time "t + Δt ".

$$E_{node}(t + \Delta t) - E_{node}(t) = \int_t^{t+\Delta t} \left(\frac{dE}{dt} \right)_{node} dt = \int_t^{t+\Delta t} \left(\frac{\delta Q}{\delta t} \right) dt = \Delta Q$$

where: ΔQ = net heat transferred to node during the time interval Δt , BTU

The change in the energy content of a node is

$$E_{node}(t + \Delta t) - E_{node}(t) = \rho \Delta Vol c_p [T(t + \Delta t) - T(t)]$$

where: ρ = mass density of the node material, lb_m/ft^3

ΔVol = volume of the node, ft^3

c_p = specific heat of the node material, $BTU/lb_m-^{\circ}F$

$T(t)$ = average temperature of the node at time t, $^{\circ}F$

t = time, sec

The net heat transferred to a node during the time interval is the sum of the heat transferred across all surfaces. Because of the assumption of symmetry in the angular direction, there is no heat transfer in that direction. Heat transfer in the vertical and radial directions contribute to the net heat transfer. The heat transferred across each surface during the time interval is

$$Q_{surface} = \dot{q} \Delta A_{surface} \Delta t$$

where: \dot{q} = heat flux, BTU/ft^2-sec

$\Delta A_{surface}$ = area of surface perpendicular to direction of heat flux, ft^2

The temperature distribution history of the specimen is affected by all three types of energy transfer, i.e., conduction, convection, and radiation. Some nodes experience only conduction, while others experience all three types of energy transfer. The heat flux equations for energy transfer to and from the various nodes are presented below:

$$\dot{q}_{cond,radial} = k \frac{T_{i,j}(t) - T_{i+1,j}(t)}{\Delta r}$$

$$\dot{q}_{cond,vertical} = k \frac{T_{i,j}(t) - T_{i,j+1}(t)}{\Delta z}$$

where: k = thermal conductivity, BTU-ft/ft²-sec-°F

subscripts $i, j, i+1$, and $j+1$ designate locations of a node and an adjacent node

$$\dot{q}_{conv} = \frac{[h_j (T_{aw,j} - T_{l,j}(t + \Delta t))] + [h_j (T_{aw,j} - T_{l,j}(t))]}{2}$$

where: h_j = convective heat transfer coefficient at surface location j , BTU/ft²-sec-°F

$T_{aw,j}$ = adiabatic wall temperature at surface location j , °F

The specimens are tested in an enclosure, so solar radiation to the specimens is negligible. It was also found that there was negligible radiation from the simulated jet engine to the specimens. Therefore, the radiation heat transfer for the specimens includes only the reradiation from the hot surface nodes of the specimens.

$$\dot{q}_{rad} = \epsilon \sigma \frac{[T_{l,j}(t)]^4 + [T_{l,j}(t + \Delta t)]^4}{2}$$

where: ϵ = emissivity of the surface of the specimen, dimensionless

σ = Stefan-Boltzmann's constant
 $= 4.83 \times 10^{-13}$ BTU/ft²-sec-F⁴

Heat flux contributions to nodes, and the resulting finite difference equations in various locations, are summarized below.

(1) Node $i=1, j=1$ (circular node at the top surface, in the center of the specimen):

Top surface: convection, reradiation

Bottom surface and circular perimeter surface: conduction

$$\begin{aligned}
T_{1,1}(t + \Delta t) = & \frac{2 h \Delta t}{\rho c_p \Delta z} \left(\frac{2 T_{aw,1} - T_{1,1}(t + \Delta t) - T_{1,1}(t)}{2} \right) \\
& - \frac{2 \varepsilon \sigma \Delta t}{\rho c_p \Delta z} \left(\frac{[T_{1,1}(t + \Delta t)]^4 + [T_{1,1}(t)]^4}{2} \right) \\
& + \frac{2 \left(\frac{\Delta z}{\Delta r} \right)^2}{M} T_{1,2}(t) + \frac{2}{M} T_{2,1}(t) + \left[1 - \frac{2 \left(\frac{\Delta z}{\Delta r} \right)^2}{M} - \frac{2}{M} \right] T_{1,1}(t)
\end{aligned}$$

where: $M = (\rho c_p \Delta x^2) / (k \Delta t)$, is called the "Modulus",
dimensionless

(Note 1: In the finite difference equation above, the term $T_{1,1}(t + \Delta t)$ appears on both sides of the equation, and cannot be isolated for an explicit solution. Therefore, the solution of the equation must be by iteration. The technique is to assume a value of $T_{1,1}(t + \Delta t)$ on the right-hand-side, and calculate the value of $T_{1,1}(t + \Delta t)$ on the left-hand-side. Then compare the assumed value and the calculated value. If they agree within a specified tolerance (say 1% difference), then stop the iteration. Otherwise, change the assumed value on the right-hand-side and repeat the process. The same situation occurs for all nodes at the top surface of the specimen, and the same iteration process is applicable to all those nodes.)

(Note 2: The grouping of variables to form the modulus M occurs in all conduction terms of the finite difference solution. For stability of the finite difference solution, $M \geq 2$. If $M < 2$, then a low value of $T_{i,j}(t)$ results in a prediction of a high value of $T_{i,j}(t + \Delta t)$, and vice versa. This is contrary to nature, which dictates that a low value of $T_{i,j}(t)$ remain low after only a short time interval. Therefore, for stability of the finite difference solutions, the increments of time and nodal spacing, Δt and Δz , respectively, are chosen so that $M = 3$ to 5 . If M is too large, the solution is stable, but the time steps are undesirable short, and the number of calculations is excessive.)

(2) Nodes $i=1, j=2$ to N_r (wedge-shaped nodes at the top surface of the specimen, between the center and the outermost nodes):

Top surface: convection, reradiation

Bottom surface and two end surfaces: conduction

$$\begin{aligned}
T_{1,j}(t + \Delta t) = & \frac{2 h \Delta t}{\rho c_p \Delta z} \left(\frac{2 T_{aw,j} - T_{1,j}(t + \Delta t) T_{1,j}(t)}{2} \right) \\
& - \frac{2 \varepsilon \sigma \Delta t}{\rho c_p \Delta z} \left(\frac{[T_{1,j}(t + \Delta t)]^4 + [T_{1,j}(t)]^4}{2} \right) \\
& + \frac{1}{M} \left(\frac{\Delta z}{\Delta r} \right)^2 \left(\frac{r - \frac{\Delta r}{2}}{r} \right) T_{1,j-1}(t) + \frac{1}{M} \left(\frac{\Delta z}{\Delta r} \right)^2 \left(\frac{r + \frac{\Delta r}{2}}{r} \right) T_{1,j+1}(t) \\
& + \frac{2}{M} T_{2,j}(t) + \left[1 - \frac{2}{M} \left(\frac{\Delta z}{\Delta r} \right)^2 - \frac{2}{M} \right] T_{1,j}(t)
\end{aligned}$$

(3) Node $i=1, j=N_r+1$ (outermost wedge-shaped node at the top surface of the specimen):

Top surface: convection, reradiation

Bottom surface and inner end surface: conduction

Outer end surface: assumed insulated ($q = 0$).

$$\begin{aligned}
T_{1,N_r}(t + \Delta t) = & \frac{2 h \Delta t}{\rho c_p \Delta z} \left(\frac{2 T_{aw,N_r} - T_{1,N_r}(t + \Delta t) T_{1,N_r}(t)}{2} \right) \\
& - \frac{2 \varepsilon \sigma \Delta t}{\rho c_p \Delta z} \left(\frac{[T_{1,N_r}(t + \Delta t)]^4 + [T_{1,N_r}(t)]^4}{2} \right) \\
& + \frac{1}{M} \left(\frac{\Delta z}{\Delta r} \right)^2 \left(\frac{r - \frac{\Delta r}{2}}{r} \right) T_{1,N_r-1}(t) \\
& + \frac{2}{M} T_{2,N_r}(t) + \left[1 - \frac{1}{M} \left(\frac{r - \frac{\Delta r}{2}}{r} \right) \left(\frac{\Delta z}{\Delta r} \right)^2 - \frac{2}{M} \right] T_{1,N_r}(t)
\end{aligned}$$

(4) Nodes $i=2$ to N_z , $j=1$ (circular nodes in the center of the specimen, except for the top surface node and the bottom surface node of the specimen):
Top, bottom, and circular perimeter surfaces: conduction

$$T_{i,1}(t + \Delta t) = \frac{4}{M} \left(\frac{\Delta z}{\Delta r} \right)^2 T_{i,2}(t) + \frac{1}{M} [T_{i-1,1}(t) + T_{i+1,1}(t)] \\ + \left[1 - \frac{4}{M} \left(\frac{\Delta z}{\Delta r} \right)^2 - \frac{2}{M} \right] T_{i,1}(t)$$

(5) Nodes $i=2$ to N_z , $j=2$ to N_r (wedge-shaped nodes vertically between the top surface nodes and bottom surface nodes of the specimen and radially between the center nodes and the outermost nodes of the specimen):
Top, bottom, and two end surfaces: conduction

$$T_{i,j}(t + \Delta t) = \frac{1}{M} \left(\frac{r - \frac{\Delta r}{2}}{r} \right) \left(\frac{\Delta z}{\Delta r} \right)^2 T_{i,j-1}(t) + \frac{1}{M} \left(\frac{r + \frac{\Delta r}{2}}{r} \right) \left(\frac{\Delta z}{\Delta r} \right)^2 T_{i,j+1}(t) \\ + \frac{1}{M} [T_{i-1,j}(t) + T_{i+1,j}(t)] + \left[1 - \frac{2}{M} \left(\frac{\Delta z}{\Delta r} \right)^2 - \frac{2}{M} \right] T_{i,j}(t)$$

(6) Nodes $i=2$ to N_z , $j=N_r+1$ (outermost nodes vertically between the top surface node and the bottom surface node of the specimen):
Top, bottom, and inner end surfaces: conduction
Outer end surface: assumed insulated ($q = 0$).

$$T_{i,N_r}(t + \Delta t) = \frac{1}{M} \left(\frac{r - \frac{\Delta r}{2}}{r} \right) \left(\frac{\Delta z}{\Delta r} \right)^2 T_{i,N_r-1}(t) + \frac{1}{M} [T_{i-1,N_r}(t) + T_{i+1,N_r}(t)] \\ + \left[1 - \frac{1}{M} \left(\frac{r - \frac{\Delta r}{2}}{r} \right) \left(\frac{\Delta z}{\Delta r} \right)^2 - \frac{2}{M} \right] T_{i,N_r}(t)$$

(7) Node $i=N_z+1$, $j=1$ (circular node at the bottom surface, in the center of the specimen):

Top surface and circular perimeter surface: conduction
 Bottom surface: assumed insulated ($q = 0$).

$$T_{N_z,1}(t + \Delta t) = \frac{4}{M} \left(\frac{\Delta z}{\Delta r} \right)^2 T_{N_z,2}(t) + \frac{1}{M} T_{N_z-1,1}(t) \\ + \left[1 - \frac{4}{M} \left(\frac{\Delta z}{\Delta r} \right)^2 - \frac{1}{M} \right] T_{N_z,1}(t)$$

(8) Nodes $i=N_z+1$, $j=2$ to N_r (wedge-shaped nodes at the bottom surface, between the center and outermost nodes):

Top surface and two end surfaces: conduction
 Bottom surface: assumed insulated ($q = 0$).

$$T_{N_z,j}(t + \Delta t) = \frac{1}{M} \left(\frac{r - \frac{\Delta r}{2}}{r} \right) \left(\frac{\Delta z}{\Delta r} \right)^2 T_{N_z,j-1}(t) + \frac{1}{M} \left(\frac{r + \frac{\Delta r}{2}}{r} \right) \left(\frac{\Delta z}{\Delta r} \right)^2 T_{N_z,j+1}(t) \\ + \frac{1}{M} T_{N_z-1,j}(t) + \left[1 - \frac{2}{M} \left(\frac{\Delta z}{\Delta r} \right)^2 - \frac{1}{M} \right] T_{N_z,j}(t)$$

(9) Node $i=N_z+1$, $j=N_r+1$ (outermost wedge-shaped node at the bottom surface of the specimen):

Top surface and inner end surface: conduction
 Bottom and outer end surfaces: assumed insulated ($q = 0$).

$$\begin{aligned}
T_{N_z, N_r}(t + \Delta t) &= \frac{1}{M} \left(\frac{r - \frac{\Delta r}{2}}{r} \right) \left(\frac{\Delta z}{\Delta r} \right)^2 T_{N_z, N_r - 1}(t) + \frac{1}{M} T_{N_z - 1, N_r}(t) \\
&+ \left[1 - \frac{1}{M} \left(\frac{r - \frac{\Delta r}{2}}{r} \right) \left(\frac{\Delta z}{\Delta r} \right)^2 - \frac{1}{M} \right] T_{N_z, N_r}(t)
\end{aligned}$$

APPENDIX REFERENCES

A.1. W. C. Reynolds, Thermodynamics, pp. 441-443, McGraw-Hill Book Company, New York, NY, 1965.

A.2. W. J. Hess and N. V. S. Mumford, Jet Propulsion for Aerospace Applications, Second Edition, pp. 44-66, Pitman Publishing Company, New York, NY, 1964.

A.3. H. Schlichting, Boundary Layer Theory, Fourth Edition, pp. 590-611, 137-140, 243-251, and 303-306, McGraw-Hill Book Company, New York, NY, 1960.

A.4. G. N. Abrahmovitch, The Theory of Turbulent Jets, MIT Press, Cambridge, MA, 1963.

Temperature	Oxygen Enthalpy	Nitrogen Enthalpy	Water Enthalpy	Carbon Dioxide Enthalpy	Methane Enthalpy	Propane Enthalpy
Deg R	BTU/lbmole	BTU/lbmole	BTU/lbmole	BTU/lbmole	BTU/lbmole	BTU/lbmole
537	0	0	-103968	-169183	-32179	-44647
600	443.2	438.4	-103471.6	-168612.3		
700	1154.2	1135.4	-102660.9	-167661.2		
800	1876.9	1834.9	-101839.4	-166660.3		
900	2612.8	2538.6	-101005.4	-165615.6		
1000	3362.4	3248.4	-100157.4	-164531.1		
1100	4125.3	3965.5	-99294.3	-163410.6		
1200	4900.7	4690.5	-98415.9	-162257.9		
1300	5687.8	5424.4	-97521.8	-161076.3		
1400	6485.3	6167.4	-96611.5	-159868.5		
1500	7292	6919.4	-95684.9	-158636.5		
1600	8107.4	7680.2	-94741.4	-157383.5		
1700	8930.5	8449.4	-93780.9	-158111.1		
1800	9760.7	9226.8	-92803.3	-154821		
1900	10597	10012.1	-91808.8	-153514.7		
2000	11438.9	10804.9	-90797.3	-152193.8		
2100	12285.8	11604.5	-89769.4	-150859.8		
2200	13137.5	12410.3	-88725.5	-149513.5		
2300	13993.7	13221.7	-87665.7	-148156.2		
2400	14854.1	14038.4	-86590.6	-146788.5		
2500	15718.3	14860	-85500.9	-145411.3		
2600	16586.3	15686.3	-84396.8	-144025.4		
2700	17457.8	16516.9	-83279.1	-142631.3		
2800	18332.7	17351.6	-82148.3	-141229.7		
2900	19211	18190	-81005.1	-139821		
3000	20092.6	19032	-79850	-138405.9		
3100	20977.4	19877.3	-78683.5	-136984.6		
3200	21865.4	20725.5	-77506.1	-135557.8		
3300	22756.5	21576.5	-76318.1	-134125.8		
3400	23650.8	22430.2	-75120.3	-132688.9		
3500	24548.2	23286.4	-73912.8	-131247.3		
3600	25448.8	24144.9	-72696.2	129801.5		
3700	26352.4	25005.6	-71470.9	128351.9		
3800	27259	25868.4	-70237.4	126898.4		
3900	28168.5	26733.3	-68996.1	-125441.5		
4000	29081	27599.9	-67747.2	-123981.1		
4200	30914.8	29338.6	-65227.9	-121050.5		
4400	32759.9	31083.6	-62682.4	-118107.4		
4600	34616.3	32834.3	-60112.7	-115152.8		
4800	36483.5	34590	-57520.8	-112187.6		
5000	38361.2	36350.3	-54908.9	-109212.5		

TABLE A-1. Enthalpies and heats of formation for compounds of the combustion of methane and propane

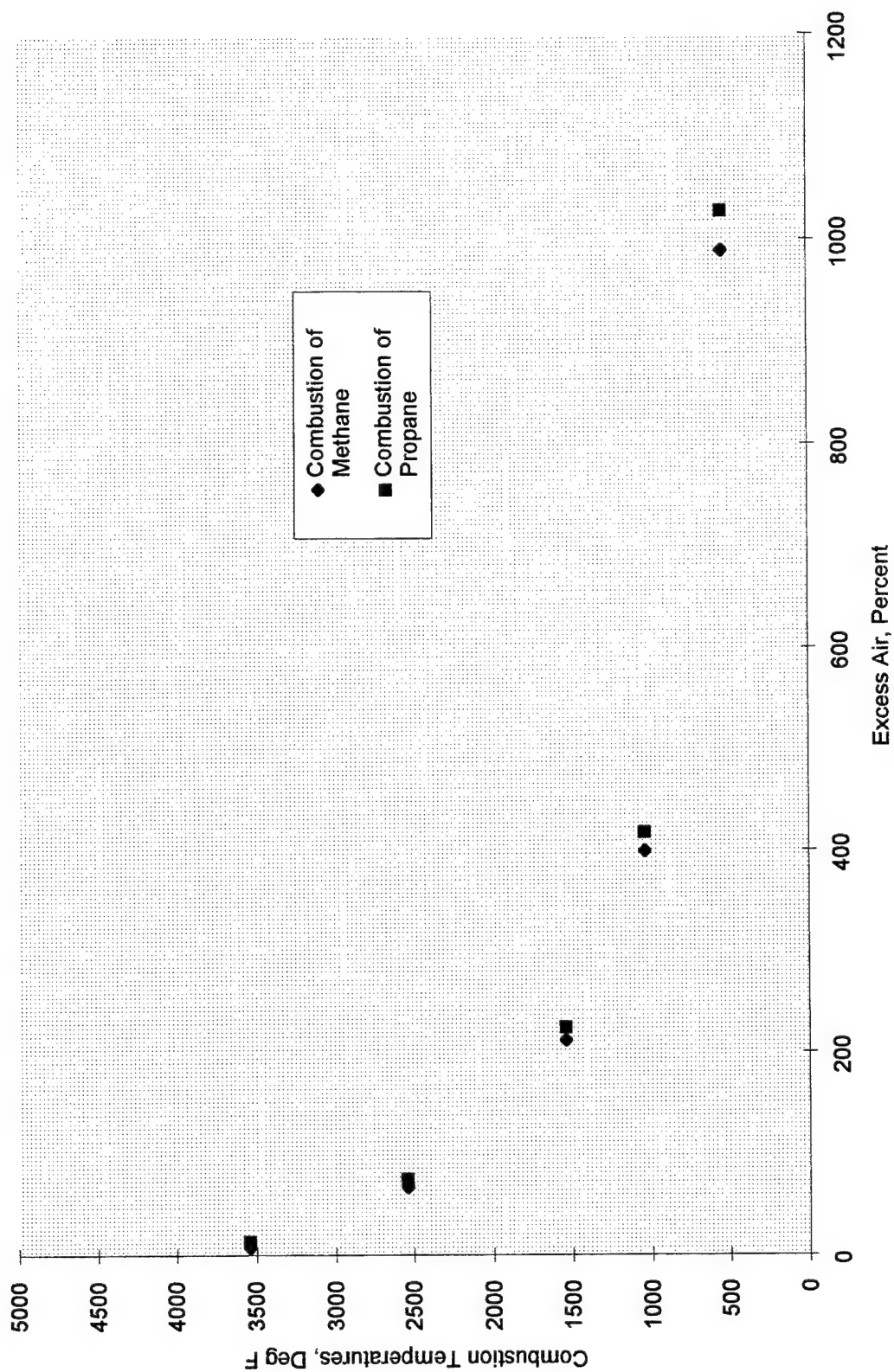


Figure A-1. Combustion temperatures as a function of excess air for methand and propane

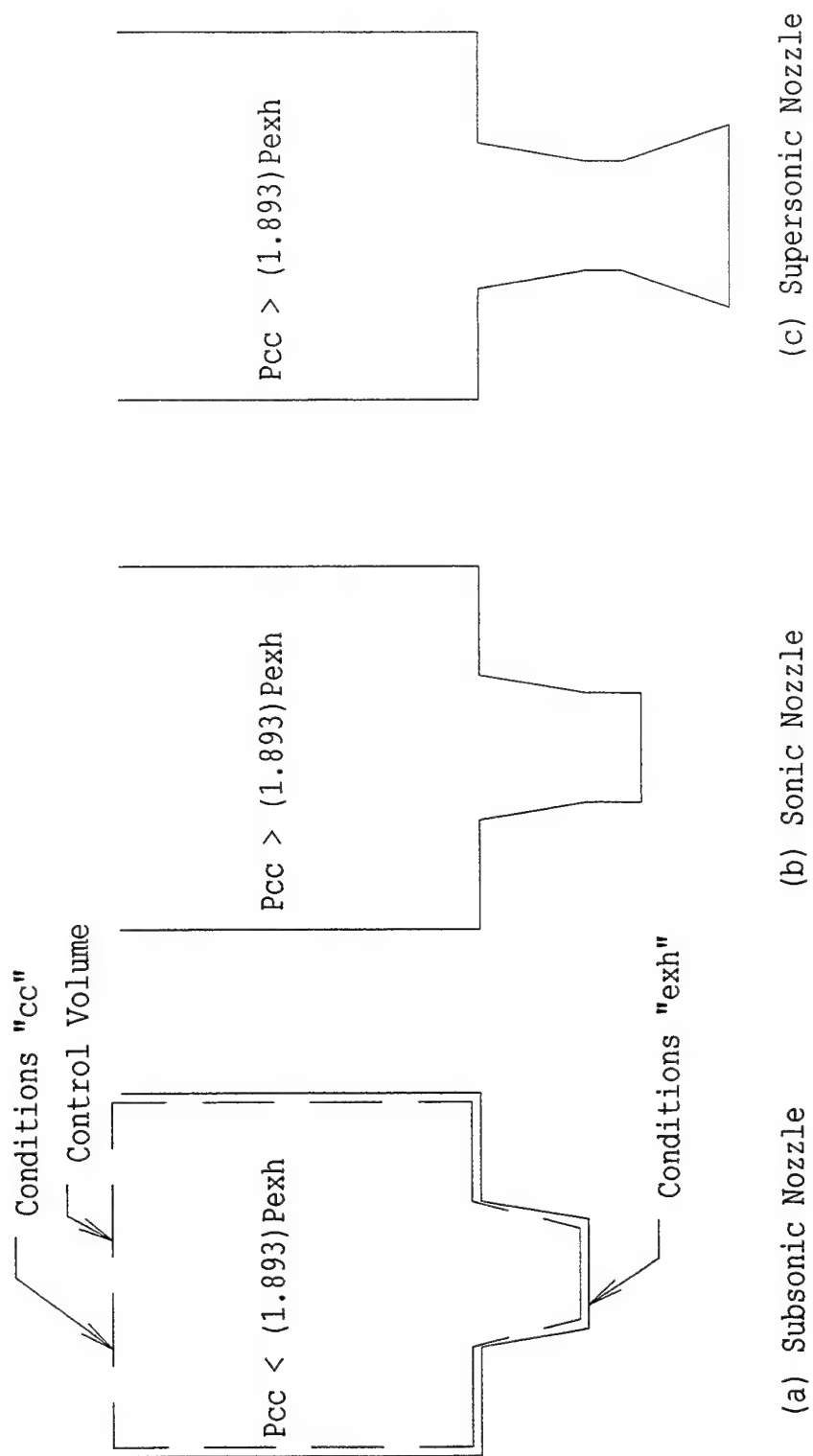


Figure A-2. Illustrations of subsonic, sonic, and supersonic nozzle configurations and required combustion chamber pressures

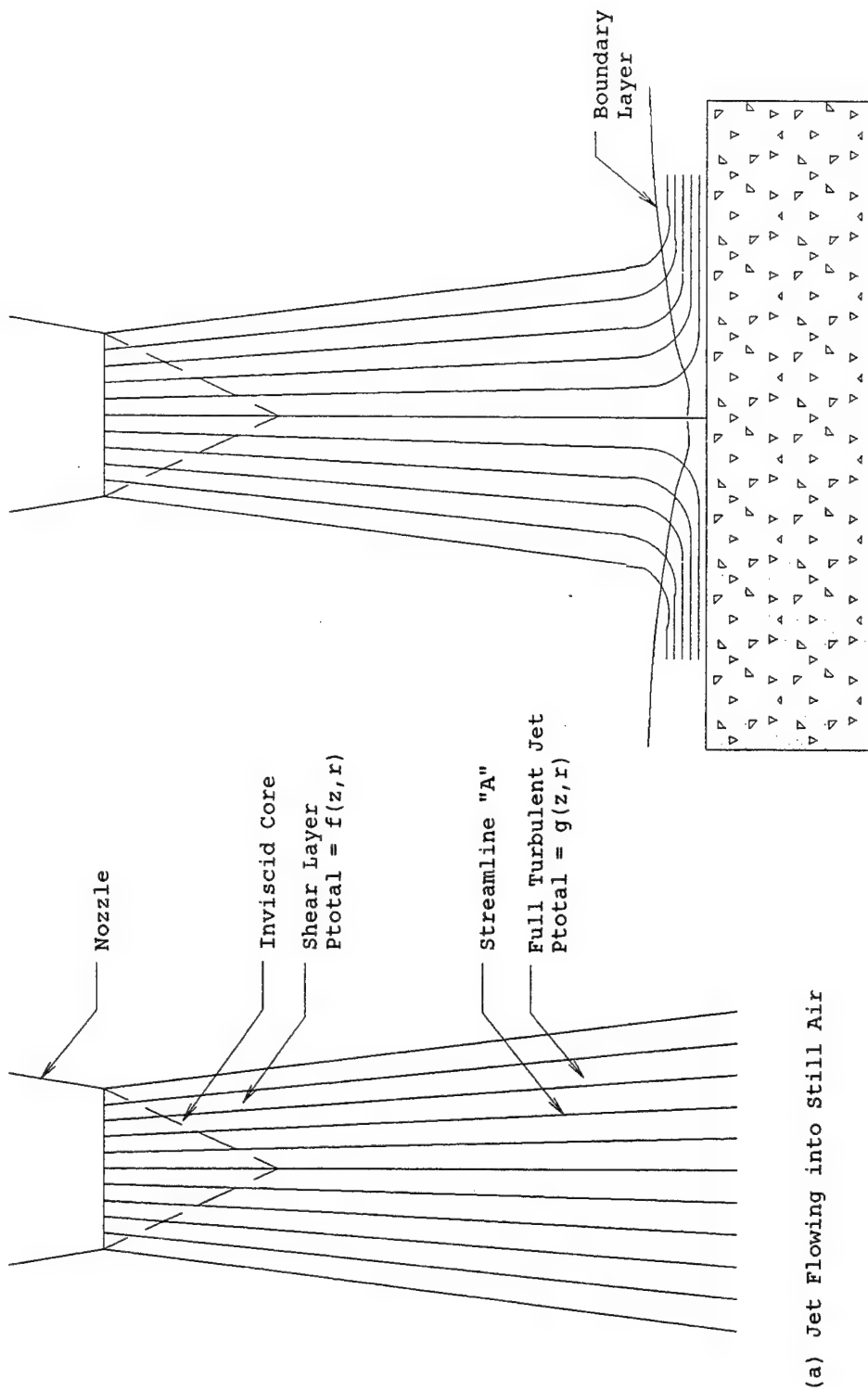


Figure A-3. Features of a turbulent jet flowing into still air, and impinging on a concrete specimen.

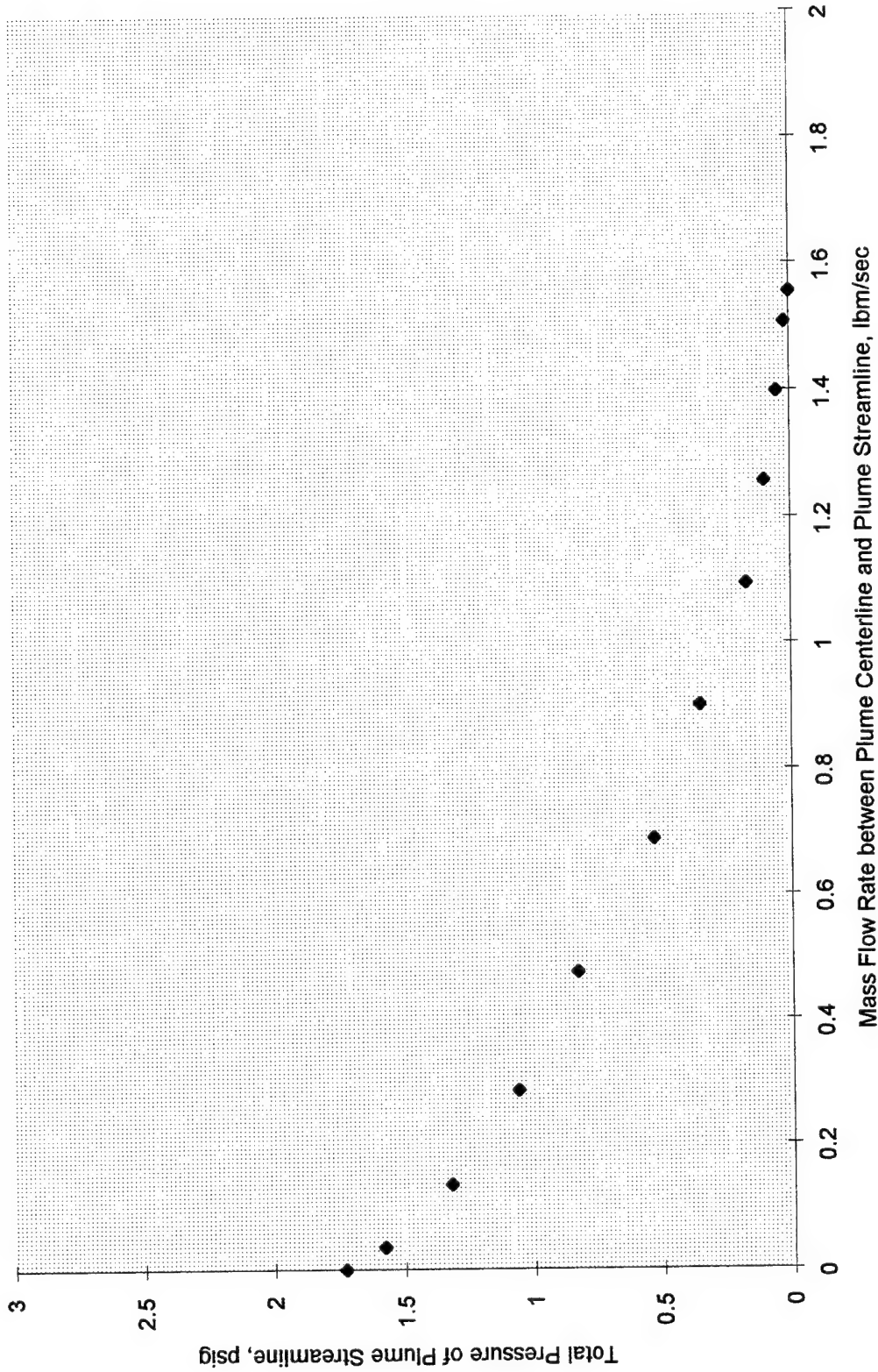


Figure A-4. Total pressure as a function of mass flow rate for streamlines of the F/A-18 APU engine plume, Z=12"

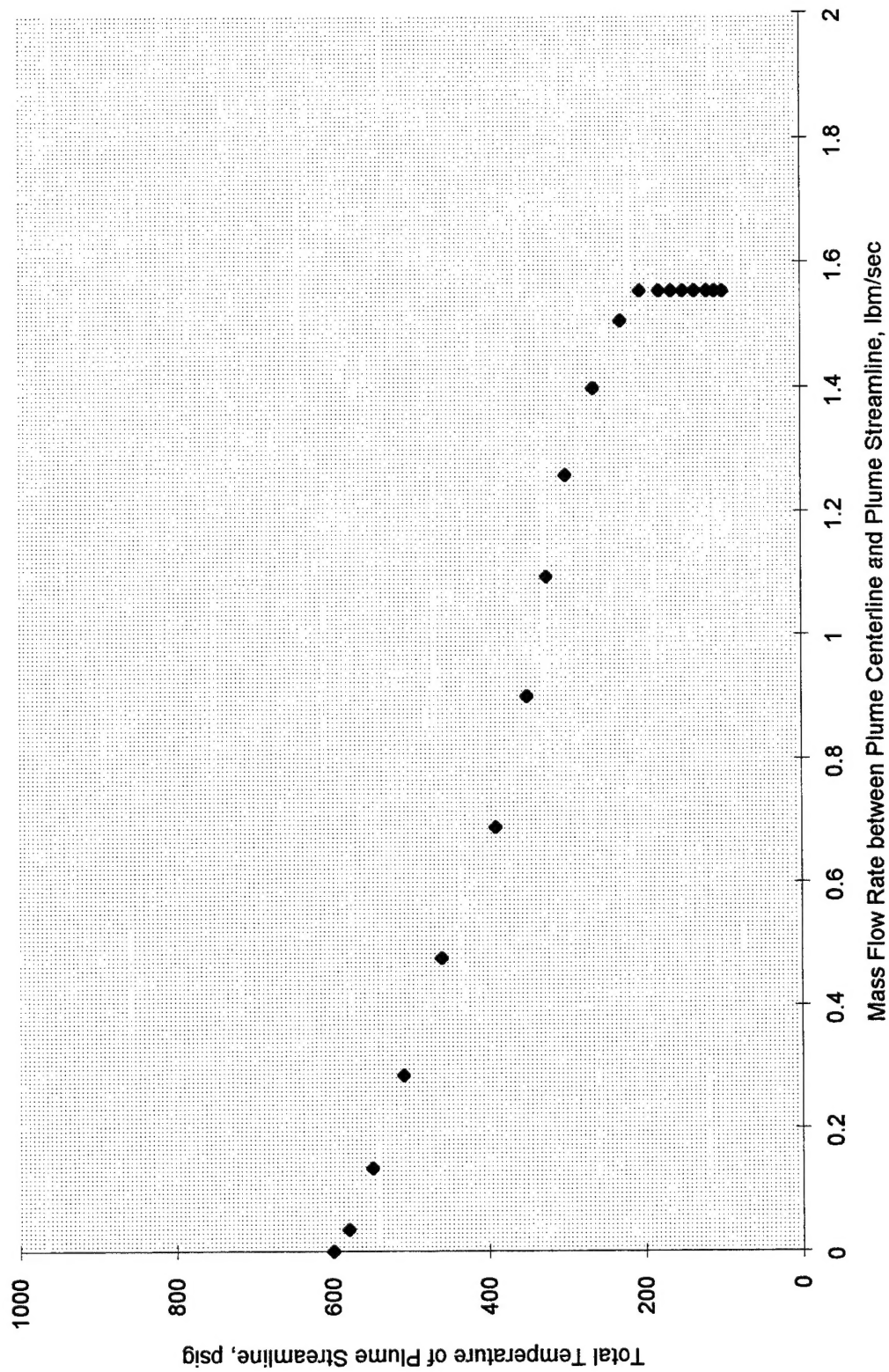


Figure A-5. Total temperature as a function of mass flow rate for streamlines of the F/A-18 APU engine plume, Z=12"

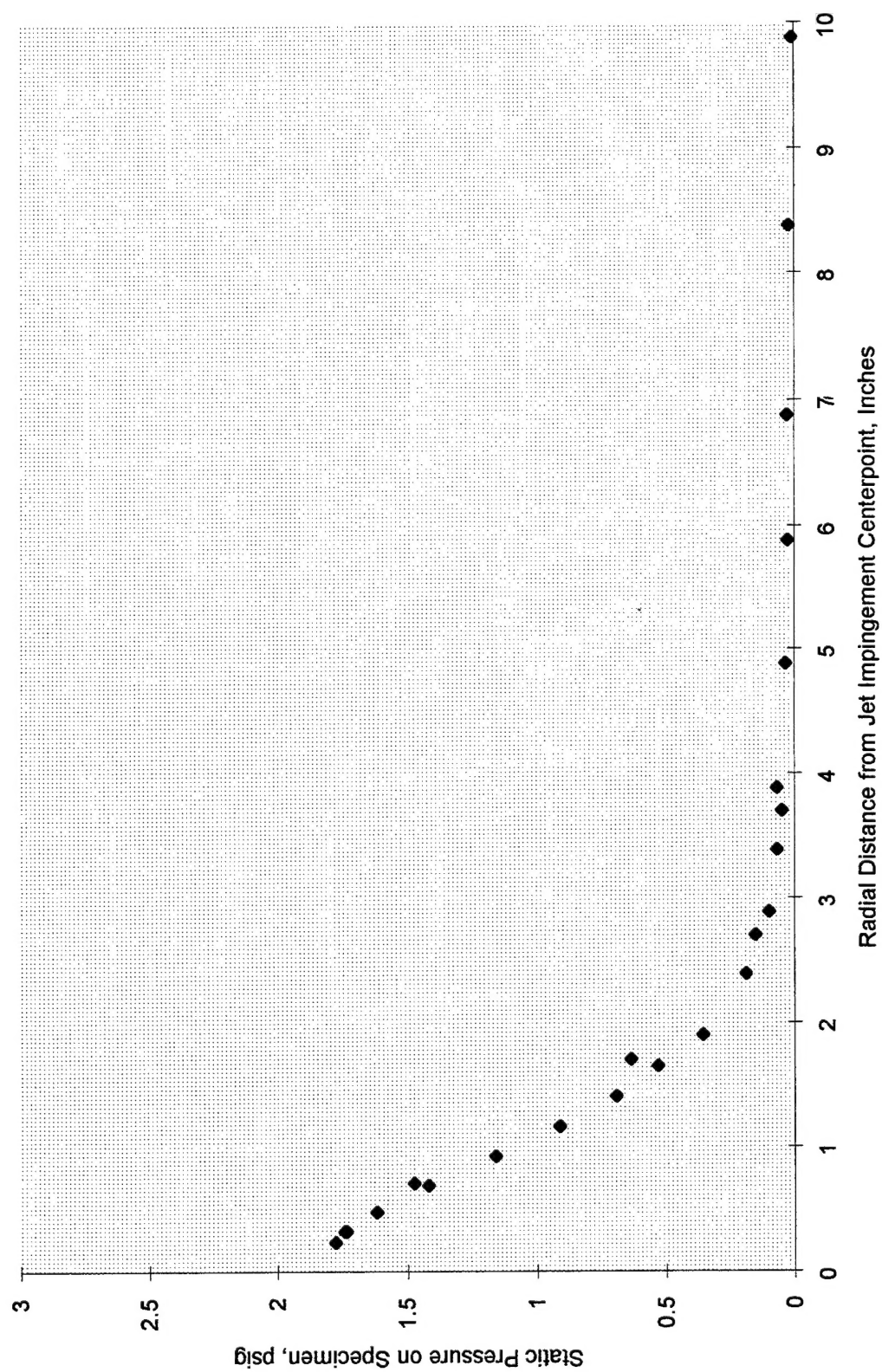
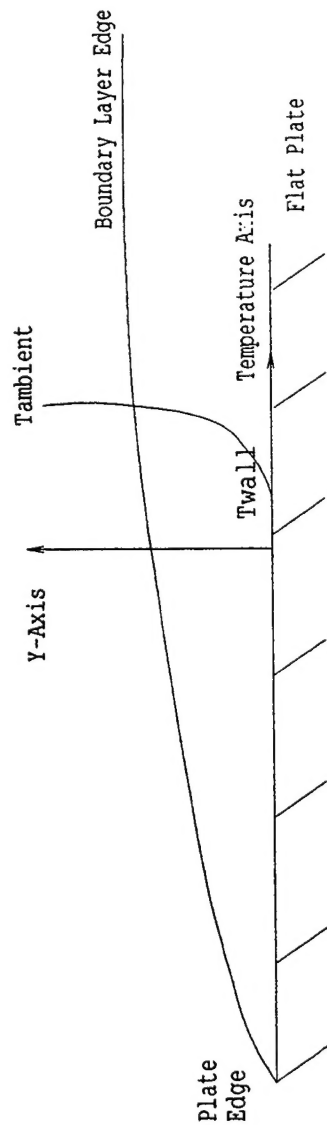
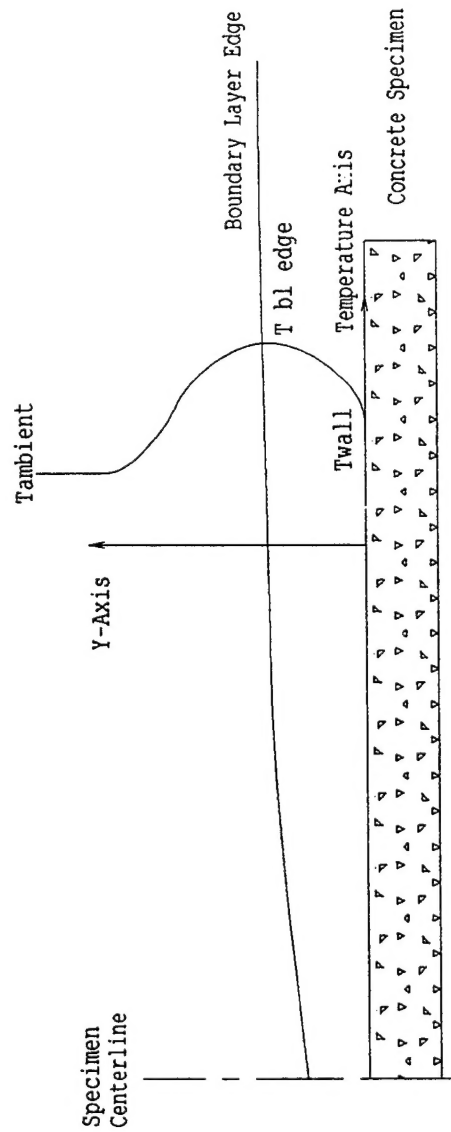


Figure A-6. Static pressure as a function of distance from stagnation point on concrete specimens exposed to the simulated F/A-18 APU plume, $Z=12"$



(a) Temperature Profile in Classical Flat Plate Boundary Layer



(b) Temperature Profile in Boundary Layer Formed by Jet Impingement

Figure A-7. Comparative illustrations of classical boundary layer and boundary layer formed by jet impingement

DISTRIBUTION LIST

AFESC / TECH LIB, TYNDALL AFB FL
ARMY CERL / LIB, CHAMPAIGN IL
ARMY CEWES / CODE GP, VICKSBURG MS
ARMY CEWES / LIBRARY, VICKSBURG MS
ARMY CRREL / LIBRARY, HANOVER NH
DTIC / ALEXANDRIA VA
FAA / CODE AAS 200 (RICE), WASHINGTON DC
FAA / CODE AAS 200 (WORCH), WASHINGTON DC
LANTNAVFACENGCOM / CODE 04C (DONNALLY), NORFOLK VA
LANTNAVFACENGCOM / CODE 411 (NOTHNAGEL), NORFOLK VA
NAVFACENGCOM / CODE 133, ALEXANDRIA VA
NAVFACENGCOM / CODE 1335 (B. CHAKRABARIT), ALEXANDRIA VA
NAVFACENGCOM / CODE 151 (SKAR), ALEXANDRIA VA
NAVFACENGCOM / CODE 15R, ALEXANDRIA VA
NFESC / CODE OOCE, WASHINGTON DC
NFESC / CODE OOCEA (JONES), WASHINGTON DC
NORTHNAVFACENGCOM / CODE 09X, LESTER PA
NORTHNAVFACENGCOM / CODE 164P, SCHIAVINO, LESTER PA
PACNAVFACENGCOM / CODE 102, PEARL HARBOR HI
PACNAVFACENGCOM / CODE 405, PEARL HARBOR HI
PACNAVFACENGCOM / LIBRARY, PEARL HARBOR HA
SOUTHNAVFACENGCOM / CODE 4023 (BEVERLY), NORTH CHARLESTON SC
SOUTHNAVFACENGCOM / LIBRARY, NORTH CHARLESTON SC
SOWESTNAVFACENGCOM / CODE 04S (LIBRARY), SAN DIEGO CA
SOWESTNAVFACENGCOM / CODE 13, SAN DIEGO CA
SOWESTNAVFACENGCOM / CODE 405, SAN DIEGO CA
WESTNAVFACENGCOM / CODE 09F4C (LIBRARY), SAN BRUNO CA
WRIGHT LAB / CODE FIVCO-OL, TYNDALL AFB FL